

Patrícia Santos Bizzotto Soares

**EXPERIMENTAL STUDY ON CONDENSATION HEAT
TRANSFER AND PRESSURE DROP OF R134a IN PARALLEL
MINICHANNELS**

Dissertação submetida ao Programa de
Pós-Graduação em Engenharia Mecâ-
nica da Universidade Federal de Santa
Catarina para a obtenção do Grau de
Mestre em Engenharia Mecânica.
Orientador: Prof. Júlio César Passos,
Dr.

Florianópolis
2017

Ficha de identificação da obra elaborada pelo autor,
através do Programa de Geração Automática da Biblioteca Universitária da UFSC.

Soares, Patrícia Santos Bizzotto
Experimental study on condensation heat transfer
and pressure of R134a in parallel minichannels /
Patrícia Santos Bizzotto Soares ; orientador, Júlio
César Passos , 2017.
241 p.

Dissertação (mestrado) - Universidade Federal de
Santa Catarina, Centro Tecnológico, Programa de Pós
Graduação em Engenharia Mecânica, Florianópolis, 2017.

Inclui referências.

1. Engenharia Mecânica. 2. Condensation. 3.
Minichannels. 4. Multi-Port Extruded tubes. 5.
R134a. I. , Júlio César Passos. II. Universidade
Federal de Santa Catarina. Programa de Pós-Graduação
em Engenharia Mecânica. III. Título.

Patrícia Santos Bizzotto Soares

**EXPERIMENTAL STUDY ON CONDENSATION HEAT
TRANSFER AND PRESSURE DROP OF R134a IN PARALLEL
MINICHANNELS**

Esta Dissertação foi julgada adequada para obtenção do Título de “Mestre em Engenharia Mecânica” e aprovada em sua forma final pelo Programa de Pós-Graduação em Engenharia Mecânica.

Florianópolis, 15 de Agosto de 2017

Prof. Jonny Carlos da Silva, Dr.
Coordenador do Curso

Banca Examinadora:

Prof. Júlio César Passos, Dr. – Orientador
Universidade Federal de Santa Catarina

Prof^a. Márcia Barbosa Henriques Mantelli, PhD
Universidade Federal de Santa Catarina

Prof. Amir Antônio Martins de Oliveira Júnior, PhD
Universidade Federal de Santa Catarina

Prof. Joaquim Manoel Gonçalves, Dr.
Instituto Federal de Santa Catarina

ACKNOWLEDGEMENTS

I would like to express my gratitude to LEPTEN/Boiling for providing facilities for this project. I wish to thank my advisor, Dr. Júlio César Passos, for this opportunity.

It is my pleasure to express my deepest appreciation to my colleagues, whose contributions and support were very helpful. I am glad to specially acknowledge Danielle Lima, Isadora Limas, Mônica Machuca, Rafael Passarella, and Selen Sousa.

I would like to thank Guilherme for his constant support. It is due to his exhaustive reviews and constructive criticism that this work has been compiled to the present form.

Finally, I would like to acknowledge the understanding, supporting and encouragement of my mother, without which it would have been impossible to complete this work.

*“What matters most is how well you walk
through the fire.”*

Charles Bukowski

ABSTRACT

The turn of the twenty-first century brought a technological advance that was evident in space technology and electronics. These two technologies mark a trend toward the miniaturization of devices. Therefore, an intensification of convective heat transfer with phase changes is needed. An example of passive methods that can be used to increase convective heat process includes, among others, diameter tube reduction. The increase in the heat transfer coefficient value serves as a measure of this intensification effectiveness. In the present study, heat transfer coefficient and pressure drop are experimentally investigated during condensation of R134a inside seven horizontal and parallel minichannels. Differential thermopile heat flux transducers were used in order to measure the heat flux, which is an innovative technique. The test conditions include pressure P , vapor quality x , heat flux q'' and mass flux G , ranging from 7.4 to 9.1 bar, 0.89 to 1, 8.2 to 10.8 kW/m² and 391 to 542 kg/(m²s), respectively. The influences of saturation temperature, heat flux, mass flux, and vapor quality on the heat transfer coefficient, h , and pressure drop, Δp , are evaluated. The results show that mass flux and vapor quality have an important influence on h , whilst heat flux does not present an evident effect. In addition, higher saturation temperatures present greater heat transfer coefficients for high vapor qualities. This influence decays as condensation occurs. The mass flux increase and the saturation temperature decrease cause a Δp increase, whereas the heat flux does not show influence. The experimental results for heat transfer coefficient and pressure drop values are compared to correlations described in literature. The results indicate that the prediction of the heat transfer coefficients requires specific correlations for small diameter channels. On the other hand, the pressure drop is well estimated by the classical correlations for large diameter channels.

Keywords: Condensation; Minichannels; Heat transfer coefficient; Pressure Drop

RESUMO

A virada do século XXI trouxe avanço tecnológico perceptível no crescimento de produção tecnológica de dispositivos espaciais e eletrônicos. Estas duas tecnologias marcam uma tendência à miniaturização destes dispositivos. Por isso, novas maneiras de realizar a troca de calor tornam-se prioridade. A realização prática dessas novas maneiras envolve implementação de métodos de transferência de calor por convecção com mudança de fase. Um dos métodos que pode ser implementado para intensificar a transferência de calor por convecção inclui a redução do diâmetro dos canais através dos quais o fluido refrigerante escoar. O aumento do valor do coeficiente de transferência de calor serve como medida da eficácia desta intensificação. No presente estudo, o coeficiente de transferência de calor e a queda de pressão são investigados experimentalmente durante a condensação de R134a no interior de sete minicanais paralelos, orientados horizontalmente. Foram utilizados fluxímetros de calor para medir o fluxo de calor, o que é uma técnica inovadora. As condições de teste abrangem os intervalos de pressão P , título x , fluxo de calor q'' e velocidade mássica G , de 7,4 a 9,1 bar, 0,89 a 1, 8,2 a 10,8 kg/m² e 391 a 542 kg/(m²s), respectivamente. As influências da temperatura de saturação, fluxo de calor, velocidade mássica e título sobre o coeficiente de transferência de calor, h , e sobre a queda de pressão, Δp , são avaliadas. Os resultados indicam que a velocidade mássica e o título possuem forte influência sobre o h . No entanto, o fluxo de calor não apresenta efeito evidente. Além disso, as temperaturas de saturação mais altas apresentam maiores coeficientes de transferência de calor para altos títulos. Esta influência diminui à medida que a condensação ocorre. O aumento da velocidade mássica e a diminuição da temperatura de saturação provocam aumento da Δp , enquanto o fluxo de calor não demonstra influência. Os resultados experimentais para os coeficientes de transferência de calor e queda de pressão são comparados às correlações descritas na literatura. Os resultados mostram que a previsão dos h 's requerem correlações específicas para escoamentos em canais de diâmetros pequenos. Já a Δp é bem estimada pelas correlações clássicas para canais de grandes diâmetros.

Palavras-chave: Condensação; Minicanais; Coeficiente de transferência de calor; Queda de pressão.

LIST OF FIGURES

Figure 1: Scale effect of tube diameter on various forces during flow boiling of R-123, $G = 200 \text{ kg/m}^2\text{s}$, $q = 1 \text{ MW/m}^2$ (Kandlikar, 2010)	39
Figure 2: Illustration of contact angles	40
Figure 3: Unbalanced forces of surface liquid molecules causes the surface tension.....	41
Figure 4: (a) Advancing contact line and (b) receding contact line of a drop on a horizontal surface (Smith et al., 2014).....	43
Figure 5: Adhesive force (Tanasawa, 1991)	43
Figure 6: Cohesive force (Tanasawa, 1991)	44
Figure 7: Classification of condensation phenomena	47
Figure 8: Typical patterns during dropwise condensation due to drainage. Gas flows from left to right (Ganzeles, 2002).....	49
Figure 9: Condensation curves for steam (Marto, 1998).....	51
Figure 10: Schematic representation of flow regimes observed in vertical upward co-current gas-liquid flow (Cheng et al., 2008)	57
Figure 11: Hewitt and Roberts flow pattern map for vertical upflow in a pipe (Hewitt and Roberts, 1969).....	58
Figure 12: Scheme of the five primary flow regimes for horizontal tubes (Thome et al., 2013).....	62
Figure 13: Schematic representations of flow regimes observed in horizontal, co-current gas-liquid flow (Carey, 1992).....	63
Figure 14: Generalized flow regime map for horizontal two-phase flow (Taitel and Dukler, 1976).....	65
Figure 15: Comparison of the proposed predictive method (lines) by Felcar et al., 2007 and the experimental data by Yang and Shieh, 2001 (Felcar et al., 2007).....	66
Figure 16: Comparison of air-water and two-phase R134a flow maps for 2.0 mm tube (Yang and Shieh, 2001)	67
Figure 17: Components of pressure when measuring Δp in microchannel manifolds (Steinke and Kandlikar, 2006)	75
Figure 18: Lockhart-Martinelli (1949) correlations	82
Figure 19: Two-phase friction pressure drop correlation (Baroczy, 1965)	84
Figure 20: Mass velocity correction vs property index (Baroczy, 1965)	85
Figure 21: Refrigerant condensation geometries of Garimella (Garimella et al., 2005).....	89
Figure 22: Idealized condensate profile during stratified flow, in-tube condensation within a horizontal tube (Marto, 1998)	92
Figure 23: Variation of the heat transfer coefficient with hydraulic diameter for fully developed laminar flow under constant heat flux boundary condition for water and R134a (Kandlikar, 2007).....	107
Figure 24: Summary of earlier heat-transfer measurements (Su et al., 2009).....	110
Figure 25: Schematic experimental setup (Modified from Zanette, 2015)	129
Figure 26: Picture of the boiler	130

Figure 27: Picture of the superheater	131
Figure 28: Test section front view	132
Figure 29: Illustrative picture of the MPE aluminum profile samples	135
Figure 30: MPE profile resulting volumetric matrix	135
Figure 31: Measurement result for sample 1	135
Figure 32: Measurement result for sample 2	136
Figure 33: Inlet manifold isometric view	137
Figure 34: Outlet manifold connections	137
Figure 35: Picture of the post condenser	138
Figure 36: Picture of the filter	139
Figure 37: Picture of the pump coupled to the electrical motor	140
Figure 38: Overview of the heat sink.....	141
Figure 39: Picture of the Coriolis flowmeter	142
Figure 40: Principle of operation of tangential gradient heat flux transducer (Modified by Carciofi et al., 2002).....	144
Figure 41: Block diagram of the test procedure.....	149
Figure 42: The "A" intervention shown in figure 41	150
Figure 43: The "B" intervention shown in figure 41.....	151
Figure 44: Measured data over a range of 100 acquisitions.....	152
Figure 45: Experimental data points on the Coleman and Garimella (2003) map	158
Figure 46: Temperatures and heat flux as a function of the test section position for $G = 481 \text{ kg}/(\text{m}^2\text{s})$ and $P = 7.9 \text{ bar}$	159
Figure 47: Temperature distribution for a parallel-flow heat exchanger (Incropera et al., 2007)	160
Figure 48: Mass flux influence on h value as a function of the position in the test section for pressure of 7 bar and heat flux of $9.2 \text{ kW}/\text{m}^2$	161
Figure 49: Mass flux influence on h value as a function of the position in the test section for pressure of 7.5 bar and heat flux of $9.3 \text{ kW}/\text{m}^2$	161
Figure 50: Mass flux influence on h value as a function of the position in the test section for pressure of 8.8 bar and heat flux of $10.1 \text{ kW}/\text{m}^2$	162
Figure 51: Reynolds number (liquid) for the same test conditions shown in figure 48.	162
Figure 52: Heat flux influence on h value as a function of the position in the test section for pressure of 7 bar and mass flux of $504 \text{ kg}/(\text{m}^2\text{s})$	163
Figure 53: Heat flux influence on h value as a function of the position in the test section for pressure of 7.8 bar and mass flux of $415 \text{ kg}/(\text{m}^2\text{s})$	164
Figure 54: Heat flux influence on h value as a function of the position in the test section for pressure of 8.6 bar and mass flux of $512 \text{ kg}/(\text{m}^2\text{s})$	164
Figure 55: Saturation temperature of working fluid influence on h value as a function of the position in the test section for mass flux of $408 \text{ kg}/(\text{m}^2\text{s})$ and heat flux of $8.9 \text{ kW}/\text{m}^2$	166
Figure 56: Saturation temperature of working fluid influence on h value as a function of the position in the test section for mass flux of $485 \text{ kg}/(\text{m}^2\text{s})$ and heat flux of $9.1 \text{ kW}/\text{m}^2$	166

Figure 57: Saturation temperature of working fluid influence on h value as a function of the position in the test section for mass flux of 524 kg/(m ² s) and heat flux of 8.3 kW/m ²	167
Figure 58: Saturation temperature of working fluid influence on h value as a function of the position in the test section for mass flux of 501 kg/(m ² s) and heat flux of 9.3 kW/m ²	167
Figure 59: Influence of vapor quality on heat transfer coefficient for different test conditions	170
Figure 60: Comparison of experimental heat transfer coefficient with Traviss et al. (1973) correlation.....	172
Figure 61: Comparison of experimental heat transfer coefficient with Cavallini et al. (2002) correlation.....	172
Figure 62: Comparison of experimental heat transfer coefficient with Dobson and Chato (1998) correlation	173
Figure 63: Comparison of experimental heat transfer coefficient with Soliman et al. (1968) correlation.....	173
Figure 64: Comparison of experimental heat transfer coefficient with Koyama et al. (2003) correlation.....	174
Figure 65: Comparison of experimental heat transfer coefficient with Cavallini et al. (2006c) correlation.....	174
Figure 66: Pressure drop contributions for all experimental runs	176
Figure 67: Mass flux effect on experimental pressure drop	177
Figure 68: Heat flux effect on experimental pressure drop.....	178
Figure 69: Temperature saturation (pressure) effect on experimental pressure drop.....	179
Figure 70: Comparison of experimental pressure drop with Lockhart and Martinelli (1949) correlation.....	180
Figure 71: Comparison of experimental pressure drop with Friedel (1979) correlation.....	181
Figure 72: Comparison of experimental pressure drop with Chisholm (1973) correlation.....	181
Figure 73: Comparison of experimental pressure drop with Garimella et al. (2005) correlation	182
Figure 74: Comparison of experimental pressure drop with Zhang and Webb (2001) correlation	182
Figure 75: Comparison of experimental pressure drop with Mishima and Hibiki (1996) correlation	183
Figure 76: Comparison of experimental pressure drop with Homogeneous Model using McAdams et al. (1942) equation for the mean two-phase viscosity	184
Figure 77: Comparison of experimental pressure drop with Homogeneous Model using Cicchitti et al. (1960) equation for the mean two-phase viscosity	184
Figure 78: Comparison of experimental pressure drop with Homogeneous Model using Dukler et al. (1964) equation for the mean two-phase viscosity	185

Figure A.1: Diagram of the heat flux sensors calibration	222
Figure B.1: Test rig at the beginning	225
Figure B.2: Thread sealant (Teflon paste) with PTFE applied to the connections in order to prevent leakage	225
Figure B.3: Seal glues used in order to prevent leakage	227
Figure B.4: Boiler at the beginning	227
Figure C.1: Serial communication at Elipe Scada Software	232
Figure D.1: Comparison of experimental pressure drop with Blasius (1913) correlation.....	236
Figure D.2: Comparison of experimental pressure drop with Phillips (1987) correlation.....	236
Figure D.3: Comparison of experimental heat transfer coefficient with Dittus- Boelter (1930) correlation	237
Figure D.4: Comparison of experimental heat transfer coefficient with Sieder and Tate (1936) correlation	238
Figure D.5: Comparison of experimental heat transfer coefficient with Petukhov (1970) correlation	238
Figure D.6: Comparison of experimental heat transfer coefficient with Gnielinski (1976) correlation.....	239

LIST OF TABLES

Table 1: Channel size classification by Mehendale et al. (2000).....	36
Table 2: Channel size classification by Kandlikar and Grande (2003).....	38
Table 3: Table of dimensionless numbers.....	54
Table 4: Summary of studies on flow patterns during condensation.....	69
Table 5: Values of the constants in Butterworth (1975) correlation for void fraction (Carey, 1992).....	72
Table 6: Typical values of loss coefficients K for various flow disturbances (Ghiaasiaan, 2008).....	78
Table 7: Condensation heat transfer correlations (Park et al., 2015).....	105
Table 8: Summary of experimental studies of condensation in small channels (Cavallini et al., 2006a,b).....	113
Table 9: Summary of relevant studies on heat transfer during condensation in small channels.....	115
Table 10: Summary of relevant studies on pressure drop during condensation in small channels.....	119
Table 11: Measurements results of area and perimeter of the two samples.....	136
Table 12: Coriolis mass flowmeter calibration (R134a, 10 bar, 65 °C) (From: Siemens).....	142
Table 13: R134a properties at 8.4 bar (From: EES software).....	145
Table 14: Tests order of execution.....	148
Table 15: Test conditions range.....	157
Table 16: Summary of the compared studies to the present study.....	188
Table A.1: Comparison of the thermal bath temperature indicated in the display to the measured by the PT100.....	218
Table A.2: Coefficients calculated from the calibration curves for each thermocouple.....	219
Table A.3: Heat Flux Sensor Calibration.....	223
Table D.1: Single-phase flow tests conditions.....	235

LIST OF ABBREVIATIONS AND ACRONYMS

CTS	Computed Tomography System
DTR	Data Terminal Ready
FI	Frequency Inverter
LEPTEN	Laboratórios de Engenharia de Processos de Conversão e Tecnologia de Energia
LMPT	Laboratório de Meios Porosos e Propriedades Termofísicas
MAE	Mean Absolute Error
MPE	Multi-Port Extruded
PID	Proportional Integral Derivative
PLC	Programmable Logic Controller
RT	Round Tubes
RTS	Request to Send
SSR	Solid State Relay
UFSC	Universidade Federal de Santa Catarina

NOMENCLATURE

A	[m ²]	Area
Bo	[-]	Bond number
C _c	[-]	Contraction coefficient
c _p	[J/(kgK)]	Specific heat at a constant pressure
D	[m]	Diameter
D _h	[L ¹]	Hydraulic diameter
f	[-]	Fanning frictional factor
F	[N]	Force
F''	[N/m ²]	Force per unit area
Fr	[-]	Froude number
g	[m/s ²]	Acceleration due to gravity
G	[kg/(m ² s)]	Mass flux
Ga	[-]	Galileo number
h	[W/m ² K]	Heat transfer coefficient
h _{lv}	[J/kg]	Latent heat of vaporization
i	[kJ/kg]	Enthalpy
j	[m/s]	Superficial velocity
j*	[-]	Wallis dimensionless velocity
Ja	[-]	Jakob number
k	[W/(mK)]	Conductivity
K	[-]	Loss coefficient
L	[m]	Channel length
Kn	[-]	Knudsen number
Nu	[-]	Nusselt number
Δp	[Pa]	Pressure drop
P	[N/m ²]	Pressure
P	[m]	Pitch
Pr	[-]	Prandtl number
q''	[W/m ²]	Heat flux
Re	[-]	Reynolds number

S	[-]	Slip ratio
T	[K]	Temperature
v	[m/s]	Velocity
V	[m/s]	Mean velocity
x	[-]	Vapor quality
X	[-]	Lockhart-Martinelli parameter
X _{tt}	[-]	Martinelli parameter for turbulent flow in the gas and liquid phases
z	[m]	Distance from channel entrance
We	[-]	Weber number

Greek:

α	[-]	Void fraction
Γ	[-]	Physical property coefficient
δ^+	[-]	Non-dimensional film thickness
ϵ	[-]	Relative roughness
ζ	[-]	Friction coefficient of conduit length considered
θ	[°]	Angle
κ	[-]	Hagenbach factor
λ	[L ¹]	Mean free path
μ	[kg/(ms)]	Viscosity
σ	[-]	Ratio between smaller and larger flow areas
σ	[N/m]	Surface tension
τ	[-]	Shear stress
ϕ^2	[-]	Two-phase frictional multiplier
ρ	[kg/m ³]	Fluid density
$\bar{\rho}$	[kg/m ³]	Homogeneous fluid density
Ω	[°]	Angle of inclination between the tube axis and the horizontal

Subscripts:

A	Advancing
a	Adhesive
ac	Acceleration
c	Cohesive
cr	Critical
cont	Contraction
decel	Deceleration
eq	Equivalent
exp	Expansion
frict	Friction
g	Gas
i	Inertia
i	Inside
inl	Inlet
l	Liquid
lim	Limit
lo	Liquid only
lv	Liquid-vapor
m	Mixture
M	Evaporation momentum
mani	Manifold
MC	Minichannel
o	Outlet
R	Receding
r	Fin root
s	Surface
s	Spreading
sl	Solid-liquid
sp	Single-phase flow
st	Cross-sectional total

sv	Solid-vapor
tp	Two-phase flow
v	Vapor
vo	Vapor only
w	Wall

TABLE OF CONTENTS

1	INTRODUCTION.....	31
1.1	MOTIVATION AND BACKGROUND OF THIS STUDY	31
1.2	WORK PURPOSES.....	34
1.3	WORK STRUCTURE.....	34
2	LITERATURE REVIEW	36
2.1	CHANNEL SIZE CLASSIFICATION.....	36
2.2	CONTACT ANGLE AND WETTING PROPERTIES .	40
2.3	TYPES OF CONDENSATION	46
2.3.1	Film condensation	48
2.3.2	Dropwise condensation	48
2.4	TWO-PHASE FLOW DISTRIBUTION	52
2.5	IMPORTANT DEFINITIONS	53
2.6	TWO-PHASE FLOW REGIMES.....	56
2.6.1	Upward vertical flow	56
2.6.2	Horizontal flow	61
2.6.3	Flow regime maps.....	64
2.6.4	Summary of studies on flow patterns during condensation.	68
2.7	VOID FRACTION.....	71
2.8	PRESSURE DROP	73
2.8.1	Single-phase flow.....	75
2.8.2	Condensation flow	79
2.9	HEAT TRANSFER.....	90
2.9.1	Single-phase flow correlations.....	90
2.9.2	Two-phase flow correlations.....	91
2.9.3	Predictions of local condensation heat transfer coefficient	103
2.10	MINICHANNEL CONDENSATION.....	106
2.10.1	Enhancement of condensation heat transfer	106
2.10.2	Numerical models	108
2.10.3	Important researches on small diameter channels	109
3	EXPERIMENTAL FACILITY	128
3.1	TEST RIG	128
3.1.1	Boiler.....	130
3.1.2	Superheater.....	131
3.1.3	Test section.....	132
3.1.4	Post condenser.....	138
3.1.5	Filter	139
3.1.6	Pump.....	139
3.1.7	Heat sink.....	140

3.2	MEASURING INSTRUMENTS	141
3.2.1	Coriolis flowmeter	141
3.2.2	Pressure transducers.....	142
3.2.3	Thermocouples.....	143
3.2.4	Heat flux sensors.....	143
3.3	WORKING FLUID: R134A	144
4	EXPERIMENTAL METODOLOGY.....	146
4.1	OPERATING PROCEDURES.....	146
4.1.1	Working fluid loading procedure.....	146
4.1.2	Test procedure.....	147
4.2	DATA REDUCTION.....	153
5	EXPERIMENTAL RESULTS	157
5.1	TEST CONDITIONS	157
5.2	HEAT TRANSFER RESULTS	158
5.2.1	Effect of mass flux	160
5.2.2	Effect of heat flux	163
5.2.3	Effect of saturation temperature	165
5.2.4	Effect of vapor quality	168
5.2.5	Comparison of the experimental heat transfer coefficient with correlations.....	170
5.3	PRESSURE DROP RESULTS.....	175
5.3.1	Effect of mass flux	176
5.3.2	Effect of heat flux	177
5.3.3	Effect of saturation temperature	178
5.3.4	Comparison of the experimental pressure drop with correlations.....	179
5.4	COMPARISON WITH OTHER STUDIES	185
5.4.1	Yan and Lin (1999).....	185
5.4.2	Zhang and Webb (2001)	186
5.4.3	Koyama et al. (2003a, 2003b).....	186
5.4.4	Bandhauer et al. (2006).....	187
5.4.5	Wang et al. (2002).....	187
5.4.1	Goss (2011a)	187
6	CONCLUSIONS AND RECOMMENDATIONS	189
7	BIBLIOGRAPHY	191
APPENDIX A	CALIBRATION.....	216
A.1	THERMOCOUPLES	216
A.2	HEAT FLUX SENSORS.....	221
APPENDIX B	SETUP CORRECTIONS.....	224
B.1	LEAKAGE.....	224
B.2	BOILER LEVEL GAUGE.....	226

B.3	IMPROVEMENTS	228
APPENDIX C	SUGGESTIONS FOR IMPROVEMENT	229
C.1	PROGRAMMABLE LOGIC CONTROLLER.....	229
C.1.1	Frequency inverter	229
C.1.2	Proportional integral derivative controller.....	230
C.1.3	Serial converter	231
C.1.4	Proposed PLC modifications	232
C.2	OTHER SUGGESTIONS	233
APPENDIX D	SINGLE-PHASE FLOW TESTS RESULTS.....	235
D.1	PRESSURE DROP	235
D.2	HEAT TRANSFER.....	237
APPENDIX E	EXPERIMENTAL UNCERTAINTY ON THE CALCULATION OF THE HEAT TRANSFER COEFFICIENT	240

1 INTRODUCTION

Microscale condensers are important components of compact heat exchangers. Its use is motivated by the reduction of the available space for heat transfer and by the cost reduction of the materials used in heat exchangers. Besides that, because of the environmental organs pressure to decrease the refrigerants use, which contributes to the increase of the greenhouse effect, the use of microscale condensers is greatly encouraged. Heat exchangers that use phase change in mini-channels present higher heat transfer coefficients than the regular ones. On the other hand, those systems operate at high pressure drop values.

This chapter presents the motivation of this study, its purposes and how it is structured.

1.1 MOTIVATION AND BACKGROUND OF THIS STUDY

Liquid-vapor phase change processes play a crucial role in the industries: power generation, chemical, pharmaceutical, heating and air conditioning. The virtually isothermal heat transfer associated with boiling and condensation processes makes their inclusion in power and refrigeration cycles highly advantageous from a thermodynamic efficiency point of view. However, during the past three decades newer applications have emerged whose performance is highly dependent on the ability to dissipate large amounts of heat within limited volume. Computer data centers, hybrid vehicle, power electronics, lasers and X-ray medical devices are examples of those newer applications (Mudawar, 2011). These applications have created a need of two-phase processes adaptation into compact configurations that promise enhancement in evaporation and condensation heat transfer coefficients compared to those possible in single-phase processes. The high heat transfer coefficients associated with boiling and condensation have made the use of these processes increasingly attractive in the thermal control of compact devices that have high heat dissipation rates. The evolution of compact heat exchangers is motivated by the requirement for reducing their size and weight as well as enhancing individual components and overall system performance.

The turn of the twenty-first century brought an abrupt technological advance that was evident in the space technology and electronics devices development. These two inseparable technologies mark a trend toward the miniaturization of devices. The absolute value of thermal

power in computer systems is not significantly large, notwithstanding the heat flux densities reaches substantial values, as much as 1 kW/cm^2 . The classical and traditional methods for transferring such heat flux densities are either minimally useful or not useful at all. Therefore, an intensification of convective heat transfer with phase changes is needed. An example of passive methods that can be used to increase convective heat process includes, among others, diameter tube reduction. Small dimensions, high heat transfer efficiency and environmentally friendly technology are criteria needed to be fulfilled in order to achieve modern and compact heat exchangers.

The current trend of electronic device miniaturization has motivated advances in several engineering fields among them space technology, defense systems, aerospace applications, manufacturing technology, industrial processes and consumer electronics. A challenge for researchers in this area is managing thermal dissipation in miniaturized devices with the aim of guaranteeing the reliability and safety during its operation. A great solution is to use microscale heat exchangers in order to manage this thermal dissipation. This subject has been studied since the pioneering work of Tuckerman and Pease (1981). Sobhan and Garimella (2001) reported that most literature in this field has focused on studying the heat transfer coefficient and pressure drop for electronic cooling applications.

Considering the architectural point of view, the reduction in volume and footprint of the systems are fundamental since refrigeration and air conditioning systems have become a part of the design of occupied spaces. These systems allow controlled thermal, humidity, cleanliness and/or other process requirements and the constraints imposed by specific dimensions of its components are becoming increasingly important. Another essential factor is the high energy cost, which motivates to improve the energy efficiency of refrigeration and air conditioning equipment.

Another challenge improving those systems is the environmental concern of releasing large quantities of refrigerants. Industries are aware of accidental leakage risks, combined with the augmented capital investment needed to manufacture the refrigerants. Therefore, refrigerant charge reduction and performance enhancement remain important to safe operation. In this way, minichannels appear as a modern and viable solution to address these concerns and are expected to be used in small and large commercial, industrial and residential systems.

One more current environmental problem is the significant proportion of electricity usage related to refrigeration and air conditioning

and its consequential fuel consumption and associated CO₂ emissions. A meaningful contribution to mitigate this problem is to improve the design and performance of refrigeration plants, which can be achieved by using miniaturized condensers, specially using minichannel tubes.

This change is manifested in increasing studies concerning evaporation and flow boiling configurations, including pool boiling (Marto and Lapere, 1982; Anderson and Mudawar, 1989; Mudawar et. al, 1997), channel flow boiling (Maddox and Mudawar, 1989; Willingham and Mudawar, 1992; Lee and Lee, 2001), jet (Katto and Kunihiro, 1973; Monde and Inoue, 1991; Wadsworth and Mudawar, 1992; Johns and Mudawar, 1996) and spray (Toda, 1972; Lin and Ponnappan, 2003; Rybicki and Mudawar, 2006; Visaria and Mudawar, 2008), as well as enhanced surfaces (Nakayama et al., 1984; Webb, 1981; Khanikar et al., 2009) and hybrid cooling configurations (Sung and Mudawar, 2006). Nevertheless, the heat acquisition is only a part of the challenge. The heat acquisition by evaporation or flow boiling is often promoted with the aid of a closed two-phase flow loop, which requires proportional heat rejection capacity that relies mostly on condensation. Hence, studies of high performance condensation are needed, with particular emphasis on increasing the ratio of heat dissipation rate to pressure drop.

A diverse range of industries uses minichannels and microchannels because of its ability to provide high surface area-to-volume ratios, high heat transfer coefficients, high efficiencies and system compactness. In this context, condensation heat transfer in minichannels and microchannels is naturally of great practical importance in developing next generation ultra-compact and high performance two-phase flow thermal systems.

The heat transfer and fluid flow processes associated with liquid-vapor phase-change phenomena are typically among the more complex transport phenomena encountered in engineering applications. The processes may have all the complexity of single-phase convective transport (nonlinearities, transition to turbulence, three-dimensional or time-varying behavior) plus additional elements resulting from motion of the interface, nonequilibrium effects, or other complex dynamic interactions between the phases. Due to the highly complex nature of these processes, development of methods to predict the associated heat and mass transfer has often proved to be a formidable task. Nevertheless, the research efforts of numerous scientists over several decades have provided a clear understanding of many aspects of condensation processes in power and refrigeration systems. On the other hand, some elements of

condensation phenomena are not well understood, and research in these areas continues.

The independent measurement of heat flux and wall temperature is what stands out this study. Most of the condensation work found in literature calculates the heat flux from the wall temperature, as shown in equation 1.1. In this study, heat flux sensors measure the heat flux and thermocouples located at the test section measure the wall temperature.

$$\bar{q}(z) = -\dot{m}_w c_{p,w} \frac{dT_w(z)}{dz} \quad (1.1)$$

Where z is the axial coordinate along the tube oriented with the refrigerant flow.

1.2 WORK PURPOSES

The main objective of this work is to study the condensation process inside seven parallel minichannels, with hydraulic diameter of 1.46 mm, in a Multi-Port Extruded aluminum profile. The fluid refrigerant used is R134a and the tests are performed for different mass flux, pressure and heat flux values. This study focus on calculating the experimental values of the heat transfer coefficient and pressure drop. These values are compared to correlations found in literature.

In order to achieve the main objective of this study, some specific objectives are pursued:

- Review the fundamentals aspects of condensation in literature, especially condensation in minichannels;
- Carry out the instrumentation of the test rig, and perform the necessary calibrations;
- Determine the best experimental procedure and data reduction;
- Perform single-phase tests to validate the rig;
- Perform condensation tests on different conditions, and calculate the heat transfer coefficient and pressure drop values;
- Analyze the data obtained and compare the heat transfer coefficient and pressure drop values to correlations proposed in literature.

1.3 WORK STRUCTURE

The work is organized as follows:

- Chapter 2 provides a comprehensive review of types of condensation, two-phase flow distribution, two-phase flow regimes, void

fraction, pressure drop, heat transfer regarding condensation, and discusses the need for further research on minichannels condensation.

- Chapter 3 presents the experimental facility used to carry out the condensation tests.

- Chapter 4 demonstrates the experimental procedures, including the data reduction, performed.

- Chapter 5 discusses the results, and presents a comparison of the experimental data with the correlations available in literature.

- Chapter 6 discusses the conclusions from this study, and presents future work recommendations.

- Appendix A presents the calibration process adopted for the thermocouples and heat flux sensors.

- Appendix B describes the setup corrections made.

- Appendix C presents improvements suggestions for the experimental setup.

- Appendix D discusses the experimental results for single-phase flow.

- Appendix E presents the experimental uncertainty on the calculation of the heat transfer coefficient.

2 LITERATURE REVIEW

This chapter presents a review of the main condensation aspects, especially regarding minichannels.

2.1 CHANNEL SIZE CLASSIFICATION

Several researchers (Coleman and Garimella, 1999; Kim et al., 2003; Chung and Kawaji, 2004) have shown that transient patterns are not the same in small and large diameter tubes. This is due to the different influence of the forces acting on the fluid flow: shear, surface tension and gravity forces. At microscale, the shear force and surface tension become more important than gravity force, the opposite behavior is noticed at conventional channels. For example, at microscale geometry channels, the stratified flow pattern is not observed, which is commonly observed in large diameter channels.

In this way, the extrapolation from conventional diameter channels correlations to minichannels may insert significant errors when evaluating heat transfer and pressure drop. Therefore, a transition limit between microscale and macroscale is needed, which is a much-discussed topic in literature.

Researchers are focused in determining a common terminology for smaller diameter channels. Notwithstanding, quite a few channel size classifications have been proposed; Cheng and Mewes (2006) discussed many of them. In that regard, several classification schemes based on hydraulic diameters were proposed. Mehendale et al. (2000) proposed a simple channel classification scheme based on the hydraulic diameter as shown in table 1:

Table 1: Channel size classification by Mehendale et al. (2000)

Classification	Hydraulic diameter
Microchannel	1 μm to 100 μm
Meso-channel	100 μm to 1 mm
Conventional passages	>6 mm

Another approach to classify the channels is to consider specific processes where they are being employed. Fukano and Kariyasaki (1993) and Serizawa et al. (2002) suggested the use of Laplace length scale L , which can be obtained by equation 2.1. This equation can be used for channel size classification based on the relative magnitudes of the surface tension and gravity forces:

$$L = \sqrt{\sigma/g(\rho_L - \rho_V)} \quad (2.1)$$

Kew and Cornwell (1997) suggested as a criterion, for flow boiling applications, the ratio of the Laplace length scale to channel hydraulic diameter.

Considering heat transfer and fluid flow phenomena, the effect of channel size is seen to be distinct between single and two-phase flow. In the case of single-phase flow, the flow passage dimensions are compared to the mean free path, λ , of the gas molecules. The Knudsen number, Kn , which is a dimensionless number defined as the ratio of the molecular mean free path length to a representative physical length scale, in that case the hydraulic diameter, D_h , is often used. The Knudsen number equation is presented in equation 2.2:

$$Kn = \lambda/D_h \quad (2.2)$$

The alteration of void fraction with the volumetric quality in adiabatic two-phase flow was studied by Kawahara et al. (2005) for different diameter tubes (50 μm , 100 μm and 251 μm). The void fraction data obtained in 50, 75, and 100 μm channels conformed to a different correlation than the data for a 251 μm diameter channel. Based on their experiment, the authors suggested that the transition limit between microchannels and minichannels consists between $D_h= 100 \mu\text{m}$ and $D_h= 251 \mu\text{m}$.

The development of a unique classification scheme considering the overall behavior of commonly encountered phase-change processes is useful and practical. Taking this into account, Kandlikar and Grande (2003) recommended a channel classification considering processes such as single-phase gas and liquid flows, two-phase adiabatic flow, flow boiling and flow condensation. The channel size classification of the two authors is shown in table 2 and it is widely used.

Kandlikar et al. (2006) modified the classification scheme above replacing the channel hydraulic diameter with the minimum channel dimension D .

Table 2: Channel size classification by Kandlikar and Grande (2003)

Classification	Hydraulic diameter
Conventional channel	$D > 3 \text{ mm}$
Minichannel	$3 \text{ mm} \geq D > 200 \text{ }\mu\text{m}$
Microchannel	$200 \text{ }\mu\text{m} \geq D > 10 \text{ }\mu\text{m}$
Transitional channel	$10 \text{ }\mu\text{m} \geq D > 0.1 \text{ }\mu\text{m}$
Transitional microchannel	$10 \text{ }\mu\text{m} \geq D > 1 \text{ }\mu\text{m}$
Transitional nanochannel	$1 \text{ }\mu\text{m} \geq D > 0.1 \text{ }\mu\text{m}$
Molecular nanochannel	$0.1 \text{ }\mu\text{m} > D$

An important approach on channel size classification is to consider the forces acting in the flow. In that way, Kandlikar (2010) presented a scaling analysis to identify the relative effects of different forces on the boiling process at microscale. The analyzed forces are inertia, surface tension, shear, gravity (buoyancy) and evaporation momentum forces. Since the relative magnitudes of these forces are of interest rather than their actual values, the forces are normalized with respect to the channel size. The normalization may be done using the volume, cross-sectional area or perimeter (diameter) of the microchannel. Since local values are of interest, normalization with respect to volume will not provide such information. The resulting equations are presented below:

$$\text{Inertia force:} \quad F''_i \sim \frac{G^2}{\rho} \quad (2.3)$$

$$\text{Surface tension force:} \quad F''_\sigma \sim \frac{\sigma}{D} \quad (2.4)$$

$$\text{Shear force:} \quad F''_{\tau} \sim \frac{\mu G}{\rho D} \quad (2.5)$$

$$\text{Gravity (buoyancy) force:} \quad F''_g \sim (\rho_L - \rho_V)gD \quad (2.6)$$

$$\text{Evaporation momentum force:} \quad F''_M \sim \left(\frac{q}{h_{lv}}\right)^2 \frac{1}{\rho_v} \quad (2.7)$$

The relative magnitudes of these forces are plotted using the forces per unit area to illustrate the effect of changing scale (diameter), as shown in figure 1. For R-123 at $G = 200 \text{ kg/(m}^2\text{s)}$ and $q = 1 \text{ MW/m}^2$, it is noted that the surface tension force is reduced as the hydraulic diameter increases. Thus, the surface tension comes out as the dominant force at microchannels, followed by inertia, shear, evaporation momentum and gravity. For large diameters ($D = 10 \text{ mm}$), gravity and inertia present the biggest values, followed by evaporation momentum, surface tension and shear. This result endorses that a transition criterion should be based phenomenologically.

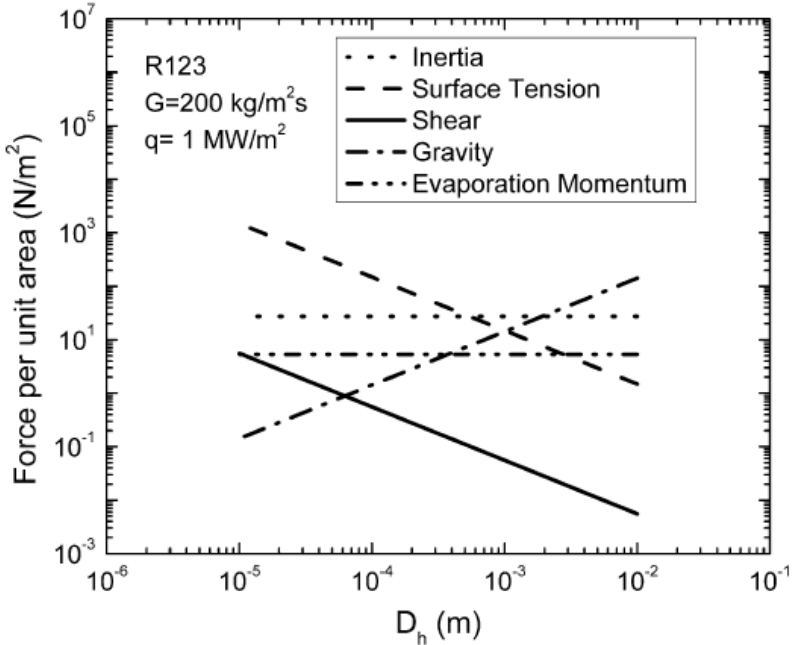


Figure 1: Scale effect of tube diameter on various forces during flow boiling of R-123, $G = 200 \text{ kg/m}^2\text{s}$, $q = 1 \text{ MW/m}^2$ (Kandlikar, 2010)

2.2 CONTACT ANGLE AND WETTING PROPERTIES

In most technological applications, a liquid-vapor phase change is accomplished by transferring energy through the walls of a container or channel into or out of a two-phase system. The vaporization or condensation processes ultimately takes place at the liquid-vapor interface. However, in these circumstances the manner in which the liquid and vapor contact the solid walls through which energy is transferred will strongly affect the resulting heat and mass transfer in the system. Consequently, the performance of heat transfer equipment in which vaporization or condensation occurs may strongly depend on the way the two phases contact the solid walls.

The affinity of liquids for solids is referred to as the wettability of the fluid. The topic of wetting has received a lot of interest from both fundamental and applied points of view. Wettability studies usually involve the measurement of contact angles as the primary data, which indicates the degree of wetting when a solid and liquid interact. High wettability corresponds to small contact angles ($\ll 90^\circ$), whereas low wettability corresponds to large contact angles ($\gg 90^\circ$). An illustration is shown in figure 2 for better understanding:

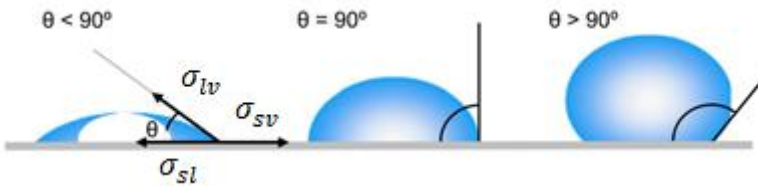


Figure 2: Illustration of contact angles

Considering a liquid drop resting in a flat, horizontal solid surface as shown in figure 2, the contact angle is defined as the angle formed by the intersection of the liquid-solid interface. The contact angle can be geometrically measured by applying a tangent line from the contact point along the liquid-vapor interface in the droplet profile. Small contact angles are observed when the liquid spreads on the surface and large contact angles are formed when the liquid beads on surface. In that way, a contact angle lower than 90° indicates a high wettability, that is, the wetting of the surface is favorable. In that case, the fluid will spread over a large area on the surface. Oppositely, a contact angle greater than 90° indicates low wettability, so the wetting of the surface is unfavora-

ble, minimizing the fluid contact with the surface and forming a compact liquid droplet.

The surface tension of the liquid will determinate the liquid shape for a stationary, free droplet. In a pure liquid, each molecule in the bulk is pulled equally in all directions by the neighboring liquid molecules. Thus, the result is a null net force. Nevertheless, the surface molecules are not exposed in the same way as the others molecules; they do not have neighboring molecules in every direction. As a result, the surface molecules are pulled inward by the others, creating internal compressive tension. Hence, the liquid contracts its surface area to maintain the lowest surface free energy. This mechanism is shown in figure 3.



Figure 3: Unbalanced forces of surface liquid molecules causes the surface tension

The liquid droplet shape is caused by the intermolecular force contracting the surface, or by the surface tension. External forces, as gravity, can also deform a droplet. Therefore, the contact angle is determined by a combination of surface tension and external forces (commonly gravity).

The contact angle, θ , of a liquid drop on an ideal solid surface is defined by the mechanical equilibrium of the drop under the action of three interfacial tensions (Young, 1805):

$$\sigma_{lv} \cos \theta = \sigma_{sv} - \sigma_{sl} \quad (2.8)$$

where σ_{lv} , σ_{sv} and σ_{sl} represent the liquid-vapor, solid-vapor and solid-liquid interfacial tensions, respectively. The vertical force $\sigma_{lv} \sin \theta$ at the three-phase point must be balanced by a vertical reaction force in the solid. However, this force is usually so small and the modulus of the elasticity of the solid is usually so high, that there is no significant deformation of the solid surface (Carey,1992).

The contact angle is represented by θ , that is also called Young's contact angle. It is the angle made by the liquid-solid interface at the point where the three interfaces meet. It is important that the angle should be measured inside (not outside) the liquid phase.

From a microscopic point of view, the three phases do not form a point (or line) of contact as shown in figure 2. Equation 2.8 holds for a finite virtual volume taken around the point of contact, which can be different from the real geometrical one.

Equation 2.8 is commonly called Young's equation. For an ideal surface, the contact angle is determined uniquely if three substances (solid, liquid and vapor) and their thermodynamical conditions (temperature, pressure, etc.) are known. However, for real surfaces exist many metastable states of a droplet on a solid and the observed contact angles are usually not equal to θ . The contact angle takes a seemingly arbitrary value between two extremes called the advancing contact angle, θ_A , and the receding contact angle, θ_R , respectively. These angles fall within a range, with the advancing angles approaching a maximum value, and the receding angles approaching a minimum value. The change of the contact angle between these two values is called hysteresis.

A better method for characterizing a solid surface is to report the maximal advancing and minimal receding contact angles, since θ_A and θ_R are extreme values and are considered means of obtaining thermodynamic properties. If the contact angle is measured while the volume of the drop is increasing, this is called the advancing angle as seen in figure 4(a). Practically, this is done just before the three-phase contact line starts to advance. Similarly, if the angle is measured while the volume is decreasing, this is called the receding angle as in Figure 4(b).

The difference between the advancing and receding angles is known as the dynamic contact angle hysteresis, $\Delta\theta$. The size of the $[\theta_A, \theta_R]$ domain is usually attributed to the surface roughness of the solid substrate, and the contact angle lies somewhere within this domain. Contact angle hysteresis is useful for characterizing surface roughness, heterogeneity, and mobility.

In addition to surface roughness, hysteresis is also influenced by microscopic chemical heterogeneity, drop size relative to physical topography, molecular reorientations, impurities on the surface and the penetration of the liquid molecules into the solid surfaces (Khandekar et al., 2010; Erbil et al., 1999). These defects affect the value of the hysteresis, which is reported as an absolute value. However, the absolute values of the angular deviations of θ_A and θ_R from the contact angle θ

are typically different, i.e. $|\theta_A - \theta| \neq |\theta_R - \theta|$ (Tadmor, 2008). That is to say, the contact angle does not necessarily fall in the center of the contact angle hysteresis.

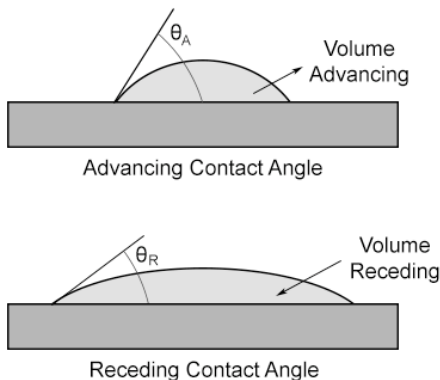


Figure 4: (a) Advancing contact line and (b) receding contact line of a drop on a horizontal surface (Smith et al., 2014)

Tanasawa (1991) presented in his study the adhesive and cohesive forces concepts which helps better understanding the wettability and contact angle relationship.

The adhesive force F_a is the force that is found between liquid and solid. It is derived from a thought experiment as shown in figure 5.

$$F_a = \sigma_{sv} + \sigma_{lv} - \sigma_{sl} \quad (2.9)$$

The first two terms on the right-hand side represent the interfacial energies corresponding to newly formed interfaces and the third term is for the interfacial energy corresponding to the vanished interface.

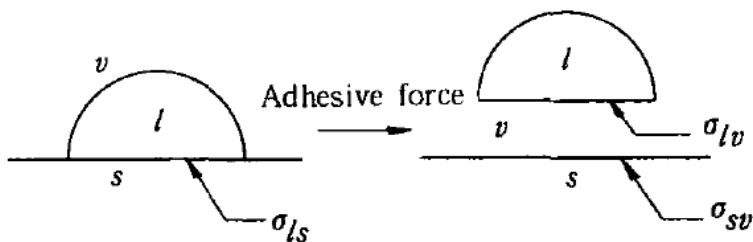


Figure 5: Adhesive force (Tanasawa, 1991)

The substitution of equation 2.8 into equation 2.9 gives rise to equation 2.10:

$$F_a = \sigma_{lv}(1 + \cos \theta) \quad (2.10)$$

Equation 2.10 shows that $F_a = 0$ when $\theta = 180^\circ$, this is, when the liquid has no wetting at all with the solid surface.

The cohesive force F_c is resulted by intermolecular attraction and a scheme is illustrated in figure 6. In the situation where the adhesive force holding the liquid on the solid surface is too strong to release the drop from the surface, the drop may be broken inside, as illustrated. If this situation happens, two liquid-vapor interfaces will be formed. Hence, the cohesive force is expressed by equation 2.11:

$$F_c = 2 \sigma_{lv} \quad (2.11)$$

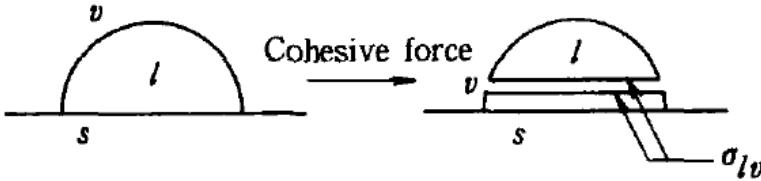


Figure 6: Cohesive force (Tanasawa, 1991)

The spreading liquid drop criterion depends on which force, adhesive or cohesive, is stronger. From equations 2.9 and 2.11, the spreading force F_s is defined as follows:

$$F_s = F_a - F_c = \sigma_{sv} - \sigma_{lv} - \sigma_{sl} \quad (2.12)$$

The energy needed to reduce the unit area of the solid-liquid interface is represented by the spreading force. Substitution of equation 2.8 into equation 2.12 gives:

$$F_s = \sigma_{lv}(\cos \theta - 1) \quad (2.13)$$

Analyzing equation 2.13, $F_s < 0$, this is, the drop does not spread over the surface when $|\cos \theta| \leq 1$, which happens if $0 < \theta \leq 180^\circ$. If $\theta = 0$, then $\cos \theta = 1$ and $F_s = 0$, representing the situation that liquid spreads all over the surface without having a finite contact angle. Alt-

though any contact angle θ fails to yield $F_s > 0$, it is possible if the solid-vapor interfacial energy σ_{sv} is sufficiently large in equation 2.12.

Smith et al. (2014) investigated the wettability of fluid-fluid interactions for advanced heat transfer applications. The tested surface materials were copper, aluminum, and Teflon PFA. The working fluids tested were traditional fluids, water and acetone, and refrigerants, R134a and HFO-1234yf. For R134a-Aluminum system, the authors presented the following results: $\theta_R = 60.11^\circ \pm 1.7^\circ$, $\theta_A = 60.88^\circ \pm 1.4^\circ$ and $\theta = 60.50^\circ$. They used the capillary rise at a vertical plate technique under the atmospheric conditions of 21°C and 54% humidity.

2.3 TYPES OF CONDENSATION

Condensation is one of the most important heat transfer processes, which is much used in diverse industries. The industrial revolution in the eighteenth century was marked by the steam engines developed by James Watt and others. Watt was very successful in improving the efficiency of the steam condenser, a direct-contact type of condenser. Many years later, the theory of heat transfer by condensation took place. Nusselt (1916) presented a pioneer study of film condensation and Schmidt et al. (1930) studied dropwise condensation.

During condensation, the vapor and liquid phases are in contact. Condensation occurs when the molecules in vapor phase trespass to liquid phase and remain in the liquid phase. Nevertheless, there are always some molecules escaping from the liquid phase into the vapor, moved by the intermolecular force field acting in the liquid phase. Thus, net condensation takes place when the number of molecules crossing a unit area of the vapor-liquid interface per unit time into the liquid phase is larger than the number crossing toward the vapor phase. Often, the adjective “net” is omitted and net condensation is simply called condensation.

In most applications involving condensation, the process is initiated by removing heat through the walls of the structure containing the vapor to be condensed. If enough heat is removed, the vapor near the wall may be cooled below its equilibrium saturation temperature for the specified system pressure. Since the heat removal process will establish a temperature field in which the temperature is lowest right at the wall of the containment, the formation of a liquid droplet embryo is most likely to occur right on the solid-vapor surface. The formation of a liquid embryo at the interface between a metastable supersaturated vapor and another solid phase is one type of heterogeneous nucleation. If the solid surface is idealized as being perfectly smooth, in general, the shape of a droplet at the surface will be dictated by the shape of the surface itself, the interfacial tension σ , and the contact angle θ .

The condensation process is classified as homogeneous or heterogeneous. The former occurs in a space where no foreign substance exists. It takes place stochastically as the result of fluctuation of motion of vapor molecules. Such a process rarely plays an important role in actual heat-transferring devices. On the other hand, the latter occurs with the aid of foreign materials, liquid or solid, forming the liquid phase on its surface or by using it as a nucleus (Tanasawa, 1991).

Furthermore, the heterogeneous condensation is divided in volume condensation and surface condensation. Volume condensation is characterized by the use of small particles of liquid or solid, which are floating in space, as the nuclei. Volume condensation is present at the clouds, mist and fog formations. However, apart this phenomenological interest, volume condensation is not currently important for the industrial applications.

Surface condensation, on the other hand, is subdivided in condensation on liquid and solid surfaces. The first includes direct contact condensation on drops, jets or films of liquid; the number of practical applications is considerable. The last consists in condensation on a solid wall kept at low temperature. However, if we observe this process more closely, the vapor phase is not always in touch directly with the solid wall, because a layer of liquid is usually formed on it. Nevertheless, this type of surface condensation is different from vapor-liquid direct-contact condensation in the sense that the solid wall plays an important role in transferring heat.

Finally, the condensation on solid surface is divided in dropwise and film condensation. This last classification is based on the liquid phase form on the solid surface. If the liquid condensate wets the surface it is referred to as film (or filmwise) condensation. If the liquid does not wet the surface, it will form into numerous discrete droplets, referred to as drop (or dropwise) condensation. These two types of condensation will be discussed in detail soon. The classification of condensation as mentioned above is shown in figure 7.

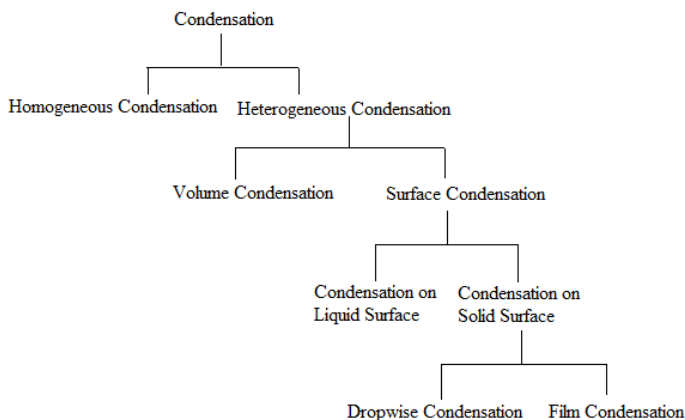


Figure 7: Classification of condensation phenomena

2.3.1 Film condensation

Film condensation is the most frequent type of condensation found in engineering systems. If the liquid phase fully wets a cold surface in contact with a vapor near saturation conditions, the conversion of vapor to liquid will take the form of film condensation. This film flows down the surface under the actions of gravity, shear force due to vapor flow, or other forces. The vapor-liquid interface releases latent heat, which is transferred through the condensate film and then through the solid wall, being finally removed by a coolant. Many times, the coolant is flowing in the other side of the condensing surface. Because the latent heat of vaporization must be removed at the interface to sustain the process, the rate of condensation is directly linked to the rate at which heat is transported across the liquid film from the interface to the surface. When the condensation rate is balanced with the condensate flow rate, a steady state is established. The rate of heat transfer by film condensation is determined by the thickness of the condensate film, which can be calculated using Nusselt's Film Theory (1916).

2.3.2 Dropwise condensation

It is quite possible for a thin microfilm of liquid to be adsorbed on all or part of a solid surface. This is particularly true for high-energy surfaces such as metals. Patches of adsorbed liquid molecules in the solid surface can thus serve as nuclei for condensation of the liquid phase when the vapor is supersaturated. Condensation on the surface can begin as formation of very small droplets on the surface at the sites of these nuclei; thus, so-called dropwise condensation.

Dropwise condensation may occur on a solid surface cooled below the saturation temperature of a surrounding vapor when the surface is poorly wetted except at locations where well-wetted contaminant nuclei exist. The poorly wetted surface condition can result from contamination or coating of the surface with a substance that is poorly wetted by the liquid phase of the surrounding vapor.

Dropwise condensation is a complex phenomenon that involves a series of randomly occurring subprocesses as droplets grow, coalesce and depart from a cold surface. The sequence of these subprocesses forms a dynamic "life cycle" that can be observed in figure 8. This illustration is part of a study developed by Ganzeles (2002), which presents the water vapor condensation over a heat exchanger made of PVDF (PolyVinylideneFluoride), in a vertical position. Five characteristic tracks are recognized:

- I. After drainage, a more or less dry track is left behind;
- II. Small droplets with almost equal sized droplets due to growth by condensation;
- III. Small and larger sized droplets mainly due to growth by coalescence;
- IV. Larger and small droplets mainly due by coalescence;
- V. Large drops with smaller ones, drainage can occur quite soon.

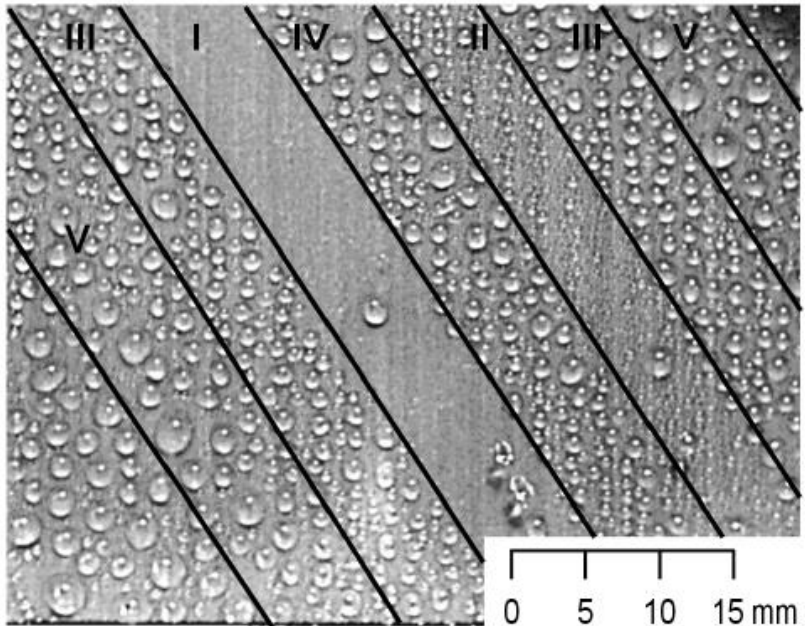


Figure 8: Typical patterns during dropwise condensation due to drainage. Gas flows from left to right (Ganzeles, 2002)

Summarily, during dropwise condensation, the condensate is usually observed to appear in the form of droplets, which grow on the surface and coalesce with adjacent droplets. When droplets become large enough, they are generally removed from the surface by the action of gravity or drag forces resulting from the motion of the surrounding gas. As the drops roll or fall from the surface, they merge with droplets in their path, effectively sweeping the surface clean of droplets. Droplets then grow anew on the freshly exposed solid surface. This sweeping and renewal of the droplet growth process is responsible for the high heat transfer coefficients associated with dropwise condensation.

Dropwise condensation is generally the preferred mode of condensation because the resulting heat transfer coefficient may be as much as an order of magnitude higher than that for film condensation under comparable circumstances (Carey, 1992).

In the last twenty years, it has been demonstrated that, just as with boiling heat transfer, a characteristic condensation curve exists that includes a dropwise region, a filmwise region and a transition region (Marto, 1998). Some representative condensation curves for steam at atmospheric pressure are shown in figure 9. Dropwise condensation occurs at a fixed vapor velocity v_g and at very low surface subcoolings ($T_s - T_w$) and can persist to relatively large subcoolings and to very large heat fluxes q'' , near 10 MW/m² for steam. Nevertheless, at large enough subcoolings, so much condensate is formed that a relatively thick, continuous liquid film begins to occur (i.e., the condensate formation rate exceeds the drop departure rate). Thus, a maximum heat flux is reached, similar to boiling. A transition region follows where the heat flux decreases and approaches the filmwise condensation curve. Further increases in subcooling result in a portion of the condensate actually freezing on the cold surface and a pseudofilm condensation will form. Analyzing the graph below, for a fixed heat flux, further to the left (decreasing the subcooling), a larger heat transfer coefficient will be found. As conclusion, the dropwise condensation is a more efficient condensation type than filmwise condensation.

Despite numerous studies of dropwise condensation over the years, its mechanism remains as a subject of debate. Two different types of models have been proposed. The first type model is based on the premise that droplet formation is a heterogeneous nucleation process. Droplet embryos are postulated to form and grow at nucleation sites, while portions of the surface between the growing droplets remain dry. This type of model was apparently first proposed by Eucken (1937). Experimental evidence supporting this physical model of the condensation process has emerged from several experimental investigations.

In the second type of dropwise condensation model, it is postulated that condensation occurs initially in a filmwise manner, forming an extremely thin film on the solid surface. As condensation continues, this film eventually reaches a critical thickness, estimated to be about 1 μm , at which point it ruptures and droplets form. Condensation then continues on the surface between the droplets that form when the film ruptures. Condensate produced in these regions is drawn to adjacent drops by surface-tension effects. Droplets also grow by direct condensation on their surfaces.

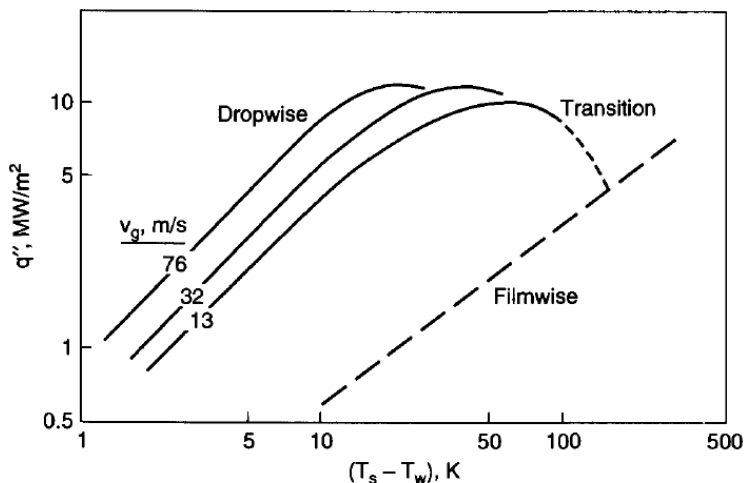


Figure 9: Condensation curves for steam (Marto, 1998)

This second model of the dropwise condensation process was apparently proposed by Jakob (1936). Modified versions of this model have also been proposed and the results of several investigations seem to support this type of interpretation of the condensation process.

In contrast, it is postulated in the first model described above that condensation occurs only on the droplets, and not on the surface between them. The rate of condensation on the larger droplets is less than on the smaller ones because of the higher resistance to heat conduction through larger drops. The large drops therefore grow primarily through coalescence. This model implies that most of the heat transfer during dropwise condensation is transferred to that portion of the surface covered with the smallest droplets.

For larger droplets the conduction path through the droplet from its surface to the solid wall is longer than for small droplets, which implies that the resistance to heat transfer is larger. For very large droplets, the larger resistance results in a heat transfer rate so low that portions of the surface covered by such drops contribute very little to the total heat transfer. It is useful, then, to think of the cold solid surface as consisting of thermally insulated regions under large droplets surrounded by thermally active regions covered with smaller droplets through which virtually all the heat is transferred.

2.4 TWO-PHASE FLOW DISTRIBUTION

In order to intensify the heat transfer in heat exchangers, multiple parallel channels are often used. The surface area increases with the number of channels, improving heat and mass transfer, whereas the inlet and outlet collectors facilitate the fluid distribution. These heat exchangers effectiveness is dependent on the uniformity of the mass flow rate distribution through parallel channels. Notwithstanding, maldistribution of the mass flow rate generally occur, resulting in significant loss of effectiveness.

An irregular two-phase distribution decreases the thermal performance of compact heat exchangers with parallel flow-circuits. The gas and the liquid are unequally distributed into the heat transfer tubes due to the two-phase separation at the manifold. Uneven distribution of the liquid in condensers may create reduced heat transfer zones as a result of high liquid loading (Vist and Pettersen, 2004).

Mueller and Chiou (1988) and Kitto and Robertson (1988) studied the many variables that affect the two-phase distribution. Variables such as geometric factors (manifold cross-section design, branch couplings, location and orientation of the tubes) and operating factors (flow rate, flow structure and vapor fraction at the manifold inlet and heat load on the tubes).

Vist and Pettersen (2004) investigated the two-phase distribution in round tube manifolds with 10 parallel tubes (4-mm diameter) using R134a as refrigerant. The authors concluded that the distribution is improved as the inlet vapor fraction increases, considering both downward and upward flow.

According to Bontemps (2005), to obtain sufficient heat or mass flow, several channels in parallel can be used. A small defect or a different roughness in a given channel can strongly affect the pressure drop and the flow distribution. The header also can play an important role in flow distribution.

Dario et al. (2013) presented a review on two-phase flow distribution in parallel channels. The authors concluded that the header and the feeding tube positions are the main factors influencing the mass flow rate distribution among parallel channels. The geometry, operating conditions and fluid properties were found as strong influences on the two-phase flow structure inside the header and, thus, also on the two-phase flow distribution in parallel channels.

2.5 IMPORTANT DEFINITIONS

In this section, important terms are defined in simplified form as a basis for the subsequent chapters. These terms are mostly related to two-phase flow and its fundamental relations.

The first definition presented is void fraction. The void fraction, α , is one of the most important parameters used to characterize two-phase flows. It is the key physical value for determining numerous other important parameters, such as the two-phase density and two-phase viscosity, for obtaining the relative average velocity of the two phases, and is of fundamental importance in predicting flow pattern transitions, heat transfer and pressure drop models. Void fraction is defined as the ratio of vapor (or gas) occupied area, A_v , to the cross sectional total area of the duct, A_{st} , at a given cross section:

$$\alpha = \frac{A_v}{A_{st}} \quad (2.14)$$

The slip ratio S is defined as the ratio of vapor (or gas) phase velocity to the liquid phase velocity, based upon the cross-sectional area available for flow.

$$S = \frac{v_v}{v_l} = \frac{\rho_l}{\rho_v} \frac{x_v}{(1-x_v)} \frac{(1-\alpha)}{\alpha} \quad (2.15)$$

The two-phase flow frictional multiplier, ϕ^2 , is defined as the ratio of the two-phase flow frictional pressure gradient to some reference single-phase flow frictional pressure gradient, usually based on one of the components flowing by itself. The reference phase can be either the liquid phase pressure gradient that results in ϕ_l^2 or the gas phase pressure gradient that results in ϕ_g^2 .

Another useful parameter is the superficial velocity of each phase. Superficial velocity j is a hypothetical flow velocity calculated as if the given phase or fluid was the only one flowing or present in a given cross sectional area with the mass flow G . The velocity of the given phase is calculated ignoring the second phase. The superficial velocity can be defined as the ratio of mass flow to the density of the phase. The liquid superficial velocity, j_l , is defined as:

$$j_l = \frac{G(1 - x_v)}{\rho_l} \quad (2.16)$$

In addition, the vapor superficial velocity, j_v , is defined as:

$$j_v = \frac{G x_v}{\rho_v} \quad (2.17)$$

The dimensionless numbers, its definition, and interpretation used in the present study are presented in table 3.

Table 3: Table of dimensionless numbers

Group	Definition	Interpretation
Reynolds Number	$Re = \frac{vL\rho}{\mu}$	Ratio of the inertial and viscous forces
Superficial Reynolds Number	$Re_l = \frac{GD(1 - x_v)}{\mu_l}$ $Re_v = \frac{GDx_v}{\mu_v}$	Reynolds Number of each phase
Reynolds Number liquid/vapor only	$Re_{lo} = \frac{GD}{\mu_l}$ $Re_{vo} = \frac{GD}{\mu_v}$	Reynolds Number considering the flow consists of one phase only (liquid or vapor)
Reynolds Number two-phase	$Re_{tp} = \frac{GD}{\mu_h}$	Reynolds Number for two-phase flow
Nusselt Number	$Nu = \frac{hD}{k_l}$	Dimensionless temperature gradient at the surface
Prandtl Number	$Pr = \frac{\mu c_p}{k}$	Ratio of momentum to thermal diffusivities

Galileo Number	$Ga = \frac{\rho_l (\rho_l - \rho_v) g D^3}{\mu_l^2}$	Ratio of gravitational force to viscous force
Jakob Number	$Ja = \frac{c_{p,l}(T_{sat} - T_w)}{i_{lv}}$	Ratio of sensible to latent energy absorbed during liquid-vapor phase change
Froude Number	$Fr = \frac{(G/\rho_l)^2}{gD}$	Ratio of inertia to gravitational forces
Weber Number	$We = \frac{G^2 D}{\rho_v \sigma}$	Ratio of inertia to surface tension forces
Bond Number	$Bo = \frac{g (\rho_l - \rho_v) D^2}{\sigma}$	Ratio of gravitational and surface tension forces

2.6 TWO-PHASE FLOW REGIMES

In internal convective vaporization and condensation processes, the vapor and liquid are in simultaneous motion inside the channel or pipe. The resulting two-phase flow is generally more complicated physically than single-phase flow. In addition to the usual inertia, viscous, and pressure forces present in single-phase flow, two-phase flows are also affected by interfacial tension forces, the wetting characteristics of the liquid on the tube wall, and the exchange of momentum between the liquid and vapor phases in the flow. The morphology of the two-phase flow very often plays a critical role in ascertaining the heat and mass transfer during vaporization and condensation processes. The morphology can be quite complex, and it can vary depending on the fluid properties and flow conditions.

The first step in understanding condensation in microchannels is distinguishing how the condensing fluid flows through the channels, because this forms the basis for the associated pressure drop and heat transfer (Garimella, 2006). The condensation process takes place when the fluid flows in the channel and the vapor phase progresses toward the liquid phase over a range of qualities. During the process, different flow patterns are established at distinct regions of the condenser. As the condensation progresses within a microchannel, the transitions between different flow mechanisms are distinct to those in larger diameter tubes, primarily due to differences in relative magnitudes of gravity, shear, viscous and surface tension forces. Therefore, extrapolation of large tube correlations to smaller diameter tubes can introduce errors into pressure drop and heat transfer predictions.

2.6.1 Upward vertical flow

For co-current upward flow in a vertical round tube, the possible observed flow regimes are indicated in figure 10. At very low vapor quality, the flow is usually found to be in the *bubbly flow* regime, which is characterized by discrete bubbles of vapor dispersed in a continuous liquid phase. In bubbly flow, the mean size of the bubbles is generally small compared to the diameter of the tube. At slightly higher qualities, smaller bubbles may coalesce into slugs that span through almost the entire cross section of the channel. The resulting flow regime is usually referred as *slug flow*.

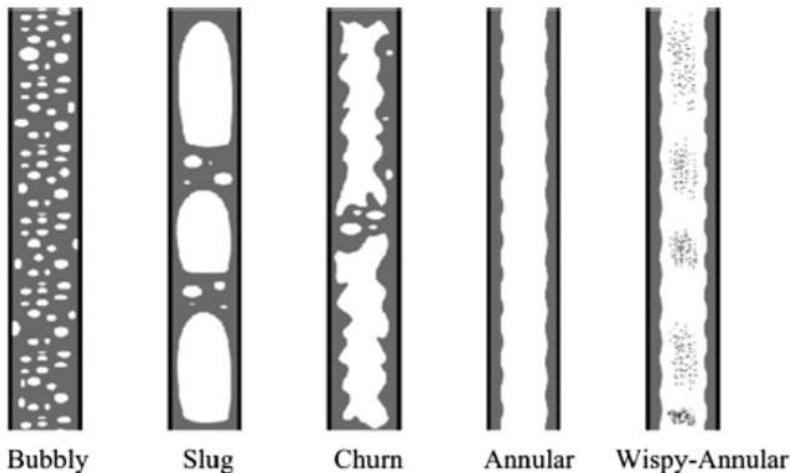


Figure 10: Schematic representation of flow regimes observed in vertical upward co-current gas-liquid flow (Cheng et al., 2008)

At much higher vapor quality levels, the two-phase flow generally assumes an annular configuration, with most of the liquid flowing along the wall of the tube and the gas flowing in the central core. As such, this regime is termed the *annular flow* regime. When the vapor flow velocity is high, the interface of the liquid film may become Helmholtz-unstable, leading to the formation of waves at the interface. Liquid droplets formed by breaking waves may then be entrained in the vapor core flow.

At intermediate qualities, one of two additional regimes may be observed. If both the liquid and vapor flow rates are high, an annular-type flow is observed with heavy “wisps” of entrained liquid flowing in the vapor core. Although this is a form of annular flow, it is sometimes designated as a separate regime, referred to as *wispy annular flow*.

For intermediate qualities, and lower flow rates, the vapor shear on the liquid-vapor interface may be near the value where it just balances the combined effects of the imposed pressure gradient and the downward gravitational body force on the liquid film. As a result, the liquid flow tends to be unstable and oscillatory. The vapor flow in the center of the tube flows continuously upward. Although the mean velocity of the liquid film is upward, the liquid experiences intermittent upward and downward motion. The flow for these conditions is highly agitated, resulting in a highly irregular interface. This oscillatory flow is referred to as *churn flow*.

The Hewitt and Roberts (1969) map is an example of flow pattern map for vertical flow in a pipe, as shown in figure 11. Since the axes are defined in terms of G_g/ρ_g and G_l/ρ_l (phase momentum flux), all the transitions are assumed to depend on the phase momentum fluxes. The boundaries between the flow regimes have been established from visual observation of the two-phase flow in a series of experiments (using a transparent tube) that spanned the entire flow regime map. Since the flow regime for a given set of conditions is a matter of judgment regarding the appearance of the flow, the boundaries should be interpreted as specifying the middle of a transition between two regimes.

From theoretical considerations, analytical expressions for the transition conditions between the two-phase flow regimes have also been obtained. Radovchich and Moissis (1962) presented arguments about the frequency of bubble collisions, which suggest that the transition from bubbly to slug flow is highly probable at void fractions above $\alpha = 0.3$. Based on a more detailed analysis, Taitel and Dukler (1977) proposed the following relation, which defines the incipient conditions for the transition from bubbly to slug flow:

$$\frac{j_l}{j_v} = 2.34 - 1.07 \frac{[g(\rho_l - \rho_v)\sigma]^{1/4}}{j_v \rho_v^{1/2}} \quad (2.18)$$

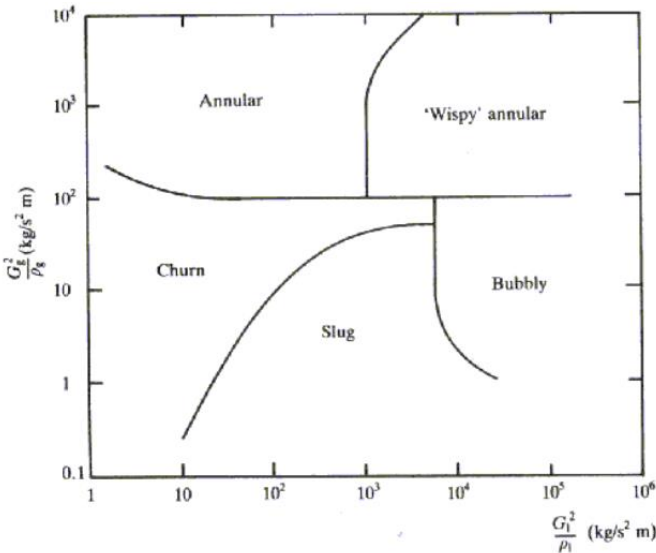


Figure 11: Hewitt and Roberts flow pattern map for vertical upflow in a pipe (Hewitt and Roberts, 1969)

As observed in the Hewitt and Roberts flow pattern map, increasing quality can lead to a transition from slug flow to churn flow. This breakdown of slug flow is a consequence of the interaction between the rising slug bubble and the liquid film between the slug and the wall. In this kind of flow, the liquid film actually moves downward as the slug moves upward at a velocity higher than the mean velocity of the two-phase flow, due to its buoyancy. As the vapor quality and void fraction increase, this countercurrent flow becomes unstable in a manner similar to the Helmholtz instability. This instability eventually leads to the breakup of the large bubbles characteristic of slug flow, initiating a transition to churn flow. Porteus (1969) presented theoretical arguments that suggest that this transition corresponds to conditions defined by equation 2.19:

$$\frac{j_l}{j_v} = 0.105 \frac{[gD(\rho_l - \rho_v)]^{1/2}}{j_v \rho_v^{1/2}} - 1 \quad (2.19)$$

where D is the tube diameter. Taitel and Dukler (1977), on the other hand, argued that for $(j_l + j_v)/(gD)^{1/2}$ greater than 50, the slug-to-churn transition occurs at conditions that correspond to $j_l/j_v = 0.16$.

The transition from churn flow to annular flow occurs at conditions where the upward shear stress of the vapor core flow plus the imposed pressure gradient balances the downward gravitational force on the liquid film. These conditions correspond to the lower vapor velocity limit for which steady upward annular flow can be sustained. Based on theoretical arguments, Wallis (1965) concluded that this transition occurred approximately at conditions specified by the relation:

$$\left[\frac{j_v^2 + \rho_v}{gD(\rho_l - \rho_v)} \right]^{0.5} = 0.9 \quad (2.20)$$

Taitel and Dukler (1977) proposed the following relation as means of predicting the transition from churn to annular flow:

$$\frac{j_v + \rho_v^{0.5}}{[g(\rho_l - \rho_v)\sigma]^{0.25}} = 3.09 \frac{(1 + 20X + X^2)^{0.5} - X}{(1 + 20X + X^2)^{0.5}} \quad (2.21)$$

where X is the Martinelli parameter, defined as:

$$X = \left[\frac{(dP/dz)_l}{(dP/dz)_v} \right]^{1/2} \quad (2.22)$$

In equation 2.22, $(dP/dz)_l$ and $(dP/dz)_v$ are the frictional pressure gradients for the liquid and vapor phases flowing alone in the pipe, respectively. These frictional gradients can be computed as:

$$\left(\frac{dP}{dz} \right)_l = - \frac{2f_l G^2 (1-x)^2}{\rho_l D} \quad (2.23)$$

$$\left(\frac{dP}{dz} \right)_v = - \frac{2f_v G^2 x^2}{\rho_v D} \quad (2.24)$$

$$f_l = B Re_l^{-n}, \quad Re_l = \frac{G(1-x)D}{\mu_l} \quad (2.25)$$

$$f_v = B Re_v^{-n}, \quad Re_v = \frac{Gx D}{\mu_v} \quad (2.26)$$

In the above friction-factor relations, for round tubes, the constants found were $B = 16$ and $n = 1$ for laminar flow (Re_l or $Re_v < 2000$), or $B = 0.079$ and $n = 0.25$ for turbulent flow (Re_l or $Re_v \geq 2000$).

The transition between wispy annular flow and annular flow is difficult to distinguish precisely because the regimes are so similar. Based on experiments that used a probe to detect wispy filaments in the core flow, Wallis (1965) proposed the following correlation for the transition condition:

$$\frac{j_v}{j_l} = \left(7 + 0.06 \frac{\rho_l}{\rho_v} \right) \quad (2.27)$$

This relation is recommended for $j_l \rho_l^{0.5} [gD(\rho_l - \rho_v)]^{-0.5} > 1.5$.

2.6.2 Horizontal flow

Mass, momentum and energy transfer between two phases flowing within a confined channel, with and without energy transfer from the walls, give rise to a huge possibilities of phase aggregations. Dispersed flow is one of these aggregations and is characterized by one of the phases widely distributed into the other phase. Another example is the separated flow, in which exists a continuous interface between the phases. These aggregations affect the transfer rates of mass, momentum and/or energy from the walls to the two-phase fluid flowing inside the channel and are often referred to as flow patterns or flow regimes.

According to Thome et al. (2003), interaction between gas-liquid or vapor-liquid flow results in primary flow regimes, including bubbly, slug or intermittent, annular, mist or dispersed, and stratified flows. These five principal regimes are depicted in figure 12, vapor being represented by white color and liquid by grey color. The bubbly, slug, and annular flows are similar to those found at upward vertical flow.

Bubbly flow is characterized by vapor dispersed into the liquid in bubbles of distinct diameters and shapes. At very low vapor quality, *bubbly flow* is often observed for horizontal flow. However, as indicated in figure 12, the bubbles, because of their buoyancy, flow mainly in the upper portion of the tube. *Slug flow* is associated with elongated bubbles or slugs and liquid slugs

At high vapor velocities and moderate liquid flow rates, *annular flow* is observed for horizontal gas-liquid flow. For such conditions, buoyancy effects may tend to thin the liquid film on the top portion of the tube wall and thicken it at the bottom. However, at sufficiently high vapor flow rates, the vapor flow is invariably turbulent, and strong lateral Reynolds stresses and the shear resulting from secondary flows may serve to distribute liquid more evenly around the tube perimeter against the tendency of gravity to stratify the flow. The strong vapor shear may also result in significant entrainment of liquid in the vapor core. Because gravitational body forces are often small compared to inertia effects and turbulent transport of momentum, the resulting flow for these circumstances is generally expected to differ from annular flow in a vertical tube under similar flow conditions.

Mist flow is frequently found in flows involving very low mass fractions of the liquid with fine spray of liquid droplets dispersed in the vapor flowing across the full channel diameter, justifying its other designation *dispersed flow*. Finally, for channels in horizontal orientation, gravity is a dominant force, which can lead to *stratified flow* with liquid

flowing along the lower wall underneath the vapor layer that fills the remaining channel cross section. One of the main differences between the regimes observed for horizontal flow and those for vertical flow is that there is often a tendency for stratification of the flow. Regardless of the flow regime, the vapor tends to migrate toward the top of the tube while the lower portion of the channel carries more of the liquid.

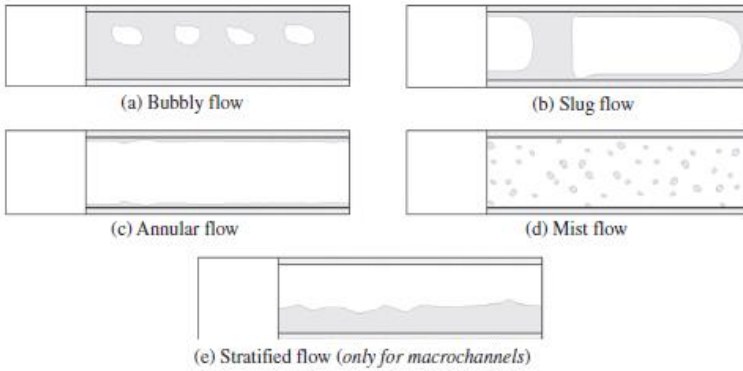


Figure 12: Scheme of the five primary flow regimes for horizontal tubes (Thome et al., 2013)

Several ways in which mass, momentum and heat transfer occur are also shown in figure 12. Nucleation and release of distinct bubbles between the wall and the flowing mixture, diffusion into and through a liquid film, and transfer to droplets from a flowing mist impacting the channel wall are the most meaningful.

In the other hand, Carey (1992) considered, for two-phase flow in horizontal round tubes, six flow regimes, as shown in figure 13. The plug flow and wavy flow are considered, unlike Thome et al. (2003). As the vapor quality is increased in the bubbly regime, coalescence of small bubbles produces larger plug-type bubbles, which flow in the upper portion of the tube. This is referred to as the *plug flow* regime. If the flow rate and/or the vapor quality is increased in the stratified flow regime, eventually the interface becomes Helmholtz-unstable, whereupon the interface becomes wavy. This type of flow is categorized as *wavy flow*.

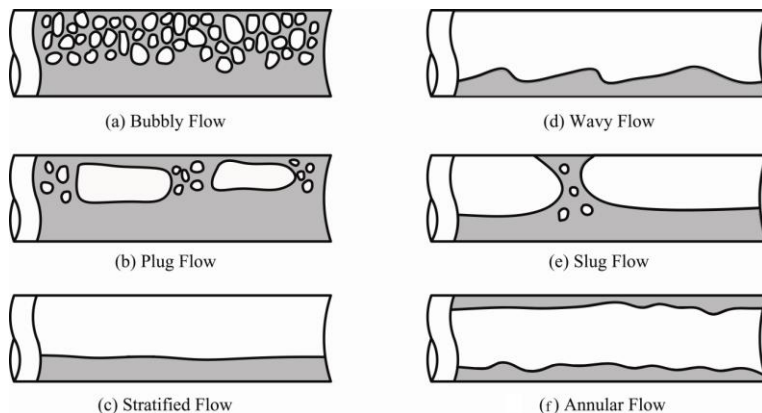


Figure 13: Schematic representations of flow regimes observed in horizontal, co-current gas-liquid flow (Carey, 1992)

Condensation heat transfer and pressure drop intimately depend on the corresponding flow regime as show by Odaymet et al. (2002). Louahlia-Gualous and Mecheri (2007) have investigated steam condensation heat transfer in a transparent circular miniature tube. The authors identified annular flow, slug or intermittent flow, and spherical bubbles flow.

The heat transfer in isolated bubbles zone inside a micro condenser was experimentally investigated by El Achkar et al. (2012). Based on energy balance, the liquid temperature in the zone was calculated and the authors showed that the liquid and vapor were not in thermal equilibrium.

According to Rahim et al. (2011), the primary flow regimes, first identified in macrochannels, may be present as well in microchannels and pipes. Nonetheless, the stratified flow, which is dominated by gravity force, is generally suppressed.

There is agreement in the open literature that the mechanisms of condensation heat transfer and pressure drop are intimately linked with the prevailing two-phase flow regime. The annular flow pattern is mostly associated with high vapor shear, while stratified, wavy and slug flows are revealed when the controlling force is gravity.

It is very important to determine the prevailing two-phase flow regime in order to evaluate the local heat transfer coefficients in condensation. The most outstanding models used to calculate the heat transfer coefficient take into consideration the effect of the flow regime.

2.6.3 Flow regime maps

Flow regime maps have been developed in order to predict the present flow regime inside tubes considering a given flow condition. These maps can be elaborated based on physical mechanisms and/or empirically. The flow regime maps often display the two-phase observations on axes of mass velocity versus the vapor quality for adiabatic vapor-liquid flows or superficial liquid velocity versus superficial gas velocity for adiabatic gas-liquid flows.

Since the 1950s, maps for two-phase flows inside conventional channels have been developed. However, flow regime maps considering microchannels were barely elaborated and the same holds true for condensation inside small diameters channels. According to Triplett et al. (1999), since the diameter of micro-scale channels are equal to, or even smaller than the Laplace length scale, the hydrodynamic interfacial process governed by the Taylor instability does not apply to capillaries, and thus, flow pattern prediction methods based on macro-scale channels will not work for smaller channels.

The bulk of the literature on two-phase flow regimes is on adiabatic flow, in which air-water, nitrogen-water and air-oil mixtures, typically in the absence of heat transfer, are used to simulate condensing flows. This approach leads to substantial simplification in experimental facilities. Felcar et al. (2007) developed a flow regime map considering adiabatic flow. The authors updated the flow pattern prediction method developed by Taitel and Dukler (1976), which was later modified by Barnea and coworkers (1983), in order to predict flow pattern transitions in micro-scale channels, i.e., diameters smaller than 3 mm. Surface tension and contact angle effects, negligible in larger tubes, were introduced in their method by including Eötvös and Weber numbers. Experimental observations for halocarbon refrigerants show that these fluids present surface tension of almost one order of magnitude lower than that of air-water and significant differences in the liquid viscosity are also observed. According to Yang and Shieh (2001), these physical properties may affect considerably the flow pattern when performing flow pattern visualizations with R134a and air-water.

Among the flow regime maps for gas-liquid flow in horizontal or slightly inclined round tubes proposed, the one proposed by Taitel and Dukler (1976) shown in figure 14, has perhaps the most carefully conceived theoretical basis. Although this map is computationally a bit more difficult to use than the others, it attempts to account for the differ-

ent combinations of physical parameters that affect different regime transitions on the map.

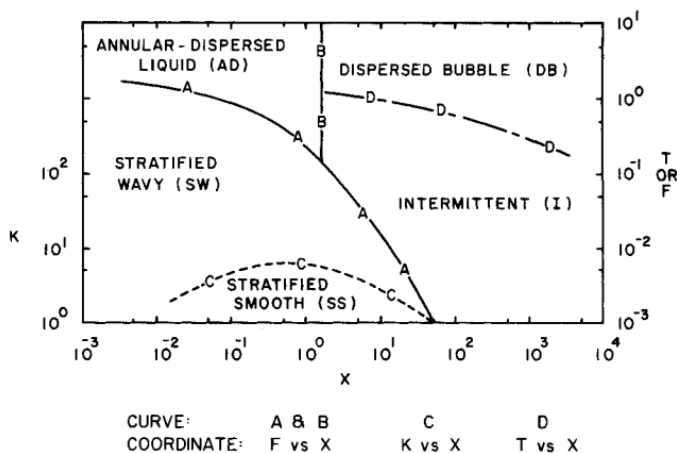


Figure 14: Generalized flow regime map for horizontal two-phase flow (Taitel and Dukler, 1976)

The horizontal axis on the Taitel-Dukler (1976) map is the Marti-nelli parameter X defined in equation 2.22. The value of this parameter fixes the horizontal position on this map regardless of the flow regime. However, the second dimensionless parameter used to determine the flow regime varies depending on the specific transition being considered.

For the stratified flow to wavy flow transition, the vertical position of the corresponding point in figure 14 is specified in terms of the parameter K , defined as:

$$K = \left[\frac{\rho_v j_v^2 j_l}{v_l (\rho_l - \rho_v) g \cos \Omega} \right]^{0.5} \quad (2.28)$$

where v_l is the kinematic viscosity of the liquid and Ω is the angle of inclination between the tube axis and the horizontal.

The wavy-annular and wavy-intermittent (plug or slug) transitions in figure 14 are evaluated in terms of X and the parameter F , defined as:

$$F = \left[\frac{\rho_v j_v^2}{(\rho_l - \rho_v) D g \cos \Omega} \right]^{0.5} \quad (2.29)$$

The transition from bubbly flow to intermittent flow is specified in terms of X and yet a third parameter T :

$$T = \left[\frac{-(dP/dz)_l}{(\rho_l - \rho_v) g \cos \Omega} \right]^{0.5} \quad (2.30)$$

Where $(dP/dz)_l$ is given in equation 2.23. The transition between intermittent and annular flow, or between bubbly and annular flow corresponds simply to $X = 1.6$ in this map.

It is displayed in figure 15 a comparison of the proposed flow pattern map by Felcar et al. (2007) with Yang and Shieh (2001) data. According to the classical form, the flow regime map was constructed considering the liquid and vapor superficial velocities, j_l and j_v , which definitions were presented in section 2.5. Stratified flow is reasonably well predicted though the data available for this flow pattern are scarce.

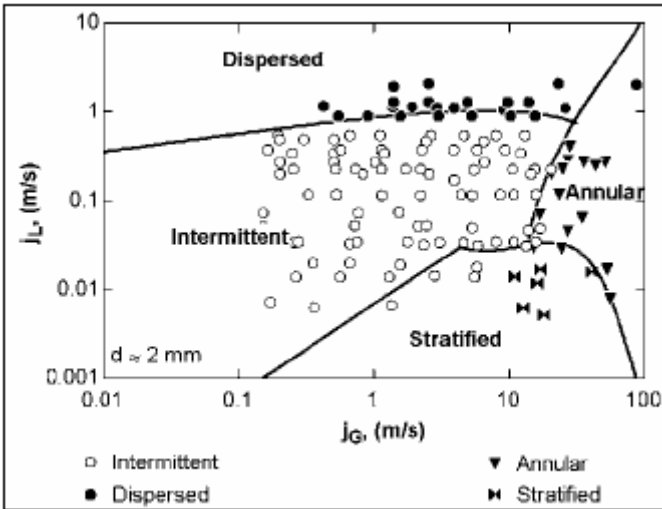


Figure 15: Comparison of the proposed predictive method (lines) by Felcar et al., 2007 and the experimental data by Yang and Shieh, 2001 (Felcar et al., 2007)

Experimental investigation of two-phase flow patterns for refrigerant R134a and air-water in horizontal tubes with internal diameter ranging from 1.0 to 3.0 mm was performed by Yang and Shieh (2001). As depicted in figure 16, the locations of bubble to plug, and slug flow transition were significantly affected by the R134a properties. The authors concluded that, beyond the buoyant force and turbulent fluctuations, surface tension force is also an important parameter for flow pattern determination in small tubes. A possible explanation is that the surface tension force makes the system minimize its interfacial area, which in case retains the circular shape of bubbles and also keep the liquid holdup between the tube walls to retard the transition from slug to annular. The air-water surface tension is much larger than that of R134a, which leads the intermittent to bubble flow transition to take place earlier for air-water than for R134a. It also causes a shift in the slug to annular transition to lower value of gas velocity for R134a. The map presented in figure 16 uses the same coordinates than that by Felcar et al. (2007). However, the symbols used are different (consider $j = u$).

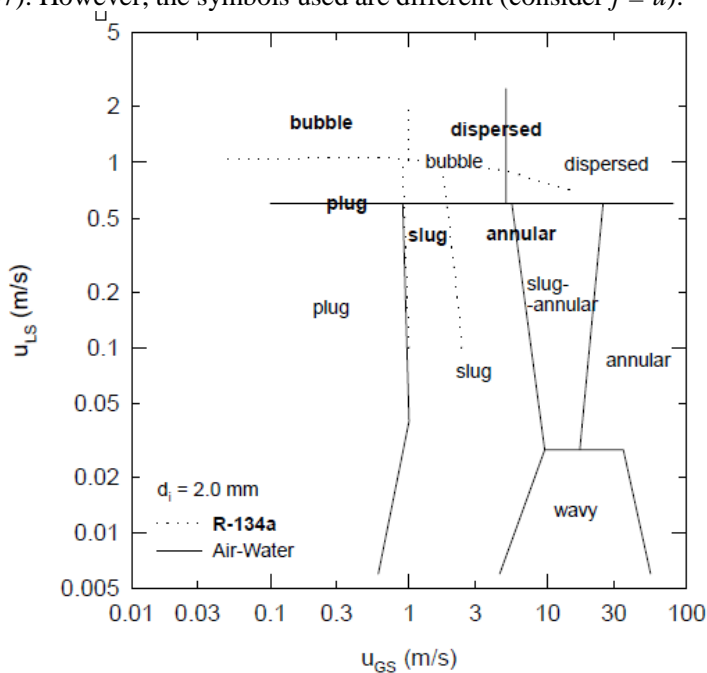


Figure 16: Comparison of air-water and two-phase R134a flow maps for 2.0 mm tube (Yang and Shieh, 2001)

Coleman and Garimella (1999) investigated the effect of tube diameter and shape on flow patterns and flow regime transitions for air-water mixture flow in tubes with small hydraulic diameters (1.3 to 5.5 mm). Gas and liquid superficial velocities were varied from 0.1 to 100 m/s and 0.01 to 10.0 m/s, respectively. The authors showed that tube diameter and surface tension may have a negligible effect on flow regime transitions in tubes with diameters greater than 10 mm, but play a crucial role on smaller tubes.

Coleman and Garimella (2003) published a study of two-phase flow regimes in round, square and rectangular tubes during condensation of refrigerant R134a. Six small diameter round (4.91 mm), square ($D_h = 4$ mm) and rectangular (4x6 and 6x4 mm: $D_h = 4.8$ mm; 2x4 and 4x2mm: $D_h = 2.67$ mm) test sections were used. The flow mechanisms were recorded over the entire range of qualities for five different mass fluxes (ranging from 150 kg/m²s to 750 kg/m²s). The flow mechanisms were categorized into four different flow regimes: intermittent flow, wavy flow, annular flow and dispersed flow. Furthermore, the large amount of data obtained enabled the delineation of several different flow patterns within each flow regime, which provides a clearer understanding of the different modes of two-phase flow. Finally, the authors concluded that for similar hydraulic diameters, flow regime transitions are not very strongly dependent on tube shape or aspect ratio.

Cavallini et al. (2002) suggested a model for evaluation of heat transfer coefficient based on flow pattern maps. This model was created on the basis of a databank consisting of over 2000 refrigerant condensation data points with 9 different halogenated fluids. The refrigerant's condensation took place inside plain tubes with inner diameter included between 3.1 mm and 21.4 mm. Stratified, slug and annular flow patterns were considered on this study. After four years, Cavallini et al. (2006a) proposed a simplified flow pattern map which was validated against 4471 data points relative to HCFCs, HFCs, carbon dioxide, ammonia and water from different laboratories.

2.6.4 Summary of studies on flow patterns during condensation

At the end of the two-phase flow section is important to present a summary of the remarkable studies on flow patterns during condensation. It is depicted in table 4, as follows. All the studies presented were conducted considering diabatic concurrent flow.

Table 4: Summary of studies on flow patterns during condensation

Author/References	Fluids and test sections positions	Main research contents	Remarks
<i>Liebenberg et al. (2005) and Liebenberg and Meyer (2006)</i>	R22, R407C, and R134a, smooth and microfin tubes, 8.11 mm, 9.081 mm, 8.936 mm, and 8.668 mm, horizontal.	The power spectral density (PSD) distribution of the fluctuating condensing pressure signal was used to identify the flow regimes.	Diabatic concurrent flow.
<i>Olivier et al (2007)</i>	R22, R407C, and R134a, smooth, helical microfin, and herringbone tubes, horizontal.	Flow regimes were observed. New flow-pattern transitions were proposed.	Diabatic concurrent flow.
<i>Louahlia-Gualous and Mecheri (2007)</i>	Steam, circular tube, 0.78 mm, horizontal.	Visualization and experimental measurements of condensation flow patterns were studied.	Diabatic concurrent flow.
<i>Mederic et al. (2004, 2006)</i>	N -pentane, circular tubes, 10 mm, 1.1 mm, and 0.56 mm, horizontal.	The effects of channel diameter on the condensation flow patterns were studied.	Diabatic concurrent flow.
<i>Chen et al. (2006)</i>	R134a, 3D microfin tubes with inner diameter inside diameter $Di=12$ mm and 14 mm, horizontal.	Flow patterns were experimentally studied and compared to models.	Diabatic concurrent flow.

Author/References	Fluids and test sections positions	Main research contents	Remarks
<i>Chen and Cheng (2005)</i>	Steam, microparallel channels, hydraulic diameter $D_h = 0.075$ mm, horizontal.	A visualization study of condensation was performed.	Diabatic concurrent flow.
<i>Coleman and Garimella (2003)</i>	R134a, round, square, and rectangular channels, hydraulic diameter $D_h = 4.91$ mm, 4 mm, 4.8 mm, and 2.67 mm, horizontal.	Flow patterns were experimentally studied and flow maps were constructed.	Diabatic concurrent flow.
<i>El Hajal et al. (2003) and Thome et al. (2003)</i>	R22, R134a, R410a, R125, R32, and R236fa, circular tube, 8 mm, horizontal.	A new flow-pattern map that is related to condensation heat transfer was developed for condensation.	Diabatic concurrent flow.
<i>Cheng and Van der Geld (2005) and Cheng et al. (2004)</i>	Air-steam mixtures, a polymer compact (PVDF) heat exchanger of 46 narrow parallel flow channels with a gap of 2 mm.	Dropwise condensation was achieved on the PVDF surfaces. Flow patterns were visualized during the condensation process.	Diabatic concurrent flow.

2.7 VOID FRACTION

The void fraction in two-phase flow is an influential parameter for the calculation of heat transfer coefficients and pressure drops. For instance, a decrease in void fraction means a smaller area for the vapor flow, which leads to an increase in its velocity, hence increasing the heat transfer coefficient and pressure drop. Void fraction is defined as the ratio of the pipe cross-sectional area occupied by the gas phase to the pipe cross-sectional area, as determined in section 2.5 of the present document. Numerous analytical theories have been presented for predicting void fractions for two-phase flows in macrochannels and in particular for the bubble, slug, annular and stratified flow regimes. According to Thome (2004), those theories are potentially applicable to microchannels for these same flow regimes.

Accurate measurements of cross-sectional void fraction in a microchannel are a challenging activity. It is fundamental to clarify that the cross-sectional void fraction is desired for calculation, not the volumetric void fraction.

This parameter calculation is an essential step that provides closure to the set of equations which must be solved to estimate pressure drop and heat transfer in two-phase flows. As the vapor and liquid phases do not flow at the same velocity (otherwise, this is referred to as homogeneous flow), the void fraction depends on the flow characteristics, while the vapor quality x is a thermodynamic quantity determined by the state of the two-phase mixture. For example, a flow is considered homogeneous in an elongated flow with individual bubbles separated by liquid slugs, if the slugs and bubbles travel at the same mean velocity. In this case the slower velocity of the liquid film between the bubble and the channel wall is ignored (Thome, 2004). The slip ratio S , also defined in section 2.5, is required to enable void fraction computation. For homogeneous flow, $S = 1.0$.

To assume homogeneous flow is the simplest consideration, as the two phases behave like a single uniform mixture, with average properties, which yields in equation 2.31 for the void fraction. The homogeneous model is in fact quite arbitrary, but it has been accepted for the microchannel modeling.

$$\alpha = \frac{x \rho_v}{(1-x)/\rho_l + x/\rho_v} \quad (2.31)$$

Several of the more widely used correlations do not take into account the flow pattern details, often assuming annular flow and relate the void fraction to a parameter that resembles the Lockhart-Martinelli parameter X_{tt} , which consider turbulent flow in both phases. Butterworth (1975) presented a generic expression that incorporate the appropriate expression for the pressure drops in the two phases:

$$\alpha = \left[1 + B_B \left(\frac{1-x}{x} \right)^{n_1} \left(\frac{\rho_v}{\rho_l} \right)^{n_2} \left(\frac{\mu_l}{\mu_v} \right)^{n_3} \right]^{-1} \quad (2.32)$$

A convenient tabulation of the leading coefficient B_B and the exponents n_1 , n_2 and n_3 for this model appears in table 5, extracted from Carey (1992), for the Zivi (1964) entropy minimization model, the Wallis (1965) separated cylinder model, the Lockhart–Martinelli (1949) model, the Thom (1964) correlation and the Baroczy (1965) correlation. This formulation facilitates comparison of different models and makes using them somewhat easier.

Table 5: Values of the constants in Butterworth (1975) correlation for void fraction (Carey, 1992)

Correlation or model	B_B	n_1	n_2	n_3
Homogeneous model	1	1	1	0
Zivi (1964) model	1	1	0.67	0
Wallis (1969) separate-cylinder model	1	0.72	0.40	0.08
Lockhart and Martinelli (1949)	0.28	0.64	0.36	0.07
Thom (1964) correlation	1	1	0.89	0.18
Baroczy (1965) correlation	1	0.74	0.65	0.13

2.8 PRESSURE DROP

The pressure drop evaluation in microcondensers has fundamental importance in experimental studies. First, the heat exchanger design is very influenced by the pressure drop. The greater the pressure drop is, the greater the pumping system has to be. Secondly, the heat transfer coefficient, h , depends on the wall tube and fluid temperatures; lastly, the function of the local pressure. Hence, an accurate measurement of the pressure drop in condensers, guarantee a low uncertainty in the fluid temperature estimate, which represents heat transfer calculation reliability. Heat transfer coefficients and pressure drops in phase change processes are strongly influenced by the local vapor quality during condensation. For condensation within tubes, distinct flow patterns are noted at different regions of the condenser, as the working fluid undergoes a transition from vapor to liquid along the channel.

The understanding of the fundamental condensation phenomena in compact geometries heat exchangers is just beginning to emerge (Garimella et al., 2016). Two-phase flow mechanisms and flow regime transitions in small channels are considerably distinct from those found in larger diameter tubes, as already presented in section 2.6 of the present document. Researches attribute this to the meaningful differences in the relative magnitudes of gravity, shear and surface tension forces, which are known as the determinant factors of the flow regime establishment. Hence, extrapolation of large channel correlations to smaller channels may introduce substantial errors into pressure drop predictions.

Idelchik (1994) proposed a method for pressure drop calculation at manifold fitted systems. Nonetheless, it is restricted to large diameter channels.

Classical pressure drop correlations for large diameter tubes (Chisholm, 1973; Friedel, 1979; Lockhart and Martinelli, 1949) continue to be extrapolated without substantiation to microscale geometries. Nonetheless, some researchers (Cavallini et al., 2002; Chen et al., 2001; Lee and Lee, 2001b; Mishima and Hibiki, 1996) have developed pressure drop correlations for small diameter tubes through simple modifications to the classical methods. However, those newer pressure drop correlations are capable of predicting data of specific researchers only.

The extrapolation of large diameter tubes correlations to small diameters tubes could introduce errors into the pressure drop predictions, rendering them useless for microscale condensation. Besides, pressure drop is a strong function of local vapor quality. In order to design precise condensation microscale devices, the two-phase flow patterns tran-

sition and its effect on pressure drop as the refrigerant changes from vapor to liquid must be completely understood (Agarwal et al., 2010; Bandhauer et al., 2006).

Steinke and Kandlikar (2006) assembled a database containing available experimental data for single-phase liquid flow in microchannels in order to evaluate this data when the pressure drop calculation for conventional channel is applied. The most common range of hydraulic diameters and the most data points are at 100-200 μm . The authors indicated that several issues need to be addressed when performing drop measurements in microchannel flows. Typically, three main components contribute to the overall pressure drop: the microchannel inlet and exit losses, the hydrodynamic developing length and the remaining length for the fully developed frictional loss.

Generally, headers or manifolds are used in minichannel experiments, as explained in section 2.4. Pressure drop is often measured between manifolds since this area has an easier access. The different components of pressure that make up the entire pressure drop are shown in figure 17. The inlet and outlet loss coefficients are represented by κ_i and κ_o . The friction factor is higher in the developing flow region. Finally, beyond the region of entry, the conventional theory for fully developed flow should apply. The components of pressure drop can be seen in equation 2.33.

$$\Delta p_{tot} = \frac{\kappa_i \rho \bar{V}^2}{2} + \frac{\kappa_o \rho \bar{V}^2}{2} + \frac{2(fRe)\mu\bar{V}L}{D_h^2} + \frac{\kappa(x) \rho \bar{V}^2}{2} \quad (2.33)$$

The first two terms represent the inlet and outlet losses, respectively. The third term is the frictional loss resulting from the fully developed flow. The last term represents the added pressure drop due to the developing flow region.

The formulations found for single-phase and two-phase flows are of significant difference. For this reason, this section is divided into two parts: single-phase flow and condensation flow.

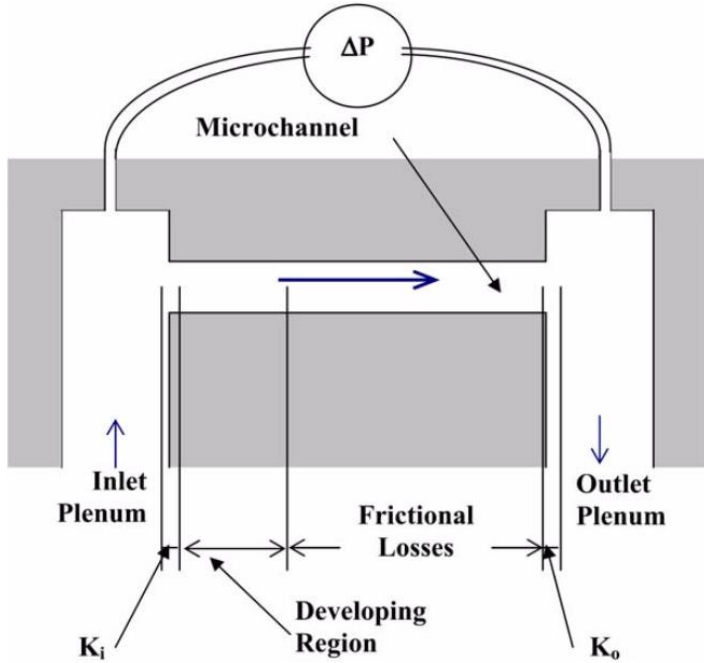


Figure 17: Components of pressure when measuring Δp in microchannel manifolds (Steinke and Kandlikar, 2006)

2.8.1 Single-phase flow

The friction losses through a straight conduit of constant cross section are calculated by the Darcy-Weisbach equation, as follows:

$$\Delta p = \zeta \frac{G^2}{2\rho} \quad (2.34)$$

where ζ represents the friction coefficient of the conduit length considered and can be quantified as shown:

$$\zeta = \frac{4fL}{D} \quad (2.35)$$

where L represents the channel length and f represents the Fanning friction factor. The Fanning friction factor depends on many factors, such

as, geometry and roughness of the tube and flow regime (laminar, transitional or turbulent).

Considering laminar flow, i.e., $Re < 2300$, within round channels, the Fanning friction factor is based solely on the Reynolds number, as given by the Hagen-Poiseuille law:

$$f = \frac{16}{Re} \quad (2.36)$$

The roughness of the pipe becomes a significant factor when turbulent flows are considered. Idelchik (1994) proposes that the limiting Reynolds number at which the influence of roughness begins to be felt is:

$$Re_{lim} = \frac{26.9}{\epsilon^{1.143}} \quad (2.37)$$

where ϵ represents the relative roughness of the walls.

A number of correlations are found in open literature for smooth tubes under turbulent flow. In light of turbulent flow, the inlet region, where the flow is not fully developed, is commonly not taken into account, since this is a small region. According to Bejan (2004), for turbulent flow, the inlet region is usually ten times greater than the diameter pipe.

The following correlation for the Fanning friction factor at fully developed turbulent flows was proposed by Blasius in 1913 (Idelchik, 1994):

$$f = 0.0791 Re^{-1/4} \quad (2.38)$$

Phillips (1987) proposed an equation for the average turbulent friction factor, as follows; this equation applies for circular tubes.

$$f = ARe^B \quad (2.39)$$

Where,

$$A = 0.09290 + \frac{1.01612}{(z/D)} \quad (2.40)$$

$$B = -0,26800 - \frac{0.31930}{(z/D)} \quad (2.41)$$

The channel entrance distance is represented by z . Equation 2.39 can be used to obtain the friction factors for both fully-developed and developing turbulent flows.

Single-phase flow pressure drops caused by flow disturbances were deeply studied and presented by Ghiaasiaan (2008). The pressure drop across any disturbance is the summation of reversible and irreversible components. The reversible component can be found from theory, but the irreversible component often needs to be found from empirical methods. Simple expansion represents one of the magnitudes of the irreversible pressure loss. However, this is a case where a simple theoretical analysis actually gives results that agree reasonably well with experimental data. According to Borda-Carnot, the following relation is proposed for the expansion loss coefficient K for that particular flow disturbance:

$$K_{ex} = (1 - \sigma)^2 \quad (2.42)$$

where σ is the ratio between smaller and larger flow areas.

The hydrodynamics downstream are different on a flow-area contraction and a flow-area expansion. Still according to Ghiaasiaan (2008), for a flow contraction:

$$K_{con} = \left(\frac{1}{C_C} - 1 \right)^2 \quad (2.43)$$

Experimental data are available in handbooks for the contraction coefficient, represented by C_C . A useful expression for the estimation of C_C is (Geiger, 1966):

$$C_C = 1 - \frac{1 - \sigma}{2.08(1 - \sigma) + 0.5371} \quad (2.44)$$

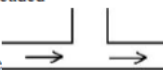



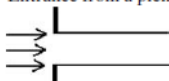
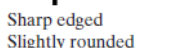
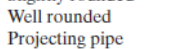
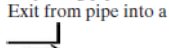

This simple curve fit to experimental data was presented by White (1999):

$$K_{con} \approx \begin{cases} 0.42(1 - \sigma) & \text{for } \sigma \leq 0.58, \\ (1 - \sigma)^2 & \text{for } \sigma > 0.58 \end{cases} \quad (2.45)$$

One should note the similarity between equations 2.42 and 2.45 for $\sigma > 0.58$.

A list of loss coefficients for a number of common flow disturbances is shown in table 6:

Table 6: Typical values of loss coefficients K for various flow disturbances (Ghiaasiaan, 2008)

Flow disturbance	K
45° bend	0.35 to 0.45
90° bend	0.50 to 0.75
Regular 90° elbow	$K = 1.49 Re^{-0.145}$
45° standard elbow	0.17 to 0.45
180° return bend, flanged	0.2
180° return bend, threaded	1.5
 Line flow, flanged tee	0.2
 Line flow, threaded tee	0.9
 Branch flow, flanged tee	1.0
 Branch flow, threaded tee	2.0
Fully open gate valves	0.15
1/4-closed gate valve	0.26
Half-closed gate valve	2.1
3/4-closed gate valve	17
Open check valves	3.0
Fully open globe valve	10
Half-closed globe valve	2.7
Fully open ball valve	0.05
1/4-closed ball valve	5.5
3/4-closed ball valve	210
Entrance from a plenum into a pipe	
 Sharp edged	0.5
 Slightly rounded	0.23
 Well rounded	0.04
 Projecting pipe	0.78
 Exit from pipe into a plenum	1.0

2.8.2 Condensation flow

The measured pressure drop included expansion and contraction losses due to the headers at both ends of the test section, and the pressure change due to deceleration caused by changing vapor fraction as condensation takes place, is represented as follows:

$$\Delta P_{measured} = \Delta P_{frict} + \Delta P_{exp+cont} + \Delta P_{decel} \quad (2.46)$$

Garimella et al. (2002, 2003 and 2005) demonstrated that the contraction and expansion loss contributions were less than 5% of the total measured pressure drop for all their data. The pressure change due to acceleration (deceleration) of the fluid (due to the change in vapor quality across the test section) was estimated as follows (Carey, 1992):

$$\Delta P_{ac} = \left[\frac{G^2 x^2}{\rho_v \alpha} + \frac{G^2 (1-x)^2}{\rho_l (1-\alpha)} \right]_{x=x_{out}} - \left[\frac{G^2 x^2}{\rho_v \alpha} + \frac{G^2 (1-x)^2}{\rho_l (1-\alpha)} \right]_{x=x_{in}} \quad (2.47)$$

where the void fraction was evaluated using the Baroczy (1965) correlation. For almost all their data, the deceleration term was extremely small compared to the overall pressure drop. These estimates were also corroborated by adiabatic flow and condensation tests at the same nominal conditions. The residual frictional component of the two-phase pressure drop, which generally was at least one order of magnitude larger than these minor losses, was used for developing condensation pressure drop models for the respective flow regimes.

The frictional pressure drop in two-phase flow represents the greater part of a heat exchanger pressure drop. Its calculation is based in a few approximations, and there are two different models for its estimate: the homogeneous and separated flow models.

2.8.2.1 The homogeneous model

The homogeneous model, also known as the ‘friction factor’ or ‘fog flow’ model, considers the two-phases to flow as a single phase possessing mean fluid properties. The basic premises upon which the model is based are the following assumptions:

- a) equal vapor and liquid velocities ($S=1$);
- b) the attainment of thermodynamic equilibrium between the phases;
- c) the use of a suitably defined single-phase friction factor for two-phase flow.

According to Collier and Thome (1994), this model is expected to be valid for the bubbly and wispy-annular flow patterns, particularly at high linear velocities and pressures. The pressure drop is calculated considering a single-phase flow and the fluid properties are the average of each phase. Therefore, the formulation used is the same as the one presented on section 2.8.1.

Furthermore, the homogeneous fluid density $\bar{\rho}$ is obtained as follows:

$$\frac{1}{\bar{\rho}} = \frac{x}{\rho_v} + \frac{1-x}{\rho_l} \quad (2.48)$$

The friction factor f has been evaluated using a mean two-phase viscosity $\bar{\mu}$ in the normal friction factor relationships. The form of the relationship between $\bar{\mu}$ and the quality x must be chosen to satisfy the limiting conditions shown in equation 2.49:

$$\begin{aligned} x = 0; \bar{\mu} &= \mu_l \\ x = 1; \bar{\mu} &= \mu_v \end{aligned} \quad (2.49)$$

Possible forms of the relationship are:

$$\frac{1}{\bar{\mu}} = \frac{x}{\mu_v} + \frac{(1-x)}{\mu_l} \quad (2.50)$$

An equation proposed by McAdams et al. (1942) is:

$$\bar{\mu} = x\mu_v + (1-x)\mu_l \quad (2.51)$$

Cicchitti et al., (1960) chose the expression:

$$\bar{\mu} = \bar{\rho} [xv_v\mu_v + (1-x)v_f\mu_f] \quad (2.52)$$

which was actually suggested by Dukler et al. (1964).

2.8.2.2 The separated flow model

The separated flow model considers the phases to be artificially segregated into two streams; one of liquid and one of vapor. In the model's simplest form, each stream is assumed to advance at a mean velocity. In case the mean velocities of the two phases are equal, the equations

reduce to those of the homogeneous model. The separated flow model has been continuously developed since 1949, when Lockhart and Martinelli published their classic papers on two-phase gas-liquid flow.

The basic premises upon which the separated flow model is based are:

- a) constant but not necessarily equal velocities for the liquid and vapor phases;
- b) attainment of thermodynamic equilibrium between the phases;
- c) use of empirical correlations or simplified concepts to relate the two-phase friction multiplier, ϕ^2 , and the void fraction, α , to the independent variables of the flow.

In separated flow model, the frictional pressure drop P_{frict} is calculated multiplying the pressure drop considering a single-phase flow by the two-phase frictional multiplier ϕ^2 . This last parameter is based on correlations, mostly empirical, where the single-phase flow considered is: liquid, vapor, liquid only or vapor only. The frictional pressure drop is given by:

$$\Delta P_{frict,tp} = \Delta P_{frict,l} \phi^2_l = \Delta P_{frict,v} \phi^2_v = \Delta P_{frict,lo} \phi^2_{lo} = \Delta P_{frict,vo} \phi^2_{vo} \quad (2.53)$$

Therefore, using the Darcy-Weisbach, equation 2.34 and the mass flux G :

$$\begin{aligned} \Delta P_{frict,tp} &= \frac{2(1-x)^2 G^2 L}{D \rho_l} f_l \phi^2_l = \frac{2x^2 G^2 L}{D \rho_v} f_v \phi^2_v \\ &= \frac{2G^2 L}{D \rho_l} f_{lo} \phi^2_{lo} = \frac{2G^2 L}{D \rho_v} f_{vo} \phi^2_{vo} \end{aligned} \quad (2.54)$$

The friction factors can be calculated using the Blasius equation (2.38) and the Reynolds number equivalent for the phase on table 3.

In order to apply the separated flow model equations, it is necessary to develop expressions for the two-phase multiplier, ϕ^2 , and the void fraction, α , in terms of the independent variables. Martinelli and co-workers were the first to achieve this. The Martinelli model was successively developed between the years of 1944 and 1949 from a series of studies of isothermal two-phase two-component flow in horizontal tubes (Collier and Thome, 1994). These studies culminated in a paper by Lockhart and Martinelli (1949), which proposed a generalized

method for calculating the frictional pressure gradient for isothermal two-component flow.

The Lockhart-Martinelli (1949) correlation considers a definite portion of the flow area assigned to each phase and assumes that conventional friction pressure-drop equations can be applied to the flow path of each phase. Interaction between the phases is thus ignored; however, Chisholm (1967) has corrected this treatment by considering interfacial shear force between the phases, which will be discussed in next subsection. Hence, it is prudent to consider the Lockhart-Martinelli correlation as purely empirical. Martinelli and his co-workers argued that the two-phase friction multipliers ϕ_l^2 and ϕ_v^2 could be correlated uniquely as a function of a parameter X , which was defined in equation 2.22.

This correlation was verified using their experimental data. The resulting graphical correlation is shown in figure 18 where ϕ (note: not ϕ^2) is plotted against X .

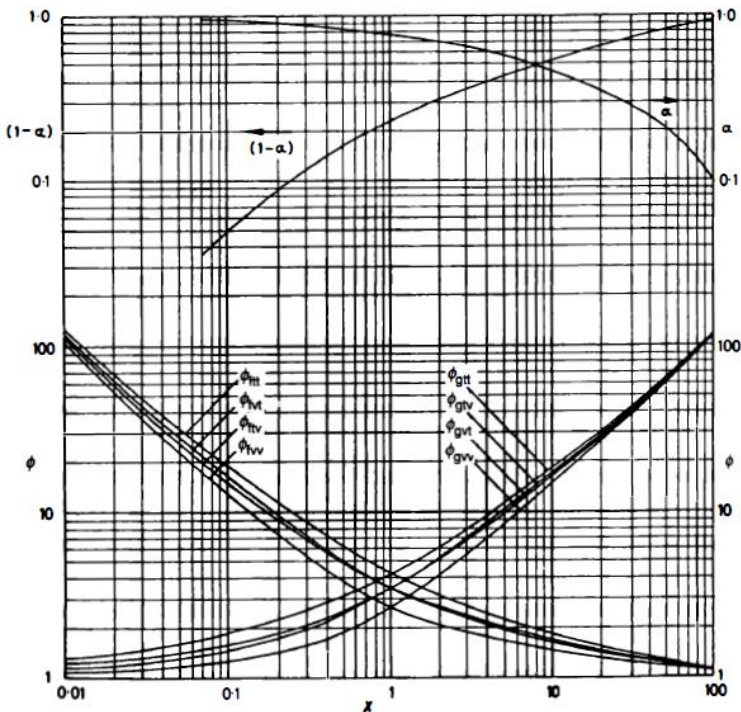


Figure 18: Lockhart-Martinelli (1949) correlations

The parameters ϕ^2_l and ϕ^2_v can be related to the parameter X by expressions of the form

$$\phi^2_l = 1 + \frac{C}{X} + \frac{1}{X^2} \quad (2.55)$$

and

$$\phi^2_v = 1 + CX + X^2 \quad (2.56)$$

The curves in figure 18 are well represented by equations 2.55 and 2.56 when C , a constant dependent on each phase flow regime, has the following values:

<i>Liquid</i>	<i>Gas</i>	<i>C</i>
Turbulent-	Turbulent (tt)	20
Viscous-	Turbulent (vt)	12
Turbulent-	Viscous (tv)	10
Viscous-	Viscous (vv)	5

In order to calculate the two-phase friction pressure gradient using the Lockhart-Martinelli correlation, it is only necessary to calculate the friction pressure gradients for each phase flowing alone in the channel and then use the correlations presented in figure 19 or alternatively equations 2.55 or 2.56. The correlation was developed for horizontal two-phase flow of two-component systems at low pressures (close to atmospheric) and its applicability to situations outside this range of conditions is not recommended.

2.8.3.3 *Homogeneous or separated flow models correlations*

Baroczy (1965), Chisholm (1973) and Friedel (1979) attempted to correct existing models for the influence of mass velocity on the frictional multiplier ϕ^2_{lo} . Baroczy (1965) proposed a method of calculation that employs two separate sets of curves. The first of these is the two-frictional multiplier ϕ^2_{lo} as a function of a physical property index and it is shown in figure 19. Mass quality x is presented as a parameter for a reference mass velocity of 1356 kg/(m²s). The physical property index is represented in equation 2.57:

$$\left(\frac{\mu_l}{\mu_v}\right)^{0.2} \left(\frac{\rho_v}{\rho_l}\right) \tag{2.57}$$

The second curve is derived from a correction factor, Ω , expressed as a function of the same physical property index for mass velocities of 339, 678, 2712 and 4068 kg/ (m²s) with mass quality as a parameter (figure 20). This curve is used to correct the value of ϕ^2_{lo} , obtained from figure 19 to the appropriate value of mass velocity.

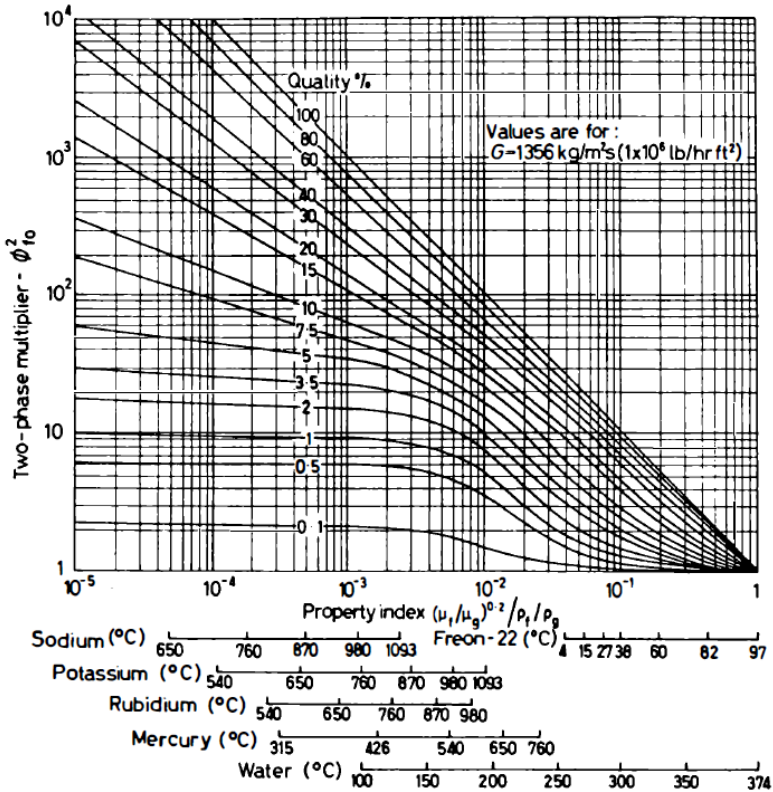


Figure 19: Two-phase friction pressure drop correlation (Baroczy, 1965)

Therefore,

$$\left(\frac{dp}{dz}\right)_{frict} = \frac{2f_{lo}G^2v_f}{D} \phi^2_{lo (G=1356)} \Omega \tag{2.58}$$

This method was tested against data from a wide variety of systems, including liquid metals and refrigerants, with satisfactory agreement between the measured and calculated values.

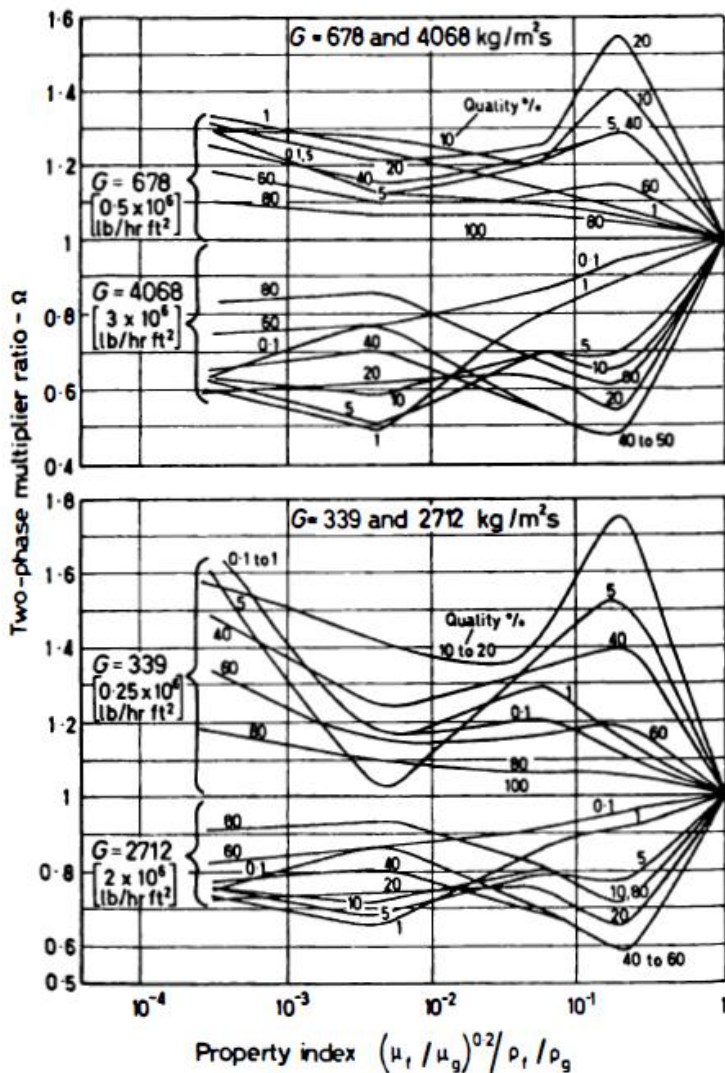


Figure 20: Mass velocity correction vs property index (Baroczy, 1965)

Chisholm (1973) showed that equation 2.55 by Lockhart-Martinelli could be transformed with sufficient accuracy for engineering purposes to:

$$\phi^2_l = 1 + (\Gamma^2 - 1)[Bx_v^{(2-n)/2} (1 - x_v)^{(2-n)/2} + x_v^{2-n}] \quad (2.59)$$

Chisholm (1973) defined the following physical property coefficient Γ , which presents a number of advantages when compared to the “physical property index” (see Baroczy (1965), equation 2.57):

$$\Gamma^2 = \frac{\Delta p_{frict,vo}}{\Delta p_{frict,lo}} \quad (2.60)$$

The B parameter is obtained as follows:

$$B = \begin{cases} \frac{55}{\sqrt{G}} & \text{for } 0 < \Gamma < 9.5 \\ \frac{520}{\Gamma\sqrt{G}} & \text{for } 9.5 < \Gamma < 28 \\ \frac{15000}{\Gamma^2\sqrt{G}} & \text{for } \Gamma > 28 \end{cases} \quad (2.61)$$

The n parameter depends on the Reynolds number (liquid only):

$$n = \begin{cases} 1 & \text{for } Re_{lo} \leq 2100 \\ 0.25 & \text{for } Re_{lo} > 2100 \end{cases} \quad (2.62)$$

Friedel (1979) elaborated one of the most accurate two-phase pressure drop correlations. It was obtained by optimizing an equation for ϕ^2_{lo} using a large database of two-phase pressure drop measurements:

$$\phi^2_{lo} = A_1 + \frac{3.2 A_2 A_3}{Fr^{0.045} We^{0.035}} \quad (2.63)$$

Where,

$$A_1 = (1 - x)^2 + x^2 \left(\frac{\rho_l f_{vo}}{\rho_v f_{lo}} \right) \quad (2.64)$$

$$A_2 = x^{0.78}(1 - x)^{0.224} \quad (2.65)$$

$$A_3 = \left(\frac{\rho_l}{\rho_v}\right)^{0.91} \left(\frac{\mu_v}{\mu_l}\right)^{0.19} \left(1 - \frac{\mu_v}{\mu_l}\right)^{0.7} \quad (2.66)$$

The above correlation is the more widely used correlation for vertical upward and horizontal flow, and is recommended by Hewit et al. (1994) for situations where surface tension data are available, and by Hetsroni (1982) for $\mu_l/\mu_v < 1000$.

2.8.2.4 Pressure drop at microscale

Yang and Webb (1996b) measured pressure drops in single-phase and adiabatic two-phase flows of refrigerant R-12 in rectangular plain and microfin tubes with $D_h = 2.64$ and $D_h = 1.56$, respectively. The channels were on horizontal orientation and at adiabatic conditions. The measurements were conducted at somewhat higher mass fluxes ($400 < G < 1400$ kg/(m²s)) than those of interest for refrigeration and air-conditioning applications and $0.1 < x < 0.9$. They found that the pressure gradient in microfin tube was higher than that of the plain tube. From their data, Yang and Webb (1996b) also concluded that surface tension did not play a role in determining the pressure drop in these tubes.

Yan and Lin (1999) studied condensation pressure drop of R134a in a 2-mm circular tube. They arranged 28 copper tubes in parallel held between copper blocks, to which were soldered similar cooling channels to form a crossflow heat exchanger that served as the test section, on the horizontal orientation. The tests were conducted under $T = 40$ - 50 °C. The resulting friction factor correlation is as follows:

$$f = 498.3Re_{eq}^{-1.074} \quad (2.67)$$

Yan and Lin's single-phase friction factors were significantly higher than the predictions of the Blasius equation (2.38). They attributed this to the influence of entrance lengths and tube roughness.

Zhang and Webb (2001) measured adiabatic two-phase pressure drops for R134a, R-22 and R-404A flowing through 3.25- and 6.25-mm circular tubes and a multi-port extruded aluminum tube with a hydraulic diameter of 2.13 mm. Other test conditions were $T = 20$ - 65 °C and $200 <$

$G < 1000 \text{ kg}/(\text{m}^2\text{s})$. They noted that the Friedel (1979) correlation, although widely recommended for larger tubes, was developed from a database with $D > 4 \text{ mm}$, and therefore did not predict their data well, especially at higher reduced pressures ($T_{sat} = 65^\circ\text{C}$). The authors postulated that the pressure drop would be a function of the reduced pressure rather than the density and viscosity ratios.

Garimella et al. developed experimentally validated models for pressure drops during condensation of refrigerant R134a in intermittent flow through circular (Garimella et al., 2002) and non-circular (Garimella et al., 2003b) microchannels (figure 21) with $0.4 < D_h < 4.9 \text{ mm}$. In addition, they developed a model for condensation pressure drop in annular flow (Garimella et al., 2003a), and further extended it to a comprehensive multi-regime pressure drop model (Garimella et al., 2005) for microchannels for the mass flux range $150 < G < 750 \text{ kg}/(\text{m}^2\text{s})$. For $D_h < 3.05 \text{ mm}$, they used flat tubes with multiple extruded parallel channels to ensure accurate measurable flow rates and heat balances. Three such tubes were brazed together (figure 21), with refrigerant flowing through the center tube, and coolant (air) flowing in counter-flow through the top and bottom tubes. The low thermal capacity and heat transfer coefficients of air maintained small changes in quality in test section, which in turn enabled the measurement of the pressure drop variation as a function of quality with high resolution. The measurement techniques were first verified by conducting single-phase pressure drop measurements for each tube in laminar and turbulent regimes for both the superheated vapor and subcooled liquid cases. The single-phase pressure drops were in excellent agreement with the values predicted by the Churchill (1977) correlation.

Mishima and Hibiki (1996) measured pressure drops in air-water flows through 1-4-mm tubes. By comparing their results with the Lockhart-Martinelli (1949) correlation, they noticed that the parameter C in Chisholm's (1967) curve-fit to the multiplier decreased with a decrease in tube diameter.

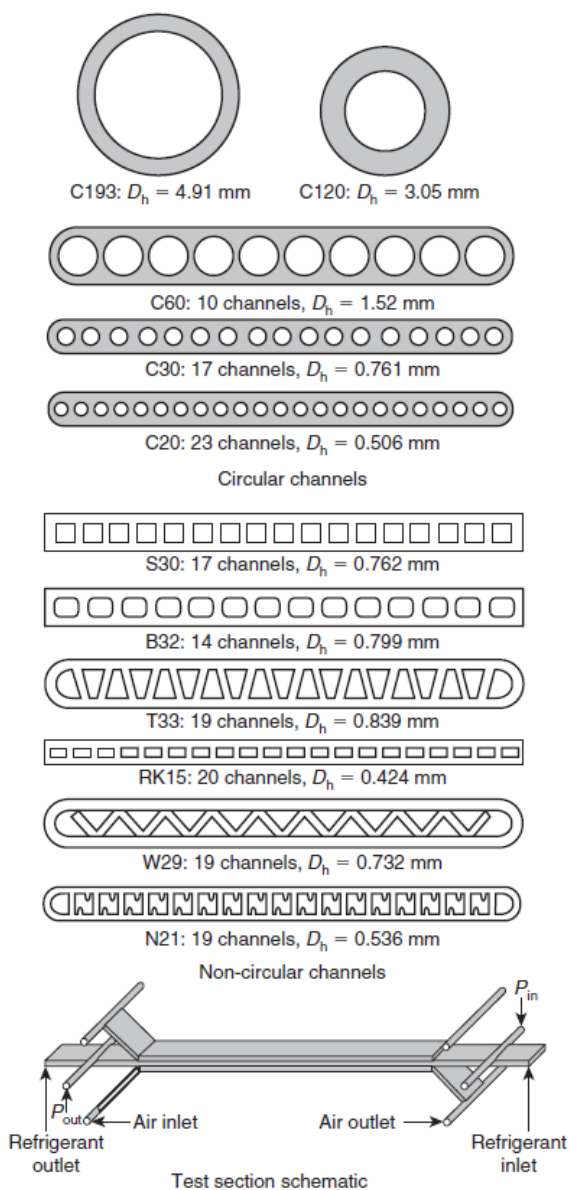


Figure 21: Refrigerant condensation geometries of Garimella (Garimella et al., 2005)

2.9 HEAT TRANSFER

In previous sections, the available information on flow regimes, void fractions, and pressure drop in two-phase flow was presented. The measurement and understanding of heat transfer in small channels ($D_h < 1$ mm) has proved to be particularly challenging. The small flow rates in microchannels, that correspond to small heat transfer rates, are difficult to measure accurately, since the spaces for measurement probes are confined. Also, the large heat transfer coefficients, which lead to very small temperature differences, are difficult to measure. There is little work to report if the scope is restricted to channels with $D_h < 1$ mm (not much information is available even for channels with $D_h < \sim 7$ mm). Therefore, in this section, an overview of the classical models of condensation is first presented to serve as a background for the work on the relatively smaller channels. Gravity-driven, shear-driven and multi-regime models will be addressed, followed by a presentation of the limited information on channels on 400 μm to 3 mm range.

Perhaps the most common flow configuration in which convective condensation occurs is in a horizontal circular tube. This configuration is found in air-conditioning and refrigeration condensers as well as condensers in Rankine power cycles. Thus, the focus here is on condensation inside horizontal tubes.

Since most of the heat transfer associated with the condensation process takes place under annular flow conditions, prediction of the condensation heat transfer coefficient for annular flow is of primary importance to the design of condensers operating at low to moderate pressures. It is not surprising, therefore, that most efforts to develop methods for predicting internal convective condensation heat transfer have been focused on annular flow. Condensation during slug, plug, or bubbly flow at the end of the condensation process has received much less attention. Annular flow is also somewhat easier to model analytically than the intermittent slug or plug flows.

2.9.1 Single-phase flow correlations

A number of single-phase flow models for heat transfer were proposed since the beginning of the last century. In this section, models developed for turbulent flow, uniform wall temperature or heat flux will be presented. Most of the correlations were developed for single-phase flow, in order to calculate the Nusselt number, Nu , which is represented in equation 2.68:

$$Nu = CRe^n Pr^m \quad (2.68)$$

The Dittus-Boelter (1930) equation is used in order to calculate the Nusselt number for turbulent flow. This equation is valid for $0.6 \leq Pr \leq 160$ and $Re > 10000$. When the fluid is being cooled, the equation is:

$$Nu = 0.023Re^{4/5}Pr^{0.3} \quad (2.69)$$

Sieder and Tate (1936) proposed a modification in Dittus-Boelter equation in order to correct the flow properties variation, which are caused by the high heat flux:

$$Nu = 0.023Re^{4/5}Pr^{1/3} \left(\frac{\mu}{\mu_w} \right)^{0.14} \quad (2.70)$$

where all the properties are evaluated in average temperature of the flow, except μ_w , which is obtained at the wall temperature.

Petukhov (1970) developed the following correlation for the Nusselt number calculation of turbulent single-phase flow, fully developed, valid for $0.5 < Pr < 2000$ and $10^4 < Re < 5 \times 10^6$:

$$Nu = \frac{(f/8)RePr}{1,07 + 12,7 (f/8)^{1/2} (Pr^{2/3} - 1)} \quad (2.71)$$

Where f is the friction factor and can be quantified using equations 2.38 and 2.39.

Gnielinski (1976) proposed an alteration in equation 2.71, in order to increase its valid intervals to $0.5 < Pr_l < 2000$ and $3000 < Re < 5 \times 10^6$:

$$Nu = \frac{(f/8)(Re - 1000)Pr}{1 + 12,7 (f/8)^{1/2} (Pr^{2/3} - 1)} \quad (2.72)$$

2.9.2 Two-phase flow correlations

Various authors have assumed that condensation occurs either in a gravity-driven mode or shear-driven mode, even in channels as small as ~3 mm. Nonetheless, gravity-driven condensation is expected to be less important at microchannel two-phase flows than at conventional channels.

2.9.2.1 Gravity-driven condensation

The heat transfer mechanism in gravity-driven condensation is based on the condensate film thickness. Most of the proposed models assume that the laminar liquid film flows from the top to the bottom of the tube through its inner surface. At the bottom portion of the tube, a pool of liquid is formed, which thickness is greater than that observed at the top of the tube.

An idealized condensate profile is illustrated in figure 22. During condensation within horizontal tubes, when the vapor velocity is very low (i.e., j_v is less than 0.5), the flow will be dominated by gravitational forces, and stratification of the condensate will occur. In this case, the condensate forms a thin film on the top portion of the tube walls and drains around the periphery by gravity alone toward the bottom of the tube, where a layer of condensate collects and flows axially due to shear forces.

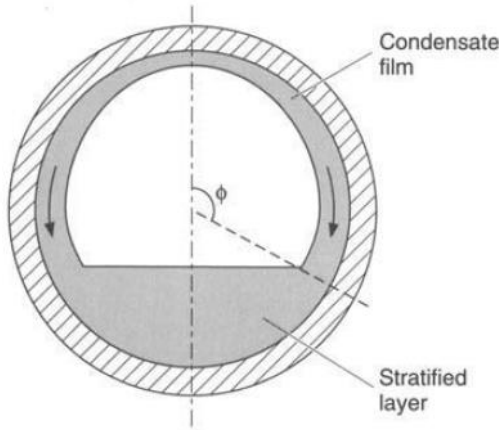


Figure 22: Idealized condensate profile during stratified flow, in-tube condensation within a horizontal tube (Marto, 1998)

The falling-film condensation analysis of Nusselt (1916) was used as basis for early work modelling of condensation heat transfer. Nusselt (1916) assumed that a thin laminar condensate film formed on an isothermal flat plate with a surface temperature less than the saturation temperature, surrounded by a stationary vapor at the saturation temperature. The condensate flows under the influence of gravity and the film thickens as it moves down the plate. Further, Nusselt assumed that the heat transfer due to conduction occur only across the film. Also,

constant film properties, negligible film subcooling, and a smooth liquid-vapor interface were assumed. An energy balance around a film element was made and after integrating with appropriate relationships for the mass flow rate, the relationship for film thickness is found, resulting in the following relationship for the average Nusselt number along a plate with length L :

$$\overline{Nu}_L = \frac{\bar{h}_l L}{k_l} = 0.943 \left[\frac{\rho_l (\rho_l - \rho_v) g \times h_{lv} \times L^3}{k_l \times \mu_l (T_{sat} - T_w)} \right]^{1/4} \quad (2.73)$$

Most of the literature on gravity-driven condensation heat transfer is based on the result presented in equation 2.73. The solution for the temperature distribution and for the condensate film in falling-film condensation was proposed by Rohsenow (1956). The difference between Rohsenow and Nusselt analysis is that Rohsenow accounted for the net fluid enthalpy change at the energy balance. For this reason, a modified enthalpy of vaporization was introduced to account for film subcooling, as follows:

$$h'_{lv} = h_{lv} (1 + 0.68 Ja_l) \quad (2.74)$$

The Jakob number, Ja , is defined in section 2.5.

Chato (1962) analyzed stratified-flow condensation inside horizontal and inclined tubes under low vapor shear using similar conditions. His analyses were validated using data for air/water mixtures flowing inside a 27.94-mm tube, and R113 inside a 14.53-mm tube at various inclinations. The following equation yields satisfactory agreement with the results, for all but fluids with low liquid Prandtl numbers:

$$Nu = \frac{hD}{k_l} = 0.468 \times K \left[\frac{\rho_l (\rho_l - \rho_v) g \times h'_{lv} \times D^3}{k_l \times \mu_l (T_{sat} - T_{wall})} \right]^{1/4} \quad (2.75)$$

The constant K is a correction for the liquid Prandtl number and a nominal value of $0.555 = 0.468K$ may be used. Equation 2.75 brings an important result for the Nusselt number related to condensation inside tubes because it is very similar to Nusselt's (1916) result for falling-film condensation on a flat plate with Rohsenow's (1956) correction for film subcooling.

The results obtained by Chato (1962) implied that stratified flow exists for inlet vapor Reynolds numbers, Re_v , less than 35,000. Predic-

tions of the analytical model and experimental data were found to agree well with an equation of the form:

$$h = 0.728 K_C \left[\frac{g \rho_l (\rho_l - \rho_v) k_l^3 h'_{lv}}{\mu_l (T_{sat} - T_w) D} \right]^{1/4} \quad (2.76)$$

In which h'_{lv} is given by equation 2.74.

Chato found that test data for R113 agreed well with this relation for $K_C = 0.76$. He further argued that heat transfer through the liquid pool at the bottom of the tube is negligible compared to transport across the thin film on the upper portion of the tube wall. Therefore, the coefficient K_C in equation 2.76 must vary with the void fraction. In a subsequent study, Jaster and Kosky (1976) suggested the following relations as means of predicting the void fraction and the factor K_C :

$$K_C = \alpha^{3/4} \quad (2.77)$$

$$\alpha = \left[1 + \frac{1-x}{x} \left(\frac{\rho_v}{\rho_l} \right) \right]^{-1} \quad (2.78)$$

This correlation applies to the stratified annular flow conditions that may exist over much of the tube length if the inlet vapor velocity is low. This circumstance has also been examined in detail by Rufer and Kezios (1966). Flow circumstances of this type may be encountered near the end of the condensation process when the void fraction is still large, but deceleration of the flow has dropped the vapor velocity enough to produce stratified flow with a thin film of condensate on the upper portion of the tube wall.

Rufer and Kezios (1966) analyzed stratified condensation in horizontal and inclined tubes using analytical approach; however, their results were distinct from those of Chato (1962). The authors neglected the vapor shear effect on the laminar condensing film, for the liquid pool and the interface. The main differences between Chato's (1962) and Rufer and Kezios's (1966) work is whether the liquid level should rise or fall as the condensation proceeds, whether the tube should be filled with liquid at the end of the condensation process and whether exit conditions should govern the holdup in the tube.

Singh et al. (1996) conducted experiments on R134a condensing at 35°C inside a 11-mm tube for the mass flux range $50 < G < 300$ kg/(m²s). The stratified-wavy, wavy-annular and annular flow regimes were

the regimes found using their data. For wavy-annular and annular regimes, a strong mass flux dependence on the heat transfer coefficient was found; meanwhile, in the stratified-wavy regime the dependence was weaker, although not negligible. The authors compared their experimental results to Traviss et al. (1973), Shah (1979), Dobson et al. (1994), Chato (1962) and Akers et al. (1959) correlations and the data was underpredicted. Seeing that, they proposed a correlation that uses the Chato (1962) correlation but using a much lower leading constant of 0.0925 for the film condensation, at the top of the tube.

Koyama et al. (2003) proposed a heat transfer correlation for condensation in minichannels. The authors investigated the condensation of pure refrigerant R134a in two kinds of 865 mm long multi-port extruded tubes having eight channels in 1.11-mm hydraulic diameter and 19 channels in 0.80-mm hydraulic diameter. The local heat transfer was measured in every subsection of 75mm in effective cooling length using heat flux sensors.

2.9.2.2 *Shear-driven condensation*

For many applications involving internal flow condensation, the flow is expected to be in annular regime over most of the passage length. There are analytical models for annular flow, which can be used as means of predicting the heat transfer performance for annular flow condensation. Such models generally require a high level of computational effort, and they can be used only if reliable closure relations for the interfacial shear and entrainment are available. As result, somewhat simpler empirical relations that correlate condensation heat transfer data more directly have also been developed by a number of investigators.

When the vapor velocity is high enough ($j_v > 1.5$), gravitational effects can be neglected, and the condensate collects as a thin annular film around the inner tube walls, with no stratification. A significant portion of most condensers operate in this flow regime. There are numerous predictive models described in the literature for annular flow. The shear-driven condensation models have a formula for the local Nusselt number:

$$Nu = Nu_l \cdot F(x) \quad (2.79)$$

Where Nu_l is a turbulent flow, single-phase, forced convention Nusselt number for the liquid, and $F(x)$ is a two-phase multiplier that depends on local quality x .

Carpenter and Colburn (1951) developed a study in order to obtain data for local and average heat transfer coefficients for the condensation of steam, methanol, ethanol, toluene, and trichloroethylene inside a vertical 11.6-mm inner diameter tube. The Nusselt equation underpredicted the values when compared to their data, due to the influence of vapor shear. The authors stated that the thin condensate layer for annular flow might become turbulent at very low liquid Reynolds numbers (~ 240). Vapor shear, gravity, and the momentum change due to condensation acting upon the condensate layer were considered. Carpenter and Colburn proposed that the major thermal resistance was caused by the laminar sublayer.

Akers et al. (1959) defined an all-liquid flow rate that provided the same heat transfer coefficient for condensing annular flow. A way to express this all-liquid flow is by an equivalent mass flux, which was used to define an equivalent Reynolds number. The equivalent mass flux and equivalent Reynolds number can be calculated using the following equations:

$$G_{eq} = G \left[(1 - x) + x \left(\rho_l / \rho_v \right)^{1/2} \right] \quad (2.80)$$

$$Re_{eq} = \frac{G_{eq} d_i}{\mu_l} \quad (2.81)$$

Substituting equations 2.80 and 2.81 into a typical single-phase turbulent heat transfer equation yields:

$$Nu = \frac{h d_i}{k_l} = C Re_l^n Pr_l^{1/3} \quad (2.82)$$

Where:

$$\begin{array}{lll} C = 0,0265 & n = 0.8 & \text{for } Re_l > 10 \times 10^4 \\ C = 5.03 & n = 1/3 & \text{for } Re_l < 10 \times 10^4 \end{array}$$

At moderate to high inlet vapor velocities, annular flow is established almost immediately at the inlet and persist over most of the condensation process. A number of investigators have proposed ways of predicting the condensation heat transfer coefficient for annular flow conditions. Three of the most useful correlations are those developed by Soliman et al. (1968), Traviss et al. (1973), and Shah (1979). In the

annular flow analysis, the shear at the interface and at the tube wall are linked directly to the transport of heat across the liquid film.

Traviss et al. (1973) used the heat-momentum analogy and the von Karman universal velocity distribution in the liquid film in order to develop a correlation for the Nusselt number in annular flow condensation. The turbulent vapor core prompted the assumption that the vapor core and vapor-liquid interface temperatures were the same. Friction, gravity, and momentum change were considered significant factors to determinate the pressure gradient. The authors computed the frictional term applying the Lockhart-Martinelli (1949) two-phase multiplier approach. They derived a relationship for the liquid Reynolds number as a function of this film thickness. The condensation heat transfer coefficient was developed as follows:

$$Nu = \frac{Pr_l Re_l^{0.9}}{F_2(Re_l, Pr_l)} F_1(X_{tt}) \quad 0.15 < F_1(X_{tt}) < 15 \quad (2.83)$$

Where,

$$Re_l = \frac{G(1-x)d_i}{\mu_l} \quad (2.84)$$

$$F_1(X_{tt}) = 0.15 \left[\frac{1}{X_{tt}} + \frac{2.85}{X_{tt}^{0.476}} \right] \quad (2.85)$$

And $F_2(Re_l, Pr_l)$ is given by:

$$F_2 = 0.707 Pr_l Re_l^{0.5} \quad Re_l < 50 \quad (2.86a)$$

$$F_2 = 5 Pr_l + 5 \ln[1 + Pr_l(0.0964 Re_l^{0.585} - 1)] \quad 50 < Re_l < 1125 \quad (2.86b)$$

$$F_2 = 5 Pr_l + 5 \ln(1 + 5 Pr_l) + 2.5 \ln(0.0031 Re_l^{0.812}) \quad Re_l > 1125 \quad (2.86c)$$

The results were compared to experiments conducted on R-12 and R-22 condensing in an 8-mm tube for $161 < G < 1533$ kg/(m²s). For qualities as low as 0.1m the authors found agreement with the experimental data. Great agreement was also found when the turbulent Martinelli parameter X_{tt} was below 0.155; nevertheless, for turbulent Martinelli parameter X_{tt} above 0.155 (most probably a mist flow condition, with high quality and mass flux) the experimental data were underpredicted by the correlation.

Shah (1979) proposed one of the most widely used general purpose condensation correlation, which is based on a purely empirical approach. He used for its development a large database, containing the works of 21 investigators. The operation conditions were $11 < G < 211$ kg/ (m²s), $21^\circ\text{C} < T_{sat} < 310^\circ\text{C}$, $7 < D < 40$ mm. In addition, it is an easy correlation to use. The reasoning behind Shah's correlation is that, in absence of nucleate boiling, condensation heat transfer may be similar to evaporative heat transfer when the tube is completely wet. This correlation is:

$$Nu = Nu_{lo} \left[(1-x)^{0.8} + \frac{3.8x^{0.76}(1-x)^{0.04}}{p_r^{0.38}} \right] \quad (2.87)$$

where,

$$p_r = P/P_c \quad (2.88)$$

and

$$Nu_{lo} = 0.023Re_{lo}^{0.8}Pr_l^{0.4} \quad (2.89)$$

P and P_{cr} are the absolute local and critical pressures, respectively.

This correlation was validated using data for water, R-11, R-12, R-22, R-113, methanol, ethanol, benzene, toluene, and trichloroethylene condensing within horizontal, inclined and vertical tubes. 474 data points were used to develop Shah's correlation and, the mean deviation between the predictions and the experimental data was 17%. As a result of the lack of lower Re_l data for the development of the correlation, Shah recommends that it should be used only for $Re_l > 350$.

Soliman (1986) elaborated a heat transfer correlation for annular-mist flow condensation using data from many researchers. The operation conditions selected included steam, R-113 and R-12 as working fluids, $7.4 < D < 12.7$ mm, horizontal and vertical orientations, $21^\circ\text{C} < T_{sat} < 310^\circ\text{C}$, $80 < G < 1610$ kg/ (m²s), $0.20 < x < 0.95$. The author found that although the Akers et al. (1959) correlation was successful in predicting data for $We > 20$, the data were seriously underpredicted for $We > 30$; the correlation proposed by Traviss et al. (1973) also underpredicted the data. Soliman assumed that the flow might occur as a homogeneous mixture in thermodynamic equilibrium.

$$Nu = 0.00345 Re_m^{0.9} \left(\frac{\mu_v h_{lv}}{k_v (T_{sat} - T_{wall})} \right)^{1/3} \quad (2.90)$$

Where the mixture Reynolds number is given by

$$Re_m = GD/\mu_m \quad (2.91)$$

and the mixture viscosity is given by

$$1/\mu_m = x/\mu_v + (1-x)/\mu_l \quad (2.92)$$

Chen et al. (1987) proposed a comprehensive film-condensation heat transfer correlation based on analytical and theoretical results from the literature. For co-current annular film flow, they argued that, for falling-film condensation in the absence of interfacial shear, the method of Churchill and Usagi (1972) can be used to determine the local Nusselt number for an arbitrary condition. Separate correlations for the laminar-wavy and turbulent film flow regimes are used. Based on such arguments, they postulated the following relation for the zero-shear Nusselt number Nu_0 at an arbitrary location:

$$Nu_0 = [(Nu_{lw})^{n_1} + (Nu_t)^{n_1}]^{1/n_1} \quad (2.93)$$

Where Nu_{lw} and Nu_t are the Nusselt numbers for wavy laminar and turbulent film flow, respectively. The Nusselt number in the correlations developed by these investigators is defined as:

$$Nu = \frac{h v_l^{\frac{2}{3}}}{k_l g^{\frac{1}{3}}} \quad (2.94)$$

In a similar fashion, Chen et al. (1987) proposed the following relation for the local Nusselt number Nu_x in the presence of vapor shear:

$$Nu_x = [(Nu_0)^{n_2} + (Nu_{sd})^{n_2}]^{1/n_2} \quad (2.95)$$

Where Nu_0 is the zero shear value as determined by equation 2.93, and Nu_{sd} is the value of the Nusselt number obtained from a prediction of shear-dominated film flow. For laminar-wavy flow with zero shear, Chen et al. (1987) used the correlation recommended by Chun and Seban (1971):

$$Nu_{lw} = 0.823Re_x^{-0.22} \quad (2.96)$$

where

$$Re_x = \frac{G(1-x)D}{\mu_l} \quad (2.97)$$

For the turbulent regime, Chen et al. (1987) used the following relation to predict Nu_t , which is a curve-fit to the theoretical results of Blangetti and Schlunder (1978):

$$Nu_t = 0.0040Re_x^{0.4}Pr_l^{0.65} \quad (2.98)$$

For the high interfacial shear stress regime, a modified form of the relation proposed by Soliman et al. (1968) was used to predict Nu_{sd} :

$$Nu_{sd} = 0.036Pr_l^{0.65}(\tau_i^*)^{1/2} \quad (2.99)$$

Where τ_i^* is a dimensionless interfacial shear stress defined as:

$$\tau_i^* = \frac{\tau_i}{\rho_l(gv_l)^{2/3}} \quad (2.100)$$

For co-current flow, Chen et al. (1987) used the following expression to determine τ_i^* , which was derived from the empirical two-phase pressure drop correlation developed by Dukler (1960):

$$\tau_i^* = A_D(Re_{ter} - Re_x)^{1.4}Re_x^{0.4} \quad (2.101)$$

where

$$A_D = \frac{0.252\mu_l^{1.177}\mu_v^{0.156}}{D^2g^{2/3}\rho_l^{0.553}\rho_v^{0.78}} \quad (2.102)$$

and

$$Re_{ter} = \frac{GD}{\mu_l} \quad (2.103)$$

Using equations 2.96 through 2.103 in order to evaluate the terms in equations 2.93 and 2.94, Chen et al. (1987) determined the values of n_1 and n_2 that provided a best fit to the measured local heat transfer coefficients obtained by Blangetti and Schlunder (1978). They found $n_1 = 6$ and $n_2 = 2$ provided a very good fit. Combining these equations for these values of n_1 and n_2 , the following correlation equation is obtained:

$$Nu_x = \frac{hv_l^{\frac{2}{3}}}{k_l g^{\frac{1}{3}}} = \left[\left(0.31 Re_x^{-1.32} + \frac{Re_x^{2.4} Pr_l^{3.9}}{2.37 \times 10^{14}} \right)^{1/3} + \frac{A_D Pr_l^{1.3}}{771.6} (Re_{ter} - Re_x)^{1.4} Re_x^{0.4} \right]^{1/2} \quad (2.104)$$

Equation 2.104 applies to annular flow condensation in vertical tubes, and includes the effects of gravity, interfacial waves, and interfacial shear. If the gravity force terms are neglected, equation 2.104 reduces to:

$$Nu_x = \frac{hv_l^{\frac{2}{3}}}{k_l g^{\frac{1}{3}}} = 0.036 A_D^{0.5} Pr_l^{0.65} (Re_{ter} - Re_x)^{0.7} Re_x^{0.2} \quad (2.105)$$

When shear forces are large compared to body forces, the tube orientation is unimportant. Equation 2.105 is therefore expected to apply to shear-dominated annular film condensation in either horizontal or vertical tubes. Although the gravitational acceleration g appears in the definitions of Nu_x and A_D , it cancels out of Equation 2.105, leaving the heat transfer coefficient independent of g . Chen et al. also used equation 2.104 to derive a relation for the average heat transfer coefficient for annular film condensation in vertical tubes, and developed a correlation for counterflow condensation.

For co-current flow, Chen et al. (1987) noted that their correlation equation (2.104) may be inaccurate near the inlet of the tube and/or at low quality near the end of the condensation process. Near the inlet, high vapor shear may result in high liquid entrainment, resulting in a mist annular flow or breakdown of a continuous liquid film. Condensation heat transfer for such conditions would be significantly different

from the annular flow postulated in their analysis. At the end of the condensation process, the flow pattern will change to slug flow for vertical tubes, or to stratified or intermittent (slug/plug) flow for horizontal tubes. For these non-annular regimes, the heat transfer mechanisms are expected to differ and the correlation for annular flow is not expected to apply.

Kosky (1971) developed a simple algebraic equation for the evaluation of non-dimensional film thickness in order to simplify closed-form computations. In that regard, the work of Dukler (1960) and Kutateladze (1963) were combined and the following expressions were developed:

$$\delta^+ = \left(\frac{Re_l}{2}\right)^{1/2} \quad \text{for } \delta^+ < 25 \quad (2.106)$$

$$\delta^+ = 0.0504 Re_l^{7/8} \quad \text{for } \delta^+ > 25 \quad (2.107)$$

In a set of related papers, Cavallini et al. (2001; 2002) determined heat transfer and pressure drop data for multiple refrigerants and blends (R22, R134a, R125, R32, R236a, R407C, and R410A) condensing in smooth 8-mm horizontal tubes. It was then elaborated multiple-flow regime models to predict their own data as well as data from other researchers. The operation conditions were $30^\circ\text{C} < T_{sat} < 50^\circ\text{C}$, and $100 < G < 750 \text{ kg}/(\text{m}^2\text{s})$. The authors found that their data showed disagreement when compared against the available correlations. The predictions of most correlations tested were not satisfactory within the stated range of applicability. In that way, most correlations were inadequate as general purpose predictive tools. Therefore, they elaborated new procedures: for annular flow, for which they chose $j_g^* > 2.5$; $X_{tt} < 1.6$ as the transition criterion. Wallis dimensionless gas velocity j_g^* can be calculated as follows:

$$j_g^* = \frac{G_t x}{\sqrt{Dg\rho_v(\rho_l - \rho_v)}} \quad (2.108)$$

For annular flow, the authors recommended the use of Kosky and Staub (1971) model, in which the heat transfer coefficient and the frictional pressure gradient are related through the interfacial shear stress τ . The frictional pressure gradient is obtained modifying the Friedel (1979) correlation in order to apply only to annular flow, consid-

ering that this correlation has originally been intended for annular and stratified regimes. Finally, the annular flow model was modified and it is given by the following equations:

$$h_{annular} = \frac{\rho_l C_{pL} (\tau / \rho_l)^{0.5}}{T^+} \quad (2.109)$$

Where the dimensionless temperature T^+ is given by equation 2.110:

$$T^+ = \begin{cases} \delta^+ Pr_l & \delta^+ \leq 5 \\ 5 \{ Pr_l + \ln [1 + Pr_l (\delta^+ / 5 - 1)] \} & 5 < \delta^+ < 30 \\ 5 [Pr_l + \ln(1 + 5 Pr_l) + 0.495 \ln(\delta^+ / 30)] & \delta^+ \geq 30 \end{cases} \quad (2.110)$$

With:

$$\delta^+ = \begin{cases} (Re_l / 2)^{0.5} & \text{for } Re_l \leq 1145 \\ 0.0504 R e_l^{7/8} & \text{for } Re_l > 1145 \end{cases} \quad (2.111)$$

Cavallini et al. (2006c) proposed a heat transfer model for condensation inside minichannels, based on analogy between heat and momentum transfer. This model takes into account the effect of the entrainment rate of droplets from the liquid film. Their correlation is applied to annular, annular-mist flow. The authors have measured heat transfer coefficients during condensation of R134a, R410A and R1236ea inside a flat multiport minichannel tube with a 1.4-mm hydraulic diameter.

2.9.3 Predictions of local condensation heat transfer coefficient

A number of parameters may affect the condensation heat transfer coefficient, like refrigerant properties, tube diameter, saturation temperature, heat flux, mass flux and vapor quality. Some studies in this matter were carried out by Cheng et al., 2007; Fang et al., 2013; Harirchian and Garimella, 2010; Kandlikar and Grande, 2003; Kew and Cornwell, 1997; Li et al., 2010; Mehendale et al., 2000. Two-phase flow heat transfer is influenced by the channel size, what was proved in a number of experiments found in open literature.

Six condensation heat transfer correlations are summarized in table 7, made by Park et al. (2015). The last three correlations (Koyama et al., 2003; Huang et al., 2010; Park et al., 2011) rely on Lockhart-Martinelli parameter, X_{tt} . Meanwhile, the Cavallini and Zecchin's (1974)

and Shah's (1979) correlations are not based on Lockhart-Martinelli parameter.

Dobson et al. (Dobson and Chato, 1998; Dobson et al., 1993, 1994) researched heat transfer coefficients for conventional channels, using R12, R22, R134a and near-azeotropic blends of R32 and R125 in 50%/50% and 60%/40% proportions as working fluids. They suggested a few correlations for gravity-dominated and shear-dominated flows, which successfully predicted data from their experiments and from other studies.

Table 7: Condensation heat transfer correlations (Park et al., 2015)

Author(s)	Correlation	Remarks
Cavallini and Zecchin	$\frac{hD_h}{k_f} = 0.05 \left[Re_g \left(\frac{\mu_g}{\mu_f} \right) \left(\frac{\rho_f}{\rho_g} \right)^{0.5} + Re_f \right]^{0.8} Pr_f^{0.33}$	x is substituted with x_e in comparison
Shah	$\frac{hD_h}{k_f} = 0.023 Re_{fo}^{0.8} Pr_f^{0.4} \left(\frac{\mu_f}{14\mu_g} \right)^n \left[(1-x)^{0.8} + \frac{3.8x^{0.76}(1-x)^{0.04}}{Pr_g^{0.38}} \right]$ for $J_g \geq 0.98(Z + 0.263)^{-0.62}$ $\frac{hD_h}{k_f} = 0.023 Re_{fo}^{0.8} Pr_f^{0.4} \left(\frac{\mu_f}{14\mu_g} \right)^n \left[(1-x)^{0.8} + \frac{3.8x^{0.76}(1-x)^{0.04}}{Pr_g^{0.38}} \right] + 1.32 Re_f^{-1/3} \left[\frac{\rho_f(\rho_f - \rho_g)\phi_g^3}{\mu_f^2} \right]^{1/3}$ for $J_g < 0.98(Z + 0.263)^{-0.62}$	$n = 0.0058 + 0.557 Pr_R$ $J_g = \frac{xG}{[\rho D_h \rho_g (\rho_f - \rho_g)]^{0.5}}$ $Z = \left(\frac{1}{x} - 1 \right)^{0.8} Pr_R^{0.4}$
Dobson and Chato	$\frac{hD_h}{k_f} = 0.023 Re_f^{0.8} Pr_f^{0.4} \left[1 + \frac{2.22}{X_{tt}^{0.89}} \right]$	x is substituted with x_e in comparison
Koyama et al.	$\frac{hD_h}{k_f} = 0.0152 \left(1 + 0.6 Pr_f^{0.8} \right) \left(\frac{\phi_g}{X_{tt}} \right) Re_f^{0.77}$	$\phi_g = 1 + 21 \left(1 - e^{-0.319 D_h} \right) X_{tt} + X_{tt}^2$ x is substituted with x_e in comparison
Huang et al.	$\frac{hD_h}{k_f} = 0.0152 \left(-0.33 + 0.83 Pr_f^{0.8} \right) \left(\frac{\phi_g}{X_{tt}} \right) Re_f^{0.77}$	$\phi_g = 1 + 0.5 \left(\frac{G}{\sqrt{g D_h \rho_g (\rho_f - \rho_g)}} \right)^{0.75} X_{tt}^{0.35}$
Park et al.	$\frac{hD_h}{k_f} = 0.0055 Re_f^{0.7} Pr_f^{1.37} \frac{\phi_g}{X_{tt}}$	$\phi_g^2 = 1 + 13.17 \left(\frac{\rho_g}{\rho_f} \right)^{0.17} \left(1 - \exp(-0.6\sqrt{Bo}) \right) X_{tt} + X_{tt}^2$

$$Re_g = \frac{Gx D_h}{\mu_g}, \quad Re_f = \frac{G(1-x) D_h}{\mu_f}, \quad Re_{fo} = \frac{GD_h}{\mu_f}, \quad X_{tt} = \left(\frac{1-x}{x} \right)^{0.9} \left(\frac{\rho_g}{\rho_f} \right)^{0.5} \left(\frac{\mu_f}{\mu_g} \right)^{0.1}, \quad Pr_R = \frac{P}{P_{ref}}, \quad Bo = \frac{g(\rho_f - \rho_g) D_h^2}{\sigma}$$

2.10 MINICHANNEL CONDENSATION

As the channel size becomes smaller, some of the conventional theories for (bulk) fluid, energy and mass transport need to be revisited for validation. This chapter presents the literature review on condensation, focusing in minichannel condensation. In order to conclude this chapter, it is important to discuss the existing researches on small diameter channels.

2.10.1 Enhancement of condensation heat transfer

In many circumstances of practical interest, most, if not all the resistance to heat flow during the condensation process, is due to conduction and/or convection through the liquid condensate on the cooled surface. Consequently, most techniques for enhancing condensation heat transfer involve controlling the condensate on the surface to reduce the heat transfer resistance associated with its presence on the surface.

A way to reduce the average heat transfer resistance of the liquid on the surface is to promote dropwise condensation. Note that, in doing so, a uniformly thick film is replaced by droplets with no film, or a microfilm between them. The usual result is that the mean heat transfer coefficient is significantly higher for dropwise condensation than for filmwise condensation under the same conditions, as shown in 2.3 section of the present document.

For film condensation, the use of extended surfaces as means of enhancing the heat transfer coefficient has received considerable attention. Gregorig (1954) pioneered the use of a wavy surface to enhance film-condensation heat transfer. He established that by changing the curvature of interfaces through surface modifications, strong pressure gradients could be generated, aiding in the removal of condensate, yielding regions of very thin films and high heat transfer coefficients.

Another way to improve the heat exchange performance during condensation is to reduce the diameter of the channel where it occurs. The heat transfer rate, in a specified heat exchanger, is given by:

$$Q = UA\Delta T \quad (2.112)$$

The overall heat transfer coefficient, U , relies on the fin efficiencies, individual side heat transfer coefficients, fouling resistances and thermal resistance of the separating wall of the heat exchanger. Accord-

ing to Kandlikar and Grande (2003), the flow inside a minichannel is expected to be laminar owing to its small channel hydraulic diameter.

Kandlikar (2007) presented an analysis of the enhancement effects of the channel size reduction, considering fully developed laminar flow. In such flow regime, the Nusselt number, Nu , is constant and the heat transfer coefficient in internal flow, h , varies inversely with the channel hydraulic diameter, D_h :

$$h = Nu \frac{k}{D_h} \quad (2.113)$$

Figure 23 shows the heat transfer coefficient variation, as a function of the channel diameter, for circular tubes under constant heat flux boundary conditions.

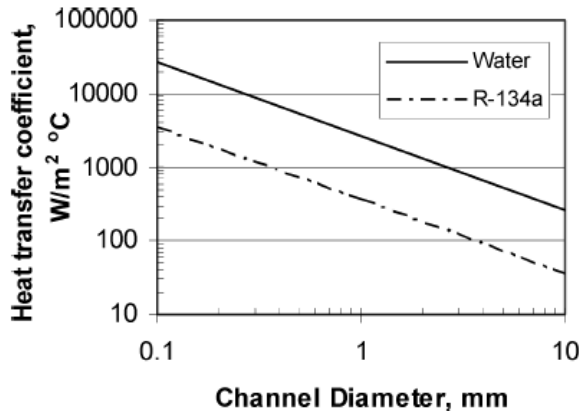


Figure 23: Variation of the heat transfer coefficient with hydraulic diameter for fully developed laminar flow under constant heat flux boundary condition for water and R134a (Kandlikar, 2007)

As one can see in figure 23, the heat transfer coefficients of minichannels and microchannels increase with the channel diameter decrease. The heat transfer coefficient with R134a in a plain, 10-mm diameter tube is only 35 W/(m²·°C), while for a 1-mm diameter tube it increases to 350 W/(m²·°C). For a 0.5-mm diameter tube, the coefficient reaches 700 W/(m²·°C). As a conclusion, minichannels provide a great opportunity to reduce overall size and cost, as well as improving the performance of heat exchangers.

2.10.2 Numerical models

A number of numerical models have been developed for condensation in channels. A theoretical model, elaborated by Wang and Rose (2005, 2011), considered gravity, viscous, and surface tension forces. The authors assumed laminar liquid film. Their model was in agreement with some of the available data. Nebuloni and Thome (2010) also assumed the liquid film to be laminar and developed a numerical model of annular flow condensation, which successfully predicted some of the test data.

Da Riva et al. (2012) performed a numerical simulation of condensation in a 1-mm diameter channel using the VOF (Volume of Fluid) method in order to track the interface between liquid and vapor. Their predictions have been compared to available data and the authors concluded that for low flow rates the assumption of laminar liquid film gives rise to great agreement with measurements. On the other hand, at high flow rates the numerical simulation matched the experimental data when turbulence was taken into account.

Heat transfer condensation inside a 1-mm hydraulic diameter channel was numerically investigated by Da Riva et al. (2011) and Bortolin et al. (2014). They have considered laminar film at low flow rates whereas turbulence was assumed at higher flow rates. Comparing their results with the experimental data, they have found great conformity. The authors concluded that under the assumption of laminar condensate flow, experimental heat transfer coefficient values at low mass fluxes can be predicted, although the computed heat transfer coefficient is found to be almost independent of mass flux and vapor quality. When turbulence is taken into account, the numerical model captures the influence of mass flux that is observed in the experimental measurements.

The development of numerical models for condensation provides insight into the phenomena, however, no author has been able to validate his model with a wide range of data. A number of published correlations were based on the researcher's own data, which is a hindrance for its practical use. The published studies by Wang et al. (2002), Koyama et al. (2003a), Bohdal et al. (2011a), Riehl and Ochterbeck (2002), Huang et al. (2010), and Park et al. (2011) are examples of numerical models that were validated on a limited database. As such, these models are not expected to have an embracing applicability.

Nonetheless, Kim and Mudawar (2013) carried on a flow pattern based model which successfully matched with a wide range database. Several fluids, horizontal and vertical channels, round and rectan-

gular channels, multi-port channels and hydraulic diameters ranging from 4.424- to 6.22-mm were used as a comparative database. However, Garimella et al. (2014) tested Kim and Mudawar's model on their database and found it in poor agreement with minichannel data. Therefore, Garimella et al. (2014) elaborated a flow pattern predictive model which showed good concordance with their own data, which consists in a wide range of pressures, flow rates, hydraulic diameters and many fluids.

2.10.3 Important researches on small diameter channels

There are relatively few experimental data available in the open literature for heat transfer in condensation at minichannel and microchannel. Most of them are for fluids with similar properties, predominantly R134a. It is shown in figure 24 the main data obtained by researchers that used, mostly, similar fluids properties, flow parameters and channel geometry. In this figure, α represents the heat transfer coefficient.

A summary of the most relevant experimental studies of condensation in small channels is presented in table 8. A review of this table reveals that some researchers focused only on the heat transfer aspect of condensation, others studied the phenomenon of pressure drop, while some looked at both.

Single phase and two-phase flow heat transfer coefficients of experimental data obtained for microchannels was analyzed by Riehl et al. (1998), who compared the data to the available analytical models. They noted large discrepancies between predicted numbers and experimental data, as the models were not able to predict accurately their data. Furthermore, correlations proposed for microchannel convective flow presented wide unconformities as well.

Four years later, Riehl and Ochterbeck (2002) studied methanol condensation, conducting experiments for two distinct saturation temperatures. Their results showed high heat transfer coefficients with Nusselt number ranging from 15 to 600. In addition, they obtained a Nusselt number correlation capable of predicting 95% of the data within 25% error band.

Baird et al. (2003) experimentally studied the local heat transfer coefficient of R123 and R11 condensation under various ranges of tube diameters, mass fluxes, heat fluxes and pressures. They identified a strong influence of mass flux and local quality and a weak influence of system pressure on the local heat transfer coefficient. In that way, the researchers developed a model based on their experimental data using a

simple shear-driven annular flow model to predict the heat transfer coefficient for condensation.

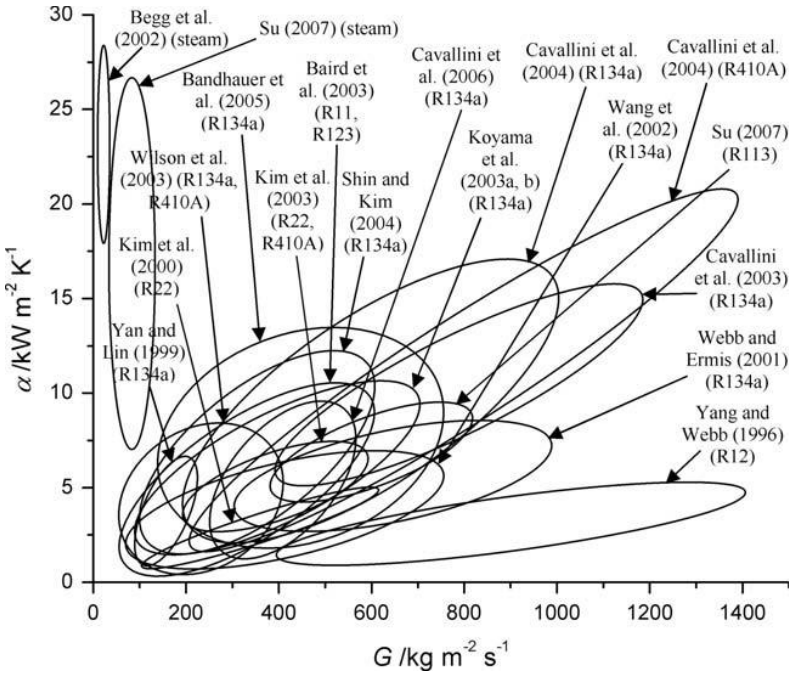


Figure 24: Summary of earlier heat-transfer measurements (Su et al., 2009)

Kim et al. (2003a, b) investigated condensation in flat aluminum multi-channel tubes using R410a and R22 as working fluids. The tubes had two internal geometries: one with a smooth inner surface ($D_h = 1.41$ mm), the other with a micro-finned inner surface ($D_h = 1.56$ mm). The authors found that for the smooth tube, R410a presented a slightly larger heat transfer coefficient than R22. Notwithstanding, for the micro-finned tube the opposite was true. Their data was compared to Webb's (1999), Koyama et al.'s (2003a, b), Akers et al.'s (1959) and Shah's (1979) correlations and Webb's predicted the data for the smooth tube reasonably well. Modifying Yang and Webb's (1997) correlation for the micro-finned tube, the authors were able to predict the data within 30%.

Garimella et al. (2002, 2005) experimentally investigated distinct shapes and sizes of microchannels and minichannels for heat transfer and pressure drop during condensation. They developed a pressure drop

model which was able to predict 90% of the experimental data within 28%. Regardless, this model requires flow visualization information, constituting a not so practical general model.

Another interesting study, conducted by Bandhauer et al. (2006), found that, in general, the experimental data presented an approximately linear trend between heat transfer coefficient and local quality over the range of qualities, 0.15 to 0.85, and mass fluxes, 150 kg/(m²s) to 750 kg/(m²s). Nonetheless, it was difficult to obtain a proper distinction between heat transfer coefficients at distinct mass fluxes, since the differences were within the measurement uncertainty. The authors developed a heat transfer calculation model using their pressure drop model to compute the interfacial shear stress and the friction velocity. This model can predict 86% of the data within 20% and also correctly showed the trends presented by the experimental data.

Son and Lee (2009) carried out experiments on condensation heat transfer in single channels; more details can be found in table 8. Annular flow was identified as the dominant flow regime for condensation in small diameter tubes. The authors also reported an earlier transition into the annular flow in minichannels. None of the correlations found in the literature was able to correctly predict their experimental results; therefore, they decided to elaborate their own model.

After many years of research on condensation in minichannels and microchannels there is not yet an agreement on the similarities with the condensation in macrochannels. Some authors, like Kim et al. (2003a, b) and Wang et al. (2002), suggested that the condensation phenomena occur differently in minichannels and macrochannels. Nevertheless, some authors perceived the opposite. For instance, Matkovich et al. (2009) presented a study of the local heat transfer coefficients for R134a and R32 condensation as shown in table 8. Their experimental data were compared to the following correlations: Moser et al.'s (1998) correlation as modified by Zhang and Web (2001), Koyama et al.'s (2003a, b) correlation and Cavallini et al.'s (2006a, 2006b) two correlations. The authors found that the models by Cavallini et al. (2006a, 2006b), which were developed based on a macro-scale tube database, fitted their experimental data better. They concluded that for circular tubes at high mass velocities, macro-scale condensation correlations apply.

To conclude, the summaries of the most important work carried out in small diameter channel condensation considering heat transfer and pressure drop are presented in table 9 and 10, respectively. Some papers will be presented in duplicate.

Analyzing the literature review, it is noticeable that most studies were developed using R134 as fluid refrigerant, the same which is used in the present work. However, there are not many studies on fluid behavior in the annular-mist and mist flow regime. Thus, this study intends to contribute with information on minichannel condensation when the annular-mist and mist flow regime are found.

Table 8: Summary of experimental studies of condensation in small channels (Cavallini et al., 2006a,b)

Author	Test section	Fluid	Dh [mm]	Aspect ratio	L [mm]	G [kg/(m ² s)]	Tsat [°C]	Measured parameter
<i>Yang and Webb (1996)</i>	H, MP, R, Smooth	R12	2.64	(0.7)a	560	400-1400	65	PD
	H, MP, R, Microfilm		1.56					
<i>Yan and Lin (1999)</i>	H, MP, C	R134a	2.0	-	200	100-200	25-50	PD, HTC
<i>Cavallini et al. (2001)</i>	H, SP, C	R22, R134a, R125, R32, R236a, R407C, R410A	8.0	-	1000	100-750	27-60	PD, HTC
<i>Zhang and Webb (2001)</i>	H,MP,C	R134a, R22, R404A	2.13	-	560	200-1000	20-65	PD
	H, SP, C		3.25, 6.25		914			
<i>Riehl and Ochterbeck (2002)</i>	H, MP, S	Methanol	1.50, 1.00, 0.75, 0.50	1	150	20-800	45, 55	HTC
<i>Baird et al. (2003)</i>	H, SP, C	HCFC-123 and R410A	0.92, 1.95	-	-	70-600	20-72	PD, HTC
<i>Kim et al. (2003a,b)</i>	H, MP, R, Smooth	R410A, R22	1.41	(0.8)a	455	200-600	45	HTC
	H, MP, R, Microfilm		1.56	(0.7)a				

Author	Test section	Fluid	Dh [mm]	Aspect ratio	L [mm]	G [kg/(m ² s)]	Tsat [°C]	Measured parameter
<i>Koyama et al. (2003a, b)</i>	H, MP, R	R134a	1.11	(0.7)a	600	100-700	60	PD, HTC
			0.8	(2.0)a				
<i>Garimella et al. (2005)</i>	H, SP, C	R22, R134a, R125, R32, R236a, R407C, R410A	4.91, 3.05	-	-	150-750	52.3	PD
	H, MP, C		1.52, 0.761, 0.506					
<i>Bandhauer et al. (2006)</i>	H, MP, C	R134a	1.524, 0.761, 0.506	-	305	150-750	-	HTC
<i>Matkovic et al. (2009)</i>	H, SP, C	R134a, R32	0.96	-	230	100-1200	40	HTC
<i>Son and Lee (2009)</i>	H, SP, C	R22, R134a, R407C	1.77	-	1220	200-400	40	HTC
			3.36		2660			
			5.35		3620			
<i>Cavallini et al. (2006a, b)</i>	H,MP,R	R134a, R245fa	0.7	7	190	50-500	30-70	PD, HTC
H: horizontal; SP: single port; MP: multiport; R: rectangular; C: circular; S: square; PD: pressure drop; HTC: heat transfer coefficient								
a: Estimated								

Table 9: Summary of relevant studies on heat transfer during condensation in small channels

Author/Reference	Hydraulic diameter (mm)	Fluid	Orientation/condition	Range/applicability	Techniques, basis, observations
<i>Yang and Webb (1996a)</i>	Rectangular plain $D_h=2.64$; microfin tubes $D_h=1.56$ mm	R-12	Horizontal	$T=65\text{ }^\circ\text{C}$ $400 < G < 1400\text{ kg}/(\text{m}^2\text{s})$	<ul style="list-style-type: none"> Shah (1979) significantly overpredicted data, Akers et al. (1959) better agreement, except at high G Enhancement due to microfins decreased with increasing G h showed heat flux dependence Surface tension drainage rationale for microfin enhancement Yang and Webb (1996b) concluded surface tension did not play role in ΔP in these same tubes
<i>Yang and Webb (1997)</i>	Extruded microchannels ($D_h=1.41$ and 1.56 mm) with microfins	R-12, R-134a			<ul style="list-style-type: none"> $G=400\text{ kg}/(\text{m}^2\text{s})$ and $x>0.5$, surface tension contribution equals and exceeds vapor shear term $G=1400\text{ kg}/(\text{m}^2\text{s})$, surface tension contribution very small h model based on shear and surface tension drainage (flooded and unflooded parts) Small fin tip radius enhanced h, larger inter-fin drainage area activated surface tension effect at lower x
<i>Kim et al. (2003b)</i>	$D_h=1.41$ smooth, $D_h=1.56$ microfin	R-22, R-410A	Horizontal	$T=45\text{ }^\circ\text{C}$ $200 < G < 600\text{ kg}/(\text{m}^2\text{s})$	<ul style="list-style-type: none"> In smooth tubes, R-410A h slightly higher than R-22, opposite true for microfin tubes Many qualitative explanations for varying enhancement trends Recommended Moser et al. (1998) model with modified two-phase multiplier for smooth tubes, and Yang and Webb's (1997) model with minor modifications for microfin tubes

Author/Reference	Hydraulic diameter (mm)	Fluid	Orientation/condition	Range/applicability	Techniques, basis, observations
<i>Yan and Lin (1999)</i>	2mm	R-134a	Horizontal	T=40-50 °C	<ul style="list-style-type: none"> • Condensation h higher at lower T_{sat}, especially at higher x • h decreased significantly as q'' increased, particularly at high x; some unusual trends in data • Re_q based h correlation
<i>Wang et al. (2002)</i>	Rectangular $D_h = 1.46$ (1.50 x 1.40 mm)	R-134a	Horizontal	T=61.5-66 °C, 75<G<750 kg/(m ² s)	<ul style="list-style-type: none"> • Large variations in x across test section • Stratification seen even at such small D_h • Akers et al. (1959) Re_q agreed with annular data, Jaster and Kosky (1976) agreed best with stratified flow data • Breber et al. (1980) and Soliman (1982,1986) transition criteria • Curve-fits for two-phase multiplier, dimensionless temperature • Stratified and annular flow correlations with interpolations
<i>Koyama et al. (2003b)</i>	Multi-port extruded al tubes	R-134a	Horizontal	T=60 °C, 100<G<700 kg/(m ² s)	<ul style="list-style-type: none"> • Local h measured every 75 mm of using heat flux sensors • Combination of convective and film condensation terms. Annular and stratified terms from Haraguchi et al. (1994a, b), two-phase multiplier replaced by Mishima and Hibiki (1996)

Author/Reference	Hydraulic diameter (mm)	Fluid	Orientation/condition	Range/applicability	Techniques, basis, observations
<i>Wang, Rose, and co-workers (Wang and Rose, 2004; Wang et al. (2004))</i>	Triangular (Wang and Rosa, 2004) $D_h = 0.577$ mm Square (Wang et al., 2004)	R-134a	Horizontal	T=50 °C 100<G<1300 kg/(m ² s)	<ul style="list-style-type: none"> Wang and Rose (2004) numerical analysis to predict varying condensate flow pattern across cross-section and length Wang et al. (2004) model for film condensation of R-134a in square, horizontal, 1-mm microchannels Surface tension, gravity, and shear terms can be turned on or off to demonstrate individual effects
<i>Cavallini et al. (2005)</i>	Multiple parallel 1.4-mm channels	R-134a, R-410A		T=40 °C 200<G<1000 kg/(m ² s)	<ul style="list-style-type: none"> h from T_{wall} measurements, available models (Akers et al., 1959; Moser et al., 1998; Koyama et al., 2003a) underestimate results Mist flow experiments might lead to high h
<i>Shin and Kim (2005)</i>	Circular and square channels ($0.5 < D_h < 1$ mm)	R-134a	Horizontal	T=40 °C, 100<G<600 kg/(m ² s)	<ul style="list-style-type: none"> Technique matched T_{out} of electrically heated air stream with similar air stream heated by condensing refrigerant R-134a Measured small, local condensation Q Most available models and correlations (Akers et al., 1959; Soliman et al., 1968; Traviss et al., 1973; Cavallini and Zecchin, 1974; Shah, 1979; Dobson, 1994; Moser et al., 1998) underpredicted data at low G At lower G, square channels had higher h than circular channels, reverse was true for high G

Author/Reference	Hydraulic diameter (mm)	Fluid	Orientation/condition	Range/applicability	Techniques, basis, observations
<i>Garimella and Bandhauer (2001); Bandhauer et al. (2006)</i>	$0.4 < D_h < 4.9$ mm	R-134a	Horizontal	$150 < G < 750$ kg/(m ² s)	<ul style="list-style-type: none"> • Thermal amplification technique for accurate h measurement • h model for circular tubes based on Traviss et al. (1973) boundary-layer analyses • Two-region dimensionless film temperature • Interfacial shear stress from models developed specifically for microchannels • Addresses annular, mist, and disperse wave regimes

Table 10: Summary of relevant studies on pressure drop during condensation in small channels

Author	Hydraulic diameter (mm)	Fluid	Orientation/Conditions	Range/Applicability	Techniques, Basis, Observations
<i>Koyama et al. (2003)</i>	1.114 mm (8 channels); 0.807 mm (19 channels)	R-134a	Horizontal	G = 100-700 kg/(m ² .s) x = 0-100%	The experimental data of frictional pressure drop agreed with the correlation of Mishima and Hibiki (1995), while the correlations of Chisholm and Laird (1958), Soliman et al. (1968), and Haraguchi et al. (1994), overpredicted.
<i>Garimella (2003)</i>	0.4-4.91 mm	R-134a	Horizontal	G = 150-750 kg/(m ² .s) x = 0-100%	His flow regime-based models yield substantially better pressure drop predictions than the traditionally used correlations that were primarily based on air-water flows for large diameter tubes.
<i>Garimella et al. (2005)</i>	0.5-4.91 mm	R-134a	Horizontal Considering the intermittent only, intermittent/discrete wavy annular transition, and annular only flow	G = 150-750 kg/(m ² .s) x = 0-100%	Presenting a multiple flow regime model for pressure drop during condensation.
<i>Hau and Koyama (2004)</i>	1.31 mm	CO ₂	Horizontal	P = 6.48-7.3 MPa T _{inlet} = 21.63- 31.33 °C q = 1.10-8.12 kW/m ² G = 123.2-315.2 kg/(m ² .s) x = 0-100%	The pressure drop was very small along the test section. The existing model failed to predict the experimental data.

Author	Hydraulic diameter (mm)	Fluid	Orientation/Conditions	Range/Applicability	Techniques, Basis, Observations
<i>Cavallini et al. (2005)</i>	0.4-3 mm	high pressure (R410A), medium (R134a) and low pressure (R236ea)	Horizontal		No model is able to predict the frictional pressure gradient of the high pressure fluid R410A, several models accurately predict the medium pressure fluid R134a and a few satisfactorily estimate the low pressure refrigerant R236ea.
<i>Chowdhury et al. (2006)</i>	0.7 mm	R-134a	Horizontal	$T_{\text{sat}} = 30 \text{ }^\circ\text{C}$; $x = 20\text{-}80\%$; $G = 130, 200 \text{ kg}/(\text{m}^2.\text{s})$	A unique process for fabrication of the microchannel involving milling and electroplating steps was adopted to maintain the channel geometry close to design values.
<i>Garimella (2006)</i>	1 mm	R-134a		$G = 300 \text{ kg}/(\text{m}^2.\text{s})$ $x = 50\%$ $P = 1500 \text{ kPa}$	Comparing different techniques for predicting the pressure drop during condensation.
<i>Agarwal and Garimella (2006)</i>	0.42- 0.8 mm	R-134a	Horizontal	$G = 150\text{-}750 \text{ kg}/(\text{m}^2.\text{s})$ $x = 0\text{-}100\%$	Their resulting model predicted 80% of the data within $\pm 25\%$. The tube shape effect on pressure drop was demonstrated.
<i>Cavallini et al. (2009a)</i>	0.96 mm	R-134a	Horizontal		Presenting a model for calculation of the frictional pressure gradient during condensation or adiabatic liquid-gas flow inside minichannels with different surface roughness.
<i>Cavallini et al. (2009b)</i>	0.96 mm	R134a and R32	Horizontal		Presenting modification of the friction factor in the proposed model previously developed by Cavallini et al. (2009a) to take into consideration also effects due to wall roughness.
<i>Park and Hrnjak (2009)</i>	0.89 mm	CO ₂	Horizontal	$T_{\text{sat}} = -15\text{-}25 \text{ }^\circ\text{C}$ $G = 200\text{-}800 \text{ kg}/(\text{m}^2.\text{s})$	Many correlations could predict their measured values of pressure drop relatively well such as the Mishima and Hibiki model.

Author	Hydraulic diameter (mm)	Fluid	Orientation/Conditions	Range/Applicability	Techniques, Basis, Observations
<i>Agarwal and Garimella (2007)</i>	100-200 μm	R134a	Horizontal	$G = 200\text{-}800 \text{ kg}/(\text{m}^2 \cdot \text{s})$; $x = 0\text{-}100\%$; $T_{\text{sat}} = 30, 40, 50, 60 \text{ }^\circ\text{C}$	The pressure drop increased with increasing vapor quality, increasing mass flux and decreasing saturation temperature.
<i>Song et al. (2010)</i>	1.5 mm x 1.0 mm	FC72 and steam	Horizontal	$q = 130\text{-}170 \text{ kW}/\text{m}^2$ for steam $q = 10\text{-}30 \text{ kW}/\text{m}^2$ for FC72	Presenting preliminary results from a new research program for making accurate heat transfer and pressure drop measurements during condensation in microchannels.
<i>Keinath and Garimella (2010)</i>	0.5-3 mm	R404a	Horizontal	$G = 200\text{-}800 \text{ kg}/(\text{m}^2 \cdot \text{s})$; $x = 5\text{-}95\%$; $T_{\text{sat}} = 30\text{-}60 \text{ }^\circ\text{C}$	Presenting a novel and accurate methodology for the quantitative investigation of two-phase flow regimes and flow parameters during condensation in minichannels.
<i>Fronk and Garimella (2010)</i>	100-200 μm	CO_2	Horizontal	$G = 600 \text{ kg}/(\text{m}^2 \cdot \text{s})$ $x = 0\text{-}100\%$ $T_{\text{sat}} = 15\text{-}20 \text{ }^\circ\text{C}$	Using the collected data to evaluate the applicability of correlations developed for larger hydraulic diameters and various fluids for predicting condensation heat transfer and pressure drop of CO_2 .
<i>Kuo and Pan (2010)</i>	135 μm	Steam	Horizontal	$2.10 \times 10^{-6}\text{-}9.11 \times 10^{-6} \text{ kg}/\text{s}$ of steam for the uniform crosssection microchannel $2.10 \times 10^{-6}\text{-}5.93 \times 10^{-6} \text{ kg}/\text{s}$ of steam for the converging microchannel	Their experimental data agreed well with the obtained correlations, with the maximum mean absolute errors of 6.4% for the two-phase frictional multiplier.
<i>Goss et al. (2011)</i>	0.8 mm	R134a	Horizontal	$G = 57\text{-}125 \text{ kg}/(\text{m}^2 \cdot \text{s})$ $P = 6.8\text{-}11.2 \text{ bar}$	The pressure drop correlation proposed by Zang and Webb (2001) gave the best results, with a deviation of 30%.

Author	Hydraulic diameter (mm)	Fluid	Orientation/Conditions	Range/Applicability	Techniques, Basis, Observations
<i>Keinath and Garimella (2011)</i>	0.5-3.0 mm	R404A			The Garimella et al. (2004) model tends to overpredict the pressure drop data. The poorest agreement is for the 3-mm tube data.
<i>Bohdal et al. (2011a)</i>	0.1-3.30 mm	R134-a	Horizontal	$G = 0-1200 \text{ kg}/(\text{m}^2 \cdot \text{s})$ $x = 0-100\%$ $T_{\text{sat}} = 30-40 \text{ }^\circ\text{C}$	The pressure drop in two-phase flow during R134a condensation is dependent on: the agent type, process parameters and the structure of two-phase flow.
<i>Bohdal et al. (2011b)</i>	0.31-3.30 mm	R134a and R404A	Horizontal	$G = 100-1300 \text{ kg}/(\text{m}^2 \cdot \text{s})$; $x = 0-100\%$; $T_{\text{sat}} = 20-40 \text{ }^\circ\text{C}$	The pressure drop during the condensation of the R134a and R404A refrigerants is described in a satisfactory manner with Friedel (1979) and Garimella (2004a) correlations.
<i>Bohdal et al. (2012)</i>	0.31-3.30 mm	R134a, R404a and R407C	Horizontal	$G = 0-1300 \text{ kg}/(\text{m}^2 \cdot \text{s})$ $x = 0-100\%$ $T_{\text{sat}} = 20-50 \text{ }^\circ\text{C}$	The pressure drop during the condensation of the R134a, R404a and R407C refrigerants is described in a satisfactory manner with Friedel (1979) and Garimella (2004a) correlations.
<i>Alshqirate et al. -2012</i>	0.6, 1.0, and 1.6 mm	CO ₂		$Re_{\text{ed}} = 2000-15000$	Using the dimensional analysis technique to develop correlations for Nusselt numbers and pressure drops.
<i>Kim and Mudawar (2012a)</i>	1 mm	FC-72 and water (counter flow)	Horizontal	For FC-72, $G = 248-367 \text{ kg}/(\text{m}^2 \cdot \text{s})$ $T_{\text{sat}} = 57.8-62.3 \text{ }^\circ\text{C}$ $x = 23-100\%$ For water, mass flow rate = 3-6 g/s	Their new model accurately captured the pressure drop and heat transfer coefficient data in both magnitude and trend, evidenced by mean absolute error values of 3.6% and 9.3%, respectively.

Author	Hydraulic diameter (mm)	Fluid	Orientation/Conditions	Range/Applicability	Techniques, Basis, Observations
<i>Kim et al. (2012b)</i>	1 mm	FC-72 and water (counter flow)	Horizontal	For FC-72, $G = 248-367$ kg/(m ² .s); $T_{sat} = 57.2-62.3$ °C; $q = 4.3-32.1$ kW/m ² For water, $G = 69-138$ kg/(m ² .s)	The homogenous flow model provides far more accurate predictions of pressure drop than the separated flow models. Among the separated flow models, Kim et al. (2012b) achieve better predictions with those for adiabatic and mini/micro-channels than those for flow boiling and macro-channels.
<i>Rose and Wang (2012)</i>		R134a	Laminar annular flow		The momentum pressure gradient is not small in comparison with the friction pressure gradient. The friction pressure gradient in the annular flow case is appreciably smaller than given by the earlier correlations.
<i>Fronk and Garimella (2012)</i>	1.435 mm	Ammonia (NH ₃)	Horizontal	$G = 75-150$ kg/(m ² .s) $T_{sat} = 30, 40, 50, 60$ °C (corresponding to $Pr = 0.10-0.23$)	The coupled influences of ammonia properties and microscale geometry were outside the applicable range of most condensation pressure drop and heat transfer models. Additional reliable data pressure drop and heat transfer for smaller tube diameters and with working fluids like ammonia were necessary.
<i>Charun (2012)</i>	1.4, 1.6, 1.94, 2.3 and 3.3 mm	R404A	Horizontal	$G = 97-902$ kg/(m ² .s) $x = 0-100\%$	The pressure drop during the R404A refrigerant condensation is satisfactorily described by the Friedel (1979) and Garimella (2004a) correlations.
<i>Kim and Mudawar (2012)</i>	0.0695- 6.22 mm	17 various working fluids (air/CO ₂ /N ₂ --water mixtures, N ₂ --ethanol mixture, R12, R22, R134a, R236ea, R245fa, R404A, R410A, R407C, propane, methane, ammonia, CO ₂ , and water)		$G = 4.0-8528$ kg/(m ² .s); $Re_{lo} = 3.9-89798$; $x = 0-100\%$; $Pr = 0.0052-0.91$	Proposing a new universal approach to predict two-phase frictional pressure drop for adiabatic and condensing in microchannel flows.

Author	Hydraulic diameter (mm)	Fluid	Orientation/Conditions	Range/Applicability	Techniques, Basis, Observations
<i>Zhang et al. (2012)</i>	1.088 and 1.289 mm	R22, R410A and R407C	Horizontal	$G = 300-600 \text{ kg}/(\text{m}^2 \cdot \text{s})$ $T_{\text{sat}} = 30, 40 \text{ }^\circ\text{C}$ $x = 10-90\%$	Two phase pressure drop and condensation heat transfer coefficients of R22 and R407C are equivalent but both higher than those of R410A. R410A as a substitute for R22, has more advantages than R407C in view of the characteristics of condensation pressure drop and heat transfer.
<i>Son and Oh (2012)</i>	1.77 mm	R22, R134a and R410A		$G = 450-1050 \text{ kg}/$ $(\text{m}^2 \cdot \text{s})$ $T_{\text{sat}} = 40 \text{ }^\circ\text{C}$	The condensation pressure drop of R134a is higher than that of R22 and R410A for the same mass flux. Presenting a new pressure drop model where the Chisholm factor (C) is a function of the two-phase Weber number (We_{tp}), and two-phase Reynolds number (Re_{tp}).
<i>Zhang et al. (2013)</i>	0.9 mm	CO ₂		$T_{\text{sat}} = -5-15 \text{ }^\circ\text{C}$ $G = 180, 360 \text{ and } 540$ $\text{kg}/(\text{m}^2 \cdot \text{s})$ $x = 20-80\%$	The measured pressure drop over the condenser increases with the mass flux and the vapor quality, but decreases with the saturation temperature.
<i>Garimella and Fronk (2012)</i>	$0.1 < D_h < 5 \text{ mm}$	synthetic and natural refrigerants and their azeotropic and zeotropic mixtures			These experiments resulted in flow-regime-based heat transfer and pressure drop models with very good predictive capabilities for such micro-channel geometries.
<i>Wang and Rose (2012)</i>		R134a, ammonia (NH ₃)	Laminar annular flow		Results for pressure gradient given by the annular laminar flow model are generally lower than those given by the correlations.

Author	Hydraulic diameter (mm)	Fluid	Orientation/Conditions	Range/Applicability	Techniques, Basis, Observations
<i>Liu et al. (2013)</i>	1.152 mm (circular); 0.952 mm (square)	R152a	Horizontal	$T_{sat} = 40-50\text{ }^{\circ}\text{C}$; $G = 200-800\text{ kg}/(\text{m}^2\cdot\text{s})$; $x = 10-90\%$	Channel geometry has little effect on frictional pressure gradients. Koyama et al. (2013) underestimates the square and circular microchannels data while Agarwal and Garimella (2006) overestimate the square microchannel data. Predictions of Cavallini et al. (2009) show large root-mean-square errors for data in both square and circular microchannels.
<i>Wang et al. (2013)</i>		R134a	Laminar annular flow		The frictional pressure gradients given by the laminar annular flow solutions are in fair agreement with the correlations at high quality and lower than the correlations at lower quality.
<i>Heo et al. (2013a)</i>	1.5 mm	CO ₂	Horizontal	$G = 400-1000\text{ kg}/(\text{m}^2\cdot\text{s})$ $T_{sat} = -5-5\text{ }^{\circ}\text{C}$	The Mishima and Hibiki model (1966) showed mean deviation of 29.1%.
<i>Ganapathy et al. (2013)</i>	100 μm	R134a	Constant heat flux	$G = 245-615\text{ kg}/(\text{m}^2\cdot\text{s})$ $q = 200-800\text{ kW}/\text{m}^2$	Using the volume of fluid approach. The mean absolute error (MAE) is 8.1% for two-phase frictional pressure drop against a recent universal predictive approach by Kim and Mudawar (2012).
<i>Heo et al. (2013b)</i>	1.5, 0.78, and 0.68 mm for the 7, 23, and 19 ports	CO ₂	Horizontal	$G = 400-800\text{ kg}/(\text{m}^2\cdot\text{s})$ $T_{sat} = -5-5\text{ }^{\circ}\text{C}$	The Mishima and Hibiki model (1996) has a mean deviation of $\pm 30.1\%$ for the frictional pressure drop.
<i>Murphy (2014)</i>	1.93 mm	Propane (R290)	Vertical	$T_{sat} = 47\text{ }^{\circ}\text{C}$ and $74\text{ }^{\circ}\text{C}$ $G = 75-150\text{ kg}/(\text{m}^2\cdot\text{s})$	The results and the corresponding correlations contribute to the understanding of condensation of hydrocarbon.
<i>Mikielewicz et al. (2014)</i>	2.23 mm	HFE7000 and HFE7100	Vertical		Satisfactory consistency of discussed model with their own experimental data for condensation has been found. The presented model can be suggested for a wider use amongst engineers, but further validation with experimental data would add value to its robustness.

Author	Hydraulic diameter (mm)	Fluid	Orientation/Conditions	Range/Applicability	Techniques, Basis, Observations
<i>Sakamata pan and Wongwises (2014)</i>	1.1 mm (14 channels), 1.2 mm (8 channels)	R134a	Horizontal	$G = 345-685 \text{ kg}/(\text{m}^2 \cdot \text{s})$ $q = 15-25 \text{ kW}/\text{m}^2$ $T_{\text{sat}} = 35-45 \text{ }^\circ\text{C}$	Proposing a new two-phase friction factor correlation using the equivalent Reynolds number (Re_{eq}) concept to predict the frictional pressure gradient during condensation.
<i>López-Belchí et al. -2014</i>	1.16 mm	R1234yf, R134a and R32	Horizontal	$G = 350-940 \text{ kg}/(\text{m}^2 \cdot \text{s})$ $T_{\text{sat}} = 20-55 \text{ }^\circ\text{C}$	Presenting a new correlation model with a mean absolute relative deviation (MARD) value of 8.32% reducing the best correlation MARD by more than 34%.
<i>Thome and Cioncolini (2014)</i>			Annular flow		Presenting unified modeling suite for annular flow, convective boiling and condensation in macro- and microchannels.
<i>Mikielewicz et al. (2014)</i>	2.23 mm	HFE7000	Vertical	$G = 240-850 \text{ kg}/(\text{m}^2 \cdot \text{s})$ $q = 47.2-368.7 \text{ kW}/\text{m}^2$ $T_{\text{sat}} = 35-93 \text{ }^\circ\text{C}$ $x = 0-100\%$	The comparisons of the experimental results with the in-house developed model for two-phase flow pressure drop with inclusion of non-adiabatic effects show satisfactory agreement.
<i>Kim and Mudawar (2014)</i>					Presenting a review of databases and predictive methods for pressure drop in adiabatic, condensing and boiling mini/micro-channel flows.
<i>Illán-Gómez et al. (2015)</i>	1.16 mm	R1234yf, and R134a	Horizontal	$G = 350-940 \text{ kg}/(\text{m}^2 \cdot \text{s})$; $T_{\text{sat}} = 20-55 \text{ }^\circ\text{C}$; $q = 4.37-20.52 \text{ kW}/\text{m}^2$ for R1234yf; $q = 5.08-20.75 \text{ kW}/\text{m}^2$ for R134a; $x = 12-87\%$ for R1234yf; $x = 13-89\%$ for R134a	Pressure drop for R1234yf is by 5-7% lower than for R134a. The existing models are able to predict frictional pressure drop reasonably well.

Author	Hydraulic diameter (mm)	Fluid	Orientation/Conditions	Range/Applicability	Techniques, Basis, Observations
<i>Ramírez-Rivera et al. (2015)</i>	0.715 and 1.16 mm	R134a and R32	Horizontal	For condensing flow: $G = 200\text{--}800 \text{ kg}/(\text{m}^2.\text{s})$; $T_{\text{sat}} = 30, 35, 40, 45, 50, 55 \text{ }^\circ\text{C}$; $q = 2.55\text{--}70 \text{ kW}/\text{m}^2$	Friedel (1979) and Müller-Steinhagen and Heck (1986) predict satisfactorily well the experimental pressure drop data. The Souza and Pimenta correlation (1995) estimates the experimental pressure gradient data very well with multiport tubes of $d_h = 1.16 \text{ mm}$, but fails to predict the experimental data in the tube of $d_h = 0.715 \text{ mm}$ with R134a and R32. The Cavallini et al. model (2005) presents the best prediction performance. Cavallini et al. (2005) and Zhang and Webb (2001) predicted with reasonable accuracy the experimental two-phase flow pressure drop data.
<i>Goss et al. (2015)</i>	0.77 mm	R134a	Horizontal	$G = 230\text{--}445 \text{ kg}/(\text{m}^2.\text{s})$ $x = 55\text{--}100\%$ $q = 17\text{--}53 \text{ kW}/\text{m}^2$ $P = 7.3 \text{ to } 9.7 \text{ bar}$	The pressure drop increases with an increase in G and a decrease in saturation temperature (T_s), whereas it is not influenced as much by the heat flux (q).

3 EXPERIMENTAL FACILITY

In this chapter, the experimental setup used for experimental evaluations in the present work is described. The construction characteristics and functions of each component are discussed, as well as the instruments used for measurement.

In terms of experimental study, the goal is to measure the heat flux, the fluid and wall temperatures and the absolute and differential pressure of the test section. These measurements are used to calculate the heat transfer coefficient and the pressure drop. For this, MPE tubes are used, which have channels where the coolant fluid, R14a, flows.

3.1 TEST RIG

The R134a convective condensation loop installed at LEPTEN, laboratory at Federal University of Santa Catarina, is shown in figure 25. The test rig used to carry out the present study was designed by Goss (2011a), and later modified by Zanette (2015). For this study, some changes were made to the tubes, fittings, measuring instruments, power supplies, boiler resistance feed, among other improvements that are discussed in appendixes B and C. The most significant difference is the test section: while Goss used eight, 0.8-mm diameter, parallel micro-channels assembled horizontally, the present study used a MPE tube of 7 minichannels, also assembled horizontally, with 1.46-mm hydraulic diameter. The test conditions have few differences, such as the present study achieved higher mass fluxes but lower vapor qualities.

The test rig components shown in figure 25 are listed below:

- 1- Boiler;
- 2- Superheater;
- 3- Coriolis flowmeter;
- 4- Test section;
- 5- Post condenser;
- 6- Filter;
- 7- Pump;
- 8- Thermal bath;
- A- Test section bypass isolation circuit;
- B- Pump bypass isolation circuit;
- T- Thermocouple;
- APT- Absolute pressure transducer;
- DPT- Differential pressure transducer.

Non-listed: Valves

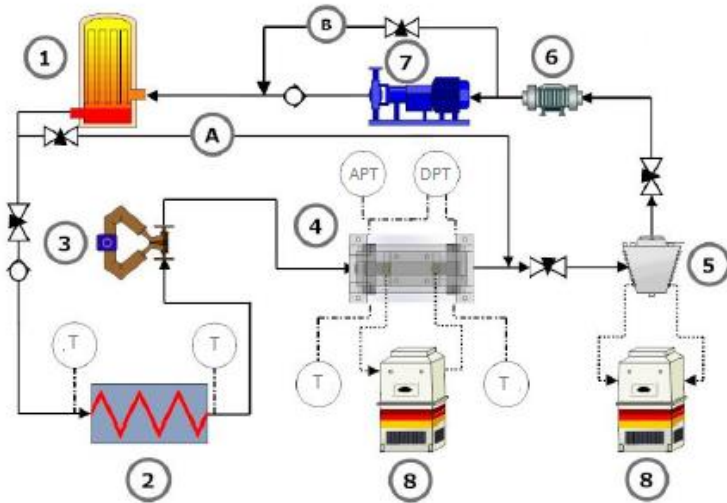


Figure 25: Schematic experimental setup (Modified from Zanette, 2015)

In order to perform the experimental tests in convective condensation, refrigerant fluid vapor is generated at the boiler (Section 3.1.1) and, after it reaches the superheater (Section 3.1.2), the fluid is directed to the test section (Section 3.1.3), where the condensation is promoted. After being partially condensed at the test section, the working fluid arrives at the post condenser (Section 3.1.4), where the remaining vapor is condensed through contact with the copper coil present inside the post condenser. Inside this copper coil, a solution of ethylene glycol and water flows, which temperature is controlled by the thermal bath. Then, the working fluid passes through the filter (Section 3.1.5), and reaches the pump (Section 3.1.6), which sends the fluid back to the boiler.

The test rig components are interconnected by 0.5- or 0.25-inch copper tubes that are connected to the equipment through flared joints, in order to avoid leakage. All measurements made on the experimental setup are sent to a data acquisition system (Agilent 34970A), which send the data to the computer. Next, the test rig components are detailed.

3.1.1 Boiler

The boiler receives subcooled liquid and raises its temperature to that of saturation or overheating, which is a condensation condition. After the refrigerant fluid reaches this point, it leaves the boiler and is directed to the superheater. A photograph of the boiler is shown in figure 26.

The boiler is used to heat the fluid refrigerant above the saturation temperature, producing R134a vapor. In the boiler, the temperature is measured by a 4-wire resistance thermometer detector, RTD (PT100), a device that contains an electrical resistance source, which changes resistance value depending on its temperature. This value change can be measured and used to determine the temperature. The values measured by the PT100 are sent to the data acquisition system and are used to monitor whether the fluid saturation temperature has been reached or not, and from that information, adjust the power supplied to the resistance. A cartridge-type electrical resistance of $48\ \Omega$ is set to deliver power of up to 1000 W to the working fluid, depending on the mass flow required for the test, forcing it in a strict unidirectional flow through a valve to the superheater, preventing the vapor to return.



Figure 26: Picture of the boiler

The resistance power supply is made by a variable transformer (specifications: 10 kVA, 40 A and 220 V). If the working fluid within the boiler has not yet reached the saturation temperature, the power supplied to the resistance is increased until that temperature is reached, and even exceeded. When that happens, the variable transformer continues to provide the same power to the resistance, and the fluid temperature at the boiler is kept constant.

The boiler is made of stainless steel cylinder, measuring 260-mm of height, 115-mm of external diameter, and 10-mm of thickness. During the tests, the boiler is thermally insulated using a 10-mm thick polyethylene insulation, which covers its external surface (not shown in figure 26). The water level inside the boiler can be monitored through a transparent hose, which is externally installed. The boiler is also equipped with a relief valve, which allows the vapor outlet if the pressure inside reaches very high values. The fluid inlet at the boiler takes place in its lower part, since it arrives in liquid state. The fluid outlet is located at the top part of the boiler, ensuring the steam output.

The boiler bypass is used during single-phase tests, preventing the fluid from flowing through the boiler.

3.1.2 Superheater

After leaving the boiler, the saturated or overheated fluid reaches the superheater, which is shown in figure 27 (not thermally insulated). It consists of a ½-inch inner diameter copper tube, and 320-mm length, having an electric nickel-chromium resistance wire of 3.5 Ω wound around the tube outer surface. A DC-power supply (Agilent Technologies N873377) is connected to the resistance wire.



Figure 27: Picture of the superheater

The superheater is used when superheated vapor is desired as initial condition or when a fine adjustment of the tests conditions is needed. It is important to consider the thermal loss in the tubes as the fluid passes through them, thus the superheater ensures that the fluid reaches the test section inlet at or above the saturation temperature, depending on the test desired conditions.

Two type-T thermocouples allow temperature measurements on the flow axis, one at the inlet and one at the outlet of the superheater, identifying the overheating degree. After the fluid passes through the superheater, it is sent to the Coriolis flowmeter, and then to the test section.

3.1.3 Test section

The test section is composed of the MPE aluminum profile containing seven minichannels, which extremities are welded to manifolds. As presented in section 3.2, 16 thermocouples and 8 heat flux sensors are attached to the test section in order to measure temperature and heat flow, respectively. A front view of the test section is shown in figure 28. The heat flux sensors are represented by the letter Q and the thermocouples by the letter T . Two heat sinks are used to remove heat from the test section, as described in section 3.1.7. The assembly formed by the MPE profile, two manifolds, 16 E-type thermocouples, 8 heat flux sensors, and two heat sinks is mounted on an acrylic structure. This acrylic structure was specially developed for this test section, and it serves as an assembly support, besides allowing different angular orientations in relation to gravity.

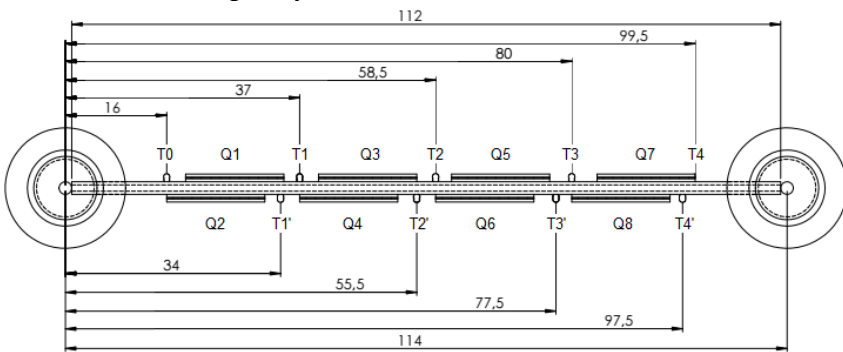


Figure 28: Test section front view

3.1.3.1 MPE aluminum profile

Nowadays, heat exchangers must meet a diversity of highly demanding requirements. They have to ensure maximum heat transfer while keeping minimum size. In addition, the durability of heat exchangers needs to be extremely high, providing trouble-free performance throughout its service life at low manufacturing costs. As such, aluminum offers clear possibilities to achieve these goals and has great chances to meet the challenges of the increasing market demands for cost effective, energy-efficient products and new customized, innovative applications.

The business attraction for aluminum heat exchangers is based on two components, the cost saving realized by substituting raw material, as cooper, with a less expensive raw material as aluminum, and the cost savings of implementing higher performance products and more efficient fabrication processes. Furthermore, aluminum has a significant potential for lightweight design, high thermal conductivity, excellent corrosion resistance, good formability, adequate strength to resist temperature and pressure cycles, easy recyclability and commercial availability, with a wide range of aluminum alloys.

Considering heat exchanger applications, there are three types of tubes that can be used: welded, folded, and extruded tubes, which can be round tubes (RT) or multiport extrusions (MPE). MPE is a flat plate where several tubes are extruded, forming multiple small channels along the length of the tube. The flat geometry of MPE tubes results in reduced aerodynamic drag and an advantageous development of the heat transfer boundary layer leading to larger heat transfer coefficients on the air-side. The enhanced heat transfer of MPE tubes results from the increased ratio of the heat transfer area to the internal volume, and a favorable impact on the coolant flow regime and the dominant heat transfer mechanism.

The two assembly techniques used for manufacturing tube / fin aluminum heat exchangers are mechanical assembly and brazing. Each technique requires distinct processes, equipment, and alloys. The preferred design and manufacturing approach for aluminum evaporators and condensers is to combine the use of multi-port extrusions with the brazing process. The considerably improved performance of these heat exchangers offers the potential for a substantial reduction in system cost through reduction of weight and size, reduced fan power requirements, and increased durability.

MPE tubes are manufactured to meet specific requirements in regard to alloy, outside dimensions, wall and web thickness, hydraulic diameter, and other attributes. With their large internal surface area, the MPE profiles (or microchannel tubes) achieve a more efficient heat transfer and are therefore ideal for use in highly effective heat exchangers. The tube material must have adequate strength (high pressure resistance) and fatigue resistance together with good air-side and water-side corrosion resistance. As more and more complex tube designs are used, the formability of the tube alloys becomes of greater importance.

Referring particularly to automotive air conditioning, the aluminum MPE tubes play a very important role. If the car has air conditioning, there is an additional heat exchanger called the air conditioner condenser, which also needs to be cooled by the air flow entering the engine compartment. In the condenser, the refrigerant (R134a) is circulating with a high-pressure range (maximum about 20 bar). The normal operating temperature ranges from room temperature up to 35 to 40 °C. The most used type of design is the parallel flow. In the parallel flow design, a pair of parallel vertical header tanks distributes the refrigerant to horizontally aligned tubes which in turn are connected to fins. Extruded multi-port tubes are mostly used for the refrigerant tubes. Aluminum multi-port extrusions offer favorable heat transfer area to volume ratio, which makes these extrusions ideal for heat exchangers with high performance requirements.

The MPE aluminum profile used in this study is made of commercial aluminum alloy 3003, containing seven minichannels, obtained by extrusion process. The aluminum alloy 3003 has moderate strength and good corrosion resistance. The strength of this alloy can be increased by cold working (Ferrasse et al., 1997).

A dimensional analysis of the MPE profile was conducted by CERTI Foundation using as measuring standard an Industrial Computed Tomography System (CTS). Two samples of the MPE aluminum profile were sent to the Laboratory, as shown in figure 29. The computed tomography was made using a ZEISS machine and the VG Studio 3.0 software. The resulting volumetric matrix is shown in figure 30.

The minichannels are not all of the same dimensions because it is made of a very ductile material. This characteristic is shown in figures 31 and 32, which consists in the measurement results of each channel cross-sectional area and wetted perimeter of the cross-section for the two samples made by CERTI Foundation.

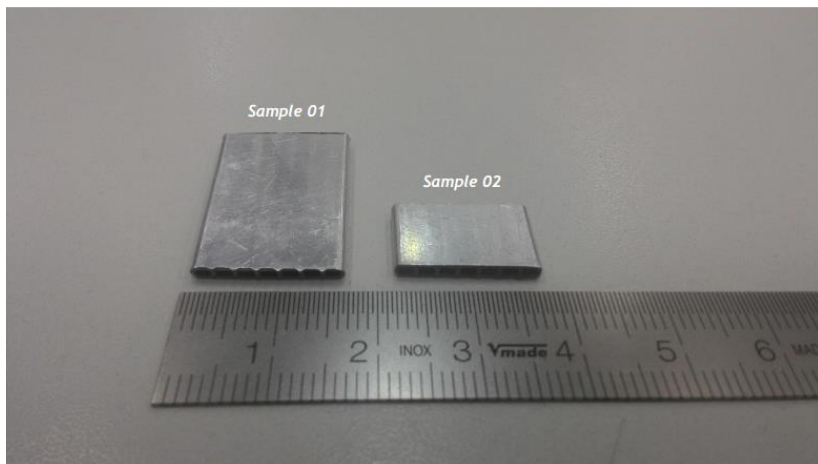


Figure 29: Illustrative picture of the MPE aluminum profile samples

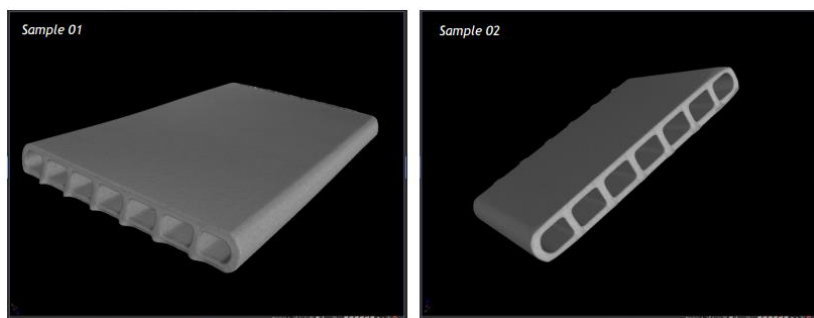


Figure 30: MPE profile resulting volumetric matrix



Figure 31: Measurement result for sample 1

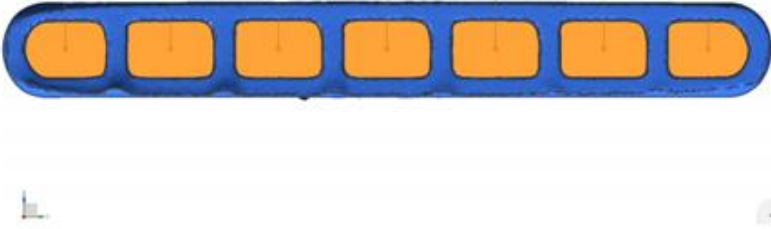


Figure 32: Measurement result for sample 2

As presented in table 11, the mean hydraulic diameter of the minichannel is calculated applying the results from the tomography into equation 3.1:

$$D_h = \frac{4A}{P} \quad (3.1)$$

where A is the cross-sectional area and P is the wetted perimeter of the cross-section of the channel.

The resulting mean hydraulic diameter of the minichannels is $D_h = 1.46$. According to channel size classification of Kandlikar and Grande (2003) shown in table 2, the channels are classified as minichannels.

Table 11: Measurements results of area and perimeter of the two samples

Sample 1			Sample 2		
Area (mm ²)	Perimeter (mm)	Hydraulic diameter (mm)	Area (mm ²)	Perimeter (mm)	Hydraulic diameter (mm)
1,7103	4,9061	1,394427	1,7734	4,9425	1,435225
1,9711	5,396	1,461156	2,0182	5,4591	1,478779
1,9938	5,4242	1,4703	2,0462	5,4877	1,491481
2,0154	5,448	1,479736	2,0491	5,4867	1,493867
2,0252	5,4654	1,482197	2,0393	5,483	1,487726
2,0051	5,4405	1,474203	2,025	5,4644	1,482322
1,7651	4,9213	1,434662	1,7545	4,9599	1,414948

3.1.3.2 Manifold

The importance of the two-phase flow distribution was discussed in section 2.4. The MPE aluminum profile was welded to manifolds in its inlet and outlet to achieve a uniform distribution in the mini-

channels. The manifolds were manufactured from a solid commercial aluminum 6351-T6 that was machined to its final shape as shown in figure 33. In order to avoid leakage problems, chamfers and recesses were machined in the manifold.

At the inlet manifold, the MPE aluminum profile is positioned perpendicularly to the plane of fluid inlet in the minichannels. In the other hand, at the output manifold, the MPE is positioned in parallel to the plane of fluid outlet. According to Dario (2013), the header position and flow orientation in parallel channels are two of the main factors influencing the two-phase flow distributions for these devices. The fluid distribution at the inlet manifold is expected to be more uniform than at the outlet manifold.

In order to couple the pressure transducers and thermocouples inside both manifolds, and to connect the manifolds to the pipe system of the test rig, connections were projected. The outlet manifold connections are shown in figure 34. A brazing process using aluminum rod MIGRARE model ISI-1 joins the connection and the manifold.

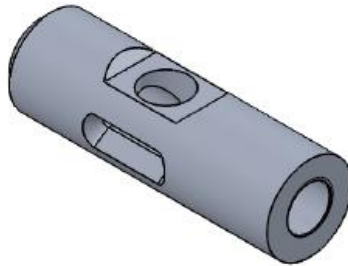


Figure 33: Inlet manifold isometric view



Figure 34: Outlet manifold connections

3.1.4 Post condenser

The post condenser, shown in figure 35, is made of stainless steel and has the same dimensions as the boiler (260-mm high, 115-mm outer diameter, and 10-mm thickness). The post condenser promotes the total condensation of the working fluid, which comes from the test section and goes to the pump. It also is used to load the experimental setup with the working fluid from the valve above the post condenser. To unload the working fluid, the valve below the post condenser is used. Like the boiler, the post condenser has a liquid display mainly used to control the fluid level during the process of loading and unloading the R134a from the test rig. The equipment has a copper coil inside it, where water from the thermal bath (LAUDA model RK8 KP) flows.



Figure 35: Picture of the post condenser

3.1.5 Filter

A hermetic filter drier Danfoss Eliminator® type DML is located after the post condenser and prevents particulates from reaching the pump. Also due to its drying action, moisture is eliminated from the working fluid. This filter, which is shown in figure 36, has a solid core of 100% Molecular Sieve, optimized for use with HFC refrigerants. The filter drier is approved for up to 46 bar, from -40 °C to 70°C.

3.1.6 Pump

After leaving the filter, the working fluid, in the liquid state, reaches the pump. The pump used was manufactured by Tuthill (D Serie), which provides a non-pulsing flow; it is accurate and leak free. It is projected to work at temperatures from -46 °C to 176°C and at pressures up to 34.5 bar. It is coupled to the electrical motor connected to a frequency inverter Dart (Serie 15). The frequency inverter is responsible for controlling the pump's rotation by acting in the electric motor. The pump coupled to the electrical motor is shown in figure 37.



Figure 36: Picture of the filter

The working fluid in the form of an undercooled liquid is directed by the pump to the boiler.



Figure 37: Picture of the pump coupled to the electrical motor

3.1.7 Heat sink

Two heat sinks are installed in contact with the MPE profile at the test section, one sink on the top, and another on the bottom. A heat sink is a passive heat exchanger, which transfers thermal energy from a higher temperature device to a lower temperature fluid medium. In the present study, the higher temperature is found at the minichannel and the lower temperature fluid consists of a solution of ethylene glycol, which temperature is controlled by the thermal bath (manufactured by MI-CROQUIMICA, model MQBMP-01). In this way, the heat sink promotes the R134a condensation, removing the heat from the test section.

The heat sink is made of copper, a material that has a high thermal conductivity. A copper pipe available at the laboratory was flattened using wooden plates that were pressed together using a vise. Afterwards, holes were drilled to serve as inlet and outlet. In these holes new pipes were welded, which can be connected to polymer tubing featuring the final cooling refrigerant. The ends of the flattened opened pipe were closed by soldering. The copper pipe has an original diameter of 15-mm and a wall thickness of 1-mm. An overview of the design is shown in figure 38.

Flattening a pipe instead of drilling a solid piece is assumed to improve cooling performance since the cavity for the transport of cooling refrigerant is centered appropriately.

A heat sink is positioned above and the other below the minichannels. Between the minichannels and each heat sink, the E-type thermocouples and heat flux sensors are positioned. Above each heat sink a polyethylene insulation is placed and then an acrylic plate. Each

plate has 4 holes and thus 4 screws are pierced ensuring that the whole setup is fully in contact.



Figure 38: Overview of the heat sink

3.2 MEASURING INSTRUMENTS

In this section, the measuring instruments are described. These instruments are used for pressure, temperature, mass flow, and heat flow measurements.

3.2.1 Coriolis flowmeter

The R134a mass flow is measured using a Coriolis mass flowmeter, sensor type MASS2100 DI 1.5 coupled with a converter type MASS6000, both produced by SIEMENS. A photograph of the MASS2100 DI 1.5 flow sensor is shown in figure 39.

The Coriolis flowmeters are designed for measurement of a variety of liquids and gases. The meters are multi-parameter devices offering accurate measurement of mass flow, volume flow, density, fraction and temperature. The manufacturer provided a calibration report, shown in table 12, when the sensor operated with R134a at an overheated condition, at pressure of 10 bar and temperature of 65 °C. The mass flowmeter is assembled upstream the test section in order to ensure that the measurement is performed when only steam passes through it.

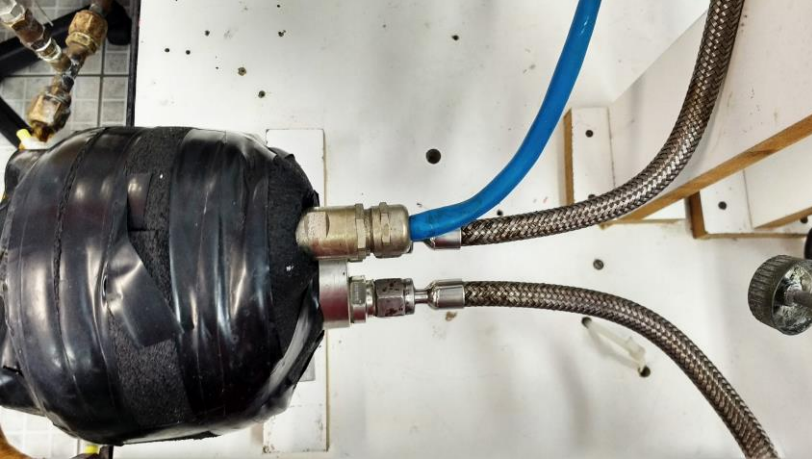


Figure 39: Picture of the Coriolis flowmeter

Table 12: Coriolis mass flowmeter calibration (R134a, 10 bar, 65 °C) (From: Siemens)

Mass flow rate (<i>kg/h</i>)	Pressure drop (<i>bar</i>)	Mass velocity (<i>m/s</i>)	Error (% mass flow)
0.10	0.00052	0.20	± 1.00
0.82	0.020	1.67	± 0.16
1.54	0.064	3.14	± 0.12
2.25	0.13	4.60	± 0.11
2.97	0.23	6.07	± 0.11
3.69	0.35	7.53	± 0.10
4.41	0.50	9.00	± 0.10
5.13	0.67	10.47	± 0.10
5.85	0.87	11.93	± 0.10
6.56	1.10	13.40	± 0.10
7.28	1.30	14.87	± 0.10
8.00	1.60	16.33	± 0.10

3.2.2 Pressure transducers

A differential pressure transducer is installed at the test section between two manifolds. The one used is manufactured by ESI Technology, Protran®PR3200 model, which has the pressure range 0-4 bar, and 4-20 mA two-wire output. Its uncertainty is 1200 Pa.

The absolute pressure is measured at the test section inlet by an absolute pressure transducer WTP-4010 manufactured by Wärme. The

pressure range is 0-10 bar, and 4-20 mA two wire output. According to the calibration report, the expanded uncertainty is 0.02 kgf/cm², the fiducial error is 0.50%, and the repeatability of 0.10%.

The connection between the pressure transducers and the manifolds are made using 2-mm inner diameter cooper tubes.

3.2.3 Thermocouples

20 thermocouples were installed at the test rig: 16 E-type (Chromel/Constantan) and 4 T-type (Copper/Constantan) thermocouples. The E-type thermocouples are attached to the test section. The temperature measurement in the test section is necessary to obtain the temperature profile and consequently the local heat transfer coefficients. The installed thermocouples are made by Omega and have 0.125-mm diameter. The E-type thermocouples are attached to the test section using a cyanide glue (Superbonder) mixed with copper powder in order to decrease the contact resistance between the thermocouple measurement junction and the MPE profile.

The T-type thermocouples are fixed along the test rig:

- 1 before the superheater;
- 1 after the superheater;
- 1 at the inlet manifold of the test section;
- 1 at the outlet manifold of the test section.

The thermocouples located at the test section inlet and outlet are important to determine the fluid state before and after submitted to the condensation within the minichannels. The thermocouples calibration is explained in Appendix A.

3.2.4 Heat flux sensors

One of the goals of this research is to study the heat transfer coefficient of the flow. The heat transfer coefficient is closely related to the heat flux. According to Fourier's law in one dimension, this relation is defined by:

$$q_x = -k \frac{dT(x)}{dx} \quad (3.2)$$

The heat flux sensors measure the heat flux removed by the heat sinks in contact with the MPE profile. The heat flux sensors are produced at the Laboratório de Meios Porosos e Propriedades Físicas de Materiais (LMPT) at UFSC. The heat flux sensors, produced specially

for this setup, have a square sensitive area of $15 \times 15 \text{ mm}^2$. The heat flux sensors calibration is presented in Appendix A.

Each heat flux sensor is mounted in contact with the external surface of the MPE profile and a copper plate is set over the heat flux sensor. In order to reduce the contact resistances in the heat flux sensor/MPE and heat flux sensor/copper plate, a thermal paste is used. An ultra-high thermal conductivity (11 W/m.K) thermal paste manufactured by Cooler Master is employed.

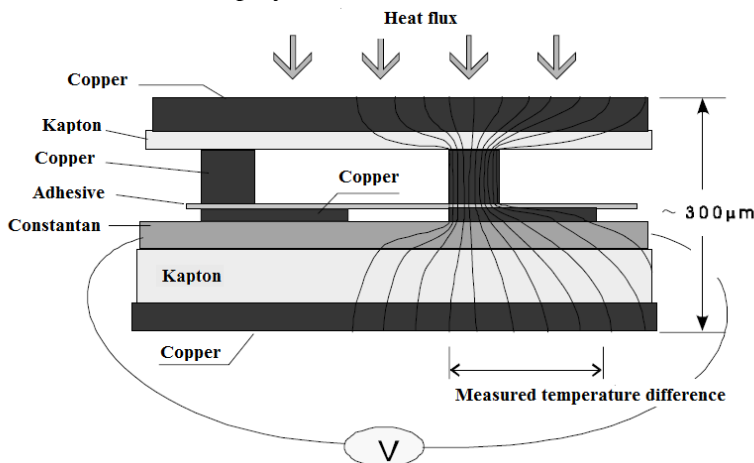


Figure 40: Principle of operation of tangential gradient heat flux transducer (Modified by Carciofi et al., 2002)

3.3 WORKING FLUID: R134A

The working fluid used in the experimental setup is the refrigerant R134a (1,1,1,2-TetraFluoroEthane), which molecular formula is $\text{CF}_3\text{CH}_2\text{F}$. R134a is from the family of HFC refrigerant and with the discovery of the damaging effect of CFCs and HCFCs refrigerants to the ozone layer, the HFC family has been widely used in their replacement. In that regard, R134a is now being used as a replacement for R12 CFC refrigerant. Currently it is being widely used in the air conditioning system of automotive vehicles and by the manufacturing industry in plastic foam blowing. In addition, the pharmaceutical industry use it as a propellant. Some properties of R134a are shown in table 13 at pressure of 8.4 bar, obtained using the EES software.

The refrigerant R134a used was produced by Chemours™ and meets AHRI 700 and SAE J2776 purity standards.

Table 13: R134a properties at 8.4 bar (From: EES software)

Property	Value	Unit
Specific heat, c_p	1.457	$kJ.kg^{-1}.K^{-1}$
Specific heat, c_v	0.923	$kJ.kg^{-1}.K^{-1}$
Thermal conductivity of liquid, k_l	0.0793	$W.m^{-1}.K^{-1}$
Density of liquid, ρ_l	1176	$kg.m^{-3}$
Density of vapor, ρ_v	41	$kg.m^{-3}$
Molar mass, M	102	$g.mol^{-1}$
Prandtl Number liquid. Pr_l	3.23	-
Critical temperature, T_{crit}	101	$^{\circ}C$
Saturation temperature, T_{sat}	33.0	$^{\circ}C$
Surface tension, σ	0.00702	$N.m^{-1}$
Dynamic viscosity of liquid, μ_l	1.76×10^{-4}	$Pa.s$
Dynamic viscosity of vapor, μ_v	1.23×10^{-5}	$Pa.s$
Critical pressure, p_{crit}	40.6	bar
Latent heat of vaporization, i_{lv}	170.20	$kJ.kg^{-1}$

4 EXPERIMENTAL METODOLOGY

In this chapter, the methodology applied for the tests, as well as data reduction procedures, are described. The tests performed are characterized by the difficulty in controlling pressure and mass flux variables. A program developed using MATLAB software, divides the test section into segments and allows the calculation of flow properties at each one of these segments.

4.1 OPERATING PROCEDURES

4.1.1 Working fluid loading procedure

The tests are performed in the test rig described in chapter 3. For this, the test rig is loaded with working fluid (R134a). This procedure is accomplished through the charging valve, which is located at the top of the post condenser.

First, using a high vacuum pump manufactured by Edwards, model E2M-18, vacuum is made during 12 hours throughout the test rig. This eliminates non-condensable gases, which could influence the condensation. High vacuum also facilitates the fluid loading. Then, all test rig valves are closed and the post condenser bath is stabilized at 0°C. The cylinder of R134a is positioned upside down above the post condenser to ensure liquid inflow only. A pressure gauge is placed between the cylinder and the loading valve. The cylinder, pressure gauge, and loading valves are opened, and the working fluid enters the post condenser at a pressure of 5 bar. The post condenser is filled until the liquid display is totally full. After that, all previously opened valves are closed and the temperature of the thermal bath is increased to 20 °C, since, at a pressure of 5 bar, the R134a saturation temperature is 15.71 °C. The temperature rise causes the increase of internal pressure in the post condenser.

After the thermal bath is stabilized at 20 °C, the valves between post condenser and boiler are opened, and the boiler fills until it reaches an equilibrium level with the post condenser. Then, the pump is turned on and all remaining fluid in the post condenser is sent to the boiler. When the post condenser is empty, the pump is turned off, valves are closed, and the thermal bath is adjusted to 0 °C. After it stabilizes, the loading procedure is repeated until both post condenser and boiler are completely full.

4.1.2 Test procedure

After the rig is loaded with working fluid, the tests can be started. Tests are performed in the following order: the first tests are carried out for the highest pressure, since it is the most difficult variable to set during the experiment. Then, the mass flux is set, starting with the highest. The change in mass flux may influence the pressure, so it is sometimes necessary to readjust the pressure. Finally, the heat flux is regulated, starting with the highest. The heat flux has less effect on the other variables and is strongly dependent on the temperature of the test section thermal bath. Nonetheless, since the thermal bath requires a long time to reach the set temperature, the heat flux is the most time-consuming variable to fix, which causes a long waiting time between tests. The variables are adjusted in descending order, as shown in table 14, in order to avoid hysteresis error.

The test routine begins by turning on the thermal baths and adjusting the desired temperatures. It is a time-consuming process, especially at lower temperatures. Then, the entire data acquisition system and power supplies are switched on, in order to stabilize the temperature of its internal components. This process helps minimizing possible thermocouple temperature reading errors. Next, the thermal bottle where the reference thermocouples are positioned is filled with ice and cold water. The variable transformer and the superheater power supply are turned on after the previous steps have already stabilized. After all variables become stable and in accordance to the desired conditions, the tests are started. The method used to achieve this is discussed next. EES software is used to obtain thermodynamic properties of the working fluid (R134a), which pressure conditions and saturation temperature are fundamental to the adjustment of the test conditions.

During the tests, the boiler, pump, and test section bypass valves are closed.

Table 14: Tests order of execution

Test number	Inlet pressure [bar]	Mass flux [kg/(m ² s)]	Heat flux [kW/m ²]
1	9	500	9.5
2	9	500	9
3	9	500	8.5
4	9	450	9.5
5	9	450	9
6	9	450	8.5
7	9	400	9.5
8	9	400	9
9	9	400	8.5
10	8	500	9.5
11	8	500	9
12	8	500	8.5
13	8	450	9.5
14	8	450	9
15	8	450	8.5
16	8	400	9.5
17	8	400	9
18	8	400	8.5

Test number	Inlet pressure [bar]	Mass flux [kg/(m ² s)]	Heat flux [kW/m ²]
19	7.5	500	9.5
20	7.5	500	9
21	7.5	500	8.5
22	7.5	450	9.5
23	7.5	450	9
24	7.5	450	8.5
25	7.5	400	9.5
26	7.5	400	9
27	7.5	400	8.5
28	7	500	9.5
29	7	500	9
30	7	500	8.5
31	7	450	9.5
32	7	450	9
33	7	450	8.5
34	7	400	9.5
35	7	400	9
36	7	400	8.5

The tests pre-established conditions are the inlet pressure at test section, P_i , mass flux, G , and heat flux, q'' . These variables depend on three factors: the thermal bath temperatures of the test section and the post condenser, $T_{b,TS}$ and $T_{b,PC}$, respectively, and the dissipated power in the boiler's electrical resistance, Q_{boiler} . The variation of any of these three factors directly affects P_i , G , and q'' variables. The method used to achieve a given condition of inlet pressure, mass flux and heat flux is shown in the block diagram of figure 41.

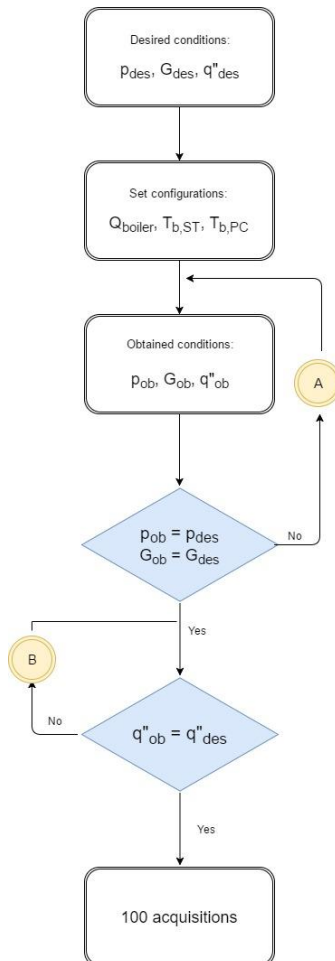


Figure 41: Block diagram of the test procedure

If the obtained pressure and/or mass flux are not equal to the desired condition, the “A” intervention showed in figure 41 is performed. The block diagram of this intervention is depicted in figure 42.

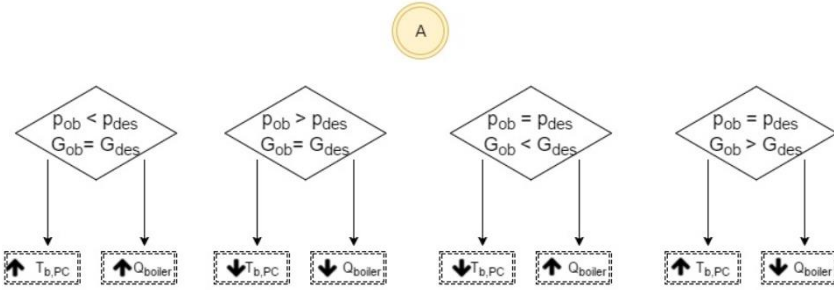


Figure 42: The "A" intervention shown in figure 41

If the obtained mass flux is equal to the desired one ($G_{ob}=G_{des}$), but the obtained inlet pressure at the test section is smaller than the desired one ($p_{ob}<p_{des}$), it is necessary to increase the temperature of the post condenser thermal bath ($T_{b,PC}$). The increase in $T_{b,PC}$ causes the pressure to increase and the mass flux to decrease. Therefore, in order to counterbalance the mass flux decrease, the dissipated power in the boiler’s electrical resistance, Q_{boiler} , is increased. The inverse is applied when the second situation shown in figure 42 happens.

If the inlet pressure is equal to the desired one ($p_{ob}=p_{des}$), but the obtained mass flux is smaller than the desired one ($G_{ob}<G_{des}$), it is necessary to increase Q_{boiler} . The increase in Q_{boiler} causes the pressure to increase. Therefore it is necessary to decrease the $T_{b,PC}$ to offset the increasing pressure. When the last scenario, $p_{ob}=p_{des}$ and $G_{ob}>G_{des}$, happens, the inverse procedure is applied.

When the conditions for pressure and mass flux meet the desired, the heat flux is adjusted. During this step, only the temperature of the test section thermal bath, $T_{b,TS}$, is altered. To increase the heat flux, q'' , it is indispensable to lower the bath temperature. To decrease q'' , the bath temperature is increased. This procedure is shown in figure 43.

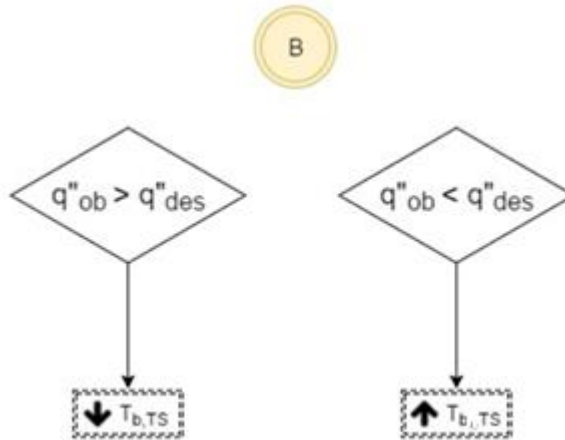


Figure 43: The "B" intervention shown in figure 41

Concisely, the voltage supplied to the boiler resistance ranged from 75 V to 100V, the temperature of the test section thermal bath ranged from $-6\text{ }^{\circ}\text{C}$ to $8.65\text{ }^{\circ}\text{C}$, and the temperature of the post condenser thermal bath ranged from $10\text{ }^{\circ}\text{C}$ to $33\text{ }^{\circ}\text{C}$. When the system reaches a steady state, a comparison between the desired and obtained conditions is made. If the desired conditions are not fulfilled, it is essential to interfere with $T_{b,PC}$ and Q_{boiler} . This intervention is shown in figure 42. In this step, no attention is paid to the heat flux, q'' . After the mass flow and the inlet pressure at the test section reach the desired values, q'' is adjusted. If the obtained and desired values for q'' are different, $T_{b,TS}$ is modified, as shown in figure 43.

When the three pre-established conditions are satisfied, 100 acquisitions are made using the data acquisition system Agilent. The adjustment procedures described above are iteratively done to obtain a present condition in the test section. The data processing is described in section 4.2.

The acquired signals of mass flux, G , total heat flow, q''_{tot} , inlet temperature at the test section, T_i , wall temperature, T_w , absolute pressure at the test section inlet, P_{abs} , and differential pressure at the test section, ΔP , are shown in figure 44. The acquired signals are presented in their measured units, without any treatment. Each presented signal is from a different test. For data reduction, mean values of the measured

variables are used. These graphs are presented to demonstrate the stable behavior of the experimental system.

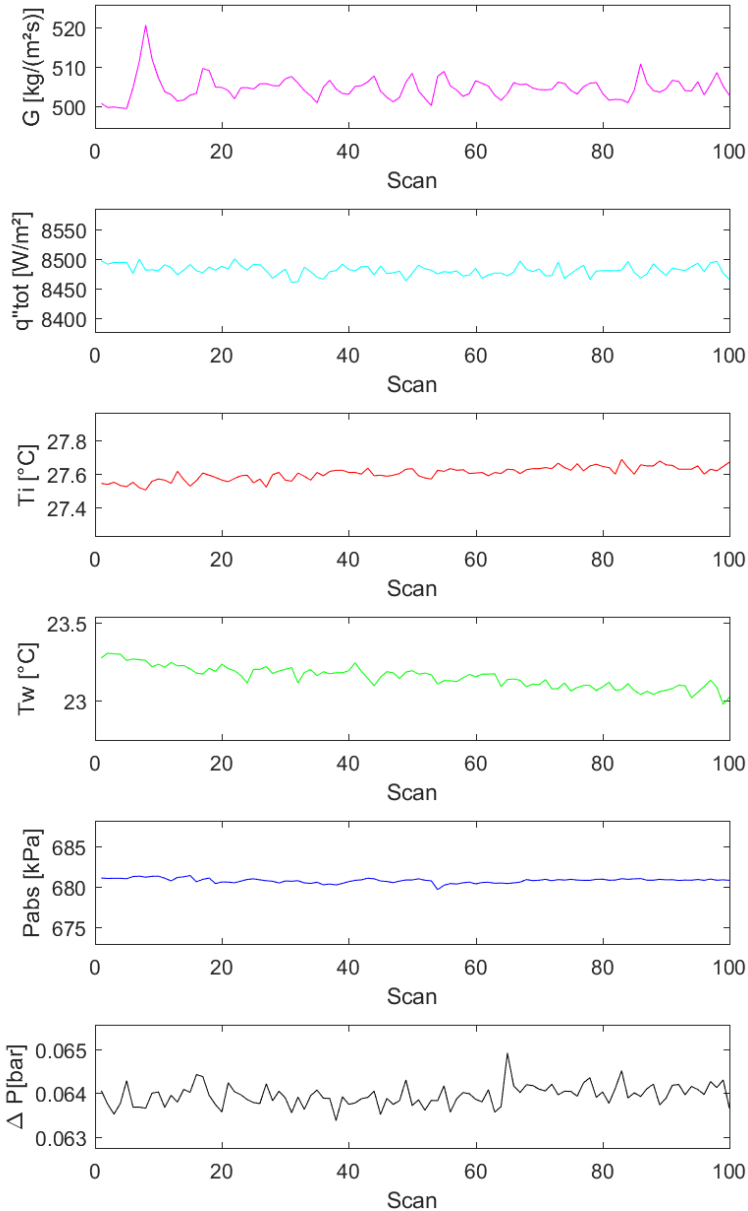


Figure 44: Measured data over a range of 100 acquisitions

4.2 DATA REDUCTION

All the obtained data are processed using MATLAB and EES software. In this section, the calculation routine adopted for the fluid properties is presented. The main goal of this procedure is to validate the tests and to calculate the heat transfer coefficients, h , the pressure drop, Δp , and the vapor quality, x .

First, the pressure drop calculation, Δp , is performed. The pressure taps for differential pressure measurements are placed at the inlet and outlet manifold of the extruded tube. Thus, entrance and exit losses are excluded of this configuration. Also, the pressure drop is obtained in a horizontal tube so that the acceleration and gravity terms are not involved in the measured pressure drop. As such, the pressure drop consists of three components:

1. Contraction at the entrance of the minichannels (single-phase flow);
2. Friction along the minichannels (single-phase and two-phase flows);
3. Expansion at the exit of the minichannels (two-phase flow).

Therefore, equation 4.1 can be used to calculate Δp :

$$\Delta p = \Delta p_{cont} + \Delta p_{frict} + \Delta p_{exp} \quad (4.1)$$

According to section 2.8.1, the first factor, Δp_{cont} , is calculated as follows:

$$\Delta p_{cont} = \zeta \frac{G^2}{2\rho} \quad (4.2)$$

$$\zeta_{cont} = \left[\left(\frac{1}{C_C} - 1 \right)^2 + 1 - \gamma^2 \right] \quad (4.3)$$

$$C_C = 1 - \frac{1 - \gamma}{2.08(1 - \gamma) + 0.5371} \quad (4.4)$$

Where G is the measured mass flux and ρ is the fluid density, which is calculated using the MATLAB wrapper CoolProp. Also, γ represents the

relation between the smaller and larger areas of the geometric change, which for minichannels has the following form:

$$\gamma = \frac{A_{MC}}{A_{mani}} \quad (4.5)$$

where A_{MC} is the area of a single minichannel and A_{mani} is the cross-sectional area of the manifold, through which the fluid enters the test section. In the present study, $A_{MC} = 1.94226 \times 10^{-6} \text{ m}^2$ and $A_{mani} = 4 \times 10^{-4} \text{ m}^2$.

Regarding the third factor of equation 4.1, Δp_{exp} , according to Goss (2011b), the pressure drop caused by the expansion in the minichannels output can be considered negligible.

Rearranging equation 4.1, it is possible to calculate Δp_{frict} since Δp was measured during the test, Δp_{cont} is given by equations 4.2-4.5, and Δp_{exp} is negligible, using the expression:

$$\Delta p_{frict} = \Delta p - \Delta p_{cont} - \Delta p_{exp} \quad (4.6)$$

Secondly, the heat transfer coefficient, h , is calculated. At this point, it is necessary to introduce the concept of local property. It is mandatory to know how the variables and the fluid properties behave locally for the following equations. In order to achieve that, the test section was divided into five parts, for which four points of interest were chosen for the calculation of the fluid local properties. The positions regarding the inlet of the minichannels, l_i , are:

i	l_i [mm]
1	34.5
2	56
3	77.75
4	96.5

These points correspond to the average location where the E-type thermocouples responsible for measuring the wall temperature, T_w , are positioned.

For the calculation of the local pressure, P_i , the following equation is applied:

$$P_i = P_{inl} - \Delta p_{frict,i} \quad (4.7)$$

where P_{inl} is the measured inlet pressure at the test section, and $\Delta p_{frict,i}$ is calculated using the expression:

$$\Delta p_{frict,i} = \frac{l_i \Delta p_{frict}}{112} \quad (4.8)$$

Note that the MPE total length is 112 mm.

Knowing the P_i value, it is possible to find the R134a local saturation temperature, $T_{sat,i}$ at each point of interest, using EES software. Afterwards, $T_{sat,i}$ is compared to the local fluid temperature, $T_{fluid,i}$ which is obtained from:

$$T_{fluid,i} = T_{inl} - \frac{l_i(T_{inl} - T_{out})}{112} \quad (4.9)$$

where T_{inl} and T_{out} are measured by two T-type thermocouples positioned at the inlet and outlet of the test section, respectively. If $T_{fluid,i} \geq T_{sat,i}$ no condensation occurred at this point (single-phase flow); if $T_{fluid,i} < T_{sat,i}$ the fluid has condensate (two-phase flow).

For the subsequent enthalpy calculation, it is crucial to know the last position where the fluid has not condensate yet. This point is found comparing $T_{sat,i}$ with $T_{fluid,i}$. At this point, $x=1$ and using the EES software it is possible to find its enthalpy value, i_{i-1} , where i_i is determined by:

$$i_i = i_{i-1} - \frac{Q_i}{\dot{m}} \quad (4.10)$$

In this expression, Q_i is the average power measured by two heat flux sensors located just before the i position, and \dot{m} is the mass flow rate of a single minichannel, calculated as follows:

$$\dot{m} = G \times A_{MC} \quad (4.11)$$

After the local enthalpy is obtained, the vapor quality, x , is calculated by:

$$x_i = \frac{i_i - i_{l,i}}{i_{vap,i}} \quad (4.12)$$

where $i_{vap,i}$ is the enthalpy of vaporization, which is a function of the local pressure P_i and $T_{fluid,i}$, and $i_{l,i}$ is the enthalpy when $x=0$ at P_i .

Finally, the local heat transfer coefficient is calculated using the equation:

$$h_i = \frac{q''_i}{T_{sat,i} - T_{w,i}} \quad (4.13)$$

where $T_{w,i}$ is the average temperature measured by the E-type thermocouples located at i , and q''_i is calculated as follows, where A_{hfs} is the area of a single heat flux sensor:

$$q''_i = \frac{Q_i}{2A_{hfs}} \quad (4.14)$$

5 EXPERIMENTAL RESULTS

In this chapter, the results obtained on the experimental setup described in Chapter 3 and using the data reduction procedure presented in Chapter 4, are discussed. First, a characterization of test conditions is made using a flow regime map (discussed in section 2.6.3). Afterwards, the influences of mass flux, G , heat flux, q'' , saturation temperature, T_{sat} , and vapor quality, x , on the heat transfer coefficient, h , and pressure drop, Δp , are presented. A comparison of experimental results to correlations proposed in literature is also performed. Finally, the present study is compared to studies conducted in the same area.

In order to ascertain the suitability of the experimental system, the heat transfer data of single-phase vapor R134a is measured first and compared to well-known correlations as shown in Appendix D.

5.1 TEST CONDITIONS

A total of 36 tests were performed, in order to achieve 4 different pressures (7, 7.5, 8, 9 bar), 3 different mass fluxes (400, 450, 500 kg/m²s), and 3 different heat fluxes (8.5, 9, 9.5 kW/m²). These were the pre-established conditions. Among the 36 tests, 10 were discarded because the fluid did not condensate.

The test conditions range is shown in table 15:

Table 15: Test conditions range

Parameter	Minimum value	Maximum value
G [kg/(m ² s)]	391	542
q'' [kW/m ²]	8.2	10.8
x [-]	0.89	1.0
P [bar]	7.4	9.1
T_{sat} [°C]	26.1	35.7
Re_l	73	396
Re_v	44572	63972

The experimental data obtained for mass flux, G , and vapor quality, x , is presented in a plot of the flow regime map developed by Coleman and Garimella (2003) as shown in figure 45. According to this map, all data are in *annular and mist* or *mist* flow regimes.

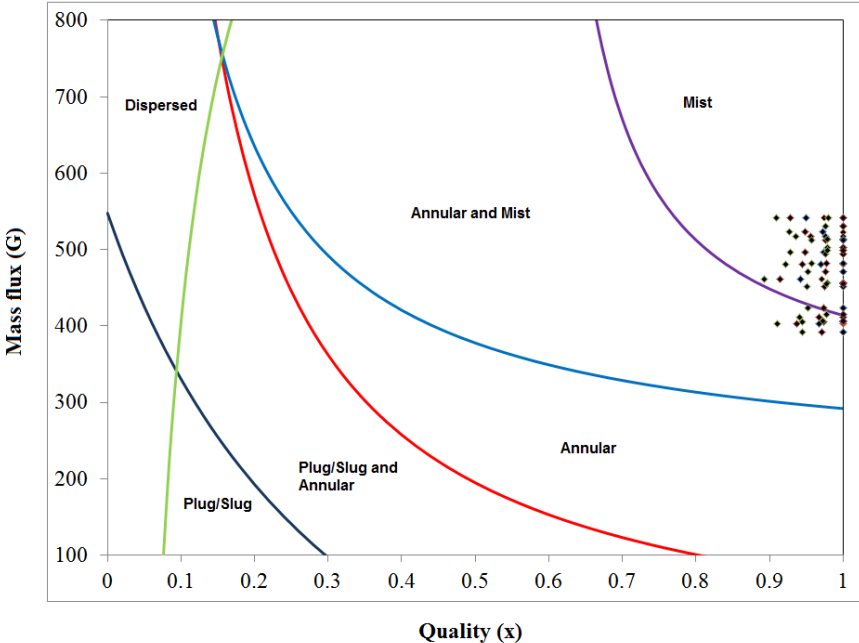


Figure 45: Experimental data points on the Coleman and Garimella (2003) map

5.2 HEAT TRANSFER RESULTS

In this subsection, the results for the heat transfer coefficient, h , are presented according to the influence of G , q'' , T_{sat} , and x . The experimental uncertainty on the calculation of the heat transfer coefficient is present in Appendix E.

For the h calculation, equation 4.13 was used and so the temperature and heat flux data are required. These data are shown in the graphs of figure 46. The test conditions for both graphs presented are $G=481 \text{ kg}/(\text{m}^2\text{s})$ and $P=7.9 \text{ bar}$.

In the first graph, saturation, fluid and wall temperatures are presented as a function of the test section length, where $z=0 \text{ mm}$ is the section inlet. As shown in figure 28, the wall temperature, T_w , is measured by thermocouples located above and below the MPE tube, and they are out of phase. At each measuring point, two thermocouples are installed, and the one at the top is located at a slightly lesser z . The water-glycol flow in the heat sinks is parallel to the fluid flow inside the minichannels. So, as shown in figure 47, the fluid temperature decreases and the

wall temperature increases as condensation occurs (in figure 47, T_w is represented by T_c , and T_{fluid} is represented by T_h). In figure 46, at $z=80$ mm, $T_{w,bottom}$ is lower than the curve trend. This happens because a liquid film is formed as condensation takes place, and due to the gravity, it is thicker at the channel bottom, creating a thermal resistance to heat transfer (Marto, 1998).

During this test, the fluid started to condense at the beginning of the test section, where the pink line (T_{fluid}) becomes inferior to the green line (T_{sat}).

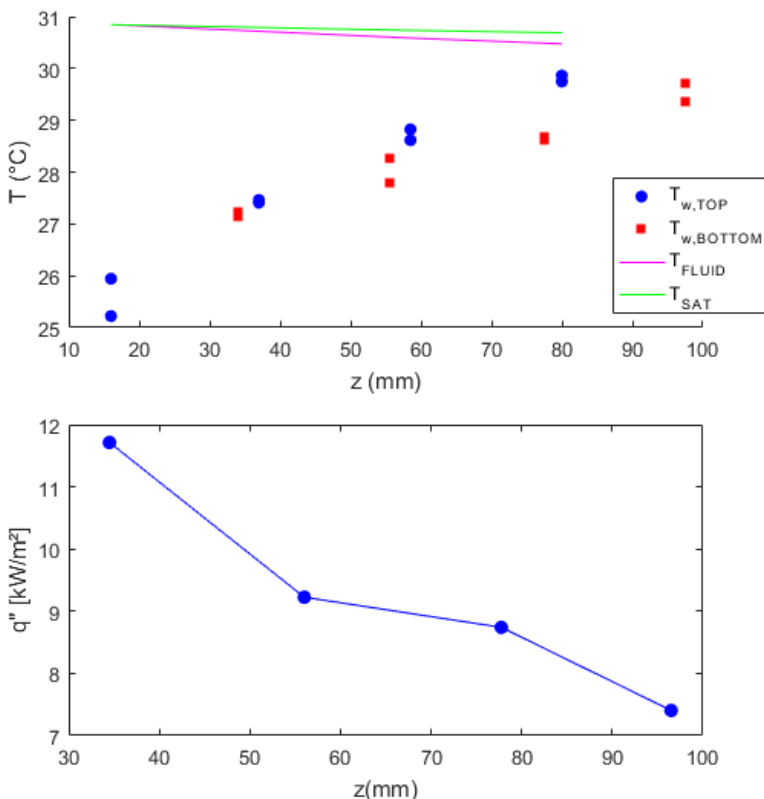


Figure 46: Temperatures and heat flux as a function of the test section position for $G = 481 \text{ kg}/(\text{m}^2\text{s})$ and $P = 7.9 \text{ bar}$

In the second graph of figure 46, the heat flux measurement is shown. As condensation occurs, q'' decreases. Such behavior is expected for two reasons: first, as shown in figure 47, in a parallel-flow

heat exchanger, the temperature difference ΔT , initially large, decays as the heat exchanger length (x) increases, causing a smaller q'' as the fluid flows. Secondly, as fluid condensates, a liquid film is formed around the channel, which serves as resistance to the heat removal.

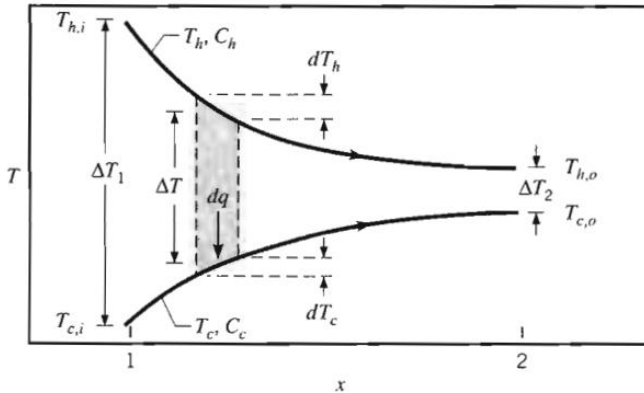


Figure 47: Temperature distribution for a parallel-flow heat exchanger (Incropera et al., 2007)

5.2.1 Effect of mass flux

In the present study, a clear influence of mass flux, G , on the heat transfer coefficient, h , is noted. G was analyzed in the range of 401 kg/(m²s) to 531 kg/(m²s), and h is plotted as function of the position at which the fluid properties are being measured and calculated. In the charts shown in figures 48-50, it is demonstrated that h increases with an increasing G , and this effect is accentuated at higher vapor qualities, i.e. at the test section inlet. This result shows that the shear stress at the liquid–vapor interface is an important force in the flow. This is a characteristic of mist and annular flow patterns.

The Reynolds number for the liquid as a function of vapor quality is presented in the graph of figure 51. The conditions are the same as those shown in figure 48. Note that Re_l increases with the mass flux: for the same x , the highest G values present the greater Re_l values. As heat flux increases, the condensate advection also increases, raising the two-phase heat transfer between the fluid and the channel wall. Regarding the vapor quality, as it increases, the convective heat transfer may play an important role in the heat removed from the fluid, as the liquid film becomes thinner. On the other hand, decreasing x , the liquid film thick-

ness increases, raising the thermal resistance to conduction through itself. In this case, the convection between the channel wall and the liquid film plays a minor role in the heat transfer.

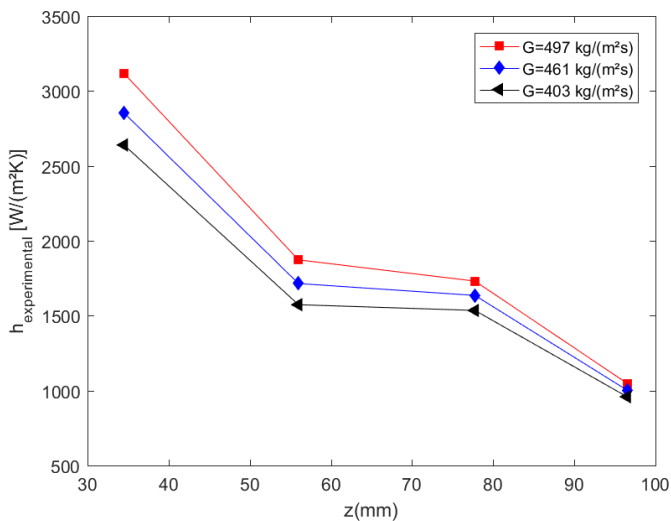


Figure 48: Mass flux influence on h value as a function of the position in the test section for pressure of 7 bar and heat flux of 9.2 kW/m^2

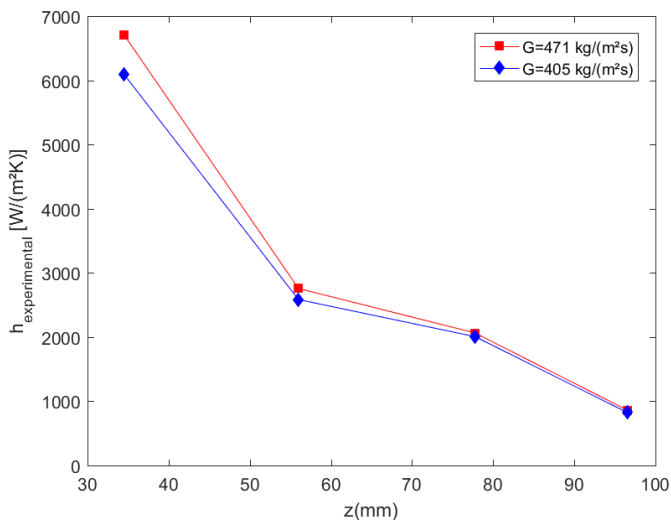


Figure 49: Mass flux influence on h value as a function of the position in the test section for pressure of 7.5 bar and heat flux of 9.3 kW/m^2 .

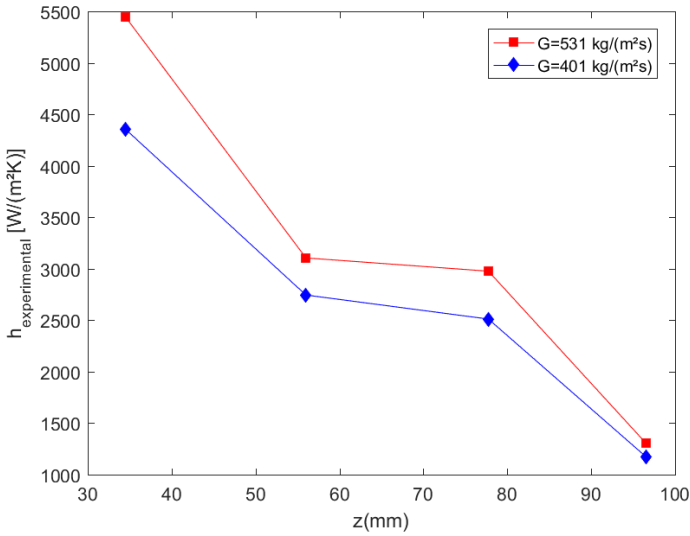


Figure 50: Mass flux influence on h value as a function of the position in the test section for pressure of 8.8 bar and heat flux of 10.1 kW/m^2 .

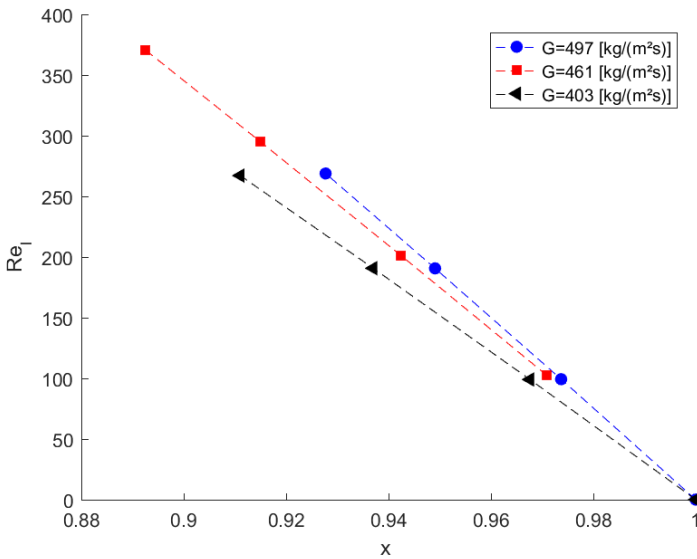


Figure 51: Reynolds number (liquid) for the same test conditions shown in figure 48.

5.2.2 Effect of heat flux

The effect of heat flux, q'' , on the heat transfer coefficient, h , is not always clear in minichannels condensation, as presented in chapter 2. For most test conditions studied, this influence was not evident. The q'' value was analyzed in the range of 8.2 kW/m² to 10.8 kW/m², and h is plotted as a function of the position at which the fluid properties are being measured and calculated.

The charts shown in figures 52 and 53 present that the highest q'' values are related to the highest h values. The other two smaller q'' values exhibit a very similar behavior. The influence of q'' on h shown in figure 54 is the opposite of that shown in figures 52 and 53. The smaller q'' , 8.2 kW/m², presents the higher h , while the two larger q'' exhibit a lower h . The test conditions shown in figure 54 are for a higher pressure, but the mass flux is very close to that of figure 52.

On these three graphs, the behavior of the lines presenting the highest h is very similar, as well as the ones with lower h . It is noted that from $i=3$, i.e., 77.75-mm away from the test section inlet, the highest h line decreases more strongly than those of lower h . Regardless of the q'' value, as condensation occurs and the thickness of the liquid film increases, h tends to the same value.

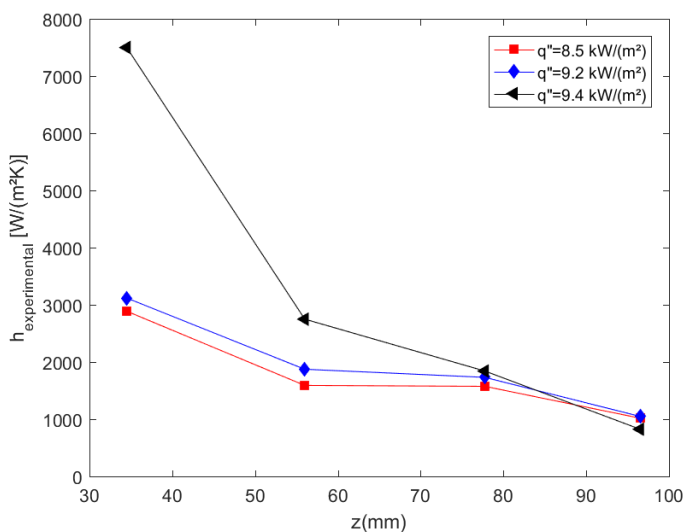


Figure 52: Heat flux influence on h value as a function of the position in the test section for pressure of 7 bar and mass flux of 504 kg/(m²s)

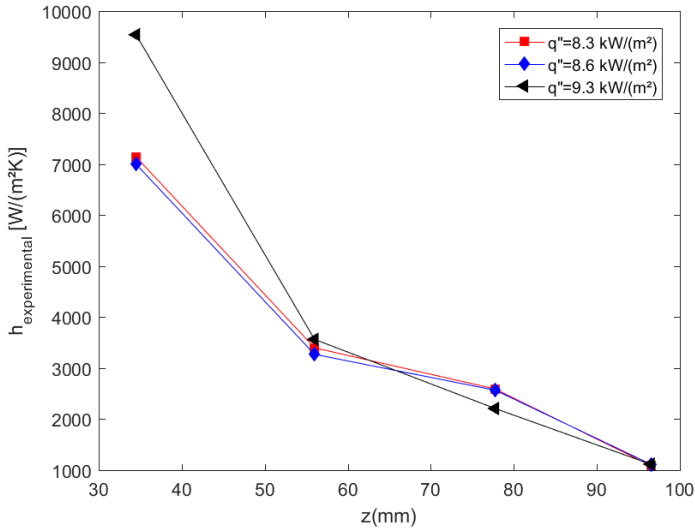


Figure 53: Heat flux influence on h value as a function of the position in the test section for pressure of 7.8 bar and mass flux of $415 \text{ kg}/(\text{m}^2\text{s})$

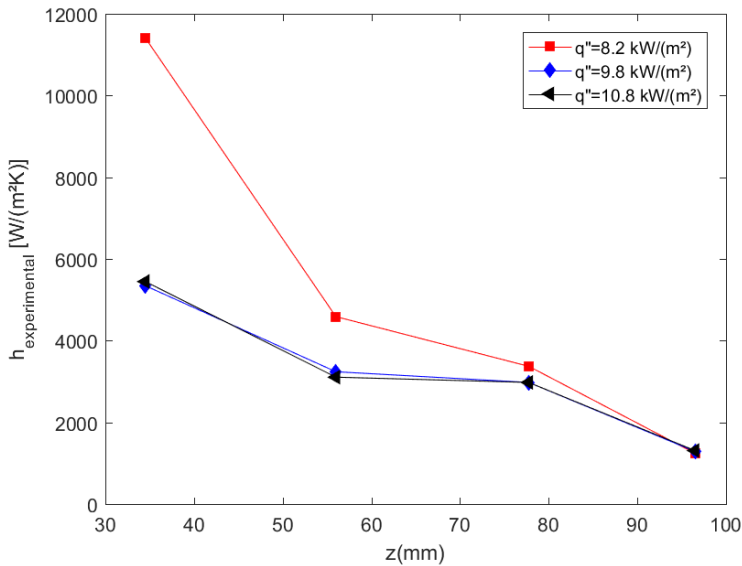


Figure 54: Heat flux influence on h value as a function of the position in the test section for pressure of 8.6 bar and mass flux of $512 \text{ kg}/(\text{m}^2\text{s})$

5.2.3 Effect of saturation temperature

The influence of the saturation temperature of the working fluid on the heat transfer coefficient, h , is shown in figures 55-58. The inlet pressure, therefore saturation temperature, have influence on h at the test section inlet, i.e., at high vapor quality. However, it does not have a significant influence on h at the test section outlet.

Three tests are compared at same mass flux, 408 kg/m², and heat flux, 8.9 kW/m², in figure 55. The inlet pressure range is from 6.95 to 7.84 bar. The trend shown in this figure is the same for the other tests performed: the increase in T_{sat} results in higher h . Also, the difference between the heat transfer coefficients at the test section inlet for different T_{sat} is significant, and it decreases as z increases. At the end of test section, the 3 lines become closer.

Three other tests are compared for conditions of mass flux, 485 kg/m², and heat flux, 9.1 kW/m², and are shown in figure 56. The inlet pressure range is from 6.96 to 8.45 bar. Another three tests are compared for the conditions of mass flux, 524 kg/m², and heat flux, 8.3 kW/m², and are shown in figure 57. The inlet pressure range is from 6.97 to 8.35 bar. Two tests are compared as shown in figure 58. The test represented by red color has as condition the inlet pressure of 7.97 bar and the blue one, 6.97 bar. The other conditions are mass flux of 501 kg/m² and heat flux of 9.3 kW/m².

According to the graphs presented, heat transfer increases with vapor quality, i.e. next to the test section inlet. At high vapor quality, the vapor moves at a higher velocity and the interfacial condensation is higher. As condensation occurs, droplets are formed, which act as a resistance to the heat transfer, causing lower heat transfer coefficients. According to the energy transport mechanisms in the condensing flow, the overall heat transfer for the condensation of R134a flow is mainly dominated by the thermal resistance associated with the convection at the vapor-liquid interface. At high vapor quality, the saturation temperature exhibits great influence on h . However, as condensation occurs, the T_{sat} influence decreases. A compensation effect appears between the condensate film properties and the flow characteristics. At a higher temperature of saturation, the thermal conductivity of the liquid R134a is lower and the associated thermal resistance of the liquid film is larger, causing a poorer heat transfer. On the other hand, the temperature increase causes a vapor velocity reduction and a liquid velocity growth. Therefore, the slip ratio is reduced and as consequence, the interfacial shear stress between liquid and vapor are reduced as well. Considering

the annular-mist and mist flow regimes, the liquid droplets in the steam core are removed by the liquid film as a function of the shear stress between the vapor and the film itself. As the interfacial shear stress decreases, a higher amount of droplets stay in the steam core and a lower amount of droplets goes to the liquid film, reducing the liquid film thickness and increasing the heat transfer coefficient.

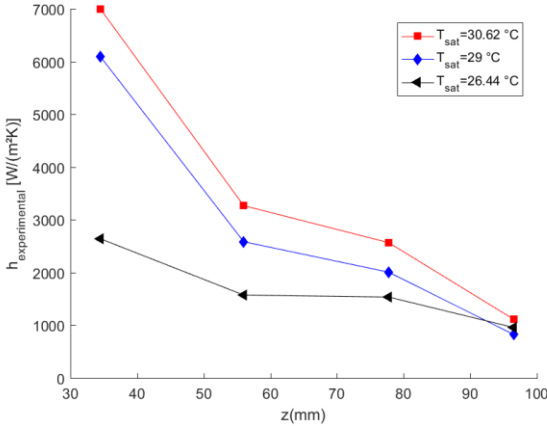


Figure 55: Saturation temperature of working fluid influence on h value as a function of the position in the test section for mass flux of $408 \text{ kg}/(\text{m}^2\text{s})$ and heat flux of $8.9 \text{ kW}/\text{m}^2$

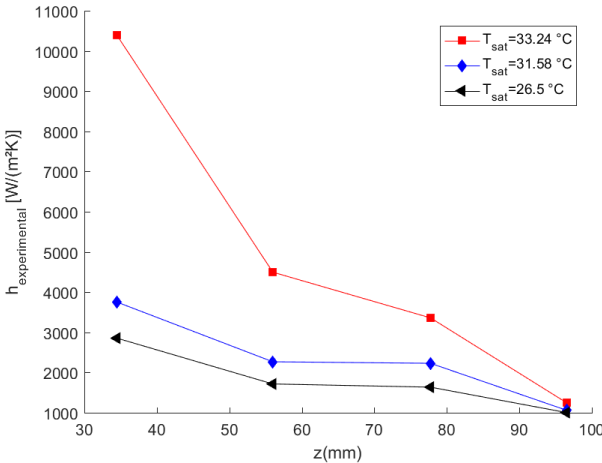


Figure 56: Saturation temperature of working fluid influence on h value as a function of the position in the test section for mass flux of $485 \text{ kg}/(\text{m}^2\text{s})$ and heat flux of $9.1 \text{ kW}/\text{m}^2$

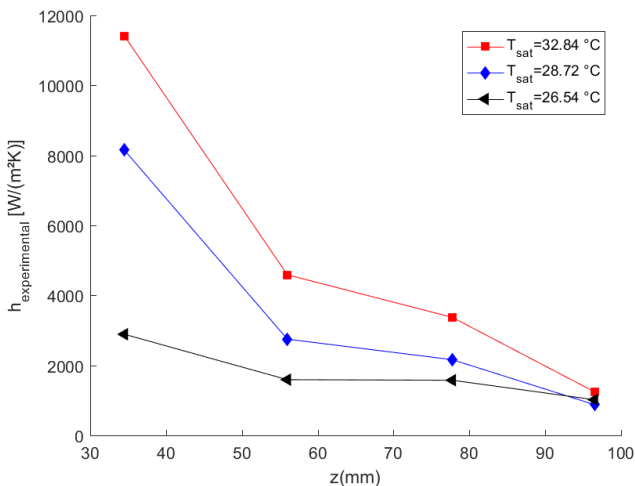


Figure 57: Saturation temperature of working fluid influence on h value as a function of the position in the test section for mass flux of $524 \text{ kg}/(\text{m}^2\text{s})$ and heat flux of $8.3 \text{ kW}/\text{m}^2$

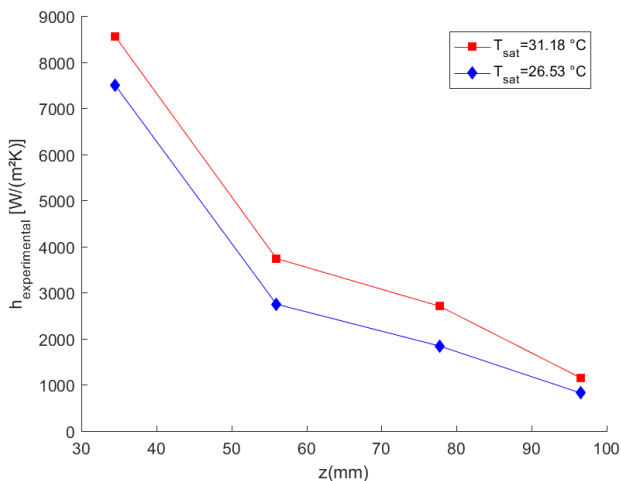


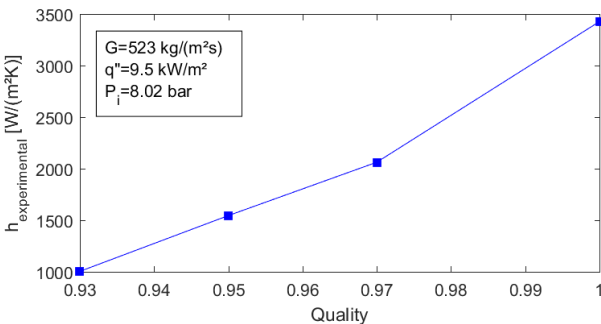
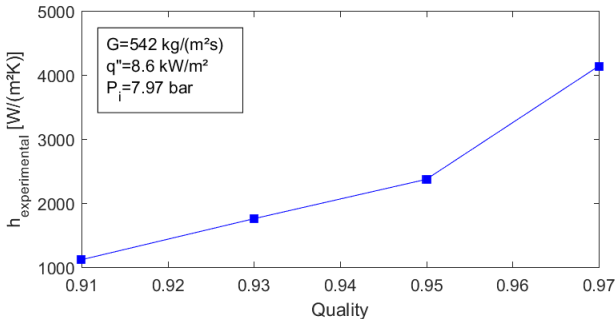
Figure 58: Saturation temperature of working fluid influence on h value as a function of the position in the test section for mass flux of $501 \text{ kg}/(\text{m}^2\text{s})$ and heat flux of $9.3 \text{ kW}/\text{m}^2$

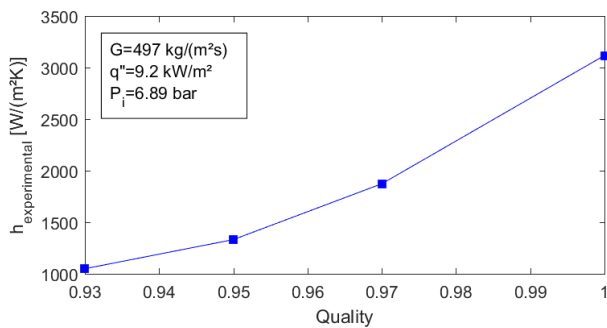
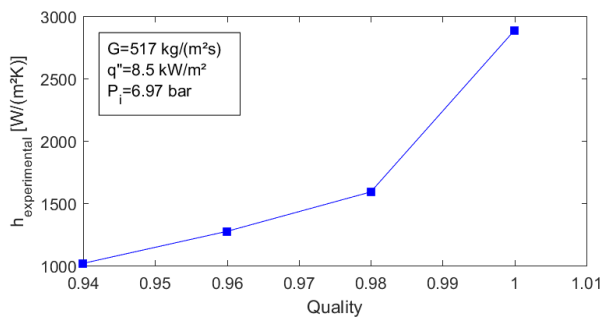
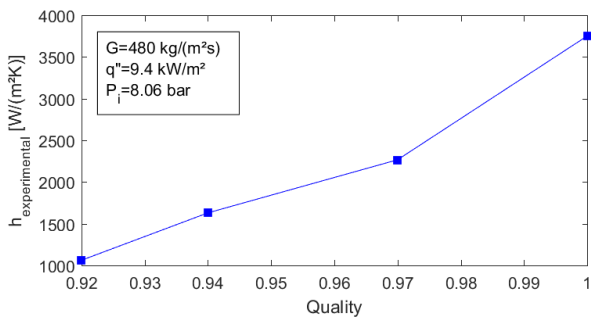
5.2.4 Effect of vapor quality

The influence of vapor quality, x , on the heat transfer coefficient, h , is analyzed for a given test condition. In all charts shown in figure 59 it is noted that h decreases with a reducing x . The test conditions for the presented graphs are: $403 \leq G \leq 542 \text{ kg}/(\text{m}^2\text{s})$, $8.5 \leq q'' \leq 9.5 \text{ kW}/\text{m}^2$, and $6.89 \leq P_i \leq 8.06 \text{ bar}$.

Mist, annular and annular-mist flows are characterized by vapor flowing in the core of the channel with a few entrained liquid droplets, while liquid flows along the circumference of the channel's wall. For those flow patterns, the thickness of the liquid film is the dominant resistance in the heat transfer process. On reducing the vapor quality, the thickness of the liquid film increases, raising the heat transfer resistance. Hence, the heat transfer coefficient decreases.

Note that the vapor quality exerts significant influence on h , mainly at high qualities. The behavior of h is very similar for all conditions, showing a pronounced drop at the beginning of the test section (higher x), since the liquid film is thinner, leading to a lower thermal resistance to heat transfer.





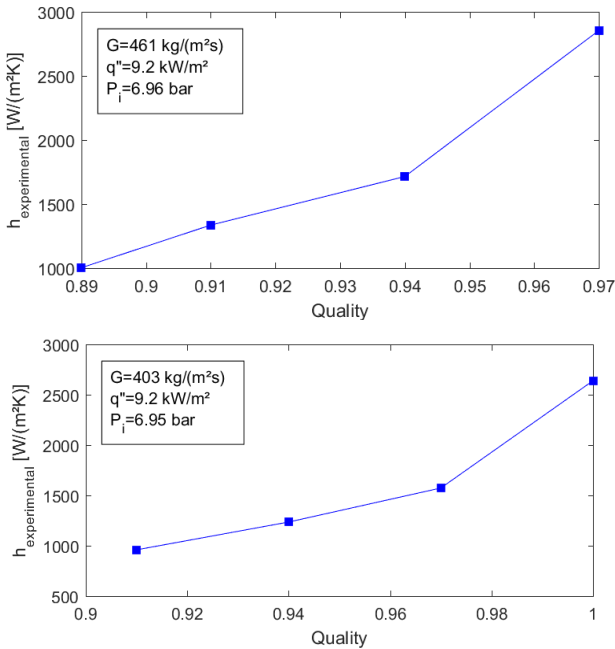


Figure 59: Influence of vapor quality on heat transfer coefficient for different test conditions

5.2.5 Comparison of the experimental heat transfer coefficient with correlations

The comparison of the experimental heat transfer coefficient values obtained in this study with those predicted by correlations can be estimated through the mean absolute error (MAE) defined as follows:

$$MAE = \frac{1}{N} \sum_1^N \left| \frac{h_{\text{experimental}} - h_{\text{predicted}}}{h_{\text{experimental}}} \times 100 \right| \quad (5.1)$$

Where $h_{\text{experimental}}$ and $h_{\text{predicted}}$ represent the experimental value and the calculated value using the correlation for heat transfer coefficient, respectively, and N represents the number of data points.

The correlations used were developed based on different test condition data, as described in section 2.9. The graphs shown in figures 60-65 exhibit such comparisons, along with the MAE value.

The correlations proposed by Chato (1962), Akers et al. (1959), and Shah (1973) presented more than 100% error when compared to the experimental data. For example, even though it is one of the most used condensation correlations, Shah's model over-predicted the data and the MAE value calculated was 193.7%. His data were obtained for lower mass fluxes and bigger hydraulic diameters than the present work test conditions. Chato (1962) proposed his correlation based on stratified-flow condensation inside conventional tubes under low vapor shear at various inclinations, i.e. he considered a gravity-driven condensation. Akers et al. (1959) assumed that an all-liquid flow rate may provide the same heat transfer coefficient for condensing annular flow. As the vapor qualities achieved on this study were no lower than 0.89, Akers et al. (1959) correlation did not fit well the experimental data.

The correlations proposed by Cavallini et al. (2002), Dobson and Chato (1998), Traviss et al. (1973), and Soliman et al. (1968) were developed for conventional channels. The one proposed by Traviss et al. (1973), shown in figure 60, is based on an 8-mm diameter tube, for high mass fluxes, from 161 kg/(m²s) to 1533 kg/(m²s). Although this correlation was proposed for large diameter channels, the mass flux conditions fit the experimental. Traviss et al. (1973) did not find great agreement for mist flow condition, resulting in a MAE value of 50.1%. Likewise, the correlation proposed by Cavallini et al. (2002), shown in figure 61, also proposed for an 8-mm diameter tube, but with the mass flux up to 750 kg/(m²s), had a calculated MAE value of 62.2%.

Dobson and Chato (1998) also developed a correlation (figure 62) for conventional channels. However, the mass flux is up to 800 kg/(m²s). Therefore, this model presented a MAE value of 43.4%. Soliman et al. (1968) over-predicted the data, as shown in figure 63. The experimental vapor velocity is outside the applicability range for this correlation. Soliman et al. (1968) tested different fluids (R113 and R12) than the one used in the present study, and also elaborated their model for conventional channels. This correlation presented the worst MAE value (86.9%).

Regarding the correlations developed for small diameter channels, it is shown in figure 64 the comparison of h experimental and h predicted by Koyama et al. (2003a). A MAE value of 41.2% was found. Finally, the correlation proposed by Cavallini et al. (2006c) is presented in figure 65. The comparison between the experimental data and predicted values show a satisfactory behavior of all models tested. This heat transfer model is proposed for minichannels and takes into account the effect of the entrainment rate of droplets from the liquid film. Since it is

a correlation applied to the annular, annular-mist flow, the MAE value calculated was the lowest (28.3%).

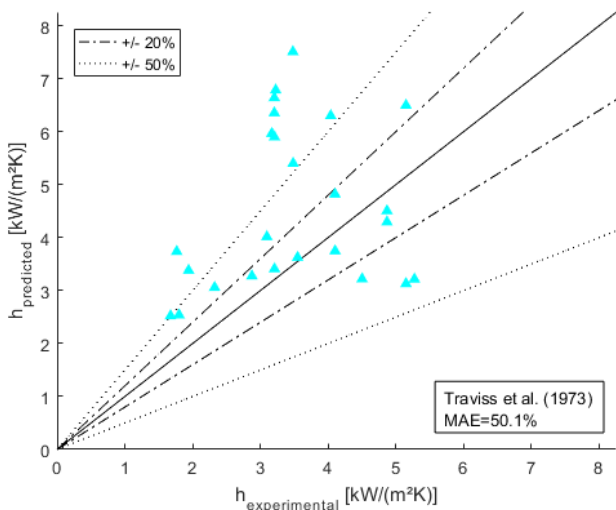


Figure 60: Comparison of experimental heat transfer coefficient with Travis et al. (1973) correlation

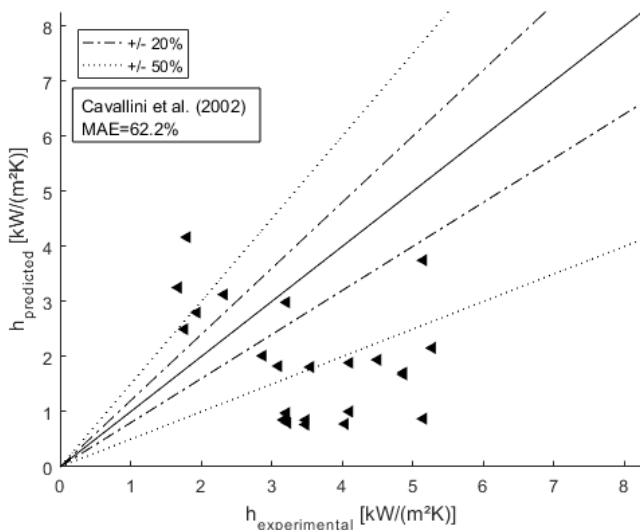


Figure 61: Comparison of experimental heat transfer coefficient with Cavallini et al. (2002) correlation

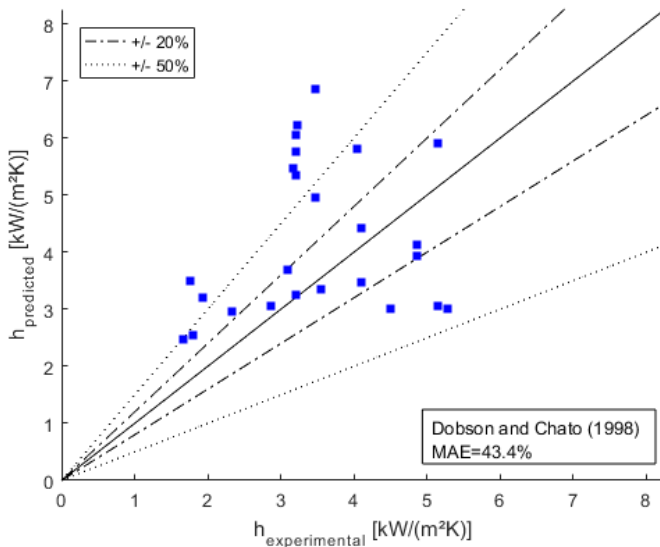


Figure 62: Comparison of experimental heat transfer coefficient with Dobson and Chato (1998) correlation

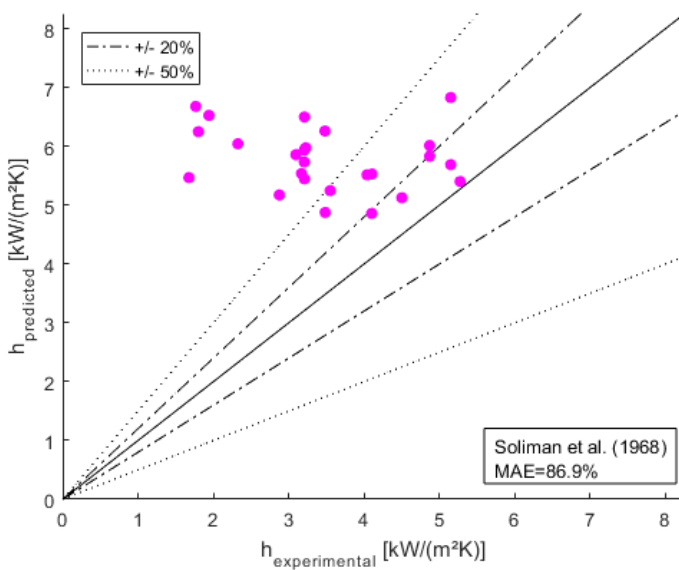


Figure 63: Comparison of experimental heat transfer coefficient with Soliman et al. (1968) correlation

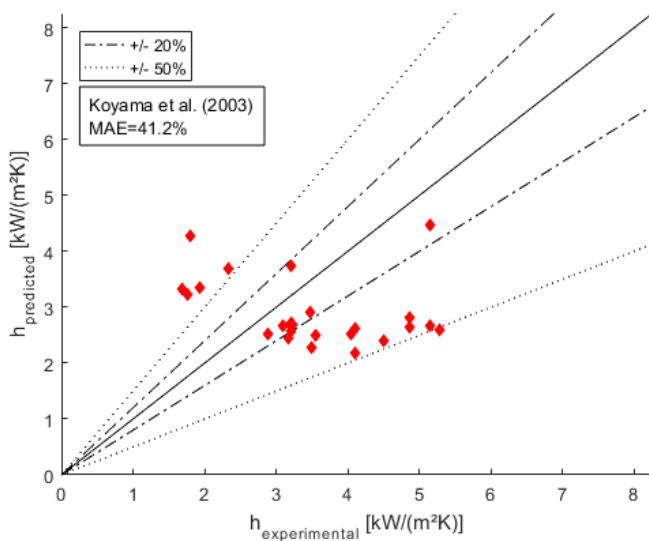


Figure 64: Comparison of experimental heat transfer coefficient with Koyama et al. (2003) correlation

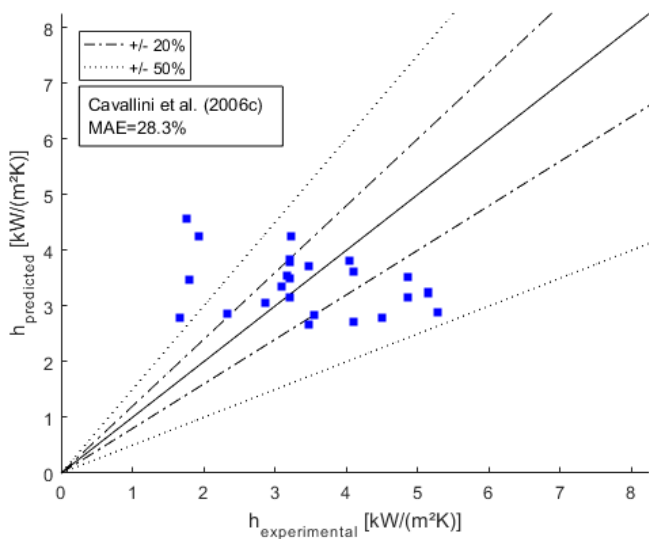


Figure 65: Comparison of experimental heat transfer coefficient with Cavallini et al. (2006c) correlation

5.3 PRESSURE DROP RESULTS

As explained in section 4.2, the pressure drop, Δp , has three components: Δp_{cont} , Δp_{frict} , and Δp_{exp} . Contraction at entrance of the minichannels, Δp_{cont} , and friction along the minichannels, Δp_{frict} , were calculated using equations 4.2 and 4.6. The pressure drops due to expansion in the minichannels outlet, Δp_{exp} , were considered negligible. In this section, Δp_{exp} is calculated in order to confirm that assumption. For this, the following equations provided by Hewitt et al. (1994) are used:

$$\Delta p_{exp} = \zeta_{exp,2P} \frac{G^2}{2\rho} \quad (5.2)$$

$$\zeta_{exp,2P} = \zeta_{exp} \Psi_S \quad (5.3)$$

$$\Psi_S = 1 + \left(\frac{\rho_l}{\rho_v} - 1 \right) [0.25x(1-x) + x^2] \quad (5.4)$$

$$\zeta_{exp} = 2\gamma (1 - \gamma) \quad (5.5)$$

The effect of each component in the total pressure drop measured between the inlet and outlet manifolds is presented in figure 66. The pressure drop due to expansion represents 1.7% of the total measured pressure drop; due to friction, 92%, and due to contraction, 6.3%. The proportions calculated for the pressure drop components are close to those found by Garimella et al. (2005). It is concluded that the expansion contribution can be neglected, and that the pressure drop is dominated by friction.

Next, the influences of mass flux, heat flux, and saturation temperature on pressure drop are presented.

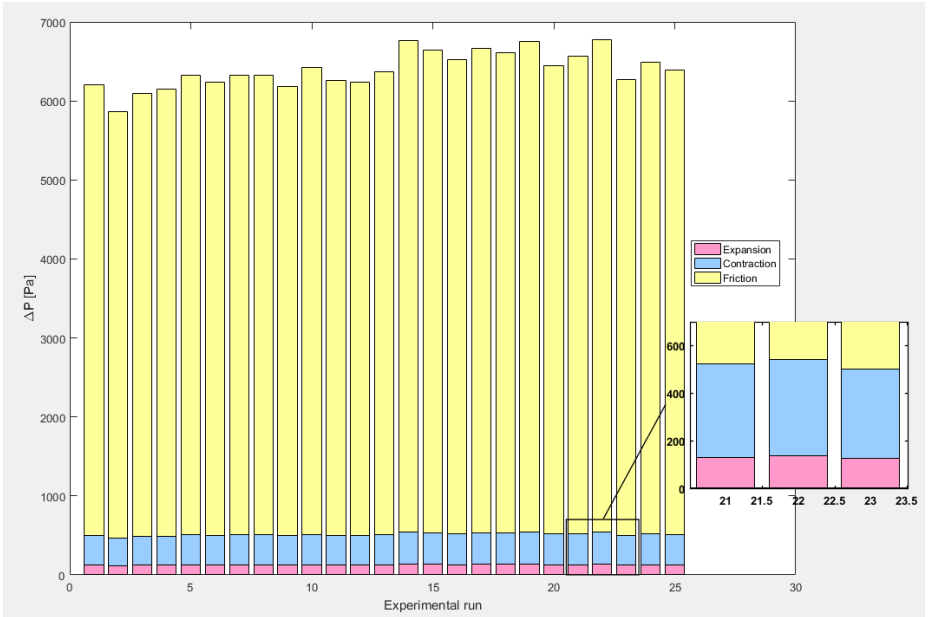


Figure 66: Pressure drop contributions for all experimental runs

5.3.1 Effect of mass flux

Values of $\Delta P_{experimental}$, obtained using the equation 5.2, are presented as a mass flux function for four different test conditions in figure 67. The inlet pressure value ranged from 6.9 bar to 8.7 bar, and the heat flux ranged from 8.4 kW/m² to 9.3 kW/m². Note that, according to figure 67, a mass flux increase causes an increase in the pressure drop. The pressure drop increase with the mass flux is expected, as shown in the Darcy-Weisbach (2.34) equation.

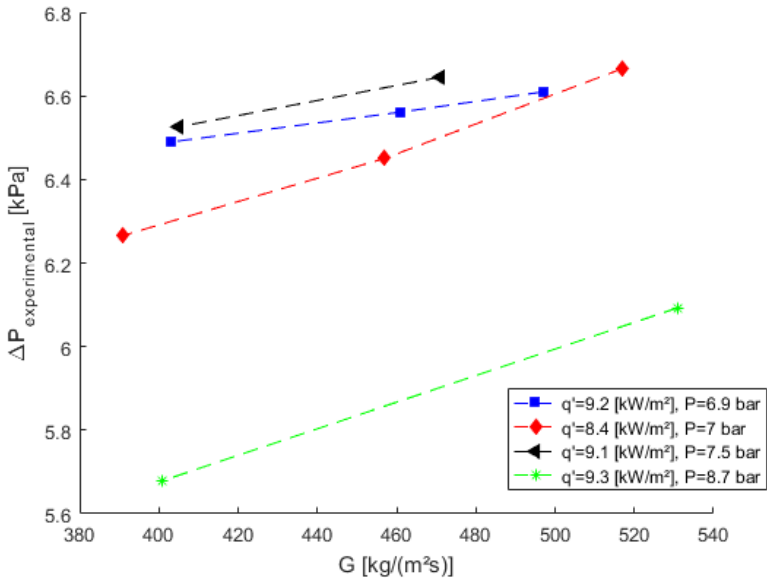


Figure 67: Mass flux effect on experimental pressure drop

5.3.2 Effect of heat flux

The heat flux influence on experimental pressure drop values is presented in figure 68 for five distinct test conditions. The inlet pressure value ranged from 6.9 bar to 8.6 bar and the mass flux ranged from 402 kg/(m²s) to 522 kg/(m²s).

According to figure 68, the pressure drop is not significantly affected by heat flux. That can be explained by some compensating effects. The pressure drop, in a two-phase flow, is composed by three friction components: liquid-wall, vapor-wall, and liquid-vapor. A higher heat flux causes a greater amount of condensate liquid, therefore, a larger liquid-wall friction. On the other hand, to increase the heat flux means to reduce the vapor quality, hence, a smaller slip ratio. Therefore, the liquid-vapor component is reduced. Finally, as condensation occurs, the liquid film formation causes a reduction in the vapor-wall component.

Additionally, it is shown in figure 68 that for the lowest inlet pressure, the highest the pressure drop value is found. It is discussed in the next subsection (5.3.3).

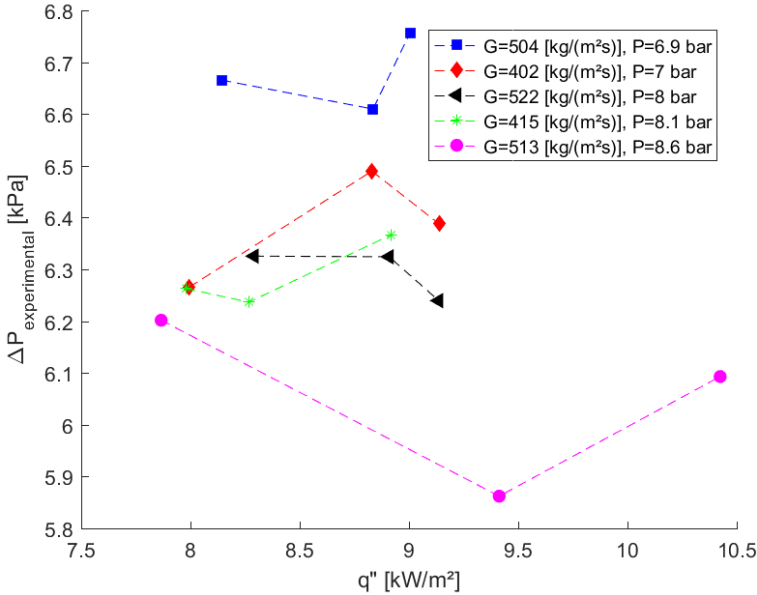


Figure 68: Heat flux effect on experimental pressure drop

5.3.3 Effect of saturation temperature

The saturation temperature (or pressure) effect on $\Delta P_{\text{experimental}}$ is presented in figure 69. The liquid mass density reduces with the increase in saturation pressure, whereas the vapor mass density increases. Hence, the slip ratio (proportional to ρ_l/ρ_v) decreases with the increase in saturation pressure (and so saturation temperature), and the liquid-vapor interfacial drag quantity is reduced. Therefore, for higher saturation temperature, lower pressure drop is found. The same behavior is noted in the graph presented in figure 67.

Also, as discussed in subsection 5.3.1, the greater mass fluxes values presented the higher experimental pressure drop values.

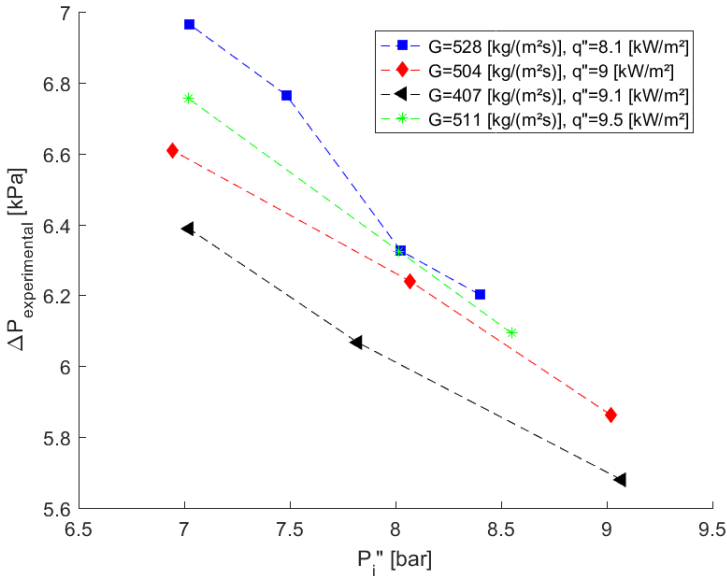


Figure 69: Temperature saturation (pressure) effect on experimental pressure drop

5.3.4 Comparison of the experimental pressure drop with correlations

The charts depicted in figures 70-75 present the comparisons of the experimental results obtained for pressure drop to the models described in section 2.8.2. Analogous to the comparative analysis of the heat transfer coefficient, in the previous subsection, the mean absolute error (MAE) is used to compare experimental and predicted pressure drop values. The MAE is defined as follows:

$$MAE = \frac{1}{N} \sum_1^N \left| \frac{\Delta P_{\text{experimental}} - \Delta P_{\text{predicted}}}{\Delta P_{\text{experimental}}} \times 100 \right| \quad (5.6)$$

Where $\Delta P_{\text{experimental}}$ and $\Delta P_{\text{predicted}}$ represent the experimental value and the calculated value using the correlation for pressure drop, respectively, and N represents the number of data points.

Lockhart and Martinelli (1949), Friedel (1979) and Chisholm (1973) correlations, compared to the experimental pressure drop, are shown in figures 70, 71, and 72, respectively. These are classical pressure drop correlations for conventional diameter tubes considering sepa-

rated flow. In general, the three correlations presented good accordance to the experimental results. Lockhart and Martinelli (1949) correlation underpredicted the data and presented a MAE value of 24.6%. Friedel (1979) and Chisholm (1973) correlations showed lower MAE values of 19.1% and 19.9%, respectively.

The correlation proposed by Garimella et al. (2005) presented the greatest convergence with the experimental data (MAE=15.7%) as shown in figure 73. This model was developed for microchannels ($0.4 < D_h < 4.9$ mm) and for a compatible mass flux range ($150 < G < 750$ kg/m²s). The void fraction was calculated using Baroczy (1965) correlation.

The model developed by Zhang and Webb (2001), shown in figure 74, also showed a good convergence with the experimental results (MAE=17.7%). The conditions used to establish this correlation were similar to the test conditions of this study. A more detailed comparison is made in section 5.4.2. Finally, the largest MAE achieved, 27.1%, was found in the comparison with the Mishima and Hibiki (1996) correlation. The experimental data was underpredicted. That was expected since, even though this model was developed to microchannels, the measured pressure drop was to air-water flows.

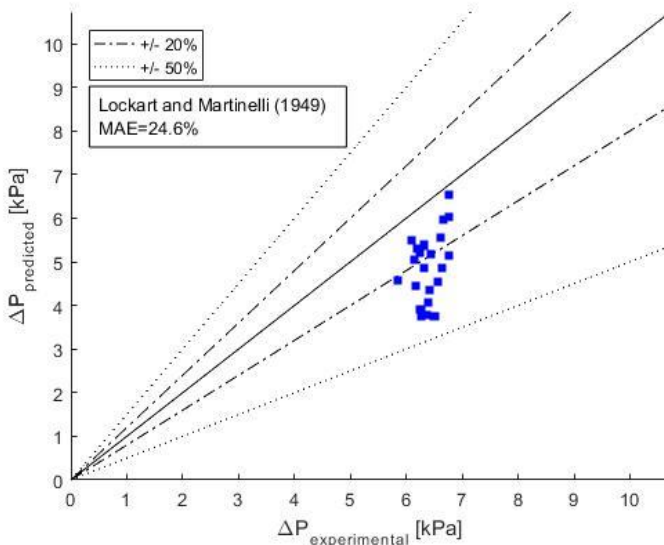


Figure 70: Comparison of experimental pressure drop with Lockhart and Martinelli (1949) correlation

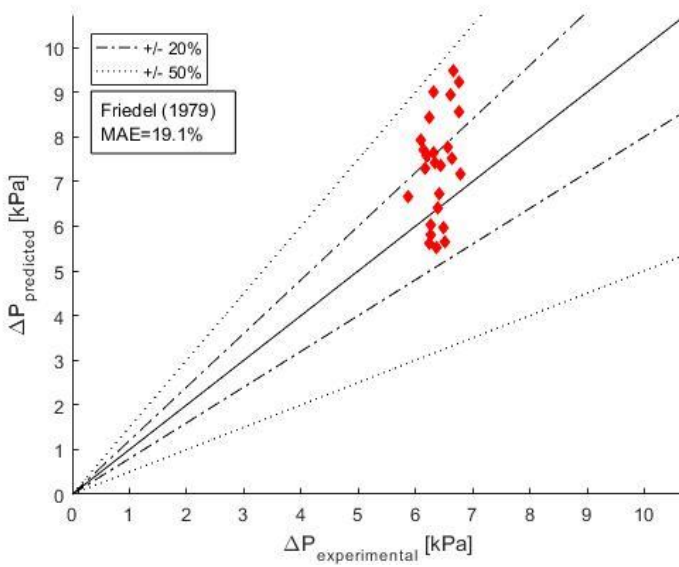


Figure 71: Comparison of experimental pressure drop with Friedel (1979) correlation

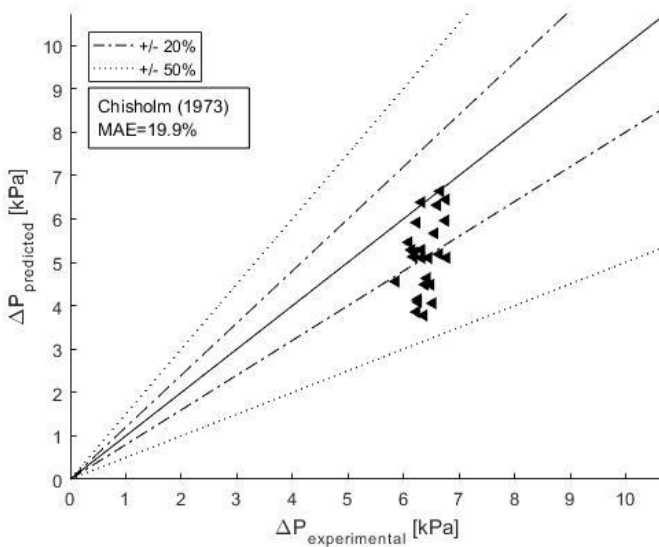


Figure 72: Comparison of experimental pressure drop with Chisholm (1973) correlation

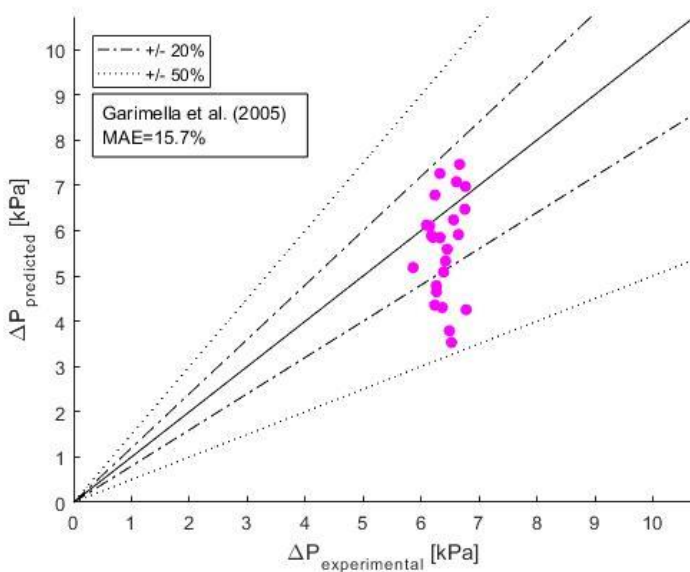


Figure 73: Comparison of experimental pressure drop with Garimella et al. (2005) correlation

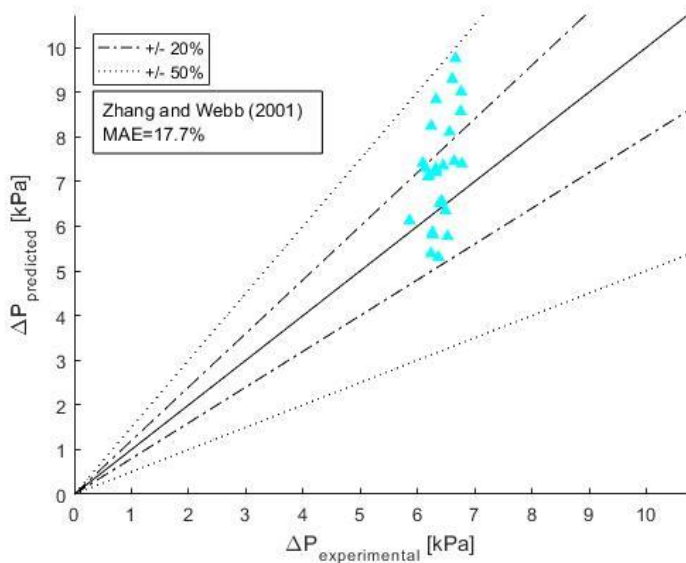


Figure 74: Comparison of experimental pressure drop with Zhang and Webb (2001) correlation

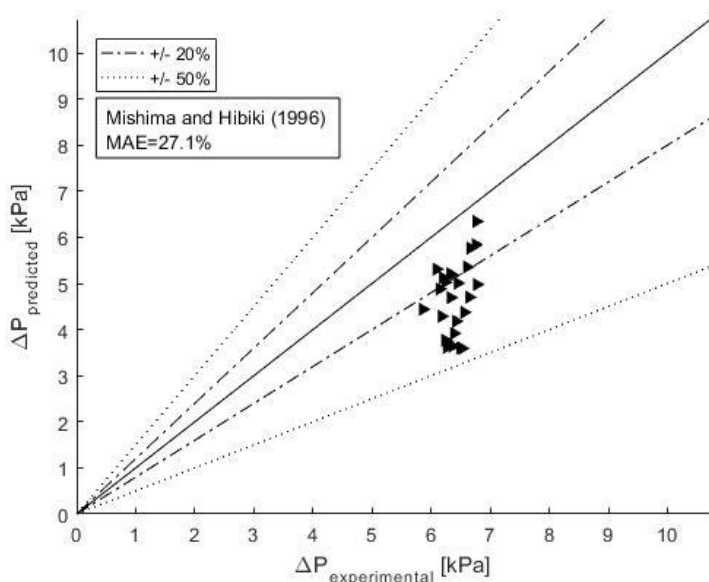


Figure 75: Comparison of experimental pressure drop with Mishima and Hibiki (1996) correlation

The comparisons to the homogeneous models are presented in figures 76-78. As described in section 2.8.2.1, the calculation of mean two-phase viscosity, $\bar{\mu}$, was performed taking into account the equations of McAdams et al. (1942), Cicchitti et al. (1960), and Dukler et al. (1964). The homogeneous model underestimates the experimental pressure drop values for all these correlations. MAE values range from 45.9% to 75.8%. This result was expected due to the nonslip condition. This hypothesis can satisfy bubbly patterns, but not annular or mist ones. The best result for pressure drop using the homogeneous model was found for the equation 2.51, of Cicchitti et al. (1960).

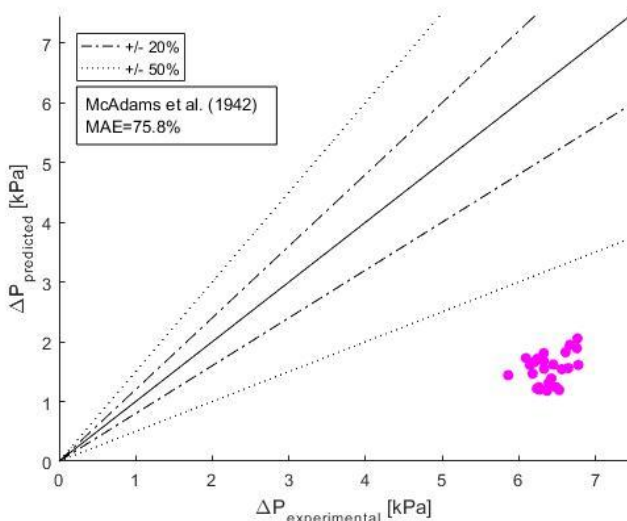


Figure 76: Comparison of experimental pressure drop with Homogeneous Model using McAdams et al. (1942) equation for the mean two-phase viscosity

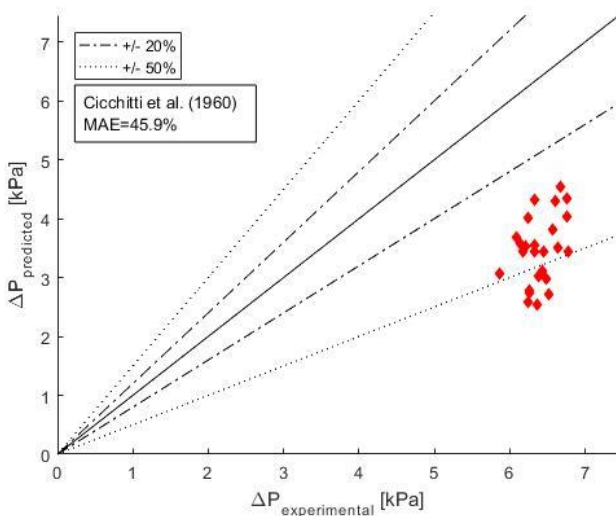


Figure 77: Comparison of experimental pressure drop with Homogeneous Model using Cicchitti et al. (1960) equation for the mean two-phase viscosity

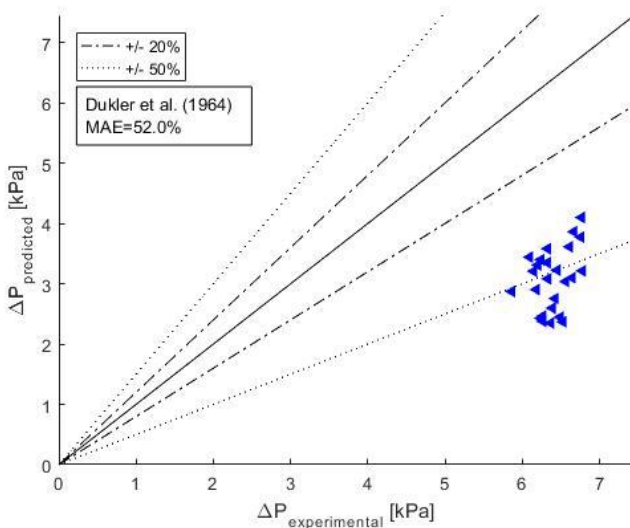


Figure 78: Comparison of experimental pressure drop with Homogeneous Model using Dukler et al. (1964) equation for the mean two-phase viscosity

5.4 COMPARISON WITH OTHER STUDIES

In this section, the present work is compared to studies conducted in the same area. A summary of these studies is presented in table 16. It is important to note that all studies used R134a as working fluid.

5.4.1 Yan and Lin (1999)

Considering the experimental apparatus and procedures of Yan and Lin (1999), the similarities with the present study are:

- A condenser (here, called post-condenser) is used to condensate the refrigerant vapor from the test section via a cold water-glycol loop.
- The test section pressure can be controlled by varying the temperature of the water-glycol loop in the condenser.
- The temperature of the hot water loop for the pre-evaporator (here, the boiler's power supply) is adjusted to keep the mass flux of R134a at the test section inlet at the desired value.
- The heat transfer rate is adjusted by changing the temperature of the cold water loop for the test section.

The main difference is that Yan and Lin (1999) calculated the amount of heat transfer from R134a by measuring the enthalpy change of the water between the inlet to the exit of the tube. In this study, heat flux sensors are used and the heat flux is directly measured.

Regarding the results, Yan and Lin (1999) noted that the heat transfer coefficient is higher at a lower heat flux, at a lower saturation temperature and at a higher mass flux. In this study, the T_{sat} and q'' influences showed no evident effect on h . The saturation temperature range analyzed by Yan and Lin (1999) is larger, and the method used to obtain the q'' value is different. However, both studies concluded that h is higher for a higher G . Considering the pressure drop, both studies concluded that Δp increases with T_{sat} decrease and G increase; although Yan and Lin (1999) found that q'' has an influence on Δp . Finally, both studies concluded that the frictional pressure drop represents more than 90% of the total pressure drop measured.

5.4.2 Zhang and Webb (2001)

One of the most important similarities between the present and the test facilities used by Zhang and Webb (2001) is the pressure taps used for differential pressure measurements. They were placed at the inlet and outlet plenums of the extruded tube. Both studies considered that the overall measured pressure drop consists of friction, contraction and expansion components. Regarding the experimental results, both studies concluded that the two-phase pressure drop increases with mass flux increase and saturation temperature decrease.

Zhang and Webb (2001) predicted the single-phase pressure drop within $\pm 10\%$ using Blasius equation. As presented in Appendix D, the MAE value of Blasius correlation of the present study is 12.3%. Finally, as shown in figure 74, the experimental results for pressure drop were compared to the correlation proposed by Zhang and Webb (2001) and the results were well predicted (MAE=17.7%).

5.4.3 Koyama et al. (2003a, 2003b)

Koyama et al. (2003b) study was very important as a reference since their experimental apparatus is similar to the one used in this work. The most interesting similarity is the use of heat flux sensors to measure the heat flux, which is considered as a local value. However, all Koyama et al.'s experiments were carried out at a constant inlet pressure of 17 bar, i.e., higher than the used in this study. Regarding data reduction, the two-phase pressure drop is estimated using homogeneous mod-

el, while in this study, as shown in figures 76-78, the homogenous model underestimates the experimental pressure drop values.

Koyama et al. (2003a) proposed a correlation of the heat transfer coefficient, which was tested and presented MAE=41.2%. Unlike the other study from the same authors (2003b), the heat flux sensors were not installed in the test section. Thus, the heat transfer rate was calculated depending on temperature change of cooling water. Moreover, this correlation was proposed to micro-fin tube ($D_h=0.8$ mm), and their test conditions were not specified.

5.4.4 Bandhauer et al. (2006)

The main difference between the test facilities is the presence of a precondenser before the test section, in the Bandhauer et al. (2006) study. The precondenser is used to achieve low vapor qualities. Although the main objective of Bandhauer et al. (2006) is to analyze the hydraulic diameter influence on heat transfer coefficient, both studies concluded that the heat transfer coefficient increases with an increase in mass flux and vapor quality.

5.4.5 Wang et al. (2002)

Wang et al. (2002) studied the heat transfer for R134a condensing inside a horizontal rectangular multi-port aluminum condenser tube with 1.46-mm hydraulic diameter. Although the channels in the present study are circular, they have the same hydraulic diameter. In this study, the R134a inlet pressure ranged from 7 to 9 bar, while Wang et al.'s (2002) ranged from 18 to 19.3 bar. Even though the main goal of Wang et al.'s (2002) work was to analyze the flow pattern, a few conclusions can be compared to the present study. Increasing the mass flux results in higher h values. As the mass flux increases, an annular film forms and forced convection prevails.

5.4.1 Goss (2011a)

Regarding the heat transfer results, both studies concluded that increasing mass flux and vapor quality causes an increase on h , and no clear influence of the fluid saturation temperature and the heat flux on h was noted. For pressure drop results, the conclusions were also the same, increasing mass flux and reducing the fluid saturation temperature causes an increase on Δp . On the other hand, the heat flux did not show influence on Δp .

Table 16: Summary of the compared studies to the present study

Author	Parameter	Orientation	Dh [mm]	L [m]	Tsat [°C]	G [kg/(m ² s)]	x
Yan and Lin (1999)	PD, HTC	H, MP, C	2.0	0.2 m	25-50	100-200	-
Zhang and Webb (2001)	PD	H, MP, C	2.13	0.56	20-65	2-001-000	0.20-0.89
Koyama et al. (2003a)	PD, HTC	H, MP, R	1.11	0.6	60	100-700	0.0-1.0
Koyama et al. (2003a)	PD, HTC	-	0.8	-	-	-	-
Bandhauer et al. (2006)	HTC	H, MP, C	0.5; 0.76; 1.52	0.3	-	150-750	0.0-1.0
Wang et al. (2002)	HTC	H, MP, R	1.46	-	61.5-66	75-750	-
Goss et al. (2011, 2015)	PD, HTC	H, MP, C	0.77	0.105	28-38	230-445	0.55-1.0
Present study	PD, HTC	H, MP, C	1.46	0.102	26-36	391-542	0.89-1.0

PD: Pressure Drop; HTC: Heat Transfer Coefficient; Dh: Hydraulic Diameter; L: Length; Tsat: Saturation Temperature; G: Mass Flux; x: Vapor Quality

6 CONCLUSIONS AND RECOMMENDATIONS

In this study, experimental results obtained for the heat transfer coefficient and pressure drop during condensation of R134a inside seven round horizontal and parallel minichannels, with hydraulic diameter of 1.46-mm, were presented. The test conditions included pressure, vapor quality, heat flux, and mass flux, ranging from 7.4 to 9.1 bar, 0.89 to 1, 8.2 to 10.8 kW/m², and 391 to 542 kg/(m²s), respectively. The following conclusions can be drawn from this study.

The test conditions are equivalent to those predicted by the annular-mist and mist flow patterns, according to Coleman and Garimella (2003) map. Mist flow is characterized by the liquid phase flowing as entrained droplets without any visible liquid film at the wall, whereas annular-mist flow is defined for most of the liquid flowing along the wall of the tube, and vapor with entrained mist flowing in the central core. Those flow patterns are distinguished by high mass flux and vapor quality values. Most heat transfer correlations proposed for shear-driven condensation consider the annular regime over most of the passage length. Nevertheless, Cavallini et al. (2006c) introduced a correlation considering the effect of entrainment rate of droplets from the liquid film, and it showed the best agreement with the experimental data. As expected, correlations proposed for conventional diameters channels showed the worse results, corroborating the fact that these formulations do not predict well heat transfer in minichannels.

A clear influence of mass flux and vapor quality on heat transfer coefficient was noted. The heat transfer coefficient increases with the increase of both mass flux and vapor quality. On the other hand, there is no evident influence of heat flux on heat transfer coefficient for the range tested. In addition, higher saturation temperatures present greater heat transfer coefficients for high vapor qualities. This influence decays as condensation occurs.

Regarding pressure drop results, expansion, contraction and friction contributions were calculated. The two-phase frictional pressure drop corresponds roughly to 92% of the net pressure drop. Pressure drop presented higher values with increasing mass velocity and decreasing saturation temperature. Moreover, it was not significantly affected by heat flux. The classical correlations proposed for conventional channels predicted the pressure drop reasonably. The model presented by Garimella et al. (2005), for minichannels, achieved the best prediction accuracy.

The recommendations for the next studies are:

- Tilt the test section in order to study gravity influence on condensation;
- Test different minichannel cross-sections in order to study superficial tension effect on the heat transfer coefficient and pressure drop;
- Extend the vapor quality range tested;
- Use hydrophobic material to cover the superficies in order to achieve the droplet condensation;
- Obtain the heat transfer coefficients in the upper and lower test section faces independently;
- Develop a model to determine the liquid film thickness on the channel bottom surface.

Other suggestions concerning the test rig are presented in Appendix C.

7 BIBLIOGRAPHY

AGARWAL, A.; BANDHAUER, T.M.; GARIMELLA, S. Measurement and modeling of condensation heat transfer in non-circular microchannels. *Int. J. Refrig.*, v. 33, n. 6, p. 1169–1179, 2010.

AGARWAL, A.; GARIMELLA, S. Modeling of Pressure Drop during Condensation in Circular and Noncircular Microchannels. *ASME Journal of Fluids Engineering*, v. 131, n. 1, Article No. (011302), 2009.

AGARWAL, A.; GARIMELLA, S. Representative Results for Condensation Measurements at Hydraulic Diameters ~100 Microns. *ASME Journal of Heat Transfer*, v. 132, n. 4, Article No. (041010), 2010.

AKERS, W.W.; DEANS, H. A.; CROSSER, O. K. Condensation heat transfer within horizontal tubes. *Chem. Eng. Prog. Symp. Series*, v. 55, n. 29, p. 171–176, 1959.

ALSHQIRATE, A. A. Z. S.; TARAWNEH, M.; HAMMAD, M. Dimensional Analysis and Empirical Correlations for Heat Transfer and Pressure Drop in Condensation and Evaporation Processes of Flow inside Micropipes: Case Study with Carbon Dioxide (CO₂). *Journal of the Brazilian Society of Mechanical Sciences and Engineering*, v. 34, n. 1, p. 89-96, 2012.

ANDERSON, T.M.; MUDAWAR, I. Microelectronic cooling by enhanced pool boiling of a dielectric fluorocarbon liquid. *J. Heat Transfer*, v. 111, n. 3, p. 752–759, 1989.

ANNAIEV, E.P.; BOYKO, L.D.; KRUSHILIN, G.N. Heat transfer in the presence of steam condensation in a horizontal tube. *Proc. 1st Int. Heat Transfer Conf.*, part II, p. 290, 1961.

BAIRD, J.R.; FLETCHER, D.F.; HAYNES, B.S. Local condensation heat transfer rates in fine passages. *Int. J. Heat Mass Transfer*, v. 46, n. 23, p. 4453-4466, 2003.

BANDHAUER, T.M.; AGARWAL, A.; GARIMELLA, S. Measurement and modeling of condensation heat transfer coefficients in circular microchannels. *J. Heat Transfer*, v. 128, n.10, p. 1050-1059, 2006.

BARNEA D.; LUNINSKI Y.; TAITEL Y. Flow pattern in horizontal and vertical two phase flow in small diameter pipes. *Can. J. Chem. Eng.*, v. 61, p. 617-620, 1983.

BAROCZY, C. J. Correlation of liquid fraction in two-phase flow with applications to liquid metals, *Chem. Eng. Prog. Symp. Series*, v. 61, n. 57, p. 179–191, 1965.

BEJAN, A. *Convection heat transfer*. 3rd ed. New Jersey, USA: John Wiley & Sons, 2004.

BLANGETTI, F.; SCHLUNDER, E.O. Local heat transfer coefficients of condensation in a vertical tube. *Proc. 6th Int. Heat Transfer Conf.*, v. 2, p. 437–442, 1978.

BLASIUS, H. Das Aehnlichkeitsgesetz bei Reibungsvorgängen in Flüssigkeiten. *Verein deutscher Ingenieure, Mitteilungen über Forschungsarbeiten auf dem Gebiete des Ingenieurwesens*. Springer-Verlag Berlin Heidelberg, 1913.

BOHDAL, T.; CHARUN, H.; SIKORA, M. Pressure drop during the condensation of R134a refrigerant in pipe minichannels. *Proceedings of 6th International Conference on Transport Phenomena in Multiphase Systems*, (Poniewski, M. E.; Alabrudziński S. (Eds.)), p. 233–240, June 28–July 02, 2011, Ryn, Poland, 2011a.

BOHDAL, T.; CHARUN, H.; SIKORA, M. Comparative Investigations of the Condensation of R134a and R404A Refrigerants in Pipe Minichannels. *International Journal of Heat and Mass Transfer*, v. 54, n. 9–10, p. 1963–1974, 2011b.

BOHDAL, T.; CHARUN, H.; SIKORA, M. Pressure Drop During Condensation of Refrigerants in Pipe Minichannels. *Archives of Thermodynamics*, v. 33, n. 1, p. 87–106, 2012.

BONTEMPS, A. Measurements of single-phase pressure drop and heat transfer coefficient in micro and minichannels. In: AL., S. K. (Ed.). *Microscale heat transfer - fundamentals and applications*. 1st ed. The Netherlands: Springer, 2005.

BORTOLIN, S.; DA RIVA, E.; DEL COL, D. Condensation in a square minichannel: application of the VOF method. *Heat Transfer Eng.*, v. 35, n. 2, p. 193–203, 2014.

BOYKO, L.D.; KRUSHILIN, G.N. Heat transfer and hydraulic resistance during condensation of steam in a horizontal tube and in a bundle of tubes. *Int. J. Heat Mass Transfer*, v. 10, p. 361–373, 1967.

BREBER, G., PALEN, J. W.; TABOREK, J. Prediction of horizontal tube side condensation of pure components using flow regime criteria, *J. Heat Trans., Transac. ASME*, v. 102, n. 3, p. 471–476, 1980.

BUTTERWORTH, D. A comparison of some void-fraction relationships for co-current gas–liquid flow. *Int. J. Multiphase Flow*, v. 1, n. 6, p. 845–850, 1975.

CARCIOFI, B.; GUTHS, S.; LAURINDO, J.B. Uso de transdutores de fluxo de calor no estudo da transferência de calor em alimentos embalados. *Ciêñ. Tecnol. Alimet.*, Campinas, v. 22, n. 3, p. 314–318, 2002.

CAREY, V. P. *Liquid-Vapor Phase-Change Phenomena*. 1a. ed. New York, NY: Hemisphere Publishing Corporation, 1992.

CARPENTER, F. G.; COLBURN, A. P. The effect of vapor velocity on condensation inside tubes. *Proc. General Discussion of Heat Transfer. IMech/ASME*, p. 20–26, 1951.

CAVALLINI, A.; ZECCHIN, R. A dimensionless correlation for heat transfer in forced convection condensation. *Proc. 5th Int. Heat Transfer Conf.*, v. 3, p. 309–313, Tokyo, Japan, 1974.

CAVALLINI, A.; CENSI, G.; DEL COL, D.; DORETTI, L.; LONGO, G. A.; ROSSETTO, L. Experimental investigation on condensation heat transfer and pressure drop of new HFC refrigerants (R134a, R125, R32, R410A, R236ea) in a horizontal smooth tube. *Int. J. Refrig.*, v. 24, n. 1, p. 73–87, 2001.

CAVALLINI, A.; CENSI, G.; DEL COL, D.; DORETTI, L.; LONGO, G. A.; ROSSETTO, L. Condensation of halogenated refrigerants inside smooth tubes. *HVAC and Research*, v. 8, n. 4, p. 429–451, 2002.

CAVALLINI, A.; DEL COL, D.; DORETTI, L.; MATKOVIC, M.; ROSSETTO, L.; ZILIO, C. Condensation heat transfer and pressure gradient inside multiport minichannels, *Heat Trans. Eng.*, v. 26, n. 3, p. 45–55, 2005.

CAVALLINI, A.; DEL COL, D.; DORETTI, L.; MATKOVIC, M.; ROSSETTO, L.; ZILIO, C.; CENSI, G. Condensation in horizontal smooth tubes: a new heat transfer model for heat exchanger design. *Heat Transfer Eng.*, v. 27, n. 8, p. 31–38, 2006a.

CAVALLINI, A.; DORETTI, L.; MATKOVIC, M.; ROSSETTO, L. Update on condensation heat transfer and pressure drop inside minichannels. *Heat Transfer Eng.*, v. 27, n. 4, p. 74–87, 2006b.

CAVALLINI, A.; DEL COL, D.; DORETTI, L.; MATKOVIC, M.; ROSSETTO, L.; ZILIO, C. A Model for Condensation Inside Minichannels. *Proceedings of the HT05 National Heat Transfer Conference, Papel No. H*, July 17-22, San Francisco, California, U.S.A, 2006c.

CAVALLINI, A.; DEL COL, D.; MATKOVIC, M.; ROSSETTO, L. Frictional Pressure Drop during Vapour-Liquid Flow in Minichannels: Modelling and Experimental Evaluation. *International Journal of Heat and Fluid Flow*, v. 30, n. 1, p. 131-139, 2009a.

CAVALLINI, A.; DEL COL, D.; MATKOVIC, M.; ROSSETTO, L. Pressure Drop during Two-Phase Flow of R134a and R32 in a Single Minichannel. *ASME Journal of Heat Transfer*, v. 131, n. 3, Article No. (033107), 2009b.

CHARUN, H. Thermal and Flow Characteristics of the condensation of R404A Refrigerant in Pipe Minichannels. *International Journal of Heat and Mass Transfer*, v. 55, n. 9-10, p. 2692-2701, 2012.

CHATO, J. C. Laminar condensation inside horizontal and inclined tubes. *ASHRAE J.*, v. 4, n. 2, p. 52-60, 1962.

CHEN, I.Y.; YANG, K.S.; CHANG, Y.J.; WANG, C.C. Two-phase pressure drop of air-water and R-410A in small horizontal tubes. *Int. J. Multiphase Flow*, n. 27, p. 1293-1299, 2001.

CHEN, Q.; AMANO, R. S.; XIN, M. Experimental Study of Flow Patterns and Regimes of Condensation in Horizontal Three-Dimensional Micro-Fin-Tubes. *IEEE Commun. Mag.*, v. 43, p. 201-206, 2006.

CHEN, S.L.; GERNER, F.M.; TIEN, C.L. General film condensation correlations. *Exp. Heat Transfer*, v. 1, p. 93-107, 1987.

CHEN, Y.; CHENG, P. Condensation of Steam in Silicon Microchannels. *Int. Commun. Heat Mass Transfer*, v. 32, p. 175-183, 2005.

CHENG, L.; MEWES, D. Review of two-phase flow and flow boiling of mixtures in small and mini channels. *Int. J. Multiphase Flow*, v. 32, n. 2, p. 183-207, 2006.

CHENG, L.; VAN DER GELD, C. W. M. Experimental Study of Heat Transfer and Pressure Drop Characteristics of Air/Water and Air-Steam/Water Heat Exchange in a Polymer Compact Heat Exchanger. *Heat Transfer Eng.*, v. 26, n. 2, p. 18-27, 2005.

CHENG, L.; VAN DER GELD, C. W. M.; LEXMOND, A. S. Study and Visualization of Droplet Entrainment From a Polymer Compact Heat Exchanger. *Int. J. Heat Exchangers*, v. 5, p. 359–378, 2004.

CHENG, P.; WU, H.Y.; HONG, F.J. Phase-change heat transfer in microsystems. *J. Heat Transfer*, v. 129, n. 2, p. 101–108, 2007.

CHISHOLM, D. Pressure gradients due to friction during the flow of evaporating two-phase mixtures in smooth tubes and channels. *Int. J. Heat Mass Transfer*, v. 16, p. 347–358, 1973.

CHISHOLM, D.; LAIRD, A. D. K. Two-Phase Flow in Rough Tubes. *Trans. ASME*, v. 80, n. 2, p. 227-286, 1958.

CHOWDHURY, S.; AL-HAJRI, E.; DESSIATOUN, S.; SHOOSHARI, A.; OHADI, M. An experimental study of condensation heat transfer and pressure drop in a single high aspect ratio micro-channel for refrigerant R134a. *Proceedings of the 4th International Conference on Nanochannels, Microchannels and Minichannels (ICNMM2006)*, v. A, p. 147-154, ICNMM2006-96211, June 19-21, Limerick, Ireland, 2006.

CHUN, K.R.; SEBAN, R.A. Heat transfer to evaporating liquid films. *J. Heat Transfer*, v. 93, p. 391-396, 1971.

CHUNG, P. M. Y.; KAWAJI, M. The effect of channel diameter on adiabatic two-phase flow characteristics in microchannels. *International Journal of Multiphase Flow*, v. 30, n. 7-8, p. 735-761, 2004.

CHURCHILL, S.W.; USAGI, R. A general expression for the correlation of rates of transfer and other phenomena. *AIChE Journal*, v. 18, p. 1121-1128, 1972.

CICCHITTI, A.; LOMBARDI, C; SILVESTRI, M.; SOLDAINI, G.; ZAVATTAREILI, R. Two-phase cooling experiments-pressure drop, heat transfer and burnout measurements. *Energia Nucleare*, v. 7, n. 6, p. 407-425, 1960.

COLEMAN, J. W.; GARIMELLA, S. Characterization of two-phase flow patterns in small diameter round and rectangular tubes. *International Journal of Heat and Mass Transfer*, v. 42, n. 15, p. 2869-2881, 1999.

COLEMAN, J.W.; GARIMELLA, S. Two-phase flow regimes in round, square and rectangular tubes during condensation of Refrigerant R134a. *International Journal of Refrigeration*, v. 26, n. 1, p. 117–128, 2003.

COLLIER, J. G.; THOME, J. R. *Convective boiling and condensation*. 3rd ed. New York: Clarendon Press -Oxford, 1994.

DA RIVA, E.; BORTOLIN, S.; DEL COL, D. Condensation in a micro-channel: application of the VOF (Volume of Fluid) method. *3rd Micro and Nano Flows Conference*. Thessaloniki, Greece, 22–24 August, 2011.

DA RIVA, E.; DEL COL, D.; GARIMELLA, S.V.; CAVALLINI, A. The importance of turbulence during condensation in a horizontal circular minichannel. *Int. J. Heat Mass Transf.*, v. 55, n. 13–14, p. 3470–3481, 2012.

DARIO E.R.; TADRIST, L.; PASSOS, J.C. Review on two-phase flow distribution in parallel channels with macro and micro hydraulic diameters: Main results, analyses, trends. *Applied Thermal Engineering*, v. 59, p. 316–335, 2013.

DITTUS, P. W.; BOELTER, L. M. K. Univ. Calif. Pub. Eng., Vol. 2, No. 13, p. 443-461, 1930, reprinted in *Int. Comm. Heat Mass Transfer*, v. 12, p. 3-22, 1985.

DOBSON, M. K.; CHATO, J. C.; HINDE, D. K.; WANG, S. P. Experimental evaluation of internal condensation of refrigerants R-12 and R134a. *Proceedings of the ASHRAE Winter Meeting*, January 23–26 1994, New Orleans, LA, USA, ASHRAE, Atlanta, GA, USA, p. 744–754, 1994.

DOBSON, M.K.; CHATO, J.C. Condensation in smooth horizontal tubes. *J. Heat Transfer*, v. 120, n. 1, p. 193–213, 1998.

DOBSON, M.K.; CHATO, J.C.; WANG, S.P.; HINDE, D.K.; GAIBEL, J.A. Initial Condensation Comparison of R-22 with R134a and R-32/R-125. *Air Conditioning and Refrigeration Center*, College of Engineering, University of Illinois at Urbana–Champaign, 1993.

DOBSON, M.K.; CHATO, J.C.; WATTELET, J.P.; WATTELET, J.A.; PONCHNER, M.; KENNEY, P.J. Heat Transfer and flow Regimes during Condensation in Horizontal Tubes. *Air Conditioning and Refrigeration Center*, College of Engineering, University of Illinois at Urbana–Champaign, 1994.

DUKLER, A. E. Fluid mechanics and heat transfer in vertical falling film systems. *Chem. Eng. Prog. Symp. Series*, v. 56, n. 30, p. 1–10, 1960.

- DUKLER, A. E.; WICKS, M.; CLEVELAND, R. G. Pressure drop and hold-up in two-phase flow Part A-A comparison of existing correlations and Part B-An approach through similarity analysis. *AIChE Journal*, v. 10, n. 1, p. 38-51, 1964.
- EL ACHKAR, G.; LAVIEILLE, P.; MISCEVIC, M. Loop heat pipe and capillary pumped loop design: about heat transfer in the isolated bubbles zone of condensers. *Appl. Therm. Eng.*, v. 33-34, p. 253-257, 2012.
- EL HAJAL, J.; THOME, J. R.; CAVALLINI, A. Condensation in Horizontal Tubes, Part 1: Two-Phase Flow Pattern Map. *Int. J. Heat Mass Transfer*, v. 46, p. 3349–3363, 2003a.
- EL HAJAL, J.; THOME, J. R.; CAVALLINI, A. Condensation in Horizontal Tubes, Part 2: New Heat Transfer Model Based on Flow Regimes. *Int. J. Heat Mass Transfer*, v. 46, p. 3365–3387, 2003b.
- ERBIL, H. Y.; MC HALE, G.; ROWAN, S. M.; NEWTON, M. I. Determination of the receding contact angle of sessile drops on polymer surfaces by evaporation. *Langmuir*, v. 15, n. 21, p. 7378-7385, 1999.
- EUCKEN, A. *Naturwissenschaften*. v. 25, p. 209, 1937.
- FANG, X.; ZHOU, Z.; LI, D. Review of correlations of flow boiling heat transfer coefficients for carbon dioxide. *Int. J. Refrigeration*, v.36, n. 8, p. 2017–2039, 2013.
- FELCAR, H. O. M.; RIBATSKI, G.; JABARDO, J. M. S. A gas-liquid flow pattern predictive method for macro and mini-scale round channels. In: *Proceedings of the 10th UK Heat Transfer Conference*. Edinburgh, UK: [s.n.], 2007.
- FERRASSE, S.; SEGAL, V. M.; HARTWIG, K. T.; GOFORTH, R. E. Microstructure and Properties of Copper and Aluminum Alloy 3003 Heavily Worked by Equal Channel Angular Extrusion. *Metallurgical And Materials Transactions A*, v. 28a, p. 1047, 1997.
- FRIEDEL, L. Improved Friction Pressure Drop Correlations for Horizontal and Vertical Two Phase Pipe Flow (Paper E2). *European Two Phase Flow Group Meeting*, Ispra, Italy, 1979.
- FRONK, B. M.; GARIMELLA, S. Measurement of heat transfer and pressure drop during condensation of carbon dioxide in microscale geometries. *Proceedings of 2010 14th International Heat Transfer Conference (IHTC14)*, IHTC14-22987, v. 2/Condensation, p. 235-243, August 8-13, 2010, Washington, DC, USA, 2010.

FRONK, B. M.; GARIMELLA, S. Heat transfer and pressure drop during condensation of ammonia in microchannels. *ASME 3rd Micro/Nanoscale Heat and Mass Transfer International Conference (MNHMT2012)*, Track 4: Nano/Microscale Boiling and Condensation Heat Transfer, Session: 4-4 Two-Phase Flow and Phase-Change Heat Transfer in Microchannels, MNHMT2012-75265, March 3-6, 2012, Atlanta, GA, 2012.

FUKANO, T.; KARIYASAKI, A. Characteristics of Gas-Liquid Two-Phase Flow in a Capillary Tube. *Nuclear Engineering and Design*, v. 141, n. 1-2, p. 59–68, 1993.

GANAPATHY, H.; SHOOSHTARI, A.; CHOO, K.; DESSIATOUN, S.; ALSHEHHI, M.; OHADI, M. Volume of Fluid-Based Numerical Modeling of Condensation Heat Transfer and Fluid Flow Characteristics in Microchannels. *International Journal of Heat and Mass Transfer*, v. 65, p. 62-72, 2013.

GANZELES, F. L. A. Drainage and condensate heat resistance in dropwise condensation of multicomponent mixtures in a plastic plate heat exchanger. PhD Thesis - Technische Universiteit Eindhoven, 2002.

GARIMELLA, S. Condensation Flow Mechanisms in Microchannels: Basis for Pressure Drop and Heat Transfer Models. *Heat Transfer Engineering*; v. 25, n. 3, p. 104-116, 2004.

GARIMELLA, S. Condensation in minichannels and microchannels. In: KANDLIKAR, S. et al. (Ed.). *Heat transfer and fluid flow in minichannels and microchannels*. 1st ed. Oxford, UK: Elsevier Publications, 2006.

GARIMELLA, S.; AGARWAL, A.; COLEMAN, J. W. Two-phase pressure drops in the annular flow regime in circular microchannels. *21st IIR International Congress of Refrigeration*. Washington, DC, International Institute of Refrigeration, 2003a.

GARIMELLA, S.; AGARWAL, A.; FRONK, B.M. The intermittent and annular flow condensation continuum: Pressure drops at the microscale. *International Journal of Multiphase Flow*, v. 84, p. 129–144, 2016.

GARIMELLA, S.; AGARWAL, A.; JESSE, D.K. Condensation pressure drop in circular microchannels. *Heat Transfer Eng.*, v. 26, n. 3, p. 28-35, 2005.

GARIMELLA, S.; BANDHAUER, T. M. Measurement of condensation heat transfer coefficients in microchannel tubes, *ASME International Mechanical Engineering Congress and Exposition*, New York, NY, American Society of Mechanical Engineers, p. 243–249, 2001.

GARIMELLA, S.; FRONK, B. M. Single- and Multi-Constituent Condensation of Fluids and Mixtures with Varying Properties in Micro-Channels. *Special Issue: ECI Eighth International Conference on Boiling and Condensation Heat Transfer*, June 3-7, 2012, Ecole Polytechnique Fédérale de Lausanne (EPFL), Lausanne, Switzerland, v. 26, n. 2-3, p. 129-168, 2013.

GARIMELLA, S.; FRONK, B.M.; MILKIE, J.A.; KEINATH, B.L. Versatile models for condensation of fluids with widely varying properties from the micro to macroscale. *Proceedings of the 15th International Heat Transfer Conference*, IHTC-15, August 10–15, Kyoto, Japan. IHTC15-10516, 2014.

GARIMELLA, S.; KILLION, J. D.; COLEMAN, J.W. An experimentally validated model for two-phase pressure drop in the intermittent flow regime for circular microchannels. *J. Fluid. Eng.*, v. 124, n. 1, p. 205–214, 2002.

GARIMELLA, S.; KILLION, J. D.; COLEMAN, J.W. An experimentally validated model for two-phase pressure drop in the intermittent flow regime for noncircular microchannels. *J. Fluid. Eng.*, v. 125, n. 5, p. 887–894, 2003b.

GEIGER, G. E.; ROHRER, W. M. Sudden contraction losses in two-phase flow. *J. Heat Transfer*, v. 88, n.1, p. 1-8, 1966.

GHIAASIAAN, S. M. *Two-Phase Flow, Boiling, and Condensation*. 1st ed. New York, NY: Cambridge University Press, 2008.

GNIELINSKI, V. New equations for heat and mass transfer in turbulent pipe and channel flow. *Ind. Eng. Chem.*, v. 16, p. 359-368, 1976.

GOSS, G. J. Transferência de calor e queda de pressão durante a condensação convectiva do R134a em microcanais paralelos, *Master Thesis*, UFSC, 2011a.

GOSS JR., G.; MACARINI, S. F.; PASSOS, J. C. Heat transfer and pressure drop during condensation of R134A inside parallel microchannels. *Proceedings of ASME/JSME 2011 8th Thermal Engineering Joint*

Conference (AJTEC 2011), AJTEC2011-44551, March 13-17, 2011, Honolulu, Hawaii, USA, 2011b.

GOSS JR, G.; PASSOS, J.C. Heat transfer during the condensation of R134a inside eight parallel microchannels. *International Journal of Heat and Mass Transfer*, v. 59, p. 9-19, 2013.

GOSS JR., G.; OLIVEIRA, J. L. G.; PASSOS, J. C. Pressure Drop During Condensation of R134a inside Parallel Microchannels. *International Journal of Refrigeration*, v. 56, p. 114-125, 2015.

GREGORIG, R. Film condensation on finely rippled surfaces with consideration of surface tension, *Z. Angewa. Mathe. Phys.*, v. 5, p. 36-49, 1954.

HARAGUCHI, H.; KOYAMA, S.; FUJII, T. Condensation of refrigerants HCFC22, HFC134a and HCFC123 in a horizontal smooth tube (1st report, proposal of empirical expressions for the local frictional pressure drop), *Transac. JSME (B)*, v. 60, n. 574, p. 239-244, 1994a.

HARAGUCHI, H.; KOYAMA, S.; FUJII, T. Condensation of refrigerants HCFC22, HFC134a and HCFC123 in a horizontal smooth tube (2nd report, proposal of empirical expressions for the local frictional pressure drop), *Transac. JSME (B)*, v. 60, n. 574, p. 245-252, 1994b.

HARIRCHIAN, T.; GARIMELLA, S.V. A comprehensive flow regime map for microchannel flow boiling with quantitative transition criteria. *Int. J. Heat Mass Transfer*, v. 53, n. 13-14, p. 2694-2702, 2010.

HAUI, X.; KOYAMA, S. An Experimental Study of Carbon Dioxide Condensation in Mini Channels. *Journal of Thermal Science*, v. 13, n. 4, p. 358-365, 2004.

HEO, J.; PARK, H.; YUN, R. Condensation Heat Transfer and Pressure Drop Characteristics of CO₂ in a Microchannel. *International Journal of Refrigeration*, v. 36, n. 6, p. 1657-1668, 2013a.

HEO, J.; PARK, H.; YUN, R. Comparison of Condensation Heat Transfer and Pressure Drop of CO₂ in Rectangular Microchannels. *International Journal of Heat and Mass Transfer*, v. 65, p. 719-726, 2013b.

HETSRONI, G. *Handbook of Multiphase Systems*. New York: Hemisphere, 1982.

HEWITT, G. F.; ROBERTS, D. N. *Studies of Two-Phase Flow Patterns by Simultaneous Flash and X-Ray Photography*. Chemical Engineering

Division, Atomic Energy Research Establishment, Harwell, Berkshire, U.K., 1969.

HEWITT, G. F.; SHIRES, G. L.; BOTT, T. R. *Process Heat Transfer*. Boca Raton: CRC Press; Begell House, 1994.

HUANG, X.; DING, G.; HU, H.; ZHU, Y.; PENG, H.; GAO, Y.; DENG, B. Influence of oil on flow condensation heat transfer of R410A inside 4.18 mm and 1.6 mm inner diameter horizontal smooth tubes. *Int. J. Refrig.*, v. 33, n. 1, p. 158–169, 2010.

IDELCHIK, I. E. *Handbook of hydraulic resistance*. 3rd. ed. Florida, USA: CRC Press, 1994.

ILLÁN-GÓMEZ, F.; LÓPEZ-BELCHÍ, A.; GARCÍA-CASCALES, J. R.; VERA-GARCÍA, F. Experimental Two-Phase Heat Transfer Coefficient and Frictional Pressure Drop inside Mini-Channels during Condensation with R1234yf and R134a. *International Journal of Refrigeration*, v. 51, p. 12-23, 2015.

INCROPERA, F.P.; DEWITT, D.P.; BERGMAN, T.L.; LAVINE, A.S. *Fundamentals of Heat and Mass Transfer*. 6th Edition, New Jersey, USA. *John Wiley & Sons*, 2007.

JAKOB, M. *Mech. Eng.*, vol. 58, p. 729, 1936

JASTER, H.; KOSKY, P.G. Condensation in a mixed flow regime. *Int. J. Heat Mass Transfer*, v. 19, p. 95-99, 1976.

JOHNS, M.E.; MUDAWAR, I. An ultra-high power two-phase jet-impingement avionic clamshell module. *J. Electron. Packag.*, v. 118, n. 4, p. 264–270, 1996.

KAKAC, S.; VASILIEV, L. L.; BAYAZITOGU, Y.; YENER, Y. (Eds.). *Microscale Heat Transfer- Fundamental and Applications*. The Netherlands: Kluwer Academic Publishers, p. 273-290, 2005.

KANDLIKAR, S.G. A roadmap for implementing minichannels in refrigeration and air-conditioning systems – current status and future directions. *Heat Transfer Engineering*, v. 28, n. 12, p. 973–985, 2007.

KANDLIKAR, S. G. Scale effects on flow boiling heat transfer in microchannels: a fundamental perspective. *International Journal of Thermal Sciences*, v. 49, n. 7, p. 705 -715, 2010.

KANDLIKAR, S. G.; GRANDE, W. M. Evolution of Microchannel Flow Passages—Thermohydraulic Performance and Fabrication Technology. *Heat Transfer Engineering*, v. 24, n. 1, p. 3–17, 2003.

KANDLIKAR, S. G.; KUAN, W. K.; WILLISTEIN, D. A.; BORRELLI, J. Experimental Evaluation of Pressure Drop Elements and Fabricated Nucleation Sites for Stabilizing Flow Boiling in Minichannels and Microchannels. *Journal of Heat Transfer*, v. 128, n. 4, p. 389–396, 2006.

KATTAN, N.; THOME, J.R.; FAVRAT, D. Flow boiling in horizontal tubes: Part 1 e development of a diabatic two-phase flow pattern map. *J. Heat Transfer*, v. 120, n.1, p. 140-147. 1998a

KATTAN, N.; THOME, J.R.; FAVRAT, D. Flow boiling in horizontal tubes: Part 2 e new heat transfer data for five refrigerants. *J. Heat Transfer*, v. 120, n. 1, p. 148-155, 1998b.

KATTAN, N.; THOME, J.R.; FAVRAT, D. Flow boiling in horizontal tubes: Part 3 e development of a new heat transfer model based on flow pattern. *J. Heat Transfer*, v. 120, n. 1, p. 156-165, 1998c.

KATTO, Y.; KUNIHIRO, M. Study of the mechanism of burn-out in boiling system of high burn-out heat flux, *Bull. JSME*, v. 16, n. 99, p. 1357–1366, 1973.

KAWAHARA, A.; SADATOMI, M.; OKAYAMA, K.; KAWAJI, M.; CHUNG, P. M.-Y. Effects of Channel Diameter and Liquid Properties on Void Fraction in Adiabatic Two-Phase Flow through Microchannels. *Heat Transfer Engineering*, v. 26, n. 3, p. 13–19, 2005.

KEINATH, B. L.; GARIMELLA, S. Bubble and film dynamics during condensation of refrigerants in minichannels. *Proceedings of 2010 14th International Heat Transfer Conference (IHTC14)*, IHTC14-22697, v. 2/Condensation, p. 177-186, August 8-13, 2010, Washington, DC, USA, 2010.

KEINATH, B. L.; GARIMELLA, S. Void fraction and pressure drop during condensation of refrigerants in minichannels. *6th International Berlin Workshop on Transport Phenomena with Moving Boundaries*, Berlin, Germany, 2011.

KEW, P.A.; CORNWELL, K. Correlations for the prediction of boiling heat transfer in small-diameter channels. *Appl. Therm. Eng.*, v. 17, n. 8-10, p. 705–715, 1997.

- KHANDEKAR, S.; PANIGRAHI, P.K.; LEFEVRE, F.; BONJOUR, J. Local Hydrodynamics of Flow in a Pulsating Heat Pipe: A Review. *Frontiers in Heat Pipes 1*, 023003, 2010.
- KHANIKAAR, V.; MUDAWAR, I.; FISHER, T. Effects of carbon nanotube coating on flow boiling in a micro-channel. *Int. J. Heat Mass Transfer*, v. 52, n. 15-16, p. 3805–3817, 2009.
- KIM, N.H.; SHIN, J.S.; HUH, C.; KIM, T.J.; SEO, K.W. A Study of Condensation Heat Transfer in a Single Mini-Tube and a Review of Korean Micro-and Mini-Channel Studies. *Paper Presented at the ASME 1st International Conference on Microchannels and Minichannels*, Rochester, New York, USA, 2003a.
- KIM, N.H.; CHO, J.P.; KIM, J.O.; YOUNG, B. Condensation heat transfer of R-22 and R-410A in flat aluminum multi-channel tubes with or without micro-fins. *Int. J. Refrigeration*, v. 26, n. 7, p. 830-839, 2003b.
- KIM, S. M.; MUDAWAR, I. Theoretical Model for Annular Flow Condensation in Rectangular Micro-Channels. *International Journal of Heat and Mass Transfer*, v. 55, n. 4, p. 958-970, 2012a.
- KIM, S. M.; KIM, J.; MUDAWAR, I. Flow Condensation in Parallel Micro-Channels - Part 1: Experimental Results and Assessment of Pressure Drop Correlations. *International Journal of Heat and Mass Transfer*, v. 55, n. 4, p. 971-983, 2012b.
- KIM, S.; MUDAWAR, I. Universal approach to predicting heat transfer coefficient for condensing mini/micro-channel flow. *Int. J. Heat Mass Transf.*, v. 56, n. 1–2, p. 238–250, 2013.
- KIM, S.M.; MUDAWAR, I. Review of Databases and Predictive Methods for Pressure Drop in Adiabatic, Condensing and Boiling Mini/Micro-Channel Flows. *International Journal of Heat and Mass Transfer*, v. 77, p. 74-97, 2014.
- KITTO JR., J.B.; ROBERTSON, J.M. Effects of maldistribution of flow on heat transfer equipment performance. *Heat Transfer Engineering*, v. 10, p. 18–25, 1988.
- KOSKY, P. G. Thin liquid films under simultaneous shear and gravity forces. *Int. J. Heat Mass Trans.*, v. 14, n. 8, p. 1220–1224, 1971.

KOSKY, P. G.; STAUB, F.W. Local condensing heat transfer coefficients in the annular flow regime. *AIChE J.*, v. 17, n. 5, p. 1037–1043, 1971.

KOYAMA, S., KUWAHARA, K., NAKASHITA, K. Condensation of refrigerant in a multi-port channel. *First Int. Conf. On Microchannels and Minichannels*, Rochester, NY, USA, pp. 193–205, 2003a.

KOYAMA, S.; KUWAHARA, K.; NAKASHITA, K.; YAMAMOTO, K. An experimental study on condensation of refrigerant R134a in a multi-port extruded tube. *Int. J. Refrigeration*, v. 26, n. 4, p. 425–432, 2003b.

KUO, C. Y.; PAN, C. The Effect of Cross-Section Design of Rectangular Microchannels on Convective Steam Condensation. *Journal of Micromechanics and Microengineering*, v. 19, n. 3, Article No. (035017), 2010a.

KUO, C. Y.; PAN, C. Two-Phase Flow Pressure Drop and Heat Transfer during Condensation in Microchannels with Uniform and Converging Cross-Sections. *Journal of Micromechanics and Microengineering*, v. 20, n. 9, Article No. (095001), 2010b.

KUTATELADZE, S. S. *Fundamentals of Heat Transfer*. New York: Academic Press, 1963.

LEE, H.J.; LEE, S.Y. Heat transfer correlation for boiling flows in small rectangular horizontal channels with low aspect ratios. *Int. J. Multiphase Flow*, v. 27, n. 12, p. 2043–2062, 2001a.

LEE, H.J.; LEE, S.Y. Pressure drop correlations for two-phase flow within horizontal rectangular channels with small heights. *Int. J. Multiphase Flow*, v. 27, n. 5, p. 783–796, 2001b.

LI, W.; WU, Z. A general criterion for evaporative heat transfer in micro/mini-channels. *Int. J. Heat Mass Transfer*, v. 53, n. 9–10, p. 1967–1976, 2010.

LIEBENBERG, L.; MEYER, J. P. The Characterization of Flow Regimes with Power Spectral Density Distributions of Pressure Fluctuations During Condensation in Smooth and Micro-Fin Tubes. *Exp. Therm. Fluid Sci.*, v. 31, p. 127–140, 2006.

LIEBENBERG, L.; THOME, J. R.; MEYER, J. P. Flow Visualization and Flow Pattern Identification With Power Spectral Density Distribu-

- tions of Pressure Traces During Refrigerant Condensation in Smooth and Micro-Fin Tubes. *ASME J. Heat Transfer*, v. 127, p. 209–220, 2015.
- LIN, L.; PONNAPPAN, R. Heat transfer characteristics of spray cooling in a closed loop. *Int. J. Heat Mass Transfer*, v. 46, n. 20, p. 3737–3746, 2003.
- LIU, N.; LI, J. M.; SUN, J.; WANG, H. S. Heat Transfer and Pressure Drop during Condensation of R152a in Circular and Square Microchannels. *Experimental Thermal and Fluid Science*, v. 47, p. 60–67, 2013.
- LOCKHART, R.; MARTINELLI, R. Proposed correlation of data for isothermal two-phase, two-component flow in pipes. *Chem. Eng. Prog.*, v. 45, p. 39–48, 1949.
- LÓPEZ-BELCHÍ, A.; ILLÁN-GÓMEZ, F.; VERA-GARCÍA, F.; GARCÍA-CASCALES, J. R. Experimental Condensing Two-Phase Frictional Pressure Drop inside Mini-Channels: Comparisons and New Model Development. *International Journal of Heat and Mass Transfer*, v. 75, p. 581–591, 2014.
- LOUAHLIA-GUALOUS, H.; MECHERI, B. Unsteady steam condensation flow pattern inside a miniature tube. *Appl. Therm. Eng.*, v. 27, p. 1225–1235, 2007.
- MADDOX, D.E.; MUDAWAR, I. Critical heat flux in subcooled flow boiling of fluorocarbon liquid on a simulated electronic chip in a rectangular channel. *Int. J. Heat Mass Transfer*, v. 32, n. 2, p.379–394, 1989.
- MARTO, P. J. Condensation. In: ROHSENOW, W. M.; HARNETT, J. P.; CHO, Y. I. (Ed.). *Handbook of Heat Transfer* (3rd Ed). New York, NY: McGraw-Hill, 1998.
- MARTO, P.J.; LEPERE, V.J. Pool boiling heat transfer from enhanced surfaces to dielectric fluids. *J. Heat Transfer*, v. 104, n. 2, p. 292–299, 1982.
- MATKOVIC, M.; CAVALLINI, A.; DELCOL, D.; ROSSETTO, L. Experimental study on condensation heat transfer inside a single circular minichannel. *Int. J. Heat Mass Transfer*, v. 52, n. 9–10, p. 2311–2323, 2009.
- MCADAMS, W. H.; WOODS, W. K.; BRYON, R. L. Vaporization inside horizontal tubes-II: Benzene-oil mixtures. *Trans. ASME*, v. 64, p. 193–200, 1942.

MEDERIC, B.; LAVIEILLE, P.; MISCEVIC, M. Heat Transfer Analysis According to Condensation Flow Structures in a Minichannel. *Exp. Therm. Fluid Sci.*, v. 30, p. 785–793, 2006.

MEDERIC, B.; MISCEVIC, M.; PLATEL, V.; LAVIEILLE, P.; JOLY, J.-L. Experimental Study of Flow Characteristics during Condensation in Narrow Channels: The Influence of the Diameter Channel on Structure Patterns. *Superlattices Microstruct.*, v. 35, p. 573–586, 2004.

MEHENDALE, S. S.; JACOBI, A. M.; SHAH, R. K. Fluid Flow and Heat Transfer at Micro- and Meso-Scales with Applications to Heat Exchanger Design. *Applied Mechanics Review*, v. 53, p. 175–193, 2000.

MIKIELEWICZ, D.; ANDRZEJCZYK, R.; MIKIELEWICZ, J. Pressure drop of HFE7000 and HFE7100 in flow condensation in minichannels with account of non-adiabatic effects. *101 Eurotherm Seminar Transport Phenomena in Multiphase Systems (HEAT2014)*, June 30-July 3, 2014, Cracow, Poland, 2014.

MIKIELEWICZ, D.; ANDRZEJCZYK, R.; WAJS, J.; MIKIELEWICZ, J. A general method for calculation of two-phase flow pressure drop in flow boiling and flow condensation. *8th ECI International Conference on Boiling and Condensation Heat Transfer*, June 3-7, 2012, Ecole Polytechnique Fédérale de Lausanne (EPFL), Lausanne, Switzerland, 2012.

MIKIELEWICZ, D.; KLUGMANN, M.; ANDRZEJCZYK, R.; WAJS J. Experimental investigations on pressure drop during the condensation in flow of HFE7000 in vertical minichannel. *Proceeding of 15th International Conference on Heat Transfer and Renewable Sources of Energy (HTRSE2014)*, 10-13 September 2014, Szczecin – Międzyzdroje, Poland, 2014.

MIROPOLSKY, Z.L. Heat transfer during condensation of high-pressure steam inside a tube. *Teploenergetika*, v. 3, p. 79-83, 1962.

MISHIMA, K.; HIBIKI, T. Effect of Inner Diameter on Some Characteristics of Air-Water Two-Phase Flows in Capillary Tubes. *Trans JSME*, v. 61, n. 589, p. 99-106, 1995.

MISHIMA, K.; HIBIKI, T. Some characteristics of air-water two-phase flow in small diameter vertical tubes. *Int. J. Multiphase Flow*, v. 22, n. 4, p. 703–712, 1996.

- MONDE, M.; INOUE, T. Critical heat flux in saturated forced convective boiling on a heated disk with multiple impinging jets. *J. Heat Transfer*, v. 113, n.3, p. 722–727, 1991.
- MOSER, K.W.; WEBB, R.L.; NA, B. A new equivalent Reynolds number model for condensation in smooth tubes. *J. Heat Transfer*, v. 120, n. 2, p. 410-417, 1998.
- MUDAWAR, I. Two-phase micro-channel heat sinks: theory, applications and limitations. *J. Electron. Packaging –Trans. ASME*, v.133, p. 1-31, 2011.
- MUDAWAR, I.; HOWARD, A.H.; GERSEY, C.O. An analytical model for near-saturated pool boiling CHF on vertical surfaces. *Int. J. Heat Mass Transfer*, v. 40, n. 10, p. 2327–2339, 1997.
- MUELLER, A.C.; CHIOU, J.P. Review of various types of flow maldistribution in heat exchangers. *Heat Transfer Engineering*, v. 9, p. 36–50, 1988.
- MÜLLER-STEINHAGEN, H.; HECK, K. A Simple Friction Pressure Drop Correlation for Two Phase Flow in Pipes. *Chemical Engineering and Processing*, v. 20, n. 6, p. 297-308, 1986.
- MURPHY, D.L. Condensation heat transfer and pressure drop of propane in vertical minichannels, M. Sc. Thesis, Georgia Institute of Technology, Atlanta, GA, 2014.
- NAKAYAMA, W.; NAKAJIMA, T.; HIRASAWA, S. Heat sink studs having enhanced boiling surfaces for cooling of microelectronic components. *ASME*, Paper 84-WA/HT-89, 1984.
- NEBULONI, S.; THOME, J.R. Numerical modeling of laminar annular film condensation for different channel shapes. *Int. J. Heat Mass Transf.* v. 53, n. 13-14, p. 2615–2627, 2010.
- NUSSELT, W. Die Oberllachenkondensation des Wasserdampfes. *Z. VDI*, v. 60, p. 541-569, 1916.
- ODAYMET, A.; LOUAHLIA-GUALOUS, H.; DE LABACHELERIE, M. Local heat transfer and flow patterns during condensation in a single silicon microchannel. *Nanoscale Microscale Thermophys. Eng.*, v. 16, p. 220-241, 2002.
- OLIVIER, J. A.; LIEBENBERG, L.; THOME, J. R.; MEYER, J. P. Heat Transfer, Pressure Drop, and Flow Pattern Recognition During

Condensation inside Smooth, Helical Micro-Fin, and Herringbone Tubes. *Int. J. Refrig.*, v. 30, p. 609–623, 2007.

OTOMANSKI, P.; SZLACHTA, A. The evaluation of expanded uncertainty of measurement results in direct measurements using the LabVIEW Environment. *Measurement Science Review*, v. 8, n. 6, p. 147–150, 2008.

PARK, C. Y.; HRNJAK, P. S. CO₂ Flow Condensation Heat Transfer and Pressure Drop in Multi-Port Microchannels at Low Temperatures. *International Journal of Refrigeration*, v. 32, n. 6, p. 1129–1139, 2009.

PARK, I.; LEE, H.; MUDAWAR, I. Determination of flow regimes and heat transfer coefficient for condensation in horizontal tubes. *International Journal of Heat and Mass Transfer*, v. 80, p. 698–716, 2015.

PARK, J.E.; VAKILI-FARAHANI, F.; CONSOLINI, L.; THOME, J.R. Experimental study on condensation heat transfer in vertical minichannels for new refrigerant R1234ze(E) versus R134a and R236fa. *Exp. Therm. Fluid Sci.*, v. 35, n. 3, p. 442–454, 2011.

PETUKHOV, B. Heat transfer and friction in turbulent pipe flow with variable physical properties. *Advanced in Heat Transfer*, v. 61, p. 503–565, 1970.

PHILLIPS, R. *Forced convection, liquid cooled microchannel heat sinks*. M. Sc. Thesis - Department of Mechanical Engineering, Massachusetts Institute of Technology, Cambridge, MA, 1987.

PLATENBURG, T. Condensation in microchannels, Internship Final Report, *Eindhoven University of Technology*, 2016.

PORTEUS, A. Prediction of the upper limit of the slug flow regime. *Brit. Chem. Eng.*, v. 14, n. 9, p. 117–119, 1969.

RADOVCICH, N.A.; MOISSIS, R. The transition from two-phase bubble flow to slug flow. *Report No. 7-7673-22*, Mechanical Engineering Department, MIT, Cambridge, MA, 1962.

RAHIM, E.; REVELLIN, R.; THOME, J.R.; BAR-COHEN, A. Characterization and prediction of two-phase flow regimes in miniature tubes. *Int. J. Multiphase Flow*, v. 37, n. 1, p. 12–23, 2011.

RAMÍREZ-RIVERA, F.; LÓPEZ-BELCHÍ, A.; VERA-GARCÍA, F.; GARCÍA-CASCALES, J. R.; ILLÁN-GÓMEZ, F. Two Phase Flow Pressure Drop in Multiport Mini-Channel Tubes Using R134a and R32

As Working Fluids. *International Journal of Thermal Sciences*, v. 92, p. 17-33, 2015.

RIEHL, R.R.; OCHTERBECK, J.M. Experimental investigation of the convective condensation heat transfer in microchannel flows. *Proceedings of the 9th Brazilian Congress of Thermal Engineering and Sciences*, Caxambu, Minas Gerais, Brazil, Oct. 15–18, Paper No. CIT02-0495, 2002.

RIEHL, R.R.; SELEGHIM, P. JR.; OCHTERBECK, J.M. Comparison of Heat Transfer Correlations for Single- and Two-Phase Microchannel Flows for Microelectronics Cooling. *Paper Presented at the Sixth Inter-society Conference on Thermal and Thermomechanical Phenomena in Electronic Systems, 1998*. IOTHERM '98. 27-30 May, 1998.

ROHSENOW, W. M. Heat transfer and temperature distribution in laminar–film condensation. *Am. Soc. Mech. Eng. – Transac.*, v. 78, n. 8, p. 1645–1648, 1956.

ROSE, J. W.; WANG, H. Pressure drop during condensation in microchannels. *ASME 3rd Micro/Nanoscale Heat and Mass Transfer International Conference (MNHMT2012)*, Track 4: Nano/Microscale Boiling and Condensation Heat Transfer, Session: 4-4 Two-Phase Flow and Phase-Change Heat Transfer in Microchannels, MNHMT2012-75187, March 3-6, 2012, Atlanta, GA, 2012.

ROSSON, H.F.; MEYERS, J.A. Point values of condensing film coefficients inside a horizontal tube. *Chem. Eng. Prog. Symp. Ser.*, v. 61, n. 59, p. 190-199, 1965.

RUFER, C. E.; KEZIOS, S. P. Analysis of two-phase, one-component stratified flow with condensation. *Am. Soc. Mech. Eng. – Transac. – J. Heat Trans.*, v. 88, n. 3, p. 265–275, 1966.

RYBICKI, J.R.; MUDAWAR, I. Single-phase and two-phase cooling characteristics of upward-facing and downward-facing sprays. *Int. J. Heat Mass Transfer*, v. 49, n. 1-2, p. 5–16, 2006.

SAKAMATAPAN, K.; KAEW-ON, J.; DALKILIC, A. S.; MAHIAN, O.; WONGWISES, S. Condensation Heat Transfer Characteristics of R134a Flowing inside the Multiport Minichannels. *International Journal of Heat and Mass Transfer*, v. 64, p. 976-985, 2013.

SAKAMATAPAN, K.; WONGWISES, S. Pressure Drop During Condensation of R134a Flowing inside a Multiport Minichannel. *International Journal of Heat and Mass Transfer*, v. 75, p. 31-39, 2014.

SCHMIDT, E.; SCHURIG, W.; SELLSCHOP, W. Versuche iiber die Kondensation von Wasserdampf in Film- und Tropfenform. *Tech. Mech. Thermodyn.*, v. 53, n. 2, p. 53-63, 1930.

SERIZAWA, A.; FENG, Z.; KAWARA, Z. Two-Phase Flow in Microchannels. *Experimental Thermal and Fluid Science*, v. 26, n. 6&7, p. 703-714, 2002.

SHAH, M. M. A general correlation for heat transfer during film condensation inside pipes. *Int. J. Heat Mass Trans.*, v. 22, n. 4, p. 547-556, 1979.

SHAH, M.M. An improved and extended general correlation for heat transfer during condensation in plain tubes. *HVAC&R Res.*, v. 15, n. 5, p. 889-913, 2009.

SHIN, J. S.; KIM, M. H. An experimental study of flow condensation heat transfer inside circular and rectangular mini-channels, *Heat Trans. Eng.*, v. 26, n. 3, p. 36-44, 2005.

SIEDER, E.; TATE, G. Heat transfer and pressure drop of liquids in tubes. *Ind. Eng. Chem.*, v. 28, p. 1429-1435, 1936.

SINGH, A.; OHADI, M. M.; DESSIATOUN, S. V. Empirical modeling of stratified-wavy flow condensation heat transfer in smooth horizontal tubes. *ASHRAE Transac.*, v. 102, n. 2, p. 596-603, 1996.

SMITH, S.M.; TAFT, B.S.; MOULTON, J. Contact angle measurements for advanced thermal management technologies. *Front. Heat Mass Transfer (FHMT)*, v. 5, p. 1-9, 2014.

SOBHAN, C.B.; GARIMELLA, S.V. A comparative analysis of studies on heat transfer and fluid flow in microchannels. *Microscale Thermo-physical Engineering*, v. 5, n. 4, p. 293-311, 2001.

SOLIMAN, H. M. On the annular-to-wavy flow pattern transition during condensation inside horizontal tubes. *Can. J. Chem. Eng.*, v. 60, n. 4, p. 475-481, 1982.

SOLIMAN, H. M. Mist-annular transition during condensation and its influence on the heat transfer mechanism. *Int. J. Multiphase Flow*, v. 12, n. 2, p. 277-288, 1986.

- SOLIMAN, H. M.; SCHUSTER, J.R.; BERENSON, P.J. A general heat transfer correlation for annular flow condensation. *J. Heat Transfer*, v. 90, p. 267-276, 1968.
- SON, C. H.; OH, H. -K. Condensation Pressure Drop of R22, R134a and R410A in a Single Circular Microtube. *Heat and Mass Transfer*, v. 48, n. 8, p. 1437-1450, 2012.
- SON, C.H.; LEE, H.S. Condensation heat transfer characteristics of R-22, R134a and R-410A in small diameter tubes. *Heat Mass Transfer*, v. 45, n. 9, p. 1153-1166, 2009.
- SONG, T. Y.; YU, G. X.; MA, X. H.; ROSE, J. W.; WANG, H. S. Pressure drop during condensation in microchannels. *Proceedings of the ASME 2010 3rd Joint US-European Fluids Engineering Summer Meeting and 8th International Conference on Nanochannels, Microchannels, and Minichannels (FEDSM-ICNMM2010)*, FEDSMICNMM2010-30230, August 1-5, Montreal, Canada, 2010.
- SOUZA, A. L.; PIMENTA, M. M. Prediction of pressure drop during horizontal two-phase flow of pure and mixed refrigerants. *ASME Conference Cavitation and Multi-Phase Flow*, HTD, v. 210, p. 161-171, South Carolina, U. S. A, 1995.
- STEINKE, M.; KANDLIKAR, S. Single-phase and liquid friction factors in microchannels. *International Journal of Thermal Sciences*, v. 45, p. 1073-1083, 2006.
- SU, Q.; YU, G.X.; WANG, H. S.; ROSE, J.W. Microchannel condensation: Correlations and theory. *International Journal of Refrigeration*, v. 32, n. 6, p. 1149-1152, 2009.
- SUNG, M.K.; MUDAWAR, I. Experimental and numerical investigation of single phase heat transfer using a hybrid jet-impingement/microchannel cooling scheme. *Int. J. Heat Mass Transfer*, v. 49, n. 3-4, p. 682-694, 2006.
- TADMOR, R.; YADAV, P.S. As-placed contact angles for sessile drops. *Journal of Colloid and Interface Science*, v. 317, p. 241-246, 2008.
- TAITEL, Y.; DUKLER, A. E. A model for predicting regime transitions in horizontal and near horizontal gas-liquid flow. *AIChE Journal*, v. 22, p. 47-55, 1976.

TAITEL, Y.; DUKLER, A.E. Flow regime transitions for vertical upward gas-liquid flow: A preliminary approach through physical modeling. *Paper presented at Session on Fundamental Research in Fluid Mechanics at the 70th AIChE Annual Meeting*, New York, 1977.

TANASAWA, I. Advances in condensation heat transfer. In: HARTNETT, J. P.; JR., T. F. I.; CHO, Y. I. (Ed.). *Advances in Heat Transfer*. [S.l.]: Elsevier, v. 21, p. 55-139, 1991.

THOM, J. R. S. Prediction of pressure drop during forced circulation boiling of water, *Int. J. Heat Mass Trans.*, v. 7, n.7, p. 709-724, 1964.

THOME, J. R. Boiling in microchannels: a review of experiment and theory. *International Journal of Heat and Fluid Flow*, v. 25, n. 2, p. 128-139, 2004.

THOME, J. R.; BAR-COHEN, A.; REVELLIN, R.; ZUN, I. Unified mechanistic multiscale mapping of two-phase flow patterns in microchannels. *Experimental Thermal and Fluid Science*, v. 44, p. 1-22, 2003.

THOME, J. R.; CIONCOLINI, A. Unified modeling suite for two-phase flow, convective boiling and condensation in macro- and microchannels. *Proceedings of the Fourth Micro & Nano Flows Conference (MNF2014)*, 7-10 September 2014, University College London (UCL), London, UK, 2014.

THOME, J.R.; EL HAJAL, J.; CAVALLINI, A. Condensation in horizontal tubes, part 2: new heat transfer model based on flow regimes. *Int. J. Heat Mass Transfer*, v. 46, n. 18, p. 3365-3387, 2003.

TODA, S. A study in mist cooling (1st report: investigation of mist cooling), *Trans. JSME*, v. 38, n. 307, p. 581-588, 1972.

TRAVISS, D. P.; ROHSENOW, W. M.; BARON, A. B. Forced-convection condensation inside tubes: a heat transfer equation for condenser design. *ASHRAE Transac.*, v. 79, n. 1, p. 157-165, 1973.

TRIPLETT, K.A.; GHIAASIAAN, S.M.; ABDEL-KAHALIK, S.I.; SADOWSKI, D.L. Gas-liquid two-phase flow in microchannels Part I: two-phase flow patterns. *Int. J. Multiphase Flow*, v. 25, p. 377-394, 1999.

TUCKERMAN, D.B.; PEASE, R.F.W. High-performance heat sinking for VLSI. *IEEE Electron Device Lett*, v. 2, n. 5, p. 126-129, 1981.

VISARIA, M.; MUDAWAR, I. Theoretical and experimental study of the effects of spray orientation on two-phase spray cooling and critical heat flux. *Int. J. Heat Mass Transfer*, v. 51, n. 9-10, p. 2398–2410, 2008.

VIST, S.; PETTERSEN, J. Two-phase flow distribution in compact heat exchanger manifolds. *Experimental Thermal and Fluid Science*, v. 28, n. 2-3, p. 209-215, 2004.

ZANETTE, G.P. Condensação convectiva no interior de um perfil de alumínio tipo MPE contendo oito microcanais paralelos, *Master Thesis*, UFSC, 2015.

ZIVI, S. M. Estimation of steady-state steam void-fraction by means of the principle of minimum entropy production, *J. Heat Trans.*, v. 86, p. 247–252, 1964.

WADSWORTH, D.C.; MUDAWAR, I. Enhancement of single-phase heat transfer and critical heat flux from an ultra-high-flux-source to a rectangular impinging jet of dielectric liquid. *J. Heat Transfer*, v. 114, n. 3, p. 764–768, 1992.

WALLIS, G.B. *One-Dimensional Two-Phase Flow*. Wiley, New York, 1965.

WANG, H. S.; ROSE, J. W. Film condensation in horizontal triangular section microchannels: A theoretical model, *Proceedings of the Second International Conference on Microchannels and Minichannels (ICMM2004)*, June 17–19 2004, Rochester, NY, USA, American Society of Mechanical Engineers, New York, NY 10016-5990, USA, 661–666, 2004.

WANG, H.S.; ROSE, J.W. A theory of film condensation in horizontal noncircular section microchannels. *J. Heat Transfer*, v. 127, n. 10, p. 1096–1105, 2005.

WANG, H.S.; ROSE, J.W. Theory of heat transfer during condensation in microchannels. *Int. J. Heat Mass Transf.*, v. 54, n. 11–12, p. 2525–2534, 2011.

WANG, H. S.; ROSE, J. W. Heat Transfer and Pressure Drop during Laminar Annular Flow Condensation in Micro-Channels. *Experimental Heat Transfer*, v. 26, n. 2-3, p. 247-265, 2013.

WANG, H. S.; SUN, J.; ROSE, J. W. Pressure Drop during Condensation in Microchannels. *ASME Journal of Heat Transfer*, v. 135, n. 9, Article No. (091602), 2013.

WANG, W.W.; RADCLIFF, T.D.; CHRISTENSEN, R.N. A condensation heat transfer correlation for millimeter-scale tubing with flow regime transition. *Exp. Therm. Fluid Sci.*, v. 26, n. 5, p. 473-485, 2002.

WEBB, R.L. The evolution of enhanced surface geometries for nucleate boiling. *Heat Transfer Eng.*, v. 2, n. 3-4, p. 46-69, 1981.

WEBB, R.L. Prediction of condensation and evaporation in micro-fin and micro-channel tubes. In: KAKAC, S.; BERGLES, A.; MAYINGER, F.; YUNCU, H. (Eds.). *Heat Transfer Enhancement of Heat Exchangers*, Kluwer Academic Pub, Netherlands, v. 355, pp. 529-550, 1999.

WHITE, F. M. *Fluid Mechanics*, 3rd ed., McGraw-Hill, 1999.

WILLINGHAM, T.C.; MUDAWAR, I. Forced-convection boiling and critical heat flux from a linear array of discrete heat sources. *Int. J. Heat Mass Transfer*, v. 35, n. 11, p. 2879-2890, 1992.

YAN, Y.-Y.; LIN, T.-F. Condensation heat transfer and pressure drop of refrigerant R134a in a small pipe. *Int. J. Heat Mass Trans.*, v. 42, n. 4, p. 697-708, 1999.

YANG, C.-Y.; SHIEH, C.-C. Flow pattern of air-water and two-phase R134a in small circular tubes. *Int. J. Mult. Flow*, v. 27, n. 7, p. 1163-1177, 2001.

YANG, C.-Y.; WEBB, R. L. Condensation of R-12 in small hydraulic diameter extruded aluminum tubes with and without micro-fins. *Int. J. Heat Mass Trans.*, v. 39, n. 4, p. 791-800, 1996a.

YANG, C.-Y.; WEBB, R. L. Friction pressure drop of R-12 in small hydraulic diameter extruded aluminum tubes with and without micro-fins. *Int. J. Heat Mass Trans.*, v. 39, n. 4, p. 801-809, 1996b.

YANG, C.Y.; WEBB, R.L. A predictive model for condensation in small hydraulic diameter tubes having axial micro-fins. *J. Heat Transfer*, v. 119, n. 4, p. 776-782. 1997.

YOUNG, T. An Essay on the Cohesion of Fluids. *Philosophical Transactions of the Royal Society of London*, v. 95, pp. 65-87, 1805.

ZHANG M.; WEBB, R. L. Correlation of Two-Phase Friction for Refrigerants in Small-Diameter Tubes. *Experimental Thermal and Fluid Science*, v. 25, n. 3-4, p. 131-139, 2001.

ZHANG, H. -Y.; LI, J. -M.; LIU, N.; WANG, B. -X. Experimental Investigation of Condensation Heat Transfer and Pressure Drop of R22,

R410A and R407C in Mini-Tubes. *International Journal of Heat and Mass Transfer*, v. 55, n. 13-14, p. 3522-3532, 2012.

ZHANG, Z.; WENG, Z. L.; LI, T. X.; HUANG, Z. C.; SUN, X. H.; HE, Z. H.; VAN ES, J.; PAUW, A.; LAUDI, E.; BATTISTON, R. CO₂ Condensation Heat Transfer Coefficient and Pressure Drop in a Mini-Channel Space Condenser. *Experimental Thermal and Fluid Science*, v. 44, p. 356-363, 2013.

APPENDIX A CALIBRATION

Calibration is a comparison between a known measurement (standard) and the measurement using an instrument. The measuring instruments calibration has two objectives: checking the accuracy of the instrument and determining the traceability of the measurement. The calibration is important for many reasons. The accuracy of all measuring devices degrades over time; hence, it is fundamental to improve the accuracy of the measuring device through calibration. In order to determine the wall temperature and the heat flux independently, it is very important to measure temperature and heat flux accurately during the experimental investigation of the condensation process.

A.1 THERMOCOUPLES

The operation principle of the thermocouples is explained in Section 3.2.3. There are 16 E-type thermocouples and 4 T-type thermocouples installed on the test rig, and they were calibrated together.

The calibration curves of the thermocouples were drawn from a calibration setup that is described as follows. A thermal bath, of the manufacturer MICROQUIMICA, model MQBBMP-01, was used. This heat bath is equipped with both a heater and a cooler, with a supporting PID controller. The thermal bath was performed with demineralized water, and a RTD (resistance temperature detector) PT100 was used to measure the thermal bath temperature. The PT100 was manufactured by ECIL, has a length of 350-mm, and a diameter of 6-mm.

For the calibration run, five reference thermocouples were used: 2 T-type and 3 E-type thermocouples. More than one of each thermocouple type is used as reference in order to create a comparative and assuring process in case of a thermocouple malfunction. The reference thermocouples are immersed in an adiabatic vessel filled with semi-frozen bath of demineralized water at atmospheric pressure. The reference temperature is known, and equal to 0°C. The insulated bottle opening, through which all the reference thermocouples are inserted, is closed using aluminum foil for further thermal insulation.

The thermocouples ends (also called cold junction) consist of thermocouples connectors, which are connected to thermocouple extension cables. Finally, these extension cables were connected to a data acquisition system AGILENT 34901A multiplexer, which was used to measure the voltage over the wire.

The hot joints are the thermocouple joints that are in contact with the surface of which it is desired to measure the temperature. In the calibration run, the thermocouples were not glued to the test section in order to prevent unnecessary gluing of broken thermocouples; instead, the hot junctions are grouped in a copper tube to ensure that all junctions remain at the same temperature. Inside the thermal bath, the copper tube is inserted into a large glass tube in order to keep the thermocouples at uniform temperature and to avoid the thermal bath convection from directly reaching the copper tube. The water exchange inside the glass tube is mainly given by the upper opening, since the thermal bath wall caps the lower opening, where the tube is supported. The hot joints of the E-type and T-type thermocouples and the PT100 are located inside the glass tube.

It is important to verify the actual temperature in the thermal bath. In order to determine the resistance at the ice point ($R_{0^{\circ}\text{C}}$), a RTD PT100 was inserted into the same insulated bottle where the reference thermocouples are located, The PT100 was calibrated by ECIL Metrology Laboratory, and the results provided by the calibration report were used. The temperature ($t^{\circ}\text{C}$) was related to the thermometer resistance $R_{t^{\circ}\text{C}}$ and the resistance at the ice point $R_{0^{\circ}\text{C}}$ by equation:

$$R_{t^{\circ}\text{C}}/R_{0^{\circ}\text{C}} = 1 + At + Bt^2 \quad (\text{A.1})$$

Where $a = 3.9116 \times 10^{-3}$, $b = -5.8279 \times 10^{-7}$ and $R_{0^{\circ}\text{C}} = 99.62649 \Omega$.

In the calibration run, the temperature measurement range should be larger than the final experimental range. Two thermocouple calibration runs were performed. The first run was carried out at increasing temperature, i.e. the thermal bath was started at 0°C and was heated up to 50°C , increasing 5°C at each run. Since the first test was conducted at 0°C , ice was formed in the heat bath, which made the bath temperature very unstable. The second calibration run was performed at decreasing temperature in order to avoid temperature instability. The tests started at 50°C and the thermal bath temperature was lowered by 5°C each test.

Using equation A.1, it becomes clear that the indicated temperature on the thermal bath display is not as accurate as the indicated by PT100, according to the table A.1:

Table A.1: Comparison of the thermal bath temperature indicated in the display to the measured by the PT100

Thermal Bath Temperature (°C)	PT100 Temperature (°C)	R (°t)	R (0°C)	a	b	c
0	0,165241944	99,69088	99,62649	-5,8E-07	0,003912	-0,00065
5	4,337293118	101,3156	99,62649	-5,8E-07	0,003912	-0,01695
10	9,431538123	103,2968	99,62649	-5,8E-07	0,003912	-0,03684
15	14,43779921	105,2408	99,62649	-5,8E-07	0,003912	-0,05635
20	19,39784425	107,164	99,62649	-5,8E-07	0,003912	-0,07566
25	24,39119061	109,0972	99,62649	-5,8E-07	0,003912	-0,09506
30	29,41102037	111,0377	99,62649	-5,8E-07	0,003912	-0,11454
35	34,49029192	112,9983	99,62649	-5,8E-07	0,003912	-0,13422
40	39,36466608	114,8769	99,62649	-5,8E-07	0,003912	-0,15308
45	44,25707229	116,7597	99,62649	-5,8E-07	0,003912	-0,17197
50	48,95872454	118,5665	99,62649	-5,8E-07	0,003912	-0,19011

The difference between the hot (where the measurement is required) and cold (located inside the multiplexer) joints is a voltage between the thermocouple wires, as shown in equation A.2:

$$T - T_{env} = f(V) = \alpha V + \beta \quad (\text{A.2})$$

Where T is the hot joint temperature and T_{env} is temperature of the cold joint. The α and β are the slope and the y-intercept of the linear equation, respectively.

The difference between the environmental temperature (cold joint) and the reference thermocouple at ice point is a function of the electromotive force, V_0 :

$$T_{env} - T_0 = f(V_0) = \alpha_0 V_0 + \beta_0 \quad (\text{A.3})$$

Adding equations A.2 and A.3, and replacing $T_0 = 0^\circ\text{C}$:

$$T = f(V) - f(V_0) = \alpha V - \alpha_0 V_0 + \beta - \beta_0 \quad (\text{A.4})$$

The desired temperature, T , is then determined by the measured voltages and the curve coefficients of each thermocouple. It is possible to group β and β_0 as β_T , and α and α_0 as α_T :

$$T = \alpha_T (V - V_0) + \beta_T \quad (\text{A.5})$$

Therefore, the thermocouple calibration equation A.5 is a function of the electromotive force measured between the thermocouple being calibrated and the reference thermocouple. Although the curve is

linear, it may have small deviations, which increase the measurement uncertainty. In order to increase the accuracy, the following third-degree polynomial function was used:

$$T = \alpha_T(V - V_0)^3 + \beta_T(V - V_0)^2 + \gamma_T(V - V_0) + \delta_T \quad (\text{A.6})$$

The reference thermocouple of each calibrated thermocouple was chosen based on the smallest standard deviation. In regard to safety, more thermocouples than necessary were calibrated, but the curve coefficients shown in table A.2 refer to the ones with the lowest error margin:

Table A.2: Coefficients calculated from the calibration curves for each thermocouple

Thermocouple	α ($^{\circ}\text{C}/\text{V}^3$)	β ($^{\circ}\text{C}/\text{V}^2$)	γ ($^{\circ}\text{C}/\text{V}$)	δ ($^{\circ}\text{C}$)
104E	2,00E+07	-135168	-17204	0,1738
106E	4,00E+07	-38444	-17033	0,4966
214E	-4,00E+06	-203893	-17175	1,5743
105E	3,00E+07	-103364	-17149	0,2881
107E	4,00E+07	-31629	-16982	0,6141
215E	9,00E+08	4,00E+06	-19767	-8,0983
216E	6,00E+06	-164530	-17095	1,6196
217E	1,00E+07	-127063	-17105	1,6333
218E	1,00E+09	5,00E+06	-18247	-7,1624
108E	7,00E+07	153073	-16694	1,1143
109E	8,00E+07	190598	-16633	1,232
111E	9,00E+07	236435	-16623	1,3521
212E	1,00E+09	5,00E+06	-18515	-7,5641
213E	-6,00E+06	-201110	-17115	1,6967
219E	1,00E+09	6,00E+06	-17113	-6,2041
220E	5,00E+07	81174	-16683	2,2975
202T	-2,00E+08	-1,00E+06	-26953	0,0492
207T	-2,00E+08	-1,00E+06	-26211	1,1414
209T	3,00E+08	455038	-24733	1,6244
210T	6,00E+07	-203631	-25337	1,6327

An uncertainty analysis of the thermocouples measurements is present in the following. The calibration polynomial function, the data acquisition system, and the RTD PT100 are all sources of uncertainty. The uncertainty of each source must be calculated in order to find the final uncertainty of the thermocouples. One method of calculating the

polynomial uncertainty is the differentiation of the function for the respective variable. Thus, deriving equation A.6 with respect to V and V_0 :

$$\frac{\partial T}{\partial V} = 3\alpha(V - V_0)^2(1) + 2\beta(V - V_0)(1) + \gamma \quad (\text{A.7})$$

$$\frac{\partial T}{\partial V_0} = 3\alpha(V - V_0)^2(-1) + 2\beta(V - V_0)(-1) - \gamma \quad (\text{A.8})$$

The expanded measurement uncertainty of the PT100 was given by its calibration report:

$$u(T_{PT100}) = 0.01 \quad [^{\circ}\text{C}] \quad (\text{A.9})$$

The polynomial obtained for each thermocouple using the coefficients of table A.2 shows a small deviation from the real value measured by the PT100. This uncertainty, $u(T_{pol})$, can be estimated by the standard deviation between the residuals, which are the differences in the temperatures indicated by the PT100 and the temperature calculated using the polynomial:

$$u(T_{pol}) = \sqrt{\left(\frac{1}{n-1}\right) \sum_{i=1}^n (T_{PT100} - T_{pol})^2} \quad (\text{A.10})$$

Where n is the number of acquisitions made, T_{PT100} is the temperature indicated by the PT100 and T_{pol} is the thermocouple temperature calculated using the polynomial. The mean polynomial uncertainties related to the E-type thermocouples were $u(T_{pol})_E = 0.07609 \text{ } ^{\circ}\text{C}$ and to the T-type thermocouples $u(T_{pol})_T = 0.11504 \text{ } ^{\circ}\text{C}$. During the calibration run, intervals were made with a total of $n=300$ acquisitions each.

According to the data acquisition system manufacturer, Agilent, its uncertainty is described by the following equations:

$$u(V) = 0.005\%V + 4E - 06 \quad (\text{A.11})$$

$$u(V_0) = 0.005\%V_0 + 4E - 06 \quad (\text{A.12})$$

However, this is the voltage uncertainty. In order to obtain the actual data acquisition system uncertainty $u(T_v)$ the propagated uncertainty concept must be used. Therefore, knowing that the temperature is a function of the voltage difference between the thermocouple being calibrated and the reference thermocouple:

$$u(T_v) = \sqrt{\left(\frac{\partial T_{pol}}{\partial V} u(V)\right)^2 + \left(\frac{\partial T_{pol}}{\partial V_0} u(V_0)\right)^2} \quad (\text{A.13})$$

The multiplexer uncertainty mean values obtained for the E-type and T-type thermocouples were $u(T_v)_E = 0.13$ °C and $u(T_v)_T = 0.10$ °C, respectively.

Finally, knowing the polynomial $u(T_{pol})$, data acquisition system $u(T_v)$, and PT100 $u(T_{PT100})$ uncertainties, it is possible to calculate the combined standard uncertainty in temperature measurement using equation A.14:

$$u_c(T) = \sqrt{u^2(T_{pol}) + u^2(T_v) + u^2(T_{PT100})} \quad (\text{A.14})$$

The results of the mean uncertainty calculated for the two thermocouples types were close: $u_c(T)_E = 0.150963$ °C and $u_c(T)_T = 0.152756$ °C. For a 95% confidence interval, the expanded uncertainty of the thermocouples can be obtained using Student's t-distribution ($t=2$). Therefore, the expanded uncertainty of the temperature measurement can be approximated for both thermocouples types and is equal to: $U(T) = \pm 0.30$ °C.

A.2 HEAT FLUX SENSORS

The operation principle of the heat flux sensors is explained in Section 3.2.4. A total of 11 heat flux sensors were calibrated together, but only 8 are actually installed in the test section. The calibration occurred at LMPT, and was conducted by Professor Saulo Guths.

The calibration of the heat flux sensors was performed using two heat flux sensors, a skin-heater resistance, and an aluminum heat sink. For the calibration run, a sandwich-shaped assembly was made with the electric resistance in the middle of the two heat flux sensors. The heat flux sensor to be calibrated is in contact with an aluminum heat sink, in

order to dissipate the heat generated by the resistor into the environment; while on the opposite side, in contact with the auxiliary heat flux sensor, a good thermal insulation is done, as show in the diagram of figure A.1.

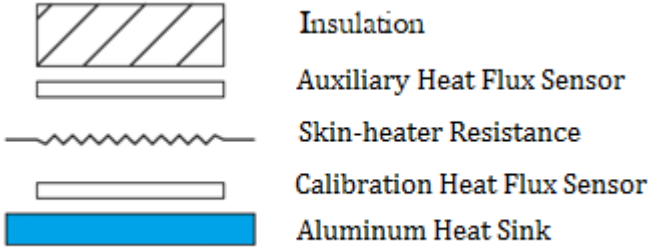


Figure A.1: Diagram of the heat flux sensors calibration

Each sensor was soldered to a simple thin wire, which was connected to the multiplexer Agilent 34901A.

The calibration procedure described in this document is called the auxiliary heat flux sensor method. The heat flux generated is transferred to both sides of the skin-heater resistance, and it will be measured by the two heat flux sensors installed in the calibration set-up. The heat flux lost by each side is negligible because of the small thickness of the sensors and the resistance.

The skin-heater resistance was connected to a power supply Agilent, model N5769A. It was supplied 2.84 V of voltage and 0.43 A of current, totalizing a power supply of 1.2212 W. Knowing the power supplied to the resistor, the voltage of both sensors were measured. By the interaction technique, it was possible to determine the calibration constants of each heat flux sensor, as shown in Table A.3. The sensors installed in the test section are marked with an X. The criterion chosen was the smallest constants; however, the heat flux sensors number 2 and 9 presented good calibration values but were damaged.

The calibration curve of a heat flux sensor is linear, and the constant-coefficient is equal to zero since when the heat flux is zero, the voltage measured by the sensor is zero. The calibration equation is as follows:

$$q = CV \quad (\text{A.15})$$

The heat flux (W) is represented by q ; C is the calibration-constant found (W/V) and V is the voltage (V) measured by the sensor.

The accuracy of each heat flux sensor is 3% of the measured value, according to the manufacturer. The sensors are impermeable, since the hoses that connect the bath to the heat sink generally get wet because the bath fluid temperature (ethylene glycol + water) is too low. The heat flux sensors lose some sensitivity due to that fact.

Table A.3: Heat Flux Sensor Calibration

	Calibration Heat Flux Sensor ($10^{-6} V$)	Auxiliary Heat Flux Sensor ($10^{-6} V$)	Constant (W/V)	Installed
1	690	20	1598,429319	X
2	735	74	1617,483444	
3	893	45	1337,568456	X
4	851	55	1402,06659	X
5	1929	64	626,5777322	X
6	1755	73	688	X
7	200	45	5550,909091	
8	543	52	2169,094139	X
9	964	49	1241,056911	
10	800	52	1489,268293	X
11	1018	72	1176,493256	X

APPENDIX B SETUP CORRECTIONS

The test rig used to carry out the present study was projected by Goss (2011), and later modified by Zanette (2015). Even though improving the experimental setup is not a goal, some setup corrections were done. As it is inherent in any experimental work, several setup problems were found. A detailed description of these problems and the measures taken to solve them is presented in this appendix.

B.1 LEAKAGE

The major problem faced while preparing the test rig was leakage. As discussed in Chapter 3, several components and equipment are connected using flared copper tubes and copper fitting connections. The test rig has already presented this problem before, as reported by Platenburg (2016). He disassembled the entire setup, tightened all connections, and redid the tube flaring. Although the leakage was vastly decreased, the problem persisted.

At the start of this study, the test rig was in accordance with figure B.1. Then, insulations were removed, and the test section was provisionally replaced with a cooper tube in order to search for leakage points.

Since it was not possible to move the test rig, submerging it in water to find leakage points indicated by air bubbles coming out was not an option. The leak testing using helium could not be done either. Thus, the chosen method for leak detection was to pressurize the test rig and then cover the area to be tested with a soap and water solution. If soap bubbles are formed, a leakage point was found. During the first test, compressed air was used to pressurize the test rig up to 7 bar. After 10 hours, the test rig pressure had decreased to 2 bar. No bubble formation was noted at the tubes, only in the fitting connections. The first step was to further tighten these connections. If it did not improve the situation, the connections were then opened and inspected. Alcohol was used to clean them, a Teflon paste was applied and, in some cases, the flare of the tube had to be redone. The Teflon paste manufactured by Quimatic, shown in figure B.2, proved to be more efficient than the Teflon tape used before. In some cases, it was necessary to buy new tubes and connections even though they were not included in the project budget.

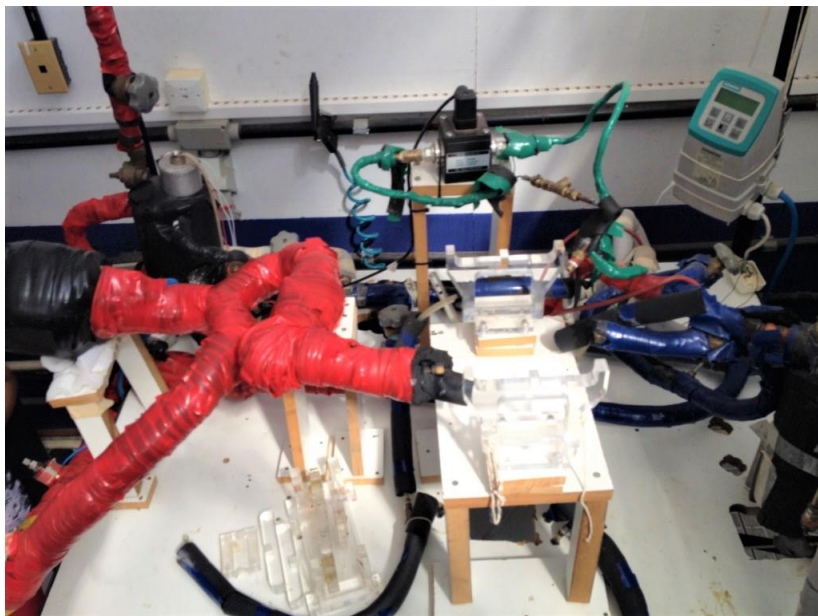


Figure B.1: Test rig at the beginning



Figure B.2: Thread sealant (Teflon paste) with PTFE applied to the connections in order to prevent leakage

As the fitting connections were being repaired, the test rig pressure drop was lower at each test. After all repairs, the last leak testing using compressed air indicated a pressure drop of less than 1 bar, but no further leakage points were found using the soap-water method. Pressurizing the setup with an air compressor, and visualizing it with a soap-water mixture allows to find most leakages, however, smaller leakages are difficult to find. The test fluid was then changed from compressed air to nitrogen. Nitrogen has a lower density than air, it is inert, dry, and does not react with refrigerants. In addition, it was possible to pressurize the test rig up to 12 bar using nitrogen. It was also helpful to use a more dense soap, and mirrors, to see all the connections angles.

Using nitrogen, micro-leaks were found. For a definitive resolution of these micro-leaks, it was essential to use appropriate glue. It is shown in figure B.3 the two glues used at this stage. The TEKBOND 115 was used in connections that could be dismantled later; while on the others, TEKBOND 138 was used. Both glues prevent leakage and loosening due to vibrations. The vast majority of connections that needed glue application were those in which the thread was badly damaged and could not be redone or changed. The glue needs 24 hours of curing, which makes this process time-consuming. Finally, a nitrogen test at 12 bar was performed and the pressure was maintained for more than 24 hours.

Although the leak detection process is time consuming, it is very important to ensure that there is no leakage in the setup, especially with the pressure range in which the tests with R134a were realized.

B.2 BOILER LEVEL GAUGE

As shown in figure B.1 and highlighted in figure B.4, the boiler did not have a level gauge. A direct consequence of the level gauge absence is the facility with which the resistance can burn, which incidentally was the case before this study started. On this opportunity, a resistance with the largest possible cold joint size was requested in order to avoid burning the resistance when the boiler level was low. In any case, the boiler still requires a minimum level of fluid. For that reason, a suitable hose, which withstands high pressures and temperatures, has been attached to the boiler, as shown in figure 26. In addition, since the hose is transparent, the boiler level can now be controlled. The fluid level inside the boiler can not be too low or too high in order to prevent the resistance from burning and the boiler from overflowing. If the fluid overflows, the liquid phase might reach the Coriolis flowmeter, which in

turn is unable to measure the mass flow when the fluid is in the two-phase form. Hence, only vapor can pass through to the mass flowmeter.



Figure B.3: Seal glues used in order to prevent leakage



Figure B.4: Boiler at the beginning

B.3 IMPROVEMENTS

A few other less complex improvements are now listed. The Coriolis flowmeter was fixed to the test rig in order to avoid measurement errors due to excessive vibration. Several connections were replaced, and the flare tubes remade. Some connections and tubes had to be replaced with new ones even though this was not the purpose of the present study. The boiler's power supply has been changed. The electrical source was previously controlled according to the desired steam temperature; which is not optimal, since the temperature is constant during the fluid phase change that occurs in the boiler. Thus, the power supplied to the resistor is now performed by a variable transformer, described in section 3.1.1. The pump was installed below the setup level to facilitate its flooding, especially during the setup loading process. A new test section was made, since the previous one was broken. Modifications were made to the manifolds as described in section 3.1.3.2.

APPENDIX C SUGGESTIONS FOR IMPROVEMENT

In this appendix, some suggestions that can improve the test rig performance are presented. These changes were not in this study scope.

C.1 PROGRAMMABLE LOGIC CONTROLLER

A programmable logic controller (PLC) is a specialized computer used to control machines and processes. In this way, it is mostly used to control automated systems in industries. A PLC was designed and assembled for Zanette's (2015) study. It was projected to automate the pump's rotation and the boiler resistance control through the differential pressure at the test section, the test rig flow rate, and the boiler temperature measurements. During his work, the PLC was responsible only for the boiler resistance control using the PT100 temperature. Thus, the PLC was never fully used and that was one the goals of this work. Nonetheless, after several different approaches, it was concluded that some modifications should be made in the PLC in order for it to fit the test rig's automation requirements. In what follows, it is presented the PLC original design and the proposed modifications.

The PLC is equipped with a frequency inverter, two proportional integral derivative (PID) controllers (LFS and LFS-mA), a serial converter, and other electrical elements as solid-state relay (SSR). Next, each equipment function is described. The Expectron Tecnologia Industrial Ltda was the company responsible for the project of the PLC.

C.1.1 Frequency inverter

A frequency inverter (FI) manufactured by WEG, model CFW500, controls the speed and torque of a three-phase induction motor, which is coupled with the pump. The FI does that by changing the output voltage frequency and magnitude. In other words, it is used to control the motor rotation, allowing the pump's control automation.

The analog input of the FI is directly connected to the analog output of the LFS-mA controller, which controls the absolute pressure at the test section inlet from an absolute pressure transducer (section 3.1.9) and mass flow rate from the Coriolis flowmeter (section 3.1.8) . The LFS-mA controller operation is explained in the next section. The FI is indirectly connected to the LFS controller, because the LFS is connected to the LFS-mA.

The FI has a mini USB output (plug-in module) that can be connected directly to a computer via a USB port with an appropriate cable. The FI data can be acquired by the SuperDrive G2 software. Also, the FI can be connected to the computer using a serial cable and the data can be acquired using the Elipse SCADA software.

Among the advantages of including a frequency inverter in the experimental setup, besides the process automation, are elimination of heavy and complicated starting elements; increased equipment life; reduction of noise level; excellent regulation of pressure and flow; and energy saving.

C.1.2 Proportional integral derivative controller

A PID is a control loop feedback mechanism, which continuously calculates an error value as the difference between a desired set point and a measured process variable. As the name suggests, PID algorithm consists of three basic coefficients: proportional, integral and derivative, which are varied to get optimal response. The basic idea behind a PID controller is to read a sensor, then compute the desired actuator output by calculating proportional, integral, and derivative responses and summing those three components to compute the output.

Two types of PID controllers are used, both manufactured by EroEletronic. The PID controller LFS controls the temperature inside the boiler using a RTD sensor, PT100. This instrument recognizes both sensors (TC or RTD).

The PT100 is connected to the LFS analog input (three-wire) while the LFS digital output is connected to a solid-state relay (SSR). An SSR is an electronic component totally in solid state, that is, it does not have mechanical elements or any type of moving part, therefore much used in the control of temperature. The SSR, in turn, is connected to the boiler resistance. In this way, the PID controller LFS receives information about the boiler temperature from the PT100, then calculates the error between the settled and measured boiler temperatures, and depending on the error value, it acts on the boiler resistance, turning it on or off.

The second PID controller, LFS-mA, controls the pump's rotation. Such control is performed from the actuation of the controller in the FI. The control is performed by either of two variables: pressure or flow rate. There is a switch on the PLC that selects between these parameters. In that way, the analogic output of the PID controller LFS-mA is connected to the analogic input of the FI. Its analogic input (4-20 mA)

is connected to the analogic output of either the Coriolis flowmeter or the pressure transducer. The LFS-mA can only receive data from one measuring instrument at a time.

C.1.3 Serial converter

Serial communication in the PLC is performed by RS-485, which is a standard that defines the data transmission scheme. Digital communications networks implementing this standard can be used effectively over long distances and in electrically noise environments. Multiple receivers may be connected to such a network in a linear, multi-drop configuration. Thereby, the RS-485 has been established for the PLC since it is necessary to connect the FI and the two PID controllers to the same network. Differently, the RS-232 standard is used for serial communication transmission of data to/from a computer in a single device-to-device interface.

Because of the different serial interfaces, a serial converter RS-485 / RS-232 is needed. It transmits data between the PLC components and a computer. The serial converter used was manufactured by Ex-pectron Tecnologia Ltda. A serial cable connects a PC to the serial converter.

The common protocol used in the PLC for data communication is Modbus. Hence, the FI, the two PDI controllers, the serial converter, and the computer driver must be properly configured in the same protocol. In order to facilitate the setup and information exchanges, Elipse Scada software was used, which has an extra driver available for connecting to the Modbus network. RTU mode is used.

The configuration used for data transmission is shown in figure C.1. The baud rate, data bits, parity and stop bits parameters must be configured the same way on all devices. The DTR (Data Terminal Ready), RTS (Request to Send) control, delay before and after send, inter-byte and inter-frame delay are crucial information for precise and reliable connection between the PC and the PLC.

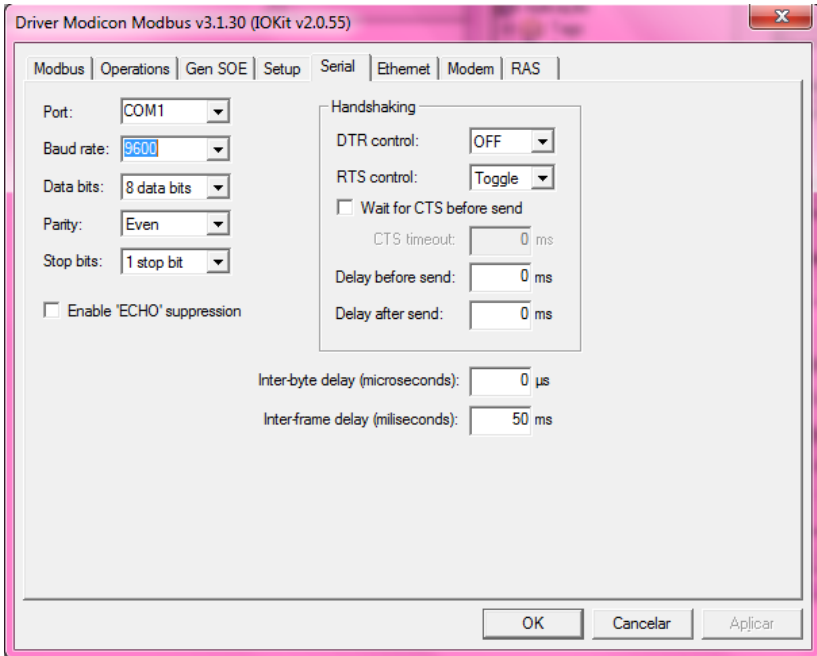


Figure C.1: Serial communication at Elipse Scada Software

C.1.4 Proposed PLC modifications

In order for the PLC to fit the test rig's automation requirements a few modifications are required:

- The boiler's resistance should not be controlled by the temperature of the fluid inside the boiler, which is measured by the PT100. As explained in section 4.1.2, the dissipated power in the boiler's electrical resistance, Q_{boiler} , directly affects the mass flux, G . Therefore, the boiler's resistance must be controlled by the mass flux value. The fluid temperature measured by the PT100 is not the ideal control method since, during the fluid boiling, its temperature is constant. Furthermore, G is a test condition, while the fluid temperature inside the boiler is not. During the tests, it was noted that the mass flux is highly susceptible to the steam production rate at the boiler; hence, to the power supplied to the boiler's resistance.

- As also presented in section 4.1.2, the temperature change of the post condenser thermal bath is a more decisive influence than the

pump's rotation, regarding the inlet pressure at test section. As such, the automation of fluid flow rate should not be performed by measuring the inlet pressure at test section, but by measuring the temperature of the post condenser.

C.2 OTHER SUGGESTIONS

Other proposed improvements for the experimental setup are summarized in this section:

- Adjust all equipment and pipework at a single level, in order to avoid unnecessary pressures losses. As the experimental setup is rigid, at least a drain valve should be installed at the lowest part of the boiler. The boiler is located at a slightly lower level than the post condenser. Thus, unloading the test rig, which is only possible by the valve located at the post condenser bottom, leaves residual fluid in the boiler. Therefore, a drain located at the boiler is necessary to avoid fluid waste.

- Install thermocouples at the heat sink. During tests, it would be valuable to compare the temperature at the heat sink with the wall temperatures of the test section.

- Since it was not possible to install an absolute pressure transducer in the boiler, a more economical solution to ascertain the state (vapor or liquid) in which the fluid leaves the boiler is to install a sight glass at the boiler outlet.

- Replace several unnecessary connections that are susceptible to leakage with a single tube.

- It is important to control the overheated temperature of the fluid during tests. It is desired that this temperature is not greater than 1°C above the saturation temperature. The fluid passes through the superheater, explained in section 3.1.2, before reaching the test section. The power supplied to the superheater resistance is kept constant. Nonetheless, it is noted that the fluid temperature at the superheater outlet oscillates. Thus, another suggestion is to replace the superheater with a boiler or, in a less complex way, a thermal bath.

- A filter before the test section inlet seems essential to keep little particles from accumulating, or even obstructing the small diameter of the minichannels. Although a filter is installed before the pump, a thinner filter should be placed right before the test section inlet in order to further prevent unwanted particles from contaminating the fluid.

- Replace the heat sinks for water jackets as Koyama et al. (2003a) work to study the heat sink influence on q'' .

- Provide a pre-condenser (that can be connect to a thermal bath, just like the post condenser) in order to achieve low vapor qualities at the test section.

- Compare the influence of the flow direction at the heat sink, i.e. compare the parallel flow and the counterflow.

- Increase the test section length, and consequently the heat sinks length, in order to raise the possibility of the fluid condensing, and also obtaining lower vapor qualities.

APPENDIX D SINGLE-PHASE FLOW TESTS RESULTS

Performing single-phase tests are extremely important for the study validation in the two-phase flow area. Correlations and models for pressure drop and heat transfer work for micro and macrochannels, and formulations have been proposed for single-phase flow since the beginning of the last century. Therefore, the measurement, data acquisition, and data reduction procedures are validated using single-phase flow results. In other words, if the experimental and theoretical results show good agreement, the test rig and the experimental procedure are well established.

The single-phase flow tests were performed with R134a in the vapor state. The conditions of the single-phase tests are similar to those of the two-phase flow tests. In this manner, single-phase flow tests were carried out in ten different conditions, as shown in table D.1, which include:

Table D.1: Single-phase flow tests conditions

Inlet temperature at the test section [°C]	$29.8 < T_i < 35.6$
Mass flux [kg/(m ² s)]	$402 < G < 512$
Heat flux [kW/m ²]	$8.5 < q'' < 9.9$
Inlet pressure at the test section [bar]	$7.5 < P_i < 8.9$

D.1 PRESSURE DROP

The experimental pressure drop values acquired during single-phase flow tests are compared to Blasius correlation (1913), presented in equation 2.38, and to Phillips (1987) correlation, shown in equation 2.39.

The charts depicted in figures D.1 and D.2 present the comparisons of experimental results obtained for pressure drop with Blasius's and Phillips's models described in section 2.8.1. The mean absolute error (MAE) is calculated analogous to that presented section 5.3.5, equation 5.6.

The MAE value reached by Blasius (1913) correlation is 12.3%, and by Phillips (1987) is 13.5%. These correlations errors can be considered acceptable, which indicate that the methodology and the pressure drop measurement are valid.

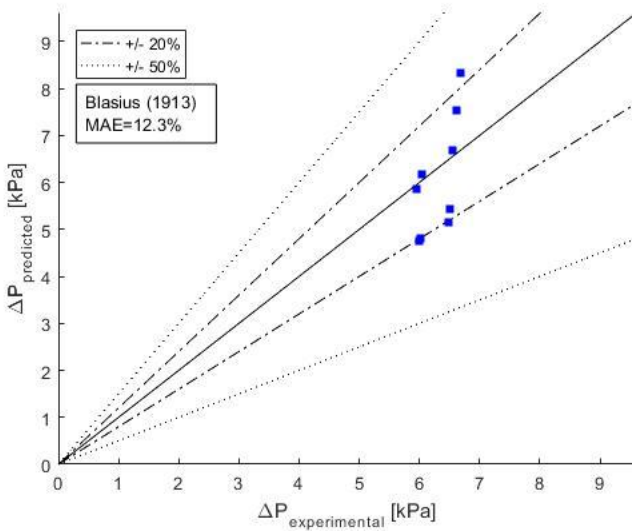


Figure D.1: Comparison of experimental pressure drop with Blasius (1913) correlation

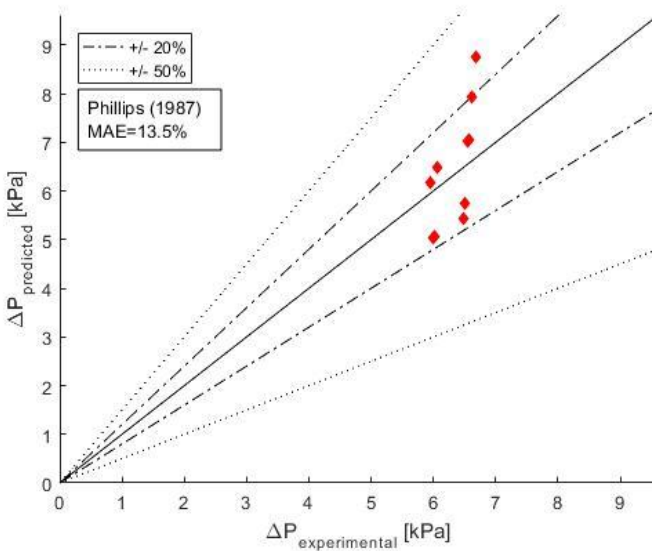


Figure D.2: Comparison of experimental pressure drop with Phillips (1987) correlation

D.2 HEAT TRANSFER

The single-phase heat transfer coefficient, h_v , is calculated similarly to the two-phase heat transfer coefficient, as shown in the chapter 4 of the present document. The correlations used to compare the predicted and experimental heat transfer coefficient values for single-phase flow are Dittus-Boelter (1930), equation 2.69, Sieder and Tate (1936), equation 2.70, Petukhov (1970), equation 2.71, and Gnielinski (1976), equation 2.72. These comparisons are shown in figures D.3-D.6.

The four models presented close and low MAE values, therefore the experimental heat transfer coefficients are well related to all formulations used.

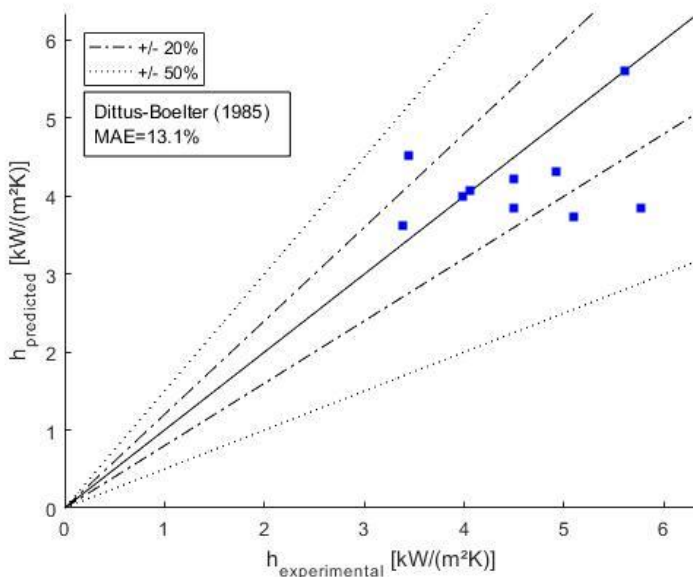


Figure D.3: Comparison of experimental heat transfer coefficient with Dittus-Boelter (1930) correlation

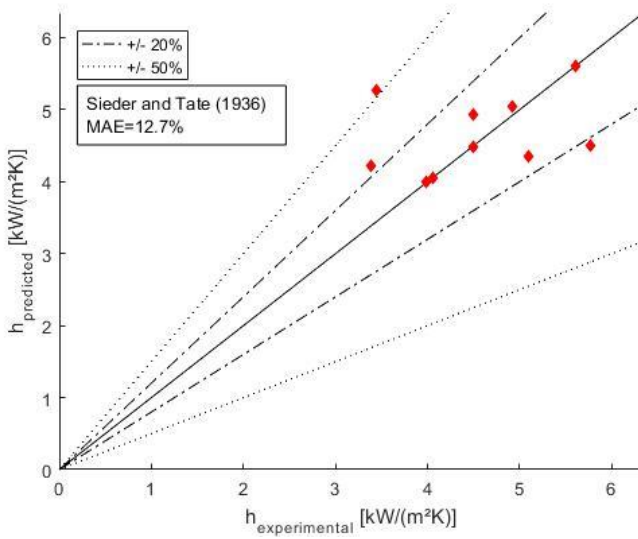


Figure D.4: Comparison of experimental heat transfer coefficient with Sieder and Tate (1936) correlation

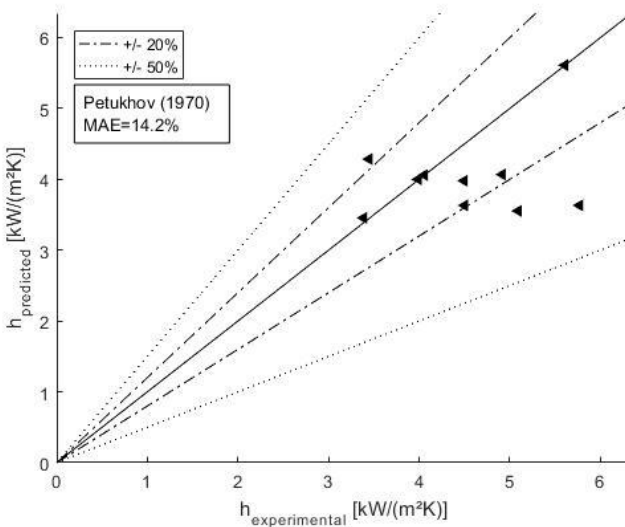


Figure D.5: Comparison of experimental heat transfer coefficient with Petukhov (1970) correlation

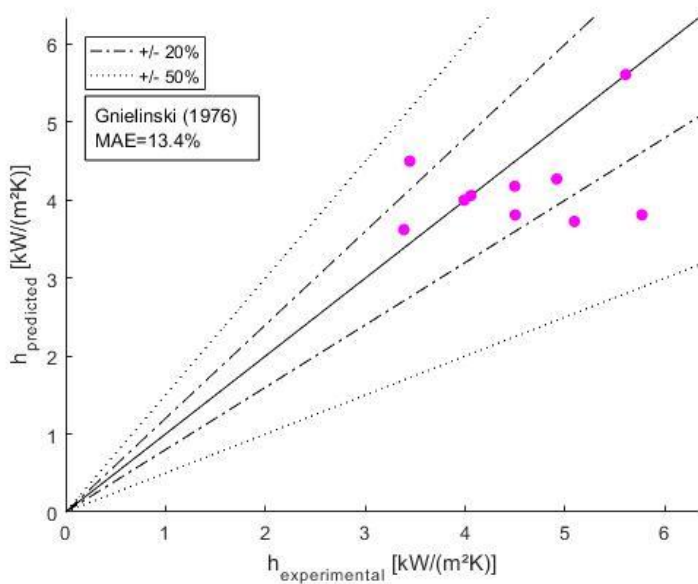


Figure D.6: Comparison of experimental heat transfer coefficient with Gnielinski (1976) correlation

APPENDIX E EXPERIMENTAL UNCERTAINTY ON THE CALCULATION OF THE HEAT TRANSFER COEFFICIENT

In this appendix, the methodology for calculating the experimental uncertainty of the heat transfer, h , is presented. It follows the method demonstrated by Otomanski and Szlachta (2008).

Equation E.1 defines the heat transfer coefficient during condensation:

$$h = \frac{q''}{T_{sat} - T_w} \quad (E.1)$$

Where q'' , T_w and T_{sat} represent heat flux [W/m²], average wall temperature [°C] and fluid temperature in function of its local pressure [°C], respectively.

The heat transfer coefficient expanded uncertainty, $U(h)$, is obtained by multiplying the combined standard uncertainty $u_c(h)$ by a coverage factor k :

$$U(h) = k \cdot u_c(h) \quad (E.2)$$

The value of the coverage factor k is chosen on the basis of the level of confidence required. Considering that the probability distribution characterized by h is approximately normal and the effective degrees of freedom of $u_c(h)$ is of significant size, it is assumed that taking $k=2$ produces an interval having a level of confidence of approximately 95 percent.

The combined standard uncertainty, $u_c(h)$, is calculated as shown in equation E.3:

$$u_c(h) = \sqrt{\left[\frac{\partial h}{\partial q''} u(q'') \right]^2 + \left[\frac{\partial h}{\partial T_w} u(T_w) \right]^2 + \left[\frac{\partial h}{\partial T_{sat}} u(T_{sat}) \right]^2} \quad (E.3)$$

Where $u(q'')$, $u(T_w)$ and $u(T_{sat})$ are the standard uncertainties of each variable.

The $u(T_w)$ value is obtained from the thermocouple calibration, presented in Appendix A, since the T_w value used on h calculation is the average of measurements. Therefore, since the wall temperature is measured using E-type thermocouples, $u_c(T_w) = 0.15^\circ\text{C}$.

The heat flux, q'' , equation is shown in E.4:

$$q'' = \frac{Q}{2A_{hfs}} \quad (\text{E.4})$$

Where Q is the power removed through the heat flux sensors [W], and A_{hfs} is the area of a single heat flux sensor [m²].

A caliper rule was used to measure the heat flux sensor dimensions. Its uncertainty is 0.01 mm, and compared to the heat flux sensor uncertainty, which is 3% of the measured value, can be disregarded. As a result, $u(q'') = 0.13 \text{ W}$.

The most difficult uncertainty value to estimate is the saturation temperature of the fluid. This value is calculated as a function of the local fluid pressure. In this study, 4 different pressures were tested at the test section inlet; 7, 7.5, 8, and 9 bar. A temperature curve as a function of pressure was plotted using EES software. The local fluid pressure, P , is the fluid pressure at the test section inlet subtracted by the pressure drop between the inlet and the location where P is being evaluated. So, the uncertainty of the local fluid pressure can be estimated as follows:

$$u(P) = \sqrt{u^2(P_{inlet}) + u^2(\Delta p)} \quad (\text{E.5})$$

As shown in section 3.2.2, $u(p_{inlet}) = 0.02 \text{ kgf/cm}^2$, or 0.0196 bar and $u(\Delta p) = 1200 \text{ Pa}$, or 0.012 bar. As a result, $u(p) = 0.023 \text{ bar}$. Finally, $u_c(h) = 3.87\%$, and $U(h) = 7.74\%$.